


ADVERTIMENT. L'accés als continguts d'aquesta tesi queda condicionat a l'acceptació de les condicions d'ús establertes per la següent llicència Creative Commons:  <https://creativecommons.org/licenses/?lang=ca>

ADVERTENCIA. El acceso a los contenidos de esta tesis queda condicionado a la aceptación de las condiciones de uso establecidas por la siguiente licencia Creative Commons:  <https://creativecommons.org/licenses/?lang=es>

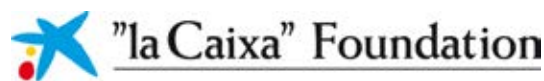
WARNING. The access to the contents of this doctoral thesis it is limited to the acceptance of the use conditions set by the following Creative Commons license:  <https://creativecommons.org/licenses/?lang=en>

Unfolding the challenges to prepare epitaxial complex oxide membranes by chemical methods

Pol Sallés Perramon

Under the supervision and tutoring of:

Dr. Mariona Coll Bau



Universitat Autònoma de Barcelona
Institut de Ciència de Materials de Barcelona (ICMAB-CSIC)

Doctoral INPhINIT "La Caixa" fellowship

Thesis submitted for the degree of Doctor of Philosophy
PhD programme in Materials Science

March 2023


Dr. Mariona Coll Bau, tenured scientist at the Institut de Ciència de Materials de Barcelona - Consejo Superior de Investigaciones Científicas

CERTIFY

That Pol Sallés Perramon carried out under her direction the research work entitled “Unfolding the challenges to prepare epitaxial complex oxide membranes by chemical methods”. This work has been developed within a PhD program in Materials Science at the department of chemistry of Universitat Autònoma de Barcelona.

For that record they sign the certificate.

Bellaterra, March 2023

A handwritten signature in black ink, appearing to read 'Mariona Coll Bau', with a large, sweeping flourish at the end.

Dr. Mariona Coll Bau

Acknowledgements

First, I would like to express my deepest gratitude to my supervisor, Dr. Mariona Coll, for always being there supportive. Mariona backed me up throughout the whole PhD, guiding, inspiring and motivating me. I particularly appreciate and will take with me her endless effort and patience, her motivation and her way of keeping the mood up in the face of setbacks and finding the best out of any outcome.

Sincere thanks go to our many collaborators who have made this thesis possible. Dr. Roger Guzmán and Prof. Wu Zhou from the University of Chinese Academy of Sciences (China) for the STEM characterizations of our heterostructures and membranes. Dr. David Zanders and Prof. Anjana Devi from Ruhr University Bochum (Germany) for kindly synthesizing the Fe precursor. Dr. Dimitris Kazazis, Dr. Helmut Schiff and Konrad Vogelsang from Paul Scherrer Institut (PSI, Switzerland) for all the work optimizing the membrane transfer and the warm welcome I received during my stay there. And all our collaborators from ICMAB: Aleix Barrera and Dr. Anna Palau for all the help with the electrical measurements, Dr. Alberto Quintana and Dr. Ignasi Fina for their help with the magnetic analyses, Raul Solanas and Dr. Florencio Sánchez for the PLD and RHEED analysis, Huan Tan and Dr. Ignasi Fina for the PFM measurements and the ferroelectric discussions and Dr. Camilla Dore and Dr. Agustín Mihi for sharing their knowledge on PDMS stamps. I should also acknowledge all the people who provided access to their experimental facilities, including Dr. Sebastian Reparaz for the equipment used for room temperature resistivity analysis (ICMAB), Prof. Josep Fontcuberta for the ferroelectric and photoresponse equipment (ICMAB) and Dr. Jose Santiso and Dr. Jose Manuel Caicedo Roque for the access to RHEED (ICN2).

I also want to express my gratitude to all the members of the research group that have shared with me these years of thesis making it more enjoyable and have contributed making this project possible in team rather than as individuals. Thank you, Pamela and Pengmei for teaching and helping me since I started this adventure and being my colleagues during the journey. I owe to Pamela my learnings in solution processing, BFO and photovoltaic devices. On the other hand, Pengmei is who introduced me into the complexity of ALD processing. Ivan, Aina, Eva and Rik also contributed in different stages of this work during their short stay as master or

graduate students. Ivan helped developing the SAO sacrificial, Aina explored other sacrificial, Eva helped optimizing ALD processes and Rik demonstrated enormous patience building the new ALD reactor. I am grateful for each of your contributions and hope that you too took the learning back with you. Finally, Martí thank you for your help during these last months, I hope that you continue this project with motivation and I will be looking forward to the outcomes!

I would like to acknowledge all the technicians that have contributed to this project. Special thanks to Mariona de Palau for taking care of the labs making our work there much easier. Thanks to Xavi Sintas for his huge contribution on the electronics of the new ALD system and for all his knowledge provided. Thanks to the XRD team, Anna, Xavi and Joan, for helping me always that I needed it and for the endless patience with my usual urgent requests (I owe you a ham!). Thanks to the NANOQUIM clean room team, Marta, Luigi, Neus and Rosa, for always being there rearranging my scheduled experiments. Thanks to Raul for all the work with PLD and RHEED, Guillaume for the XPS, Bernat and Ferran for the SQUID and Maite for the AFM.

I acknowledge the doctoral INPhINIT “La Caixa” fellowship for the financial support. The project that gave rise to these results received the support of a fellowship from “la Caixa” Foundation (ID 100010434). The fellowship code is LCF/BQ/DI19/11730026. This work was also funded by MICIN/AEI/10.13039/501100011033/FEDER through the projects Severo Ochoa MAT2017-83169-R, FUNFUTURE CEX2019-00917-S, PID2020-114224RBI00 and TED2021-130402B-I00. We also acknowledge the financial support from the 2020 Leonardo Grant for Researchers and Cultural Creators BBVA Foundation, the i-link A20346-CSIC project and the EU’s Horizon 2020 research and innovation programme under grant agreement N^o 101007417, having benefited from the access provided by PSI in Switzerland within NFFA-ID069.

Last but not least, I would like to extend my gratitude to my family and friends that accompanied me during these years. In ICMAB I have been privileged to share my stay with many people that have made this period of my life a very special one, specially my lunch team (Marina, Eulalia, Juan, Rubén, Charlotte, Pablo, Rafa, Taniya, Espe, Marta, Raul, Alejandro, Martí...) and all the people in SUMAN group (Pamela, Aleix, Thomas, Jordi, Arthur,...). At home, my deepest gratitude goes to my family and Aina for their constant support and unconditional love over the years.

Abstract

Epitaxial complex oxide materials exhibit a vast range of functional properties desirable for next-generation electronic, spintronic, magnetic, and energy applications. However, because the epitaxial layers are covalently bonded to monocrystalline substrates, only limited applications were explored. The recent development of lift-off techniques has introduced a new way to produce freestanding membranes providing an unprecedented opportunity to study these materials free from the substrate restrictions, which offers the possibility to explore novel heterointegration approaches and expands the toolkit for engineering their functional parameters. One of the most promising lift-off strategies is the use of a sacrificial layer which allows the epitaxial growth of an oxide on top and then it can be dissolved by selective etching. In particular, water-soluble $\text{Sr}_3\text{Al}_2\text{O}_6$ (SAO) has demonstrated great potential and high versatility using high vacuum and in-situ deposition techniques. Nonetheless, this sacrificial layer could have wider applicability by finding low-budget and versatile synthesis approaches that could deliver less strict deposition conditions allowing to prepare more freestanding oxide compositions and further intricate heterostructures.

This thesis explores the pioneering idea of introducing chemical deposition techniques as cost-effective, sustainable and potentially scalable route to prepare freestanding epitaxial complex oxides by means of a SAO sacrificial layer. In order to tackle such an ambitious goal, this study focus on the synthesis process prioritizing the use of chemical solution deposition (CSD) and atomic layer deposition (ALD). The key challenges at each step of the process are identified from the development of the SAO sacrificial and the heterostructure materials compatibility to the release of the freestanding epitaxial oxides. Special emphasis has been placed on the preparation of CoFe_2O_4 (CFO), $\text{La}_{0.7}\text{Sr}_{0.3}\text{MnO}_3$ (LSMO) and BiFeO_3 (BFO) membranes and combinations of them, to ultimately fabricate a functional device.

First, a low-cost and facile CSD process is developed to prepare SAO for its use as sacrificial layer. Two different chemical formulations are proposed and their resulting characteristics compared in terms of morphology and crystalline quality in order to obtain dense, homogeneous and epitaxial SAO films. Nevertheless, ambient exposure of the sacrificial layer results on an

amorphous capping layer that hinders the possibility to grow an epitaxial oxide on top. In this regard, special focus goes to overcome the SAO instability and broaden its applicability opening the possibility to ex-situ growth deposition techniques. To tackle this issue it has been combined cation engineering in SAO together with an in-vacuum post-annealing process. Here a systematic study on the influence of Ca-substitution in $\text{Sr}_{3-x}\text{Ca}_x\text{Al}_2\text{O}_6$, (SC_xAO) demonstrates that it is an effective tool to tune the sacrificial layer lattice parameter, crystallinity, reactivity with water and ambient stability, while the vacuum post-annealing on the sacrificial allows to reverse the damage caused by ambient exposure

Then, the viability to use SAO-CSD to obtain epitaxial oxide membranes is explored. Prioritizing the use of chemical methods, the challenges behind the use of ALD and CSD to direct deposit the oxide on the sacrificial layer have been investigated with special focus on crystallinity, cation intermixing at the interface and transfer yield. It has been found out that ALD allows to obtain CFO and BFO membranes whose crystalline quality is dictated by the quality of the SC_xAO underneath. On the other hand, the direct deposit of BFO-CSD on SAO has shown to put the stability of the system at risk. As an alternative path, it is explored an hybrid approach in which it is combined LSMO prepared by pulsed laser deposition (PLD) on SC_xAO -CSD sacrificial layer aiming to improve the membrane quality and offering a more versatile platform to prepare membranes. An exhaustive study on the role of Ca-substitution in the sacrificial to the subsequent LSMO growth is carried out showing the critical effect on parameters such as LSMO crystallinity, strain, interface reactivity and electrical properties. Upon SC_xAO etching, it is achieved the release of epitaxial LSMO membranes with crack density directly related the strain released and a metal-insulator transition around 300 K. The possibility to integrate the freestanding membranes to arbitrary substrates is also demonstrated.

Taking the preparation of epitaxial LSMO membranes as a building block, it is aimed to prepare a multilayered oxide heterostructure to ultimately fabricate a photovoltaic device integrating the photoferroelectric BFO component. To pursue this goal, first it has been optimized the growth of the different oxide components (ZnO, Al-ZnO and BFO) by chemical methods on rigid substrates. Then, it has been combined with LSMO membranes to finally deliver an all-oxide device showing ferroelectric behaviour and photoresponse as a proof of principle and laying the groundwork for further improvement.

Overall, this thesis presents an unprecedented platform to widen the library of freestanding complex oxide membranes from the more robust SC_xAO sacrificial layer working in a less restrictive conditions and it opens the door to all the know-how on epitaxial complex oxides by chemical methods to be merged in the novel and promising world of the freestanding epitaxial oxides.

Resumen

Los óxidos complejos epitaxiales presentan una amplia gama de propiedades funcionales deseables para futuras aplicaciones en electrónica, espintrónica, magnetismo y energía. Sin embargo, estas capas epitaxiales están unidas covalentemente a sustratos monocristalinos y hace que las aplicaciones que se han explorado sean muy limitadas. El desarrollo reciente de técnicas que permiten separar las capas epitaxiales del sustrato de crecimiento ha introducido una nueva forma de producir membranas que brindan una oportunidad sin precedentes para estudiar estos materiales sin las restricciones del sustrato, lo que ofrece la posibilidad de explorar nuevos enfoques de heterointegración y amplía las herramientas para manipular sus parámetros funcionales. Una de las estrategias de separación más prometedoras es el uso de una capa de sacrificio que permita el crecimiento epitaxial del óxido sobre ella y que luego pueda disolverse selectivamente. En particular, la fase hidrosoluble $\text{Sr}_3\text{Al}_2\text{O}_6$ (SAO) ha demostrado un gran potencial y versatilidad preparada mediante técnicas de deposición de alto vacío e in-situ. No obstante, esta capa de sacrificio podría tener mayor aplicabilidad si se encontraran métodos de síntesis versátiles y económicos que proporcionaran condiciones de deposición menos estrictas, permitiendo así preparar una mayor variedad de composiciones y heteroestructuras complejas.

Esta tesis explora la idea pionera de introducir técnicas de deposición química como ruta de bajo coste, sostenible y potencialmente escalable para preparar óxidos complejos epitaxiales sin soporte mediante la capa de sacrificio SAO. Para abordar este ambicioso objetivo, este estudio se centra en el proceso de síntesis priorizando el uso de la deposición química en solución (CSD) y la deposición de capas atómicas (ALD). Se han identificado los retos más importantes en cada paso del proceso, desde el desarrollo de la capa SAO y su compatibilidad con los otros materiales de la heteroestructura hasta la separación de los óxidos epitaxiales para conseguir membranas. Se ha hecho particular énfasis en la preparación de membranas de CoFe_2O_4 (CFO), $\text{La}_{0.7}\text{Sr}_{0.3}\text{MnO}_3$ (LSMO) y BiFeO_3 (BFO), así como en la combinación de las mismas, para finalmente fabricar un dispositivo funcional.

En primer lugar, se ha desarrollado un proceso CSD para preparar SAO para su uso como capa

de sacrificio. Se proponen dos formulaciones químicas distintas y se comparan sus características resultantes en términos de morfología y calidad cristalina para obtener capas de SAO densas, homogéneas y epitaxiales. No obstante, la exposición ambiente de la capa de sacrificio da lugar a una fina capa amorfa superficial que dificulta la posibilidad de hacer crecer un óxido epitaxial encima. En este sentido, se presta particular atención a superar la inestabilidad del SAO y ampliar su aplicabilidad abriendo la posibilidad a técnicas de deposición ex-situ. Para tratar este factor, se ha combinado la ingeniería de cationes en SAO junto con un post-procesado en vacío. Un estudio sistemático sobre la influencia de la sustitución de Ca en $\text{Sr}_{3-x}\text{Ca}_x\text{Al}_2\text{O}_6$, (SC_xAO) demuestra que es una herramienta eficaz para ajustar el parámetro de celda de la capa de sacrificio así como su cristalinidad, reactividad con el agua y estabilidad ambiental, mientras que el post-procesado en vacío sobre la capa de sacrificio permite revertir el daño causado por la exposición ambiental.

A continuación, se ha explorado la viabilidad de utilizar SAO-CSD para obtener membranas de óxidos epitaxiales. Priorizando el uso de métodos químicos, se han investigado los desafíos que plantea el uso de ALD y CSD para depositar un óxido directamente sobre la capa de sacrificio, con especial interés en la cristalinidad, la interdifusión de cationes en la interfase y la calidad de la transferencia. Se ha constatado que el ALD permite obtener membranas de CFO y BFO cuya calidad cristalina viene dictada por la calidad del SC_xAO subyacente. Por otro lado, se ha revelado que el depósito de BFO-CSD directo sobre SAO pone en riesgo la estabilidad del sistema.

Como vía alternativa, se explora un enfoque híbrido en el que se combina LSMO preparado por deposición por láser pulsado (PLD) sobre la capa de sacrificio SC_xAO -CSD con el objetivo de mejorar la calidad de la membrana y ofrecer una plataforma más versátil para preparar membranas. Se ha llevado a cabo un estudio exhaustivo sobre la influencia que tiene la sustitución de Ca en la capa de sacrificio sobre el posterior crecimiento de LSMO, mostrando un efecto crítico en ciertos parámetros del LSMO como su cristalinidad, tensión, reactividad en la interfase y propiedades eléctricas. Tras la disolución de SC_xAO , se consigue la liberación de membranas epitaxiales de LSMO con una densidad de fisuras directamente relacionada con la tensión liberada y mostrando comportamiento metálico a temperatura ambiente. También se demuestra la posibilidad de integrar las membranas liberadas en otros sustratos arbitrarios.

Tomando como base la preparación de membranas epitaxiales LSMO, se ha querido preparar una heteroestructura multicapa de óxidos para finalmente fabricar un dispositivo fotovoltaico que integre el componente fotoferroeléctrico BFO. Para alcanzar este objetivo, en primer lugar se ha optimizado el crecimiento de los diferentes componentes de óxido (ZnO, Al-ZnO y BFO) por métodos químicos sobre sustratos rígidos. A continuación, se ha combinado con membranas LSMO para obtener finalmente un dispositivo compuesto íntegramente por una multicapa de óxidos sin soporte fijo que ha demostrado comportamiento ferroeléctrico y fotorrespuesta, constituyendo así una prueba de concepto y sentando las bases para futuras mejoras.

En conjunto, esta tesis presenta una plataforma sin precedentes para ampliar la biblioteca de membranas de óxidos complejos a partir de una capa de sacrificio SC_xAO más robusta y en unas condiciones menos restrictivas usando métodos químicos. Por lo tanto, se abre una posibilidad inmensa de ampliar el conocimiento establecido hasta el momento sobre óxidos complejos epitaxiales trasladándolo en el novedoso y prometedor mundo de los óxidos epitaxiales sin soporte.

Resum

Els òxids complexes epitaxials presenten una àmplia gamma de propietats funcionals desitjables per a futures aplicacions en electrònica, espintrònica, magnetisme i energia. No obstant, aquestes capes epitaxials estan unides covalentment a substrats monocristal·lins el qual fa que les aplicacions que s'han explorat siguin molt limitades. El recent desenvolupament de tècniques que permeten separar les capes epitaxials del substrat de creixement ha introduït una nova forma de produir membranes que brinden una oportunitat sense precedents per estudiar aquests materials sense les restriccions del substrat, cosa que ofereix la possibilitat d'explorar nous enfocaments d'heterointegració i amplia les eines per manipular els seus paràmetres funcionals. Una de les estratègies de separació més prometedores és l'ús d'una capa de sacrifici que permeti el creixement epitaxial de l'òxid sobre ella i que després es pugui dissoldre selectivament. En particular, la fase hidrosoluble $\text{Sr}_3\text{Al}_2\text{O}_6$ (SAO) ha demostrat un gran potencial i versatilitat preparada mitjançant tècniques de deposició d'alt buit i in-situ. Tot i així, aquesta capa de sacrifici podria tenir una aplicabilitat més amplia si es trobessin mètodes de síntesi versàtils i econòmics que proporcionessin condicions de deposició menys estrictes, permetent així preparar una major varietat de composicions i heteroestructures complexes.

Aquesta tesi explora la idea pionera d'introduir tècniques de deposició química com a ruta de baix cost, sostenible i potencialment escalable per preparar òxids complexes epitaxials sense suport mitjançant la capa de sacrifici SAO. Per abordar aquest ambiciós objectiu, aquest estudi es centra en el procés de síntesi prioritzant l'ús de la deposició química en solució (CSD) i la deposició de capes atòmiques (ALD). S'han identificat els reptes més importants en cada pas del procés, des del desenvolupament de la capa SAO i la seva compatibilitat amb els altres materials de l'heteroestructura fins a la separació dels òxids epitaxials per aconseguir membranes. S'ha posat particular èmfasi en la preparació de membranes de CoFe_2O_4 (CFO), $\text{La}_{0.7}\text{Sr}_{0.3}\text{MnO}_3$ (LSMO) i BiFeO_3 (BFO), així com en la combinació d'aquestes, per finalment fabricar un dispositiu funcional.

En primer lloc, s'ha desenvolupat un procés CSD per preparar SAO per ser utilitzat com

a capa de sacrifici. Es proposen dues formulacions químiques diferents i se'n comparen les característiques resultants en termes de morfologia i qualitat cristal·lina per obtenir capes de SAO denses, homogènies i epitaxials. No obstant, l'exposició ambiental de la capa de sacrifici dona lloc a una fina capa amorfa superficial que dificulta la possibilitat de fer-hi créixer un òxid epitaxial a sobre. En aquest sentit, s'ha posat èmfasi en superar la inestabilitat del SAO i ampliar-ne l'aplicabilitat obrint la possibilitat a tècniques de deposició ex-situ. Per tractar aquest factor, s'ha combinat l'enginyeria de cations en SAO juntament amb un post-processat en buit. Un estudi sistemàtic sobre la influència de la substitució de Ca a $\text{Sr}_{3-x}\text{Ca}_x\text{Al}_2\text{O}_6$, (SC_xAO) demostra que és una eina eficaç per ajustar el paràmetre de cel·la de la capa de sacrifici així com la seva cristal·linitat, reactivitat amb l'aigua i l'estabilitat ambiental, mentre que el post-processat en buit sobre la capa de sacrifici permet revertir els danys causats per l'exposició ambiental.

A continuació, s'ha explorat la viabilitat de fer servir SAO-CSD per obtenir membranes d'òxids epitaxials. Prioritzant l'ús de mètodes químics, s'han investigat els reptes que planteja l'ús d'ALD i CSD per dipositar un òxid directament sobre la capa de sacrifici, amb un interès especial en la cristal·linitat, la interdifusió de cations en la interfase i la qualitat de la transferència. S'ha constatat que l'ALD permet obtenir membranes de CFO i BFO, la qualitat cristal·lina de les quals ve dictada per la qualitat del SC_xAO subjacent. D'altra banda, s'ha vist que el dipòsit de BFO-CSD directe sobre SAO posa en risc l'estabilitat del sistema.

Com a via alternativa, s'explora un enfocament híbrid en què es combina LSMO preparat per deposició per làser polsat (PLD) sobre la capa de sacrifici SC_xAO -CSD amb l'objectiu de millorar la qualitat de la membrana i oferir una plataforma més versàtil per preparar membranes. S'ha dut a terme un estudi exhaustiu sobre la influència que té la substitució de Ca en la capa de sacrifici sobre el posterior creixement de LSMO, mostrant un efecte crític en certs paràmetres del LSMO com la seva cristal·linitat, tensió, reactivitat a la interfase i propietats elèctriques. Després de la dissolució de SC_xAO , s'aconsegueix l'alliberament de membranes epitaxials de LSMO amb una densitat d'esquerdes directament relacionada amb la tensió alliberada i mostrant comportament metàl·lic a temperatura ambient. També es demostra la possibilitat d'integrar les membranes alliberades en altres substrats arbitraris.

Prenent com a base la preparació de membranes epitaxials de LSMO, s'ha volgut preparar una

heteroestructura multicapa d'òxids per finalment fabricar un dispositiu fotovoltaic que integri el component fotoferroelèctric BFO. Per assolir aquest objectiu, en primer lloc, s'ha optimitzat el creixement dels diferents components òxids (ZnO, Al-ZnO i BFO) per mètodes químics sobre substrats rígids. Tot seguit, s'ha combinat amb membranes LSMO per obtenir finalment un dispositiu compost íntegrament per una multicapa d'òxids sense suport fix que ha demostrat comportament ferroelèctric i fotoresposta, constituint així una prova de concepte i establint les bases per a futures millores.

En conjunt, aquesta tesi presenta una plataforma sense precedents per ampliar la biblioteca de membranes d'òxids complexes a partir d'una capa de sacrifici SC_xAO més robusta i en unes condicions menys restrictives utilitzant mètodes químics. Per tant, s'obre una possibilitat immensa d'ampliar el coneixement establert fins el moment sobre òxids complexes epitaxials traslladant-lo al emergent i prometedor món dels òxids epitaxials sense suport.

Contents

Acknowledgements	iii
Abstract	v
1 Introduction	1
1.1 Complex oxides for energy and electronic applications	1
1.1.1 Heteroepitaxial growth	3
1.1.2 Freestanding epitaxial complex oxides	4
1.1.3 $\text{Sr}_3\text{Al}_2\text{O}_6$ (SAO) sacrificial layer	15
1.2 Chemical deposition techniques for complex oxide thin films	20
1.2.1 Chemical Solution Deposition (CSD)	21
1.2.2 Atomic Layer Deposition (ALD)	23
1.3 Scope and outline of this thesis	29
1.3.1 Scope	29
1.3.2 Thesis outline	30
2 Experimental	33
2.1 Thin films synthesis	33
2.1.1 Chemical Solution Deposition (CSD)	33
2.1.2 Atomic Layer deposition (ALD)	40
2.1.3 Pulsed Laser Deposition (PLD)	48
2.2 Sacrificial etching and membrane lift-off	49
2.3 Characterization	51

2.3.1	Solution characterization	52
2.3.2	Structure characterization	53
2.3.3	Surface morphology characterization	60
2.3.4	Thickness analysis	62
2.3.5	Chemical composition characterization	64
2.3.6	Physical properties characterization	64
3	Facile chemical route to prepare water soluble epitaxial $\text{Sr}_3\text{Al}_2\text{O}_6$ sacrificial layers for free-standing oxides	69
	Supporting Information	84
4	Bendable polycrystalline and magnetic CoFe_2O_4 membranes by chemical methods	85
	Supporting Information	106
5	On the role of the $\text{Sr}_{3-x}\text{Ca}_x\text{Al}_2\text{O}_6$ sacrificial layer composition for epitaxial $\text{La}_{0.7}\text{Sr}_{0.3}\text{MnO}_3$ membranes	107
5.1	Introduction	108
5.2	Results and Discussion	111
5.2.1	Structural analysis	111
5.2.2	Electrical properties	118
5.2.3	Freestanding epitaxial LSMO	119
5.3	Conclusion	122
5.4	Supporting Information	123
6	Towards freestanding BiFeO_3 heterostructures for all-oxide photovoltaics	129
6.1	Introduction	130
6.2	ZnO, Al-doped ZnO and BiFeO_3 by ALD-type approach towards all-oxide photovoltaics	135
6.2.1	ZnO electron transport layer	135
6.2.2	Al-doped ZnO transparent conducting oxide	136

6.2.3	BiFeO ₃ photoabsorber	139
6.2.4	All-oxide heterostructure	145
6.3	Freestanding BiFeO ₃ -based heterostructures	148
6.3.1	BiFeO ₃ -CSD / Sr ₃ Al ₂ O ₆	148
6.3.2	BiFeO ₃ -ALD / SrCa ₂ Al ₂ O ₆	150
6.3.3	BiFeO ₃ -CSD / La _{0.7} Sr _{0.3} MnO ₃ / SrCa ₂ Al ₂ O ₆	152
6.4	Conclusions	158
6.5	Supporting Information	160
7	Conclusions and perspectives	171
7.1	Conclusions	171
7.2	Future perspectives	175
	Scientific Contributions	177
	Abbreviations	179
	List of tables	181
	List of figures	186
	Bibliography	187

Chapter 1

Introduction

1.1 Complex oxides for energy and electronic applications

The study of new materials for energy and electronic applications is a rapidly growing field and research is focused on developing environmental-friendly materials with improved performance, durability and adaptability to be integrated into different technologies such as Si-based electronics or other emerging flexible and wearable electronics. To fulfil the demanding technological requirements, special focus is put in developing and studying alternative materials but also in using fabrication techniques to produce these materials in a cost-effective way and at large scale.

Among the different classes of materials being investigated, metal oxides are particularly appealing because of the unique and versatile characteristics that they can offer including high chemical, thermal and mechanical stability. As the oxygen atom in metal oxides is highly electronegative and it has a small ionic radius with -2 charge (O^{2-}), it efficiently forms thermodynamically stable phases of countless oxides with most of the elements of the periodic table, including phases constituted of several sort of cations, so-called complex oxides. Moreover, given the bonding properties of O^{2-} , oxides can crystallize in a broad variety of structures.

On the other hand, the scarcely overlapping and partially occupied d orbitals of the transition metal cations results in a narrow bandwidth responsible of the unique physical properties of these materials. Still, this remarkable chemical diversity is only partially responsible for the complexity attributed to complex oxides, as their properties are sensitive to several other factors including minimal chemical variations (e.g. doping), phase transitions and boundary conditions (e.g. thickness, strain, grain boundaries and interfaces), among others.¹

This diversity in compositions and structures of the complex oxides leads to exotic physical properties and multi-field coupling between them. For example, changes in the cation composition of a perovskite oxide ABO_3 can lead to properties as different as thermoelectricity ($SrTiO_3$), ferromagnetism ($La_{0.7}Sr_{0.3}MnO_3$), ferroelectricity ($BaTiO_3$, $PbZr_{1-x}Ti_xO_3$), multiferroicity ($BiFeO_3$) or high-temperature superconductivity ($YBa_2Cu_3O_7$). As shown in **Figure 1.1**, these tunable functionalities make complex oxides appealing for several advanced applications in the fields of energy and electronics, including catalysis, energy storage and conversion, spintronics, photonics and optoelectronics, to name a few. Some examples are shown below:

Superconducting films. High-temperature superconductors based on complex oxides such as $YBa_2Cu_3O_7$ have attracted great interest in many areas and in particular towards the idea of transporting large currents with no losses for power applications.²

Memory devices. Several new approaches are being investigated as alternative mechanisms for data storage including ferroelectric tunnel junctions or multifunctional oxides. Ferroelectric tunnel junctions are composed of a thin ferroelectric layer, like $BaTiO_3$, sandwiched between two electrodes that could also be a complex oxide such as $La_{0.7}Sr_{0.3}MnO_3$. By reversal polarization, the tunnel resistance is largely modified, being attractive to be used as non-volatile memories. These devices present key advantages compared to other non-volatile technologies such as fast writing speed, low power operation and high read/write endurance.^{3,4} On the other hand, multifunctional memory devices based on oxides such as the magnetic $CoFe_2O_4$ present great potential combining resistive switching with magnetization switching.⁵

Cathode in Li-ion batteries. Since they commercialization, Li-ion batteries have relied on the use of layered oxides, Li_xMO_2 ($M = Co, Mn, Ni, Li$), as cathode. These materials permit

the deintercalation/intercalation of Li^+ upon charging/discharging. The use of layered oxides allows to achieve high capacity and high voltage in these energy storage technologies.⁶

Photovoltaics (PV). Oxides in solar cells are a promising approach to help overcome some of the most important challenges in the current and emerging PV technologies: the use of stable, abundant and non-toxic elements, lower processing costs and facile materials integration. Indeed, the diversity of functionalities and the versatility to do nanoengineering in oxides allows to envisage an all-oxide photovoltaic device. The use of photoferroelectric oxides as photoabsorbers such as BiFeO_3 could also envisage higher power conversion efficiencies (PCE).^{7,8}

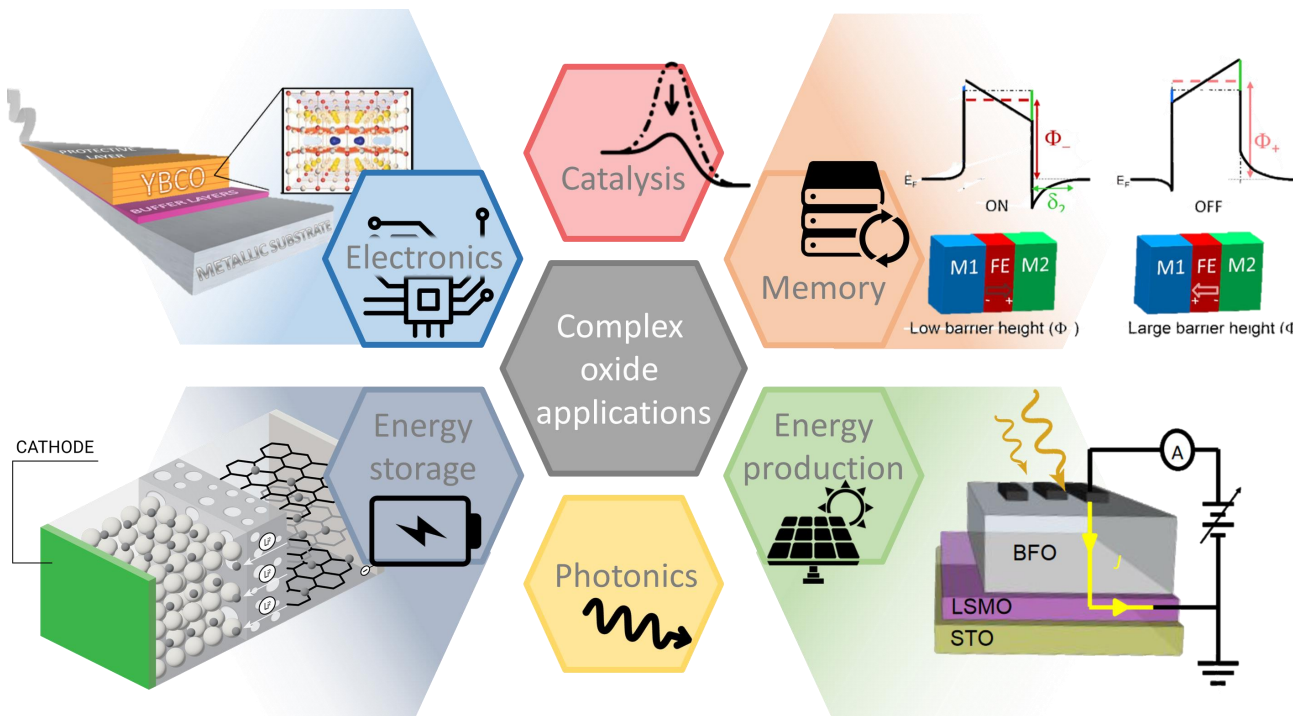


Figure 1.1: Main applications of complex oxides. Some of the fields where complex oxides show great potential are electronics and optoelectronics, energy storage and conversion, catalysis, memory and photonics. Examples are presented from top left to bottom right: Superconducting film, ferroelectric tunnel junction for memory devices, layered oxides as cathode in Li-ion batteries, all-oxide photovoltaic devices. *Figure adapted from Ref.¹ and⁸.*

1.1.1 Heteroepitaxial growth

The crystalline structure plays an essential role on the properties of the oxide materials, to such an extent that many metal oxides need to be crystalline to show the physical properties that

ultimately define their functionality. When talking about thin films, a typical way to control their crystallinity is through the epitaxial growth on a single-crystal oriented substrate. In this sense, heteroepitaxial growth (growth on a substrate of a dissimilar material) is widely extended to prepare epitaxial complex oxide thin films and heterostructures. Nevertheless, achieving heteroepitaxial growth is not straightforward and the crystalline quality of the thin film could be jeopardized because of incompatibilities with crystal structure and lattice parameter, see **Figure 1.2**. Strains of $\pm 3\%$ are common in epitaxial oxide films, which are an order of magnitude higher than those where materials would break in bulk.⁹ Such strain might be advantageous as it can be used as a tool to tune the oxide electronic structure and so its physical properties.¹⁰ For example, SrTiO₃ that is not ferroelectric at room temperature can become ferroelectric by inducing biaxial strain.¹¹ On the other hand, large mismatch in the lattice constant and in the thermal expansion coefficient between the two materials can lead to epitaxial defects and dislocations which could be detrimental for the physical properties of the film.^{12,13} Indeed, note that here the interface plays a key role on the heteroepitaxial growth¹⁴ and phenomena such as interface dislocations and interfacial reactivity/diffusion must be considered. Moreover, the use of single-crystal substrates involves other restrictions: they must sustain the high-temperature treatments needed to achieve epitaxy, they are generally rigid, brittle and expensive, representing an important part of the economic cost of the heterostructure, and the range of commercially available single-crystal substrates is limited. Clearly, the demanding requirements to ensure epitaxial oxide growth on single-crystal substrates are an important limitation towards the fabrication of epitaxial oxide devices in versatile substrates including amorphous, flexible, polymeric and temperature sensitive materials. Therefore, the detachment of the oxide thin film from the substrate would be very appealing, although the strong chemical bond at the interface film/substrate makes it extremely challenging.

1.1.2 Freestanding epitaxial complex oxides

In the last few years there has been an important effort on trying to detach the epitaxial complex oxides grown on single-crystal substrates. Freestanding epitaxial oxide films can open new

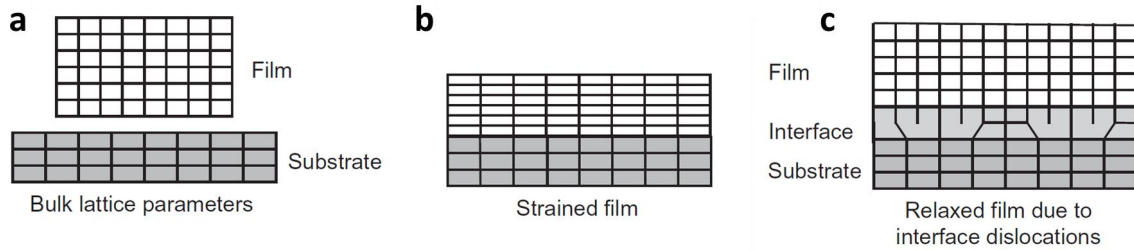


Figure 1.2: Heteroepitaxial growth. (a) Schematic of a substrate and a film with different lattice parameters. When grown epitaxially, the film can grow either (b) strained or (c) with epitaxial defects and dislocations. *Figure adapted from Ref.¹⁵.*

opportunities from integration into flexible devices and stacked artificial heterostructures, but also to study unexplored changes in physical properties by strain manipulation or at artificial interfaces.^{12,16} First, the opportunities related to these freestanding epitaxial oxides are discussed showing its main applications, and then some of the leading lift-off technologies to achieve the detachment of the oxide film from the single-crystal substrate are summarized.

Opportunities and applications.

Flexible devices. Bulk oxide materials are always thought to be inherently brittle because of the strength of its ionic bonds and lack of dislocation glide planes compared to organic or metallic materials. Nevertheless, when dimensionality is reduced to the nanoscale, nanostructured oxides offer atomic displacement tolerance and additional strain that exceeds the elastic limit of bulk materials.^{26,27} For example, as shown in **Figure 1.3a**, a BaTiO_3 freestanding film could undergo a 180° folding with a small bending radius ($\sim 1 \mu\text{m}$) with no cracks.¹⁷ This improved elasticity allows integrating epitaxial oxide thin films into flexible devices. Some examples are flexible displays, integration into clothing or skin electronics,¹⁸ see Fig. 1.3b,c. Moreover, because the oxide properties might be sensitive to its flexion, they can also be used as flexible sensors or piezoelectric nanogenerators, see Fig. 1.3d.

Stacked Van der Waals (VdW) heterostructures. The release of freestanding epitaxial oxides from its original substrate is not only interesting for integration into flexible devices, but also to integrate them in artificial stacked heterostructures which would be inaccessible otherwise because of incompatible chemistry, structural matching and/or high temperature synthesis.²⁸

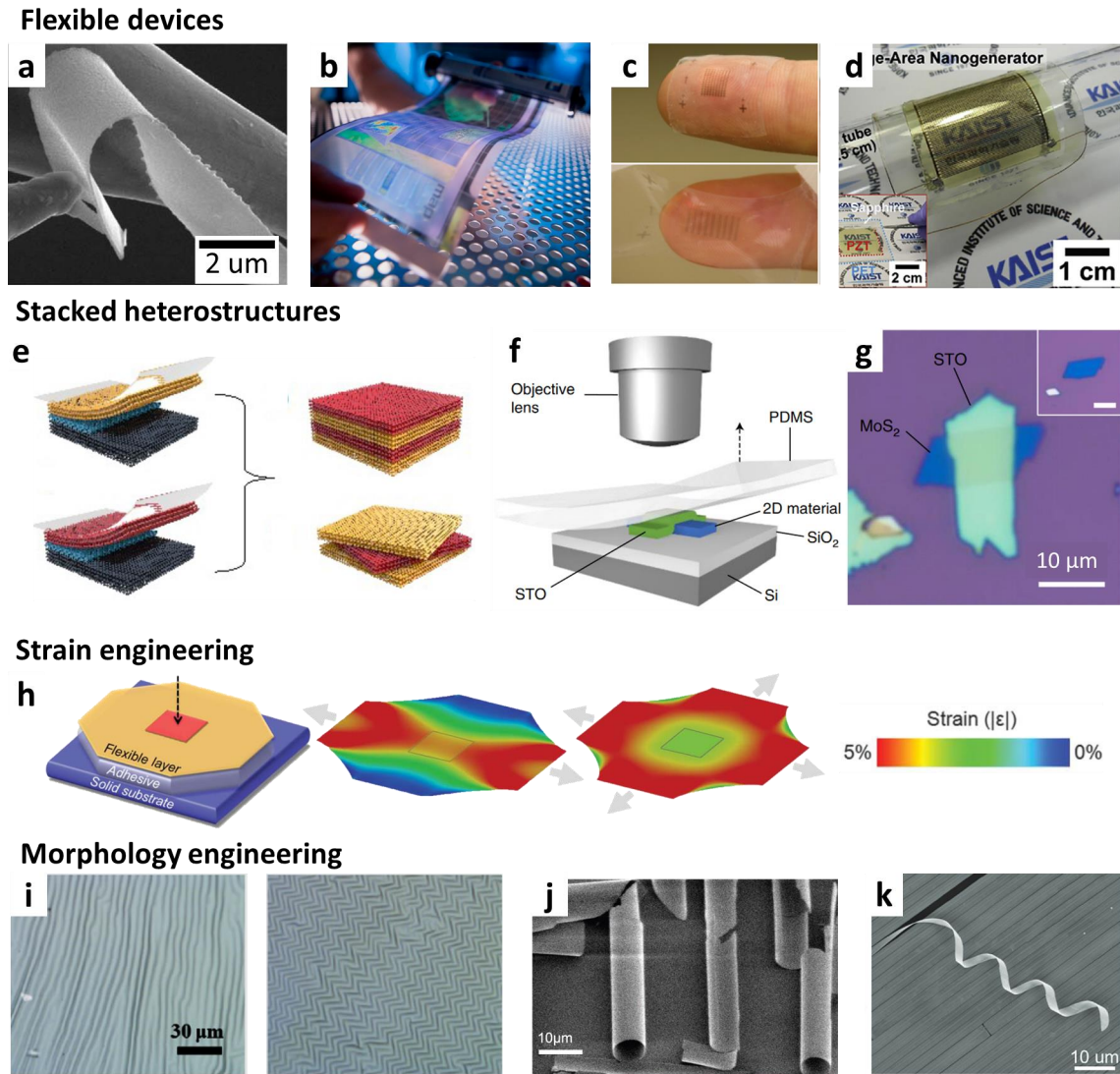


Figure 1.3: Freestanding epitaxial oxide films: opportunities and applications. **Flexible devices:** (a) SEM image of a bended freestanding BaTiO_3 membrane;¹⁷ (b) Flexible display; (c) Skin electronics;¹⁸ (d) nanogenerator based on piezoelectric PZT thin film.¹⁹ **Stacked heterostructures:** (e) Artificial stacks with heterointerfaces of twisted freestanding complex oxide thin films;²⁰ (f) Integration of freestanding SrTiO_3 with 2D semiconductors (MoS_2 flakes) and (g) corresponding magnified image of the stacked flakes.²¹ **Strain engineering:** (h) Platform for straining oxide membranes under uniaxial and biaxial stress.²² **Morphology engineering:** (i) BaTiO_3 membranes with varied wrinkle pattern depending on the mechanical properties of soft polymer supports;²³ (j) SEM image of freestanding $\text{BaTiO}_3/\text{PbTiO}_3$ superlattice on SrRuO_3 heterostructure curled up into tubes;²⁴ (k) SEM image of freestanding $\text{La}_{0.7}\text{Sr}_{0.3}\text{MnO}_3/\text{BaTiO}_3$ bilayer heterostructure self-assembled into nanosprings.²⁵ *Figure adapted from Ref. ¹⁷⁻²⁵.*

For example, integration of single-crystalline complex oxide thin films into silicon technology is highly pursued to incorporate their unique variety of functionalities into new electronic applications. However, direct synthesis of these oxides on silicon remains challenging and, therefore,

the incorporation of freestanding epitaxial oxides offers an attractive and alternative path.²⁹ Similarly, the freestanding epitaxial oxides can be used to integrate dissimilar materials in VdW heterostructures through clean and flat interfaces. Some examples are artificial stacks with twisted epitaxial oxide films (Fig. 1.3e)²⁰ or integration of freestanding epitaxial oxides with organic³⁰ or 2D materials,³¹ see Fig. 1.3f-g.²¹

Strain engineering. Freestanding thin films, in contrast to epitaxial films clamped on a substrate, are released from this clamping effect and therefore strain can be tuned by designing and controlling the applied external stress. Moreover, the applied strain can be far exceeding what achieved for epitaxial oxide films. For example, PbTiO_3 freestanding films could be in-plane strained up to +6.4 %, which is substantially larger than the achievable value ever reported on the oxide as epitaxial film.³² These externally driven changes in atomic spacing can have a direct effect on the phase and functionalities of the material, providing unique opportunities to study accurately controlled strain-induced responses. The most common way to tune the strain of epitaxial oxide membranes is by bending it as freestanding or attached on a flexible support, but another way would be using a stretchable support to apply controlled uniaxial or biaxial stress, as shown in Fig. 1.3h.²²

Morphology engineering. On the other hand, when released from its growth clamping rigid substrate, freestanding single-crystal films tend to minimize its epitaxial strain trying to recover its natural (bulk-like) lattice parameters. This strain relaxation of the released film can become into cracking of the freestanding oxide or into different morphologies such as wrinkling and bending, depending on the strain gradients of the structure.³³ Therefore, engineering of these relaxation pathways through controlled strained heterostructures can be used in advantage for morphology engineering of the released freestanding epitaxial oxide membranes, as shown in Fig. 1.3i-k. For example, the wrinkle patterning of a membrane can vary depending on film thickness, pre-stretched mechanical stress or heat treatment (Fig. 1.3i).^{23,34} Some other examples are self-assembled curled up tubes²⁴ (Fig. 1.3j) or oxide nanosprings²⁵ (Fig. 1.3k), both due to strain accommodation of freestanding lattice-mismatched epitaxial heterostructures.

Lift-off technologies.

Exfoliation and isolation of atomically-thin oxides has been pursued for a long time. In some specific cases this can be achieved from the exfoliation of the corresponding bulk crystal. For example, some very specific oxide structures such as a few layered crystalline oxide structures such as titanium-based oxides³⁵ or layered perovskites³⁶ exfoliate when there is proton intercalation exchange in solution.³⁷ This intercalation results in nanosheets with small areas (tens to hundreds of square microns) dispersed in a colloidal solution, which hinders the manipulation of single sheets. On the other hand, in the last few years, several lift-off technologies have been developed to prepare high-quality freestanding epitaxial complex oxide films thanks to the rapid progress on both epitaxial growth of complex oxides on single-crystal substrates and mechanical exfoliation of 2D materials.^{12,16,38} **Figure 1.4** shows some of the most popular lift-off technologies, which can be divided into physical or chemical techniques based on the separation mechanism:

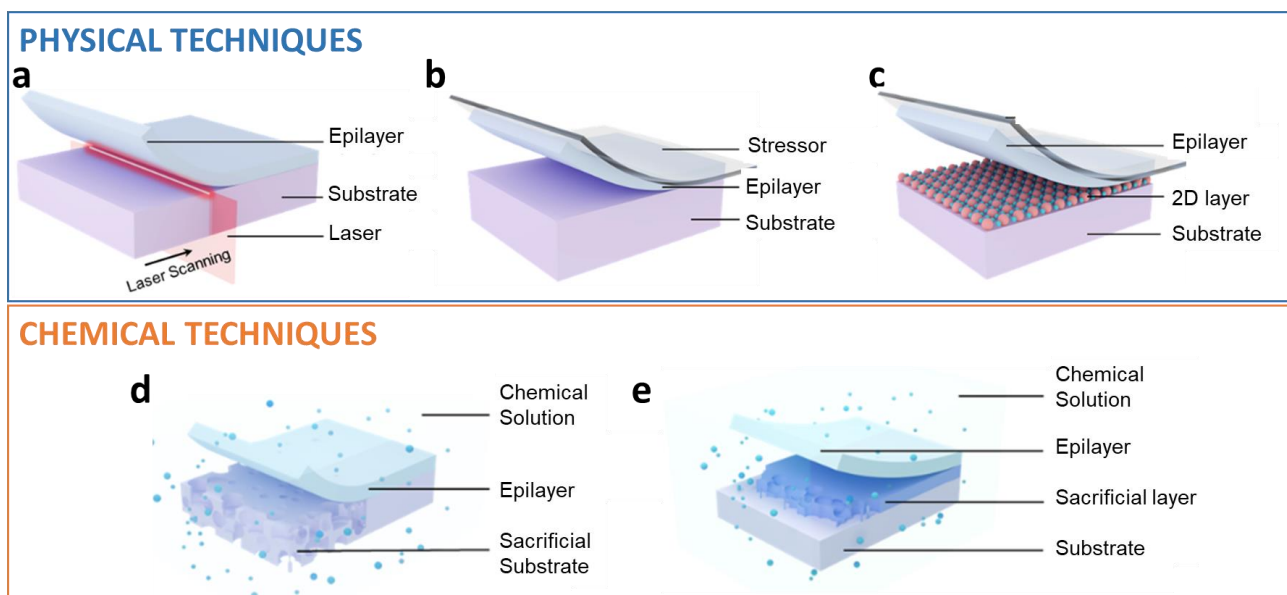


Figure 1.4: Lift-off technologies for freestanding epitaxial oxide films. Physical techniques include (a) laser lift-off, (b) mechanical lift-off and (c) 2D-assisted lift-off. Chemical techniques include (d) etching of the substrate and (e) the use of a sacrificial layer for selective etching with a chemical solution. *Figure adapted from Ref.¹⁶.*

Laser lift-off. As shown in Fig. 1.4a, in laser lift-off a transparent substrate is used to allow the laser beam to reach the interface with the epitaxially grown oxide film. There, if the film

material has a lower band gap than the laser beam energy, the interface between the substrate and the film is vaporized resulting in a damage-free separation from the substrate. For example, a $\text{Pb}(\text{Zr}_{0.2}\text{Ti}_{0.8})\text{O}_3$ (PZT) thin film deposited on transparent sapphire was successfully transferred to a flexible polyethylene terephthalate (PET) substrate using this approach.¹⁹ However, this technique is limited to small band gap oxides which can be epitaxially grown on specific transparent substrates. Moreover, because of the laser interface decomposition, after laser lift-off the substrate is roughened and its subsequent reusability for epitaxial growth cannot be done unless the substrate is chemically and mechanically polished.³⁹

Mechanical lift-off. In some cases, when the interface bonding is relatively weak, mechanical lift-off has been demonstrated to obtain freestanding oxide films separated from their growth substrate simply by a brute force. As shown in Fig. 1.4b, a stressor can be used to help guiding the crack propagation along the weak interface. For example, a Ni stressor was used to mechanically separate a 500 nm thick epitaxial complex perovskite $\text{Pb}(\text{Mg}_{1/3}\text{Nb}_{2/3})\text{O}_3\text{-PbTiO}_3$ (PMN-PT) from a SrRuO_3 buffered SrTiO_3 substrate thanks to weak bonding between PMN-PT/ SrRuO_3 .⁴⁰ Although this method is simple and economic, it is limited to materials with weak bonding at the interface and still cracking damages at the film surface and substrate can occur due to the high stresses.

2D-assisted lift-off. Following the same idea of weakening the interface bonding for the subsequent exfoliation of the oxide film, VdW 2D buffer layers can be used, as shown in Fig. 1.4c.⁴¹ For example, layered muscovite (mica), which has an exfoliating structure, can be used as substrate for epitaxial oxide growth and then the film can be peeled off together with a few layers of mica and integrated on a flexible device.⁴² However, having mica attached on one side of the membrane limits its applicability for stacked heterostructures, and polymer supports are still preferred upon mica for flexible devices commercialization. More recently, Kum et al.⁴⁰ discovered that by adding a buffer layer of graphene on a single-crystal substrate, they could still epitaxially grow complex oxide films while allowing mechanical lift-off afterwards, this process is so-called remote epitaxy.⁴³ The graphene buffer layer between the substrate and the oxide film is enough to screen the covalent bonding between them, while being transparent to ionic

interaction and so allowing epitaxial growth.⁴⁴ They demonstrated the general applicability of this approach growing and then exfoliating perovskite SrTiO_3 and BaTiO_3 , spinel CoFe_2O_4 and garnet $\text{Y}_3\text{Fe}_5\text{O}_{12}$ (YIG) from graphene-coated SrTiO_3 , MgAl_2O_4 and $\text{Gd}_3\text{Ga}_5\text{O}_{12}$ (GGG), respectively. Compared to typical mechanical exfoliation with no 2D assisted buffer layer, in this case exfoliation yield was greatly enhanced, minimizing the damage to the substrate upon peeling and promoting the reusability of the substrates. Note, however, that the crystalline quality of the freestanding oxide is very dependent on the quality of the graphene layer, with defects caused by graphene thickness variations or organic/metal residues.

On the other hand, chemical lift-off techniques are based on the selective chemical etching in solution of either the substrate, the interface region or a sacrificial layer. Therefore, it is primordial to use chemical etchant solutions which rapidly dissolve the selected chemical phase (substrate or sacrificial layer) without damaging the oxide film of interest during the process.

Substrate chemical etching. The selective etching of the substrate after depositing the oxide film is a direct approach to obtain freestanding films, see Fig. 1.4d. For example, freestanding SrRuO_3 films could be obtained by selectively etching the SrTiO_3 substrate in acid solution.⁴⁵ However, etching the entire substrate is a very time-consuming and wasteful approach. Therefore, patterning the oxide film before immersing it in the etching solution has found to be an alternative pathway to facilitate the etching of the substrate at the interface.^{46,47} In this way freestanding oxide films could be obtained without etching the entire substrate, although the patterning needed in this case thereby hinders its applicability for the acquisition of integral freestanding films.

Sacrificial layer. The use of a sacrificial layer is emerging as one of the most reliable methods to obtain high-quality freestanding epitaxial complex oxide films. In this case, as shown in Fig. 1.4e, a sacrificial layer is epitaxially grown between the substrate and the film, and then it is selectively wet etched releasing the freestanding film. Therefore, this sacrificial layer should fulfill a few key requirements in order to ensure the release of high-quality epitaxial films. First, the sacrificial layer should enable the subsequent high-quality epitaxial growth of the complex

oxide of interest. This involves having the appropriate lattice parameters and structure to avoid mismatch-related defects, as well as having an atomically smooth and clean surface which will determine the properties of the oxide film grown on top. Moreover, it should have inert reactivity at the interface between structures. In this sense, the quality of the interface could be jeopardized if there was reactivity or cation interdiffusion between the different components of the heterostructure induced for example during the high-temperature processing usually used to obtain epitaxial growth.⁴⁸ Second, the sacrificial layer should be selectively removed with a chemical etchant (preferably non toxic) in such a way that neither the released film nor the substrate are damaged or altered. In this way the substrate can be reused, being a more cost-effective and fast process compared to the substrate chemical etching. Nevertheless, as the sacrificial layer is sandwiched between the substrate and the oxide film, it can only be attacked by the etchant from its sides. Thus, the etching rate of the sacrificial layer is a critical factor for the integration of this lift-off technique into large-scale production. Within this context, approaches developed in further advanced industries such as for lift-off of large area III/V thin film devices could be adapted to improve the etching rate and diminish the time required in this step.⁴⁹

In 2009, Pellegrino et al.⁵⁰ demonstrated the fabrication of an epitaxial SrTiO₃ suspended bridge by partial selective etching of a La_{0.7}Sr_{0.3}MnO₃ layer. However, to the best of our knowledge, it was not until 2016 when there was the first report of a complete release of epitaxial complex oxides (PZT and CaTiO₃/SrTiO₃ superlattice) using the La_{0.7}Sr_{0.3}MnO₃ structure as sacrificial layer.²⁹ Since then, few different sacrificial layer compositions have been developed for the release of epitaxial complex oxide films. **Table 1.1** summarizes the characteristics of the different sacrificial layer compositions and **Figure 1.5** shows their pseudo-cubic in-plane lattice parameters.

Perovskite oxides La_{0.7}Sr_{0.3}MnO₃,^{29,31,51} SrRuO₃,⁵² YBa₂Cu₃O₇,⁵³ and SrVO₃⁵⁴ have been used as sacrificial layers for the release of films with similar perovskite structures. La_{0.7}Sr_{0.3}MnO₃ and YBa₂Cu₃O₇ are etched by acid solutions and their selective etching depends on the difference in etching rate between different oxides, which therefore limits the range of oxides

Table 1.1: Sacrificial layer compositions for the preparation of freestanding epitaxial complex oxide films.

Sacrificial Layer	Substrate	Etching solution	Released epitaxial oxide
$\text{La}_{0.7}\text{Sr}_{0.3}\text{MnO}_3$	SrTiO_3 (001)	KI + HCl	BaTiO_3 , ^{31,51} PZT, $\text{CaTiO}_3/\text{SrTiO}_3$ superlattice ²⁹
SrRuO_3	SrTiO_3 (001)	$\text{NaIO}_4(\text{aq})$	LSMO ⁵²
$\text{YBa}_2\text{Cu}_3\text{O}_7$	SrTiO_3 (001)	HCl	LSMO ⁵³
SrVO_3	SrTiO_3 (001)	50 °C Water	SrTiO_3 ⁵⁴
$\text{SrCoO}_{2.5}$	SrTiO_3 (001), (110), (111)	Weak acids	SrRuO_3 ⁵⁵
MgO	SrTiO_3 (001)	$(\text{NH}_4)_2\text{SO}_4(\text{aq})$	CoFe_2O_4 ⁵⁶
BaO	SrTiO_3 (001)	RT Water	BaTiO_3 , SrTiO_3 ⁵⁷
$(\text{Ca,Sr,Ba})_3\text{Al}_2\text{O}_6$	SrTiO_3 (001), (110), (111), LaAlO_3 (001)	RT Water	See 1.1.3 $\text{Sr}_3\text{Al}_2\text{O}_6$ (SAO) sacrificial layer

Sacrificial material (etchant)

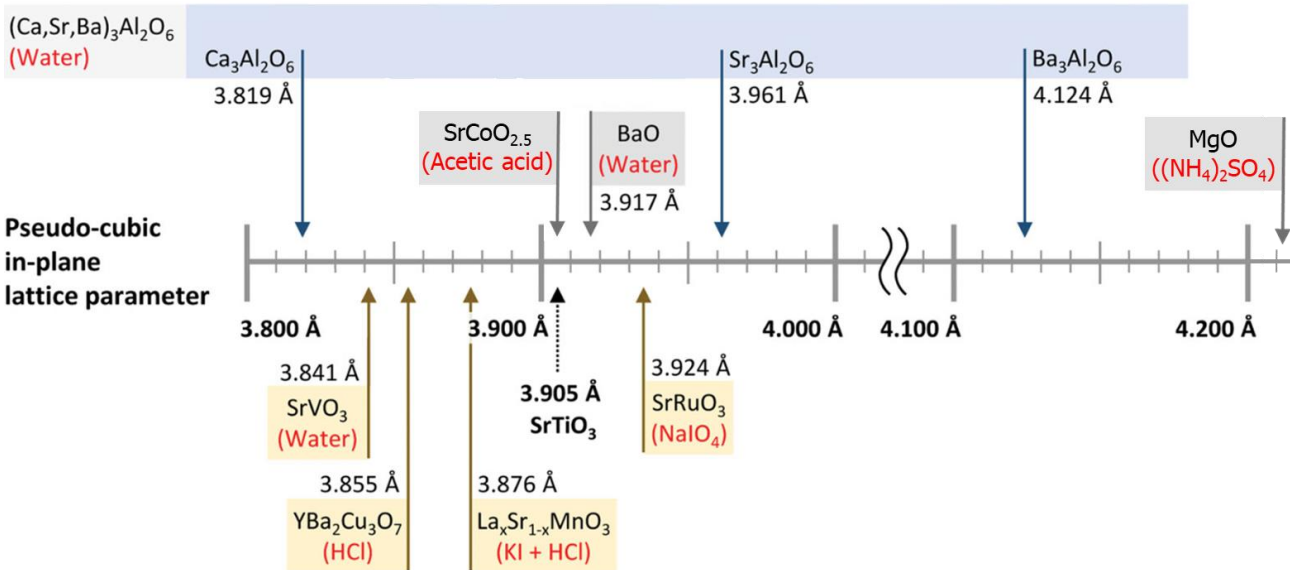


Figure 1.5: Compatible sacrificial layers with epitaxial complex oxides. Pseudo-cubic in-plane lattice parameters of the different sacrificial layer compositions included in Table 1.1. The yellow frames correspond to perovskites, the blue one corresponds to the $(\text{Ca,Sr,Ba})_3\text{Al}_2\text{O}_6$ family and the grey ones to other alternative structures. SrTiO_3 , as typical single-crystal substrate for the growth of epitaxial complex oxides, is depicted as reference. *Figure adapted from Ref.⁵⁸.*

that can sustain such conditions and be transferred from these sacrificial layers. On the other hand, SrRuO_3 is etched in a NaIO_4 solution with near-neutral pH, allowing the transfer of acid-sensitive films such as $\text{La}_{0.7}\text{Sr}_{0.3}\text{MnO}_3$ with no damage. Yet, this solution may partially

degrade the polymer support used for the transfer of the released film, as observed by Pesquera et al.⁵² SrVO₃ also offers an interesting approach as it can be simply dissolved in hot water, as demonstrated by Bourlier et al. with the release of freestanding SrTiO₃ films.⁵⁴

Alternative structures such as brownmillerite SrCoO_{2.5}⁵⁵ or metal oxides with rock salt structure such as MgO⁵⁶ and BaO⁵⁷ have also demonstrated to fulfil the requirements to be used as sacrificial layer for the release of different epitaxial complex oxides, including perovskites and spinels. SrCoO_{2.5} has an orthorombic structure with in-plane lattice parameter close to SrTiO₃ and it can be grown epitaxially in different directions (001), (110), (111). It is easily dissolved in weak acids including eco-friendly solutions as acetic acid, vinegar, and even carbonated drinks, although not in water, which makes this material promising to be used as sacrificial layer. Regarding BaO,⁵⁷ it has a lattice parameter similar to that of SrTiO₃ when rotated 45° in-plane, allowing the subsequent epitaxial growth of oxide perovskites and their release when immersed in water. On the other hand, MgO has a cubic lattice parameter which has been demonstrated to be useful for the preparation of freestanding spinel CoFe₂O₄.

Finally, the family of (Ca,Sr,Ba)₃Al₂O₆ has been the most studied and largely used sacrificial layer for the preparation of many different kind of freestanding epitaxial complex oxides, mainly because it can be selectively etched with water. Since this Thesis is devoted to study this family of sacrificial layers, further details are presented in Section 1.1.3.

Challenges behind the transfer process of freestanding oxides

The release of integer freestanding epitaxial oxides using a sacrificial layer is a key step towards their integration in actual devices. This step remains an arduous task since the integrity and quality of the membrane is largely affected by the releasing process and handling techniques, which can generate many defects including cracks and wrinkles.^{59–61} The well-established wet transfer process of 2D VdW materials, like graphene,⁶² has been mimicked for the emerging field of complex oxide membranes, although in this case the stress that arise during the etch and transfer have to be carefully taken into account because of the more brittle nature of oxide membranes compared to graphene.^{38,58} The transfer process generally consists of using a

support to stamp the film for the lift-off from its original substrate, then transfer it to the desired substrate and finally removing the stamp support.⁵⁸ Typical stamp supports are polymer materials such as polydimethylsiloxane (PDMS),^{61,63} polyethylene terephthalate (PET),^{64,65} polypropylene carbonate (PPC)^{22,66} and polymethyl-methacrylate (PMMA),^{67,68} or combinations of them, because of their flexibility, mechanical strength and adhesive contact. This stamp support is usually added on the oxide before etching the sacrificial layer to prevent cracking and folding of the freestanding membrane during the etching process.⁶⁰ However, even the stress generated by flexible polymer supports can be sometimes a source of defects.⁶⁹ Recently, the use of a rigid holder bonded to the oxide via a metallic Au/Ag bonding layer demonstrated achieving the transfer of integer epitaxial SrRuO₃ and SrRuO₃/SrTiO₃ membranes to a Si substrate,⁷⁰ showing great promise as an alternative to flexible polymers. A support-free transfer method was also developed producing crack-free membranes of SrRuO₃ and BaTiO₃ floating on the etching solvent surface that could be obtained by scooping.^{71–74}

Besides the support material used as stamp, there are several other parameters that can affect the quality of the transferred membrane. Part of the cracks and wrinkles in freestanding epitaxial oxides arise because of the use of mismatched sacrificial layers which involve strain relaxation when the oxide film is released, thus the use of a matching sacrificial layer can help lowering the internal stress of the oxide improving the membrane quality.^{22,75} On the other hand, other characteristics such as the sacrificial and complex oxide thicknesses or even the tensions generated from the defects at the edges can play also a role on the resulting membrane.⁶¹ An interesting strategy that has proved to facilitate the suppression of cracks is adding a 20 nm amorphous Al₂O₃ capping layer on the oxide that will be released.⁷⁶ Nevertheless if the capping layer is epitaxial and involves more strain, it could also be a source of defects.⁶¹

Last but not least, the manual manipulation of the process can involve uncontrolled stress and sample contamination. Alternatively, special complex setups have been developed for the deterministic placement of 2D materials and have demonstrated to allow their manipulation with unmatched precision to fabricate VdW heterostructures with high control on position and angle.⁷⁷

Therefore, the release and subsequent transfer of freestanding oxides is a challenging step and needs thorough optimization.

1.1.3 $\text{Sr}_3\text{Al}_2\text{O}_6$ (SAO) sacrificial layer

Recently, $\text{Sr}_3\text{Al}_2\text{O}_6$ (SAO) has been demonstrated to show huge potential as epitaxial template and sacrificial layer to prepare freestanding epitaxial complex oxide membranes.

$\text{Sr}_3\text{Al}_2\text{O}_6$ has a pseudoperovskite structure with a cubic unit cell ($a = 15.844 \text{ \AA}$), space group Pa_3 and $Z = 24$, see **Figure 1.6a**. From an ABO_3 perovskite structure standpoint, $\text{Sr}_3\text{Al}_2\text{O}_6$ could be rewritten as $\text{Sr}_{7/8}\square_{1/8}(\text{Sr}_{1/4}\text{Al}_{3/4})\text{O}_{9/4}\square_{3/4}$: the A site is partially occupied by Sr, the B site is occupied by both Sr and Al, and oxygen occupies only 75% of its sub-lattice with regularly positioned vacancies.⁷⁸ The reason of the water-sensitivity of this oxide can be found in its structure. As shown in Fig. 1.6b, this crystal structure conforms discrete Al-O networks based on rings of six AlO_4 tetrahedra, with two nonbridging oxygens for each tetrahedron ($\text{Al}_6\text{O}_{18}^{18-}$). Because of the high electronegativity of Al relative to that of Sr, Al-O bonding have a more significant covalent character, while the bonds Sr-O through the nonbridging oxygens have more ionic character. This makes the structure to easily hydrolyse in water through the protonation of these nonbridging oxygens.⁷⁹ By cation substitution of the Sr^{2+} ions with either Ca^{2+} or Ba^{2+} , isostructural $\text{Ca}_3\text{Al}_2\text{O}_6$ (CAO) and $\text{Ba}_3\text{Al}_2\text{O}_6$ (BAO) are obtained respectively. This cation substitution has a direct effect on the rate of hydrolysis of the respective structures because of the difference in the cations electronegativity: the lower the cation electronegativity, the higher its bonding ionicity and so the easier to hydrolyse (see **Table 1.2**). Therefore, the rate of hydrolysis is higher for BAO, then SAO and finally CAO.⁷⁵ Moreover, due to the different cation size, this cation substitution allows engineering the lattice parameter of the crystalline structure from $a_{\text{Ca}_3\text{Al}_2\text{O}_6} = 15.262 \text{ \AA}$ to $a_{\text{Ba}_3\text{Al}_2\text{O}_6} = 16.498 \text{ \AA}$.⁸⁰ Despite its apparent structural complexity, $\text{Sr}_3\text{Al}_2\text{O}_6$ shares similar lattice parameter to other simpler perovskite oxides as SrTiO_3 (STO), a typical perovskite substrate used for the epitaxial growth of many functional perovskite oxide thin films, see Fig. 1.6c-d for comparison. The SAO unit cell closely matches 4 unit cells of STO ($a_{\text{SAO}}/4 = 3.961 \text{ \AA}$; $a_{\text{STO}} = 3.905 \text{ \AA}$), with

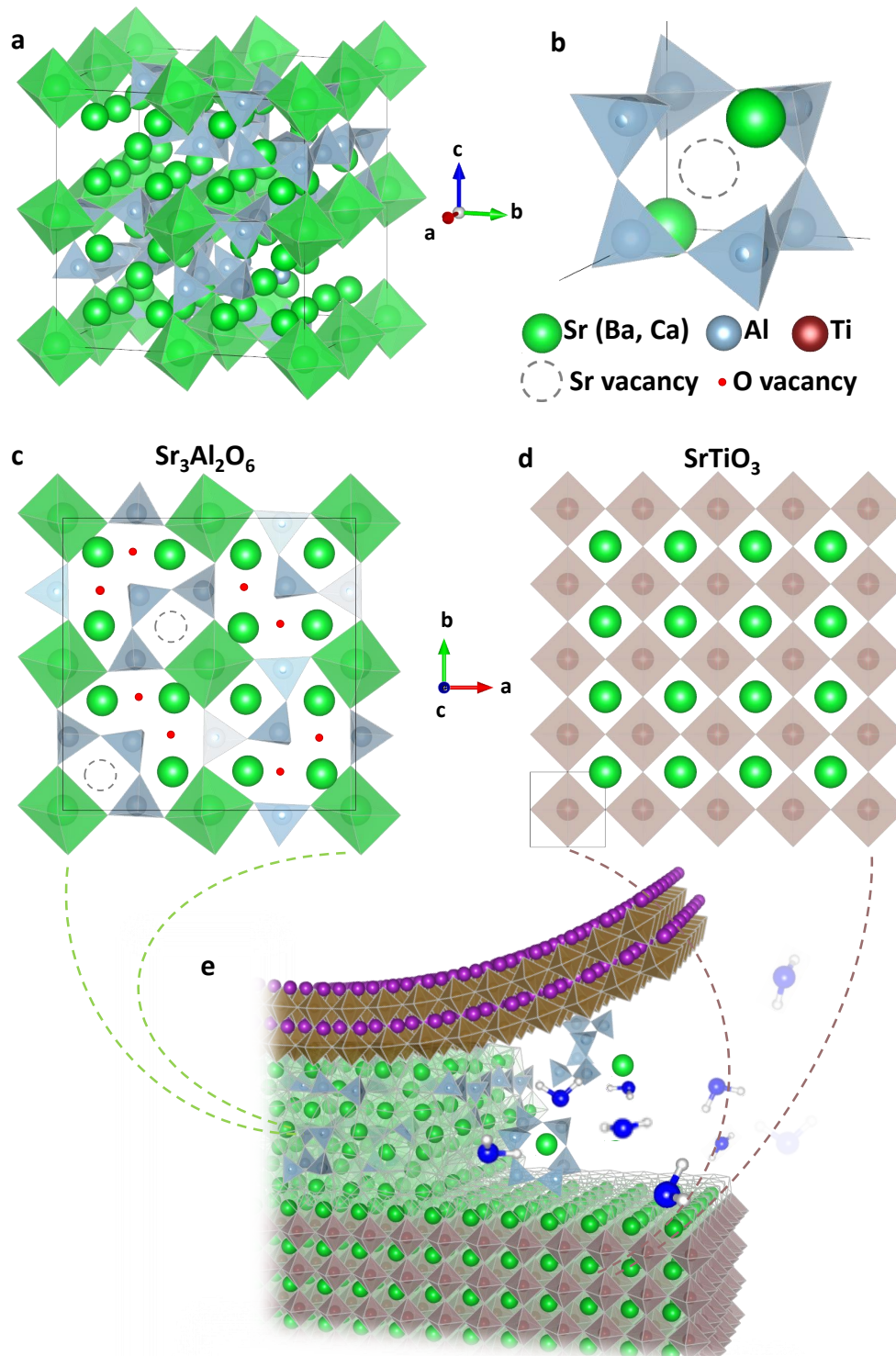


Figure 1.6: Crystal structure of $\text{Sr}_3\text{Al}_2\text{O}_6$. (a) Cubic unit cell of $\text{Sr}_3\text{Al}_2\text{O}_6$. (b) Al-O networks based on rings of six AlO_4 tetrahedra. Oxygens not shown to simplify sketch. (c) 1/4 of $\text{Sr}_3\text{Al}_2\text{O}_6$ unit cell projected along (001) plane. In order to differentiate the Sr positions in a ABO_3 perovskite perspective, Sr at B-site are represented with the corresponding octahedra and Sr at A-site without it. (d) 4x4 SrTiO_3 unit cells projected along (001) plane. (e) Release process of a freestanding perovskite oxide by water etching of SAO.

Table 1.2: (Ca, Sr, Ba)₃Al₂O₆ characteristics

Cation	Cation electronegativity	Ionic radius (pm)	a (Å)	a/4 (Å)
Ca ²⁺	1.00	114	15.262	3.819
Sr ²⁺	0.95	132	15.844	3.961
Ba ²⁺	0.89	149	16.498	4.124

a mismatch of only 1 %.

Thanks to the resemblance in structure, single-phase epitaxially oriented SAO can be grown on STO, as showed for first time in 2016 by D. Lu, H. Y Hwang, et al.⁸¹ They discovered that if this SAO thin film was used as buffer layer for the epitaxial growth of another perovskite oxide, then it could be selectively etched in water, releasing thus a freestanding perovskite oxide membrane (Fig.1.6e). Since then, there has been a growing interest about the use of Sr₃Al₂O₆ as water-soluble sacrificial layer, expanding its use for many different applications as it can be visualized from the exponential number of articles published in the last few years, see **Figure 1.7a**. Here, the wide variety of studies related to SAO and its derivates has been analyzed and summarized in a way to show the versatility and potential of this sacrificial layer including the variety of freestanding structures that can be prepared, which substrates can be used, the advantages related to cation substitution in the sacrificial layer composition, other applications for SAO rather than freestanding oxides, and finally which deposition techniques have been used to prepare it.

Freestanding oxide structures. Since its discovery in 2016, more than 100 publications prove the use of SAO as a generic method to prepare many freestanding structures. As illustrated in Fig. 1.7b, epitaxial perovskite oxides have been the most common choice when using the SAO sacrificial to prepare freestanding membranes (> 80 % of publications), counting at least 20 different types. Within these, the most typical ones have been STO,^{81,82} BaTiO₃,⁸³ BiFeO₃,^{26,84} La_{0.7}Sr_{0.3}MnO₃⁸⁵ and SrRuO₃.⁶⁸ Nevertheless, the use of SAO as sacrificial layer is not limited to epitaxial perovskite oxides, but it has also been proved useful to obtain other epitaxial oxide structures as spinels,^{64,86} anatase TiO₂⁶⁵ or inverse spinel Fe₃O₄,^{63,87} as well as other

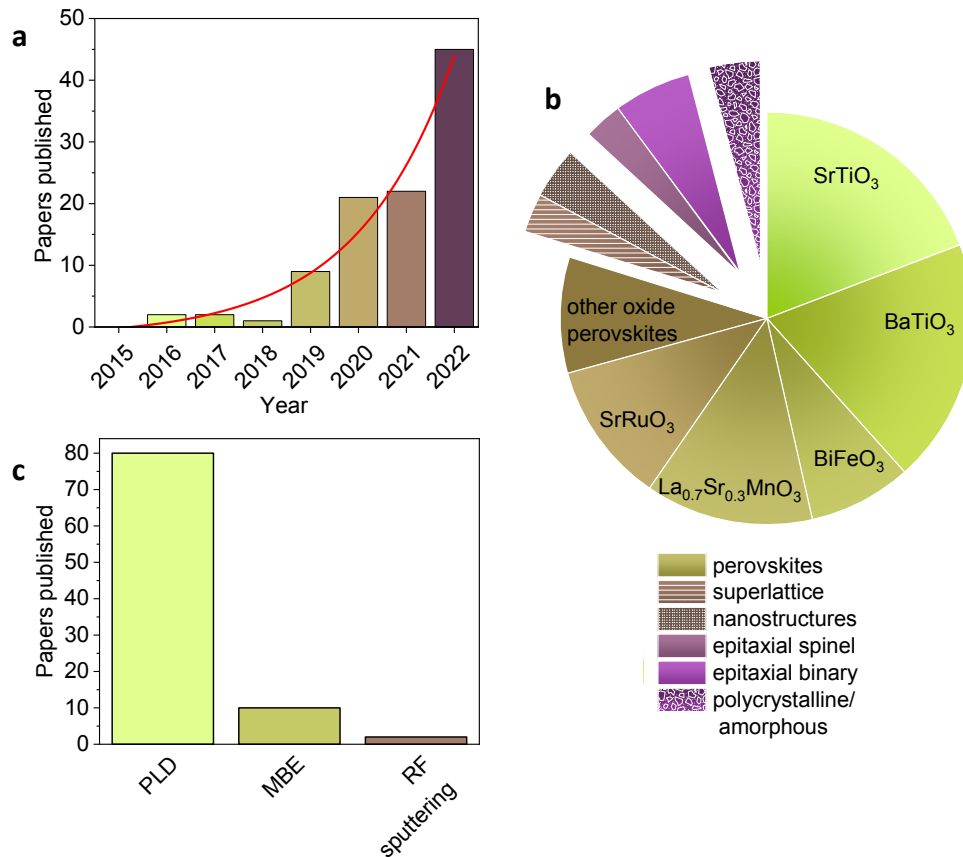


Figure 1.7: Statistics of publications about the SAO sacrificial layer. (a) Published papers on the use of SAO as sacrificial layer from 2015 to 2022. (b) Classification of the different freestanding structures achieved using SAO as sacrificial layer. (c) Deposition techniques to prepare epitaxial SAO.

amorphous and polycrystalline oxides.⁸⁸ Moreover, the combination of several compounds in simple heterostructures or more complex designs such as superlattices^{24,81} and vertically aligned nanostructures^{67,72} have also been achieved using this method.

Substrates. Although most of the work published has been done using (001) STO as monocrystalline substrate, the growth of epitaxial SAO is not limited to only this substrate. For example, in some cases (001) LAO has also been used to grow (001) SAO.^{72,89} Regarding other epitaxial orientations, (110) SAO and (111) SAO have been also achieved using (110) STO and (111) STO, respectively.^{68,85,90} On the other hand, in cases where epitaxy is not pursued, polycrystalline or amorphous water-soluble SAO has been grown in different substrates such as Al₂O₃ and GGG.^{74,88} Note that the high re-usability of the substrates is one of the main advantages of the use of SAO as water-soluble sacrificial layer with no organic traces after transfer.⁹¹

(Ca,Sr,Ba)₃Al₂O₆ cation substitution. As previously explained, the cation substitution of Sr with either Ba or Ca allows engineering the lattice parameters of the crystalline structure (See Fig. 1.5 and Table 1.2) as well as tuning the solubility in water with different rates of hydrolysis. These variations in the properties of the sacrificial layer were exploited for example to diminish the mismatch with the oxide grown on top, allowing a less strained growth and so an improved transfer yield due to lower strain released.^{22,66,75}

Other uses for SAO. Besides the use of epitaxial SAO as sacrificial layer, some other applications show the versatility that this crystal structure offers. For example, regarding its use as buffer layer, a few nm of SAO have been shown to be an efficient strain-releasing layer thanks to its 50-60% smaller elastic modulus compared to typical perovskites.⁹² Following the same concept of strain tuning, different SAO thicknesses can be used to modify the strain on the perovskite oxide grown on top.⁸⁹ On the other hand, taking advantage of the SAO easy solubility in water, another application is making nanostructures by the selective dissolution of SAO. For example, nanoporous films can be achieved by dissolving SAO in heteroepitaxial nanocomposite films with separated phases.⁹³ Amorphous SAO grown at room temperature is also water-soluble and it has been proved useful as hard mask for selective area epitaxy of oxide heterostructures.⁹⁴ Using the same principle, Luo et al. showed how amorphous SAO could be used to prepare dissolvable memristors based on Pt/SAO/Pt heterostructures.⁹⁵ Finally, it should be mentioned that a totally different application where SAO is being investigated intensively is in the form of Sr₃Al₂O₆ powders doped with rare earth elements (Eu, Sm, Dy, Er) to be used as phosphors for displays and lightning devices.⁹⁶

Deposition techniques. The fast hydrolysis of the SAO crystalline structure when in contact with water is a key limiting factor when it comes to the preparation of the sacrificial layer. A minimum exposure to air humidity is enough to degrade the SAO surface, which would block the transfer of epitaxy to the following oxide grown on top.⁸¹ For this reason, the growth of SAO to be used as epitaxial sacrificial layer has been limited mainly to high-vacuum physical techniques such as Pulsed Laser Deposition (PLD) or Molecular Beam Epitaxy (MBE) which avoid the air-exposure of the sacrificial layer and allow the subsequent in-situ deposition of the

functional oxide on top. As shown in Fig. 1.7c, PLD is the most typical deposition technique, followed by MBE and just a few used radio frequency magnetron sputtering as well.⁷³ Indeed, note that not only SAO but all the other sacrificial layers presented in this chapter coincides in the use of high vacuum deposition technique to prepare them.

Therefore, despite the wealthy properties of SAO there are still many aspects that need further investigation to exploit its full potential. Overcome the ambient instability and identify a cost-efficient, chemical synthetic procedure that does not use vacuum remain important challenges.

1.2 Chemical deposition techniques for complex oxide thin films

The development of deposition techniques for the growth of complex oxide thin films with an accurate control at atomic-scale is crucial for the advancement of material science and their integration in the industry. With no doubt, PLD, MBE and Sputtering are among the most relevant techniques as they allow high crystal quality and precise control of composition and thickness. Nevertheless, when evaluating the suitability of an oxide material it is important to consider cost-effective and sustainable processing techniques enabling conformal deposition while ensuring fine composition control. Over the past few years, Chemical Solution Deposition (CSD) and Atomic Layer Deposition (ALD) have emerged as an inexpensive and potentially scalable alternative demonstrating significant progress towards the production of high quality epitaxial complex oxide films. In this section, CSD and ALD are briefly introduced and the advantages and limitations associated with each technique are discussed using some case examples of epitaxial complex oxides. Further details on the fundamentals of each technique and their critical processing parameters are described in Chapter 2, Experimental.

1.2.1 Chemical Solution Deposition (CSD)

A **CSD process** consists in the deposition of a thin film from a liquid precursor solution. The process is divided in three main steps, as shown in **Figure 1.8**: solution synthesis, deposition and thermal treatment. It starts from an appropriate selection of chemical precursors that are mixed in stoichiometric ratio, according to the desired film composition, with a compatible solvent. The resulting solution is deposited on a substrate by either spin-coating, dip-coating, ink-jet printing or spray pyrolysis, among others, and after deposition a thermal treatment of the film is carried out for film drying, decomposition of the organic components and ultimately crystallization of the oxide phase.

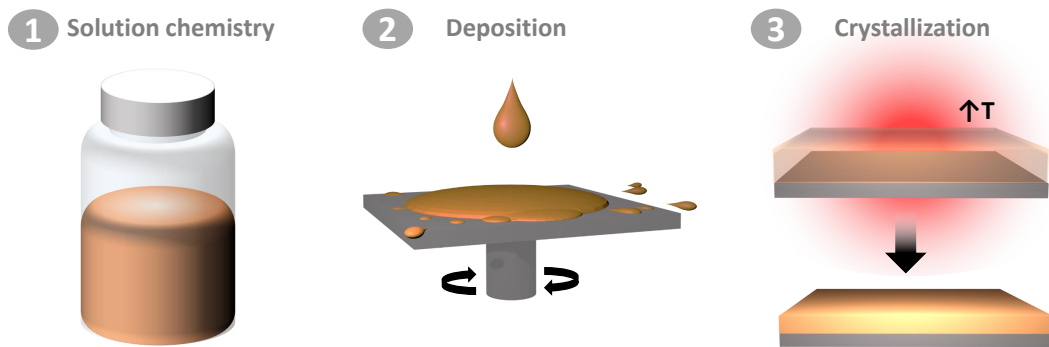


Figure 1.8: Chemical Solution Deposition. Schematic of a CSD process including (1) the preparation of the coating solution to (2) the deposition of the solution on a substrate and finally (3) the thermal processing and crystallization of the film.

CSD is already a quite mature technique for the preparation of functional oxide thin films and its versatility offers plenty of possibilities, as represented in **Figure 1.9**.^{97–100} A wide variety of epitaxial complex oxides including metastable phases have been prepared, such as perovskite-type oxides like the electronic conductor $\text{La}_{0.7}\text{Sr}_{0.3}\text{MnO}_3$,¹⁰¹ the high-temperature superconductor $\text{YBa}_2\text{Cu}_3\text{O}_7$,¹⁰² multiferroic BiFeO_3 ,^{103,104} or more complex structures like layered misfit cobaltates $[\text{Bi}_2\text{Ca}_2\text{O}_4][\text{CoO}_2]_x$ ¹⁰⁵ (Fig.1.9a), among many others. Moreover, CSD presents great capability to form different nanostructures (nanoislands,¹⁰⁶ nanorods and nanowires¹⁰⁷) and nanocomposites,¹⁰⁸ in which it is spontaneously crystallized different structures such as perovskite and spinels during the growth process, see Fig. 1.9b.¹⁰⁹ Another interesting possibility of CSD is the colloidal incorporation of nanoparticles in the precursor solution, permitting to

create epitaxial nanocomposites when deposited as thin film (Fig. 1.9c).^{102,110}

The thickness in CSD films can be controlled by modifying the molar concentration of the precursor solution and use specific solvents and additives, together with adjusting the deposition conditions. Also, CSD offers an easy way to control and change the composition by modifying the starting salts. In particular, polymer assisted deposition (PAD) is a versatile method to pursue the preparation of more complex oxide compositions with molecular control through the use of a polymer.^{100,111} Note that films with surface roughness down to 1 nm can be obtained as demonstrated for example in Fig. 1.9d, where the terrace-like morphology imposed by the conformal growth of a 10 nm thick $\text{La}_{0.92}\text{MnO}_3$ film on top of a STO substrate can be clearly observed.¹¹² In order to achieve thicker films ($>1 \mu\text{m}$), appropriate multilayer deposition or the use of inkjet printing allow to prepare films with no cracks.¹¹³

Another major advantage of CSD compared to other deposition techniques is the fact that

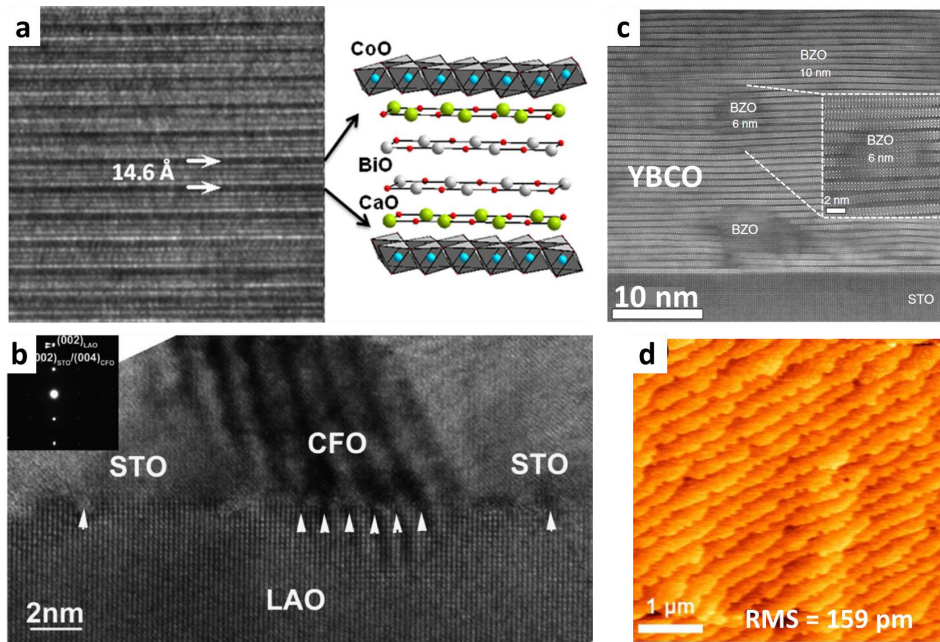


Figure 1.9: Examples of CSD epitaxial oxides. High resolution transmission electron microscopy (HR-TEM) images of (a) $[\text{Bi}_2\text{Ca}_2\text{O}_4][\text{CoO}_2]_x$ film compared to the crystal model;¹⁰⁵ (b) epitaxial nanocomposite of $\text{SrTiO}_3:\text{CoFe}_2\text{O}_4$ grown on a LaAlO_3 single crystal substrate;¹⁰⁹ (c) nanocomposite of BaZrO_3 nanoparticles embedded in an epitaxial $\text{YBa}_2\text{Cu}_3\text{O}_7$ (YBCO) layer grown on a STO single crystal substrate;¹⁰² (d) AFM topographic image of a 10 nm thick $\text{La}_{0.92}\text{MnO}_3$ film on STO.¹¹² Figure adapted from Refs.^{102,105,109,112}.

vacuum is not required and therefore the processing cost is mainly attributed to the energy

consumption of the high temperature thermal treatment to crystallize the oxide phase. Therefore, this technique is considered cost-effective and with potential scalability. To reduce the cost associated to the high temperature treatment, some promising energy-efficient synthesis alternatives are being investigated. For example, playing with the solution chemistry there is the solution combustion synthesis approach¹¹⁴ where a fuel is included in the solution to achieve self-sustained combustion with strong exothermic reactions, or there is the use of photosensitive precursors which allow to lower the crystallization temperature by the action of light.⁹⁹ Another appealing approach is the use of non-equilibrium reactions to reduce the thermal treatment time in which ultrafast growth rates (i.e. 100 nm s^{-1}) have been demonstrated.¹⁰² Overall, CSD can offer high versatility, cost-effectiveness and scalability in the fabrication of highly crystalline functional oxide heterostructures with complex compositions. Nevertheless, despite the many advantages described for CSD, there are still many compositions with novel functionalities that remain unexplored, envisaging plenty of advancements that can be done specially in the new field of freestanding oxides.

1.2.2 Atomic Layer Deposition (ALD)

Thermal ALD is a low-temperature ($<400 \text{ }^\circ\text{C}$) and low-vacuum (10^{-2} to 10 mbar) chemical deposition technique based on the sequential use of gas-phase precursors which react with the surface of a material one at a time in a sequential and self-limiting manner as illustrated in **Figure 1.10a**. This self-limiting growth allows to obtain pinhole-free thin films with high conformality and thickness control with atomic precision, Fig. 1.10b.¹¹⁵ To achieve this level of control, many different deposition parameters need to be carefully controlled and they are described in detail in Chapter 2.

Although firstly developed in the 1970s,¹¹⁷ it has only been in the last decade when this technique has acquired widespread attention. Nowadays, ALD is a key deposition technique in the semiconductor manufacturing industry and it is expanding to areas such as photovoltaics,^{118,119} organic electronics,¹²⁰ energy storage,¹²¹ and catalysis,¹²² among others.¹²³ ALD has become a

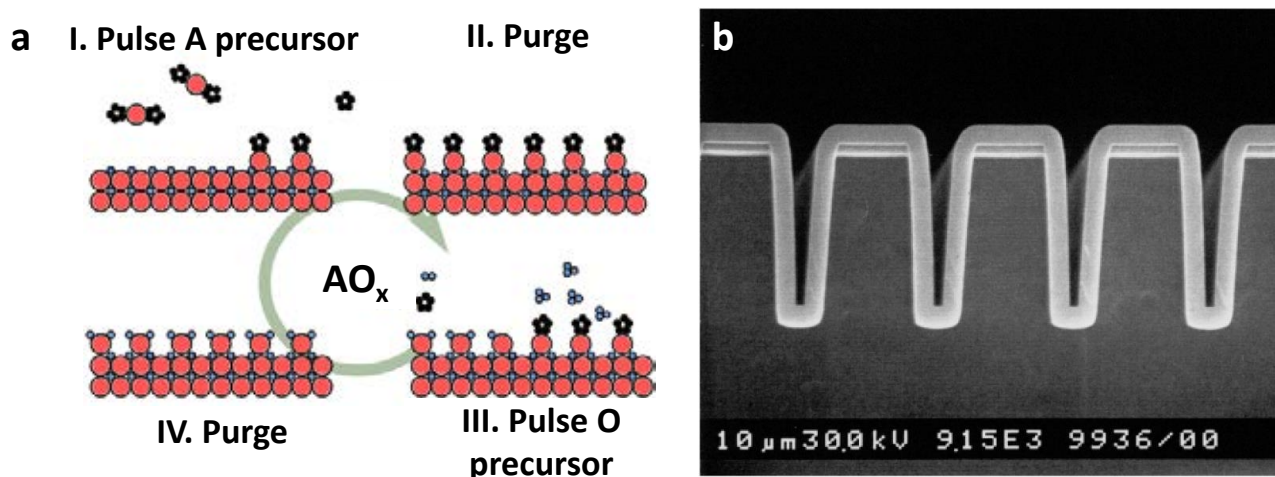


Figure 1.10: ALD binary process. (a) ALD cycle sequence for the preparation of a binary oxide AO_x ; (b) Cross-sectional SEM image of an Al_2O_3 ALD conformal film with a thickness of 300 nm on a nanostructured Si wafer. (Figure adapted from Ref.^{115, 116}).

well established technique for the deposition of several binary materials with special emphasis in amorphous and polycrystalline oxides such as Al_2O_3 , TiO_2 , SiO_2 or ZnO thanks to their well controlled precursor chemistry. Indeed, the chemistry of the ALD precursors is of paramount importance to have an effective ALD process and there are certain demanding requirements which need to be fulfilled. This includes being sufficiently volatile but with a high decomposition temperature to prevent decomposition during the process and being highly reactive toward the surface groups but without reacting with itself or with its surface-adsorbed species. It is also desired that during the ALD process the precursors generate volatile by-products that do not adsorb or etch the growing film. Additional criteria for an ideal ALD precursor should be easiness to handle, low toxicity, low production cost and suitability for upscaling. All these requirements make it challenging to find suitable precursors for each ALD process, and although there are already some well established commercial precursors, much effort is being put into tailor-made precursors to make the reactions more efficient, especially for ternary and quaternary compositions. There, the chemistry of the precursors should ensure the surface reaction with the varying surface chemical species after each cycle.¹²⁴

To further improve the reactivity in an ALD process, there is the so-called plasma-enhanced ALD (PE-ALD).¹²⁵ In this case, upon plasma exposure, radicals with enhanced reactivity facilitate the chemical reaction in contrast to conventional thermal ALD where the necessary

energy for the surface reaction is provided entirely by thermal energy. Therefore, PE-ALD allows to lower the substrate temperature which might be preferable in some applications. Note, however, that this strategy is not so suitable for 3D structures because of the short lifetime of the reactive species. New appealing ALD technologies are also being investigated to work at atmospheric pressure and achieve larger deposition areas at faster rate. In this line, atmospheric pressure spatial ALD is very attractive.¹²⁶ The ALD cycles are being spatial-separated instead of time-separated allowing faster deposition rates and facile integration into industrial processes like roll-to-roll.^{127,128} Other important areas of study in the field of ALD are towards the fabrication of nanostructures by limiting the growth or etching to specific areas by exploiting differences in local surface chemistry such as area selective ALD (AS-ALD)¹²⁹ and atom layer etching (ALE),¹³⁰ respectively. Importantly, all these advances in the field of ALD are nourished by in-depth simulation studies and in-situ characterisation techniques which help to better understand the reaction mechanisms and to develop new processes.¹³¹ As a result, although most of the established processes are based on the use of ALD to grow binary oxides, ALD has also proved useful for the deposition of more versatile chemistries such as ternary, quaternary, and even quinary compounds including oxides, nitrides, sulphides, selenides, arsenides, and tellurides.¹³² The research in molecular layer deposition (MLD) is focused on the deposition of organic materials, especially pure polymers and metal-based hybrid polymers and allows to address many technical challenges in microelectronics, catalysis, energy conversion, luminescent devices, organic magnets, surface engineering, and many others.^{133,134}

The synthesis of complex oxide films by ALD is a burgeoning field of research but the deposition process is far more complicated than that described for binary materials in Fig, 1.10a. It consists in the combination of multiple ALD cycles of binary oxides into supercycles, as illustrated in **Figure 1.11**. Depending on the desired structure (homogeneously mixed cations, structured multilayers or doped oxides) the cycling sequence is modified. Here, ALD parameters such as precursor chemistry, growth temperature and substrate/surface material, which play an important role on the film properties,¹³⁵ will depend on each component and how they are combined. Therefore, new variables need to be considered like the reactivity of the

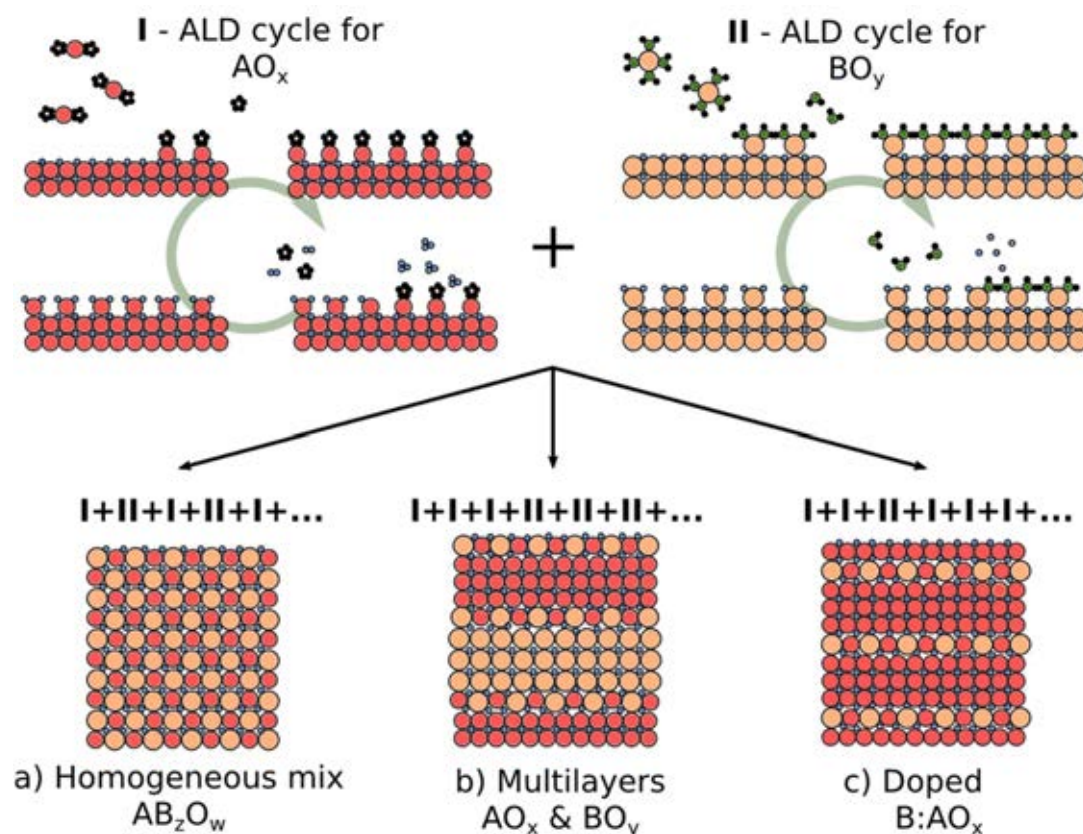


Figure 1.11: Combination of ALD cycles to prepare complex oxides. Schematic of the alternating combination of two ALD processes corresponding to AO_x and BO_y binary oxides. Depending on the sequence of combination, (a) homogeneously mixed film AB_zO_w , (b) multilayered structure of AO_x and BO_y , or (c) doped oxide $B:AO_x$ can be formed. *Figure adapted from Ref.¹¹⁶*

different precursor chemistries and their thermal stability as well as the design of the cycling sequences in ALD supercycles to obtain the desired stoichiometry.^{116,136} Although challenging, this approach has already proved successful to achieve a wide variety of complex oxides by ALD, as shown in **Figure 1.12**, including doped oxides, perovskites (ABO_3), spinels (AB_2O_4), delafossites (ABO_2) and scheelites (ABO_4).^{116,137} Alternatively, another pathway to obtain complex oxides is the use of bimetallic precursors which enable the simplified direct formation of the stoichiometric complex oxide in a single cycle, as proved for $SrTa_2O_6$ and $Gd-Fe-O$ compounds.^{138,139}

Note that the characteristic low temperature growth in ALD results in most of the cases to amorphous and polycrystalline films and to achieve epitaxy a post-annealing is routinely performed. This, for example, is the case of $BiFeO_3$ which as shown in **Figure 1.13a** can be grown

as a superlattice of the corresponding binary oxides Fe_2O_3 and Bi_2O_3 and then become epitaxial BiFeO_3 when annealed at 500-600 °C.^{140,141} On the other hand, direct epitaxial growth during the ALD process at temperatures significantly lower than the typical deposition temperatures has been demonstrated for some complex oxides such as $\text{In}_{2-x}\text{Sn}_x\text{O}_3$ (ITO),¹⁴² Co_2FeO_4 ¹⁴³ and LaNiO_3 ¹⁴⁴ to name a few. For example, as shown in Fig. 1.13b, $\text{BaTiO}_3/\text{SrTiO}_3$ superlattices were recently achieved by ALD at 360 °C, which is 400 °C lower than the typical deposition temperatures utilized in PLD, MBE and MOCVD.¹⁴⁵

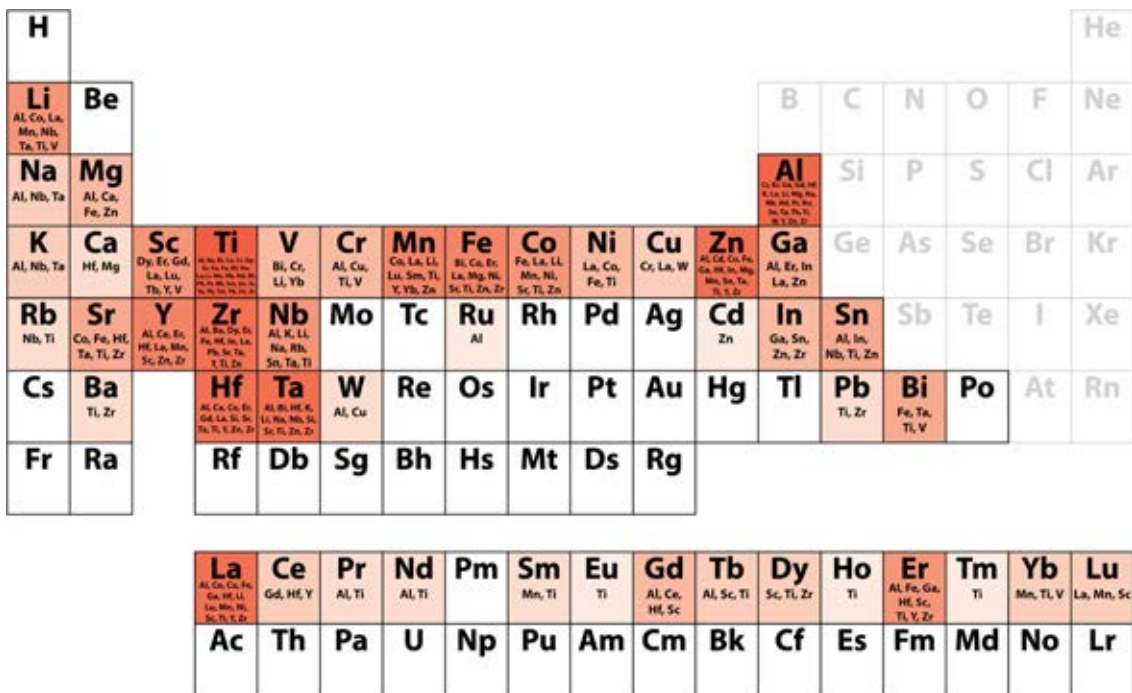


Figure 1.12: Overview of complex oxides deposited by ALD. Periodic table indicating which elements have been combined with another metal as ternary oxide by ALD (until 2019). Figure adapted from Ref.¹³².

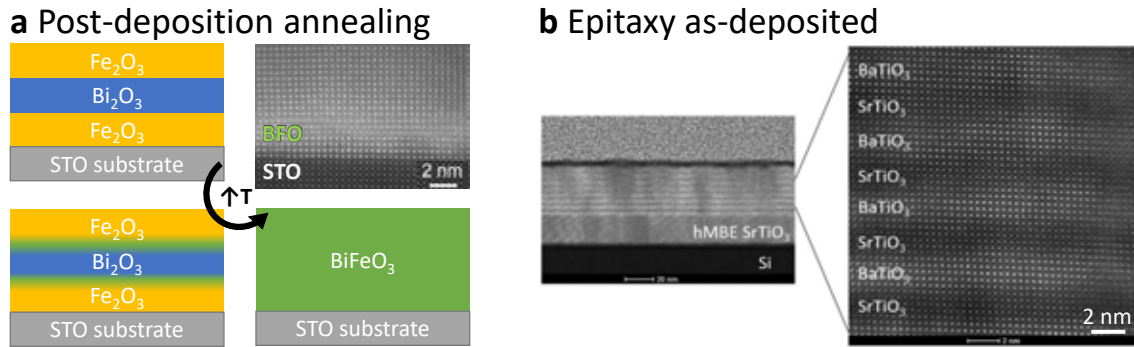


Figure 1.13: Epitaxial growth of complex oxides by ALD (a) Epitaxial growth of BiFeO₃ on a STO substrate by annealing a superlattice of Fe₂O₃ and Bi₂O₃ deposited by ALD. HAADF-STEM image of the resulting annealed film;¹⁴¹ (b) HAADF-STEM image of a BaTiO₃/SrTiO₃ superlattice as-deposited at 360 °C by ALD on a STO-buffered Si substrate.¹⁴⁵ *Figure adapted from Ref.^{141, 145}.*

In summary, ALD is a low-cost chemical deposition technique with atomic control over thickness and composition and conformal free-pinhole growth that offers many opportunities to prepare and develop functional thin films. The synthesis of ALD multicomponent (epitaxial) oxides can deliver remarkable properties although its processing can be extremely challenging because of the many different parameters that must be precisely controlled.

The preparation of freestanding complex oxide membranes involving CSD and ALD is totally unexplored and would open a plethora of new opportunities from fundamental and technological standpoints.

1.3 Scope and outline of this thesis

1.3.1 Scope

Recently, the emerging field of freestanding epitaxial complex oxides has become a hot topic due to the huge potential behind the integration of their advanced functionalities into next-generation electronic and energy-related technologies. Indeed, the development of fabrication approaches that allow detaching the complex oxide from the growth substrate and freely manipulate it has opened a new ground of research from their integration in stacked heterostructures or bendable, wearable and light-weight devices to strain and morphology engineering.

On the other hand, in the last decade the low-cost and potentially scalable CSD and ALD processing techniques have demonstrated significant progress on the preparation of high quality epitaxial oxide thin film. Despite the promising perspectives of these approaches, yet challenges remain on the synthesis level to accurately prepare and nanoengineer many unexplored complex oxides such as $\text{Sr}_3\text{Al}_2\text{O}_6$. Also, to this day, the use of these chemical methods to prepare freestanding epitaxial oxides has never been studied leaving a niche with great potential yet to be explored.

Aiming to explore the opportunities to prepare freestanding epitaxial oxides by chemical methods, in this PhD manuscript I have investigated the preparation of $\text{Sr}_3\text{Al}_2\text{O}_6$ sacrificial layer by

chemical solution deposition to subsequently obtain CoFe_2O_4 (CFO), $\text{La}_{0.7}\text{Sr}_{0.3}\text{MnO}_3$ (LSMO), BiFeO_3 (BFO) and BFO/LSMO membranes.

1. $\text{Sr}_3\text{Al}_2\text{O}_6$ (SAO) sacrificial layer

SAO is one of the most important material used as sacrificial layers and it has been proved effective using high-vacuum deposition methodologies. Motivated by the design of an unexisting process to prepare this sacrificial by chemical meethods the goals are:

- **1.a)** Prepare epitaxial SAO sacrificial layer by solution processing.
- **1.b)** Overcome air instability to broader its applicability through post-annealing and cation engineering ($\text{Sr}_{3-x}\text{Ca}_x\text{Al}_2\text{O}_6$, SC_xAO).

2. Epitaxial complex oxide membranes

To prove the viability of solution processed SAO sacrificial layer to obtain epitaxial complex oxide membranes several approaches have been considered:

- **2.a)** Combination of chemical methods (ALD, CSD) to direct deposit the complex oxide (CFO, BFO) on SC_xAO .
- **2.b)** Explore an hybrid approach combining LSMO-PLD on SC_xAO -CSD sacrificial layer to improve membrane quality.
- **2.c)** Study the the integration of different components in an all-oxide device based on photoferroelectric BFO/LSMO membranes

1.3.2 Thesis outline

This Thesis is presented as a compendium of publications where we aim to provide answers to the questions generated in the process of producing membranes by chemical methods, see **Figure 1.14**. As such, it is organized as follows:

- **Chapter 1** provides an introduction to the topic of research.

- **Chapter 2** describes the synthetic methodologies (ALD and CSD) and a summary of the characterization techniques.

Chapter 3 and 4 are presented as publications in agreement with the Doctoral Committee.

- **Chapter 3** describes a facile chemical route to prepare $\text{Sr}_3\text{Al}_2\text{O}_6$ sacrificial layer.
- **Chapter 4** provides the feasibility to prepare bendable polycrystalline and magnetic CoFe_2O_4 membranes by chemical methods.

The work carried in the last part of the PhD thesis that could not be presented as a form of accepted manuscript due to time restrictions is presented in Chapter 5 and Chapter 6.

- **Chapter 5** provides deep insights on the chemical composition of $\text{Sr}_{3-x}\text{Ca}_x\text{Al}_2\text{O}_6$ sacrificial layer to prepare $\text{La}_{0.7}\text{Sr}_{0.3}\text{MnO}_3$ membranes.
- **Chapter 6** tackles the preparation of freestanding BiFeO_3 heterostructures for all-oxide photovoltaics.
- **Chapter 7**, finally conclusions and perspectives close this thesis.

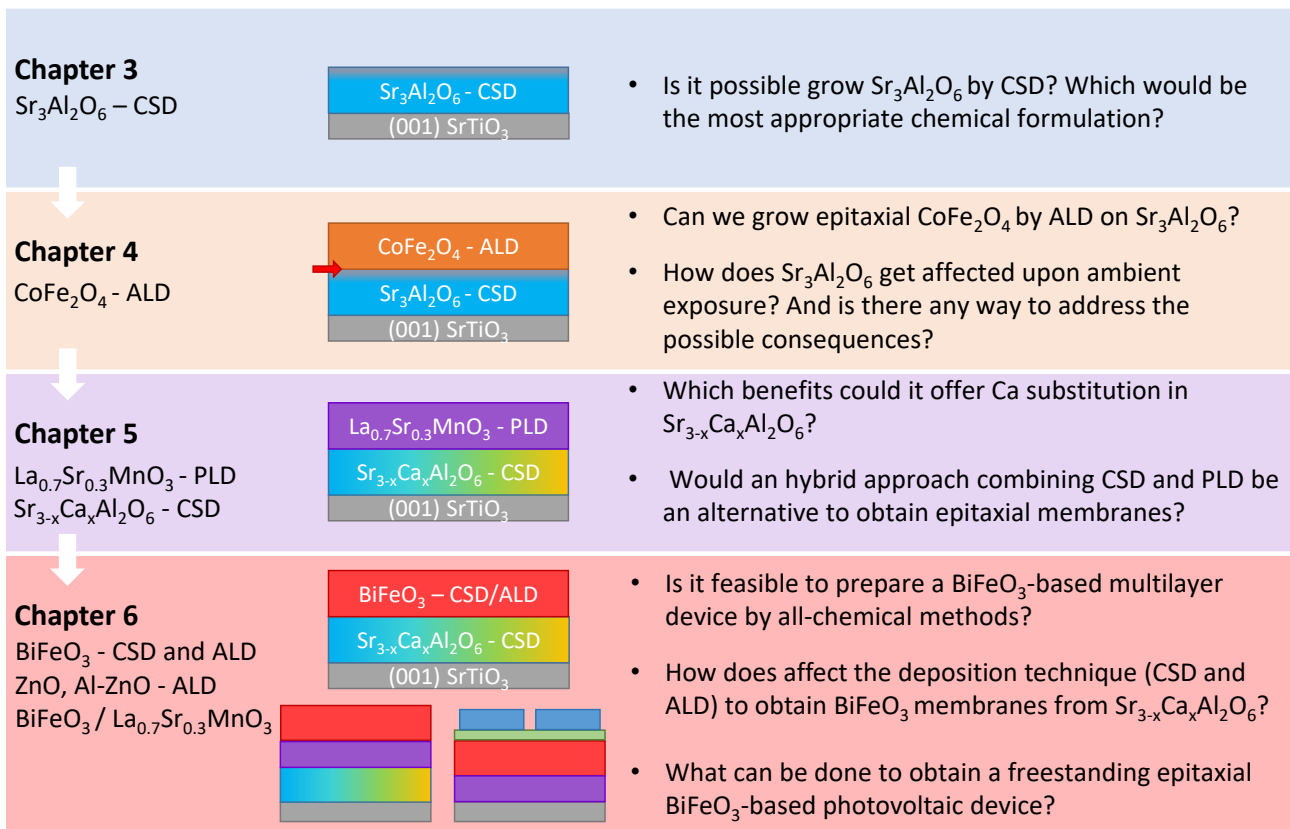


Figure 1.14: Outline of this thesis.

Chapter 2

Experimental

In this study a strong effort has been devoted to synthesize and study complex oxides prepared by chemical deposition techniques. In particular, chemical solution deposition (CSD) and atomic layer deposition (ALD). Therefore, in the first part of this chapter it is detailed the fundamentals and key parameters of these two techniques and followed by the recipes developed for the different oxides when they are not described in the specific chapters. Note that PLD has been utilized as a scientific service and therefore it is only briefly mentioned. In the second part of the chapter it is listed the characterization techniques and the measurement conditions according to the implication in the measurement and data analysis.

2.1 Thin films synthesis

2.1.1 Chemical Solution Deposition (CSD)

In this thesis, two complex oxides have been prepared by CSD: $\text{Sr}_{3-x}\text{Ca}_x\text{Al}_2\text{O}_6$ (SC_xAO) and BiFeO_3 (BFO). The unprecedented preparation of epitaxial SC_xAO has been a backbone of this thesis and there are two chapters dedicated to the synthesis details (Chapters 3 and 5). On the other hand, the preparation of BFO has been carried out using a well-established process previously developed in the group (Chapter 6).¹⁰³ Below, a general CSD process and its key processing parameters is first presented and then the specific synthetic routes followed for SC_xAO and BFO are described.

CSD process

As briefly described in the Introduction Chapter 1.2, a CSD process can be divided in three main steps: solution synthesis, deposition and thermal treatment. Film fabrication begins with the **solution synthesis**, where the main chemical precursors (salts, carboxylates or other metalorganic compounds) are mixed with the desired stoichiometry in a solvent, see **Figure 2.1a**. The selection of the appropriate solvent, ligand chemistry and the use of complexing agents helps designing the optimal solution formulation to ensure an homogeneous deposition (viscosity, surface tension). The homogeneous mixing of the precursors is ensured by magnetic stirring and sometimes refluxing at higher temperatures is used to improve their solubility (Fig. 2.1b). Finally, prior to the deposition, the solution is filtered with a microfilter to avoid any particulate on the deposited thin film (Fig. 2.1c). The **deposition** of the coating solution on a

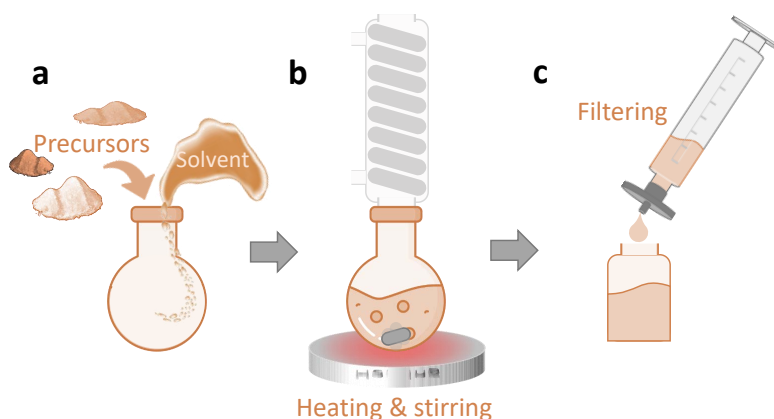


Figure 2.1: CSD: solution preparation. The steps followed to prepare a coating solution are (a) the mixing of precursors, additives and solvent; (b) homogeneous dissolution with magnetic stirring and temperature; and (c) filtering of the final solution.

substrate in this thesis is done by **spin coating** which is the most extensively used deposition technique in a lab scale because of its simplicity, uniformity and reproducibility. In spin coating a liquid solution is cast onto a substrate and then spinned at high speed to finally form an even covering. This process influences the final film thickness. As shown in **Figure 2.2**, the whole process can be divided into 4 main steps: deposition, spin up, spin off and evaporation.

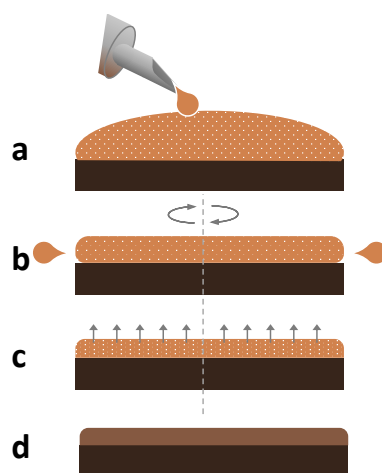


Figure 2.2: CSD: spin coating. Scheme of a typical spin coating process including (a) deposition, (b) spin up, (c) spin off and (d) evaporation.

In the initial step (Fig. 2.2a), the deposition of the liquid solution on the desired substrate is generally done using a micropipette with a controlled liquid volume to cover the entire surface. This can be done while the substrate is already spinning or with a static substrate which is spinned afterwards. Second, in the spin up step (Fig. 2.2b), the substrate spinning is accelerated up to the desired rotation speed and the solution is spread across the substrate. The spin speed, ω , will have an important effect on the final thickness of the film, t , as $t \propto 1/\sqrt{\omega}$. During the spin off step (Fig. 2.2c), most of the solution is expelled from the substrate because of the centrifugal motion, until at some point when the fluid gets dominated by viscous forces becoming a level film. Finally, fluid outflow stops, and solvent evaporation takes over as the dominant process in thinning (Fig. 2.2d). The evaporation rate will depend on solvent volatility as well as the ambient conditions (humidity and temperature). Note that spin coating allows to obtain thin even coatings over most of the substrate but it becomes non-uniform around the edges where a thicker film is formed, phenomenon known as edge effect.¹⁴⁶ Other defects on the film can occur when precipitates or bubbles are present in solution, the substrate is not homogeneous, dirty or the wettability is not adequate.

Finally, the wet as-deposited gel is dried, pyrolyzed and crystallized through a controlled **thermal treatment**. Following the deposition by spin coating, the as-deposited film is a viscoelastic gel composed of an inorganic network with bound organic moieties and solvent entrapped.

Therefore, to achieve a crystalline inorganic oxide, first the organic groups and the solvent must be removed from the film requiring structural rearrangements that occur over a range of temperatures. **Figure 2.3** shows a typical transformation with thermal treatment of an as-deposited wet film to the crystalline state.

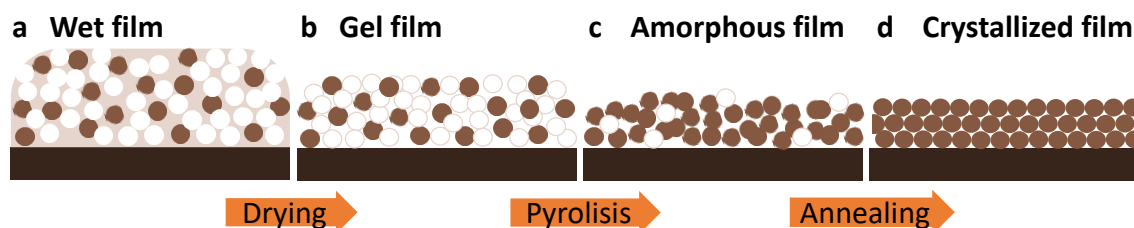


Figure 2.3: CSD: thermal treatment. Scheme of a thermal treatment of (a) an as-deposited thin film, through drying into (b) a gel film, then pyrolyzed into (c) an amorphous inorganic film, and finally annealed until (d) the desired crystalline state is achieved.

During the first heating of the film ($<300\text{ }^{\circ}\text{C}$), evaporation of the solvent entrapped in the film tends to be the dominant process and so the wet film is dried to a gel film (Fig. 2.3b). As the solvent is removed from the pore spaces within the film, the amorphous network collapses due to capillary contraction. Following gelation, by further increasing the temperature ($200\text{-}400\text{ }^{\circ}\text{C}$), the film is pyrolyzed. Pyrolysis means that the organic constituents are removed through conversion to volatile organic molecules, such as CO and CO₂, usually by combustion under an oxidizing atmosphere (either O₂ or air). During this step, residual OH and OR groups contained in the M-O-M oxide network also condensate creating additional M-O-M linkages, which contributes to shrinkage the film resulting in a dense inorganic film (Fig. 2.3c). After pyrolysis, the film is typically amorphous, but upon higher processing temperatures ($600\text{-}1000\text{ }^{\circ}\text{C}$) it transforms to a crystalline state (Fig. 2.3d), process known as annealing. This crystallization occurs through nucleation and growth mechanisms which depend on the thermodynamic and kinetics of the material and the intermediate phases, and such mechanisms will define the main features of the final microstructure of the film.^{147,148} Depending on if the nucleation is homogeneous or heterogeneous (nucleation at the interface with the substrate), it will determine the orientation of the film and the size of the grains.¹⁴⁹ Note that heterogeneous nucleation is required for the growth of epitaxial films.

The temperature at which specific reactions and structural rearrangements occur depend on solution chemistry, where thermogravimetric analysis techniques can be an effective tool to study the decomposition over temperature, but it also depends on thin film processing parameters, such as substrate, film thickness, heating rate and atmosphere. Therefore, these parameters need to be controlled and optimized in each case, as an inaccurate thermal treatment could give place to undesired microstructural phenomena such as uncompleted crystallization and film orientation, secondary phases, dewetting or cracking of the film.¹⁵⁰ Note also that the use of high processing temperatures to achieve highly crystalline films is based on favoring the atomic diffusion by overcoming kinetic barriers, but this can easily induce undesired interdiffusion between the layers of an heterostructure as well. Therefore, sometimes a compromise needs to be found to achieve high crystallinity without having interdiffusion between layers.

SC_xAO film preparation

Solution preparation. Two different precursor chemistries have been investigated for the synthesis of SAO films: metalorganic and metal nitrate. From the study presented in Chapter 3 metal nitrates have been adopted as the most robust approach. In this route, for each SC_xAO composition stoichiometric amounts of strontium nitrate, Sr(NO₃)₂, calcium nitrate, Ca(NO₃)₂, and hydrated aluminum nitrate, Al(NO₃)₃·9H₂O, were weighted and dissolved in Milli-Q water with citric acid (CA), C₆H₈O₇, in a molar ratio of CA to total metal cations CA:M of 2:1. The precursor solution was stirred overnight at 90 °C in a reflux condenser to obtain a 0.25-0.1 M solution. Depending on the solution molarity the SC_xAO film thickness could range from 100 nm (Chapter 3) to 20 nm (Chapters 4, 5 and 6). Finally, prior to deposition the solution was filtered with a polytetrafluoroethylene (PTFE) hydrophilic filter of 0.45 μm pore size.

Spin coating deposition. Prior to the deposition, the substrate must be appropriately cleaned and pre-treated to improve the wettability. Here, bare (001) STO of 5 x 5 mm² was the typical substrate used and it was cleaned with acetone and methanol. When water-based solutions were used (SAO and SC_xAO), the substrate was treated for 10 min with UV-ozone to make

it more hydrophilic, improving its wettability. Note that recycled (001) STO substrates could be used as well. The procedure followed for their recycling is explained in Section 2.2. The deposition was carried out with a spin coater Ossila. 15 μm of precursor solution were cast onto the substrate and then spin at 6000 rpm for 30 s. Because of the effect of the ambient conditions on the final quality of the spin-coated film, all the depositions were done in a N_2 chamber with controlled low humidity (20-30 %) to improve the reproducibility, see **Figure 2.4a**.

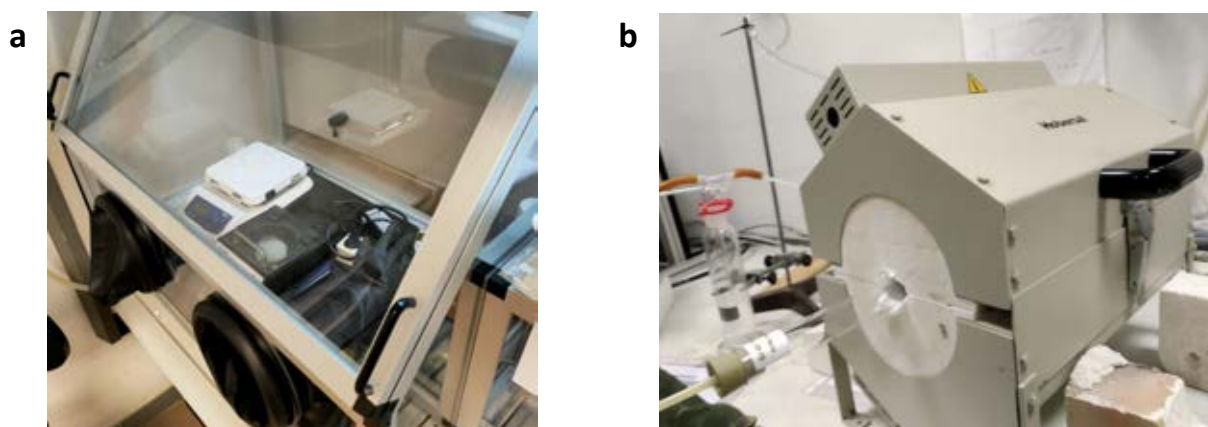


Figure 2.4: CSD equipment. (a) Photo of the equipment containing the spin coating and a hot plate for the first stage of the thermal treatment. The equipment consists of a chamber with gloves to manipulate and low humidity controlled through continuous N_2 gas flow, with a smaller prechamber to introduce/remove the material; (b) Photo of the tubular furnace used for the annealing step with O_2 gas flow regulated by a mass flow controller.

Thermal treatment. The optimized thermal treatment of the 20 nm thick SC_xAO layers consists of two steps: (1) low temperature baking (10 min at 120 $^\circ\text{C}$) in a hot plate (Fig. 2.4a) to evaporate the water and (2) annealing in a tubular furnace (Fig. 2.4b) with a constant 0.6 l min^{-1} O_2 flow at 25 $^\circ\text{C min}^{-1}$ up to 800 $^\circ\text{C}$, with a dwell of 30 min and then cooled down at 25 $^\circ\text{C min}^{-1}$ to room temperature. Because of the air sensitivity of these samples, they were immediately sealed in vacuum after the annealing. Prior to PLD-epitaxial oxide deposition on this sacrificial, a recrystallization process was performed to restore the SC_xAO surface crystallinity after air exposure. In this case, following the growth of SC_xAO , upon sample air-exposure, the film was introduced in the PLD chamber to perform an in-vacuum annealing with a heating ramp of 15 $^\circ\text{C min}^{-1}$ up to 825 $^\circ\text{C}$ with a dwell of 30 min at an oxygen partial pressure PO_2

of 0.1 mbar and then the oxide was in-situ deposited by PLD. A complete thermal profile for a SC_xAO film is represented in **Figure 2.5**.

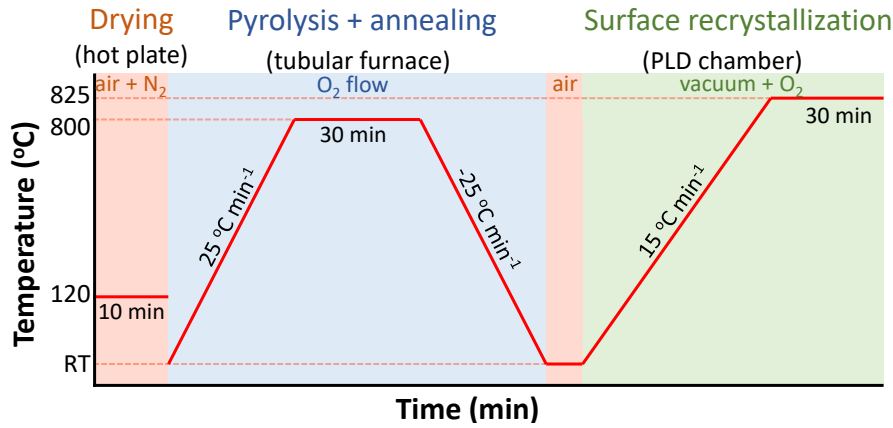


Figure 2.5: SC_xAO thermal profile. Schematic representation of temperature versus time for a typical SC_xAO thermal treatment. After spin-coating deposition, the SC_xAO film is directly dried on a hot plate within a dry chamber with controlled low humidity. Then the SC_xAO film is introduced in a tubular furnace where annealing up to 800 °C under O_2 flow is performed. Finally, when epitaxial oxides are deposited by PLD, a surface recrystallization process is done up to 825 °C in-vacuum with controlled PO_2 .

BFO film preparation

Solution preparation. To prepare the BFO precursor solution stoichiometric amounts of hydrated bismuth nitrate, $Bi(NO_3)_3 \cdot 5H_2O$, iron nitrate and $Fe(NO_3)_3 \cdot 9H_2O$ were dissolved in a solvent blend 3:1 of 2-methoxyethanol and acetic acid to obtain a 0.25 M solution as previously reported by the group.¹⁰³ This solution was first stirred for 2 h at 60 °C and then overnight at room temperature. Before deposition the solution was filtered with a PTFE filter of 0.22 μm pore size.

Spin coating deposition. The process of deposition was carried out using spin coating in the N_2 box (humidity $\sim 20\%$). 17.5 μm of 0.25 M BFO precursor solution was deposited on the substrate and then spin at 6000 rpm for 30 s. This deposition was performed on $5 \times 5 \text{ mm}^2$ SAO//((001)STO and LSMO-PLD/ SC_xAO //((001)STO, as further explained in Chapter 6.

Thermal treatment. The spin-coated BFO film was first heated on a hot plate at 90 °C for 10 min to dry it and then at 270 °C for 4 min to pyrolyze it. This process, from the spin coating

of precursor solution to the hot plate heating steps, was repeated 3 times in order to achieve a 100 nm BFO film. Then, the sample was directly introduced in a pre-heated tubular furnace at 600 °C (flash heating) with a dwell of 2.5 h and a constant O₂ flow of 0.6 l min⁻¹ and directly cooled down in air to room temperature (quenching).

2.1.2 Atomic Layer deposition (ALD)

In this thesis ALD was used to prepare thin films of different functional oxides including binary, doped and complex oxides. In particular, it has been developed the procedure to prepare ZnO, Al-doped ZnO (AZO), CoFe₂O₄ (CFO) and BiFeO₃ (BFO). ZnO and AZO were prepared using a combination of precursor and co-reactant that is well established, but the growth conditions had to be studied and adapted to our ALD reactor (Chapter 6).¹³⁶ Regarding CFO and BFO, a new combination of precursors was studied using a tailor-made Fe metalorganic precursor¹⁵¹ and the growth conditions were investigated in each case (Chapters 4 and 6). Below, it is first presented a general ALD process together with some key processing parameters, and then details about the equipment, precursors and process systems used for the ALD depositions in this thesis.

ALD process

A typical ALD process consists of pulsing gas-phase reactants into the reaction chamber by cycles divided in two half reactions as displayed in **Figure 2.6**. First, a precursor is dosed, which is a metal center surrounded by chemical functional groups and after a purging step a co-reactant is dosed, which is a molecule with a nonmetal center such as O, N, S, etc. Both precursor and co-reactant are dosed (separated in time) until saturation, i.e. all available reactive surface sites are consumed after a certain exposure time. What makes ALD unique is the as-mentioned self-limiting surface reaction, therefore, only the precursors that reacted with the

surface remains defining an atomic layer and leading to a characteristic growth per cycle (GPC) in contrast to conventional chemical vapour deposition (CVD). As briefly explained in section 1.2 with Fig. 1.11, when multication structures are pursued such as complex oxides, multilayers or doped oxides, the most typical way to proceed is to combine the above-mentioned ALD binary oxide cycles into supercycles modifying the cycling sequence depending on the desired final structure.

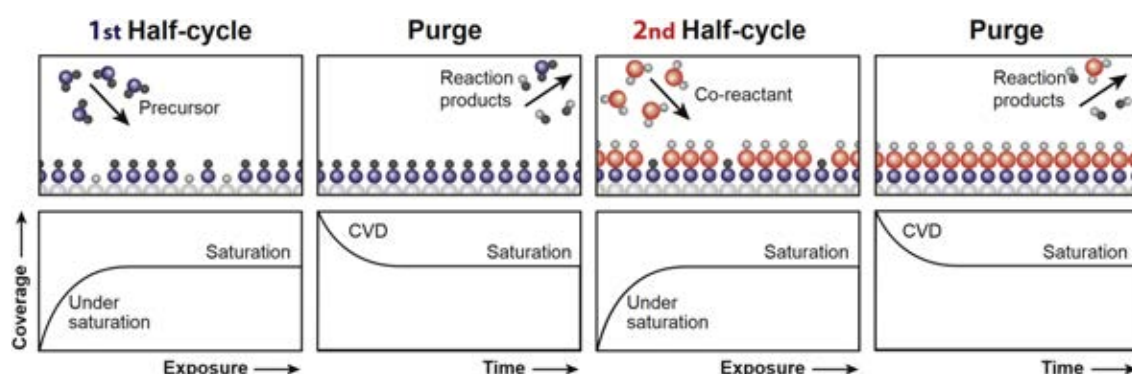


Figure 2.6: ALD cycle for the preparation of a binary oxide. Schematic of an ideal ALD cycle which is divided into two half-cycles: dosing of the precursor (inorganic coordination compound) and co-reactant (oxygen source), separated by purging steps. First the gas precursor is dosed into the reactor chamber until saturation. Then the byproducts are purged, otherwise simultaneous exposure of both reactants could lead to CVD effects. The same process is done with the gas co-reactant, and these half-cycles are repeated in an ABAB fashion until reaching a certain film thickness. *Figure adapted from Ref.¹⁵².*

ALD behaviour with self-limiting growth is not straight-forward and it is only achieved when a different set of chemical and physical conditions are met. Among these conditions there is a specific temperature window in which ALD behavior is obtained. As shown in **Figure 2.7**, the temperature window, which is represented as an horizontal line, is the range of temperatures over which the GPC shows weak or no temperature dependence. Outside the temperature window, several chemical and physical processes can hinder the ALD behavior. At lower temperatures some reactants can condense on the surface leading to higher GPC, or on the contrary the GPC could diminish because of limited thermal energy that leads to lower reactivity of the molecules. On the other hand, too high temperatures can decompose the reactants leading to a CVD growth and therefore higher GPC, or on the contrary the GPC could be lowered because

of desorption from the reactive surface groups.¹⁵²

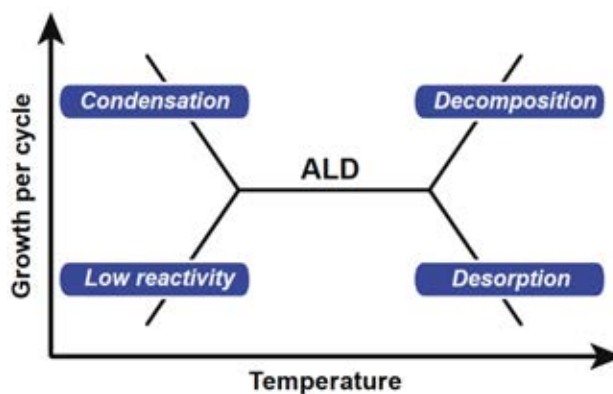


Figure 2.7: ALD temperature window. An ALD process can follow different behaviours, indicated in this idealized graph of growth per cycle as function of temperature. *Figure adapted from Ref.¹⁵².*

Another key parameter that determines the ALD processing conditions and therefore the final film quality is the precursor chemistry, as briefly introduced in Chapter 1. Identifying thermally compatible precursors, cheap and commercially available is not an easy task. The opportunity to work with tailor-made precursors allows to prepare wider variety of compositions while defining a more efficient deposition process.

ALD equipment

The ALD preparation of oxides in this thesis has been carried out in a commercial Savannah 100 ALD system (Cambridge NanoTech Inc.), shown in **Figure 2.8a**. This ALD system, located in a 10,000 class cleanroom, is equipped with an LG-7 ozone generator (Corona Discharge), a dry vacuum pump and connected to a computer which allows for programming and executing process recipes through a Savannah software. As shown in Fig. 2.8b, the ALD reactor consists of a reaction chamber of 10 cm diameter, with a gas inlet on one side and a gas outlet on the other side. The gas inlet is connected to a gas line with the precursor cylinders connected in series along the carrier gas manifold. Here, N_2 is the carrier gas and its flow is electronically controlled. In the same way, the ozone generator is connected as one of the precursor inlets. On the other side, the gas outlet is connected to the pumping line with a stop valve that can

be used to close the connection between the reaction chamber and the dry vacuum pump.

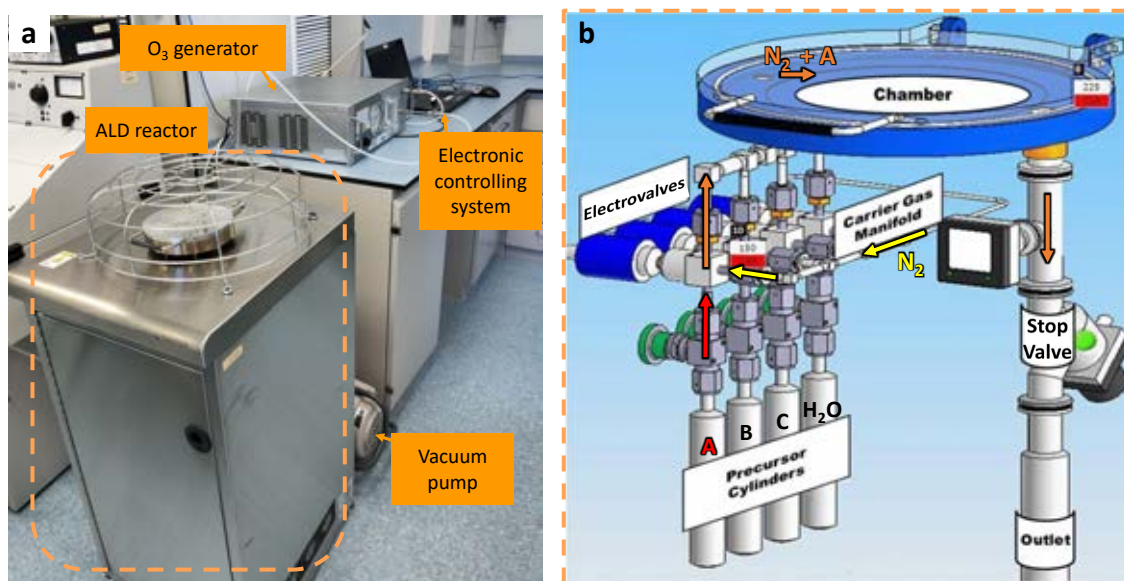


Figure 2.8: ALD: commercial Savannah 100 ALD system. (a) ALD equipment comprising the ALD reactor, O₃ generator, vacuum pump and electronic controlling system. (b) Sketch of the main components of the ALD reactor. Colored arrows indicate the flow direction of the N₂ carrier gas (yellow), a precursor (red), and the mixture of both (orange).

Precursors

The ALD deposition of oxides has been carried out with five main metalorganic precursors, see **Figure 2.9**. These include DEZ (diethylzinc), TMA (trimethylaluminum), Co(Cp)₂ (Cp = cyclopentadiene), Fe(ⁱpki)₂ (ⁱpki = N-isopropyl ketoiminate) and Bi(tmhd)₃ (tmhd = tetramethyl heptanedionate). Alternative Bi and Fe metalorganic precursors such as Bi(Ph)₃ (Ph = phenyl) and Fe(Cp)₂ (Cp = cyclopentadiene) were also used but discarded because showed poor performance. All these precursors are commercial and they were purchased and used as received, except for tailor made Fe(ⁱpki)₂ which was synthesized and characterized by our collaborators Dr. D. Zanders and Prof. A. Devi from the Ruhr University Bochum, Germany.¹⁵¹ The precursors were stored and handled in a glove box and they were filled into ALD cylinders with seal valve. Regarding the co-reactants, Milli-Q water (H₂O) and ozone (O₃) were used as oxidizers. H₂O was filled in a precursor cylinder, while O₃ was produced with a LG-7 ozone generator with a 5 wt.% concentration and an output of 5 g·h⁻¹.

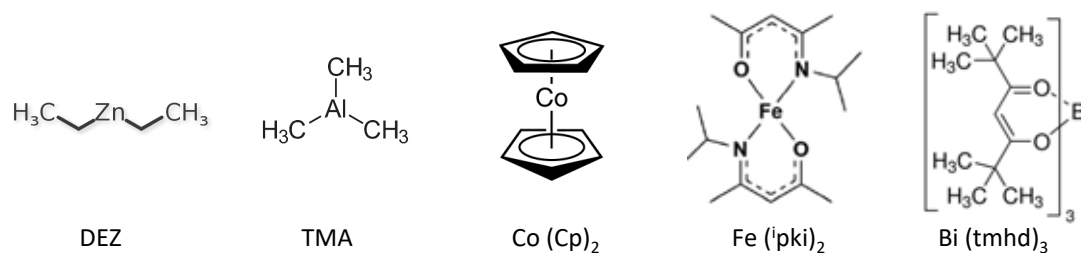


Figure 2.9: ALD precursors. Molecular structures of the main metalorganic precursors used for the ALD oxide depositions.

Process and valving system

An ALD process is controlled with a Savannah software following a recipe as the one shown in **Figure 2.10**. Initially, the system is heated to the desired temperature, including the precursor cylinders (RT - 150 °C), chamber (150 - 250 °C) and intermediate connections (150 °C). With the system heated, a Si wafer with the samples adhered by silver paste is introduced in the chamber and brought into vacuum. Once temperature and pressure are stabilized with a constant N₂ flow (20-50 sccm), the samples are exposed to O₃ pulses to activate the surface forming hydroxyl-terminated groups and facilitating the chemical reaction with the precursors. Then it is when the core of the ALD process starts, with *a* cycles consisting of alternate pulses of precursor and co-reactant, separated by a purging step. Depending on the precursors, two different configurations of valving systems were used, namely flow mode (F) and pressure-boost mode (PB). The difference between both modes is the way in which the precursor is pulsed. In F mode, a continuous flow of inert gas is held helping to carry the pulsed precursor from the cylinder to the chamber where it reacts, and then it is evacuated. On the other hand, when the precursor has low vapor pressure or it has a heavy molecular weight that hinders its arrival into the chamber, the PB mode is used. In this case, a more complex valving system allows the carrier gas filling up the precursor cylinder and elevating the pressure inside and, subsequently, the precursor is pulsed with the filled nitrogen.

For complex and doped oxides A_xB_yO_z, where the ALD process involves two metalorganic

ALD process for a binary oxide (AO_x):

- 1) Heating of precursor cylinders, chamber and connections
- 2) Sample introduced into the chamber
- 3) Vacuum pump
- 4) Continuous carrier gas flow (N_2) determines the base pressure (P_0)
- 5) Substrate pre-treatment with O_3 pulses

Flow mode:

- 6) Pulse precursor A
- 7) Purge
- 8) Pulse oxidizer (H_2O or O_3)
- 9) Purge
- 10) Go to step (6) for a n° of cycles

Pressure-boost mode:

- I. Close stop valve (N_2 accumulates, $\uparrow P$)
- II. Open precursor A valve (N_2 goes into the cylinder)
- III. Close A
- IV. Open stop valve (P_0 is restored)
- V. Pulse A (N_2 trapped + precursor go out)

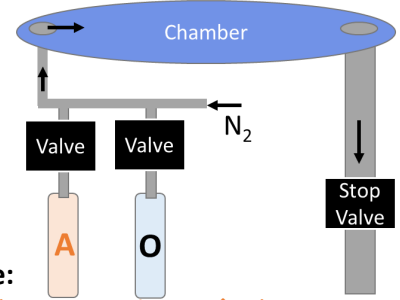


Figure 2.10: ALD process. Recipe of a typical ALD process for the deposition of a binary oxide AO_x . Flow mode is compared to the pressure-boost mode.

precursors (A and B), the same steps (6)-(10) shown in Fig. 2.10 are followed for each precursor, combining a cycles of AO_x and b cycles of BO_y in the so-called subcycles. The total sequence $a \cdot (A + O) + b \cdot (B + O)$ conforms a supercycle, where the ratio a/b has a determining role on the stoichiometric relation between A and B. This supercycle can be repeated for N times to reach the desired thickness. Therefore, the final cycle sequence for a complex/doped oxide $A_xB_yO_z$ comes determined by

$$N[a(A + O) + b(B + O)] \quad (2.1)$$

where A, B and O stand for pulse and purge of the metalorganic precursors A and B and the co-reactant O, respectively. The optimal conditions used in each oxide deposition are summarized in Table 2.1.

Note that the deposition processes to prepare BFO and CFO films have been adapted from previous studies performed in the group^{143,153} and, as a novelty, in this thesis it has been replaced the use of $Fe(Cp)_2$ by $Fe(i\text{pki})_2$. The conditions have been re-adapted to the already established ALD processes and no further analysis on the precursor saturation for the complex oxide has been carried out. Therefore, this process is called an ALD-type approach.

Table 2.1: ALD general conditions for the deposition of $A_xB_yO_z$ oxides. A, B = metalorganic precursors, O = co-reactant (same co-reactant chemistry used for both precursors), F = flow mode, PB = pressure-boost mode.

Oxide	Chamber T [°C]	A (T [°C])	Pulse mode	O	a cycles	B (T [°C])	Pulse mode	b cy- cles
ZnO	160	DEZ (RT)	F	H ₂ O	40-600	-	-	-
AZO	160-200	DEZ (RT)	F	H ₂ O	15-35	TMA (RT)	F	1
CFO	250	Co(Cp) ₂ (90)	PB	O ₃	5	Fe(ⁱ pki) ₂ (130)	PB	13
BFO	250	Fe(ⁱ pki) ₂ (130)	PB	O ₃	3-18	Bi(tmhd) ₃ (150)	PB	3-18

Post-annealing treatment

After the low-temperature deposition by ALD, some of the oxides were thermally treated at higher temperatures to promote their crystallization and epitaxy. The thermal treatments were performed using a tubular furnace pre-heated at a specific setpoint temperature (400-700°C) depending on the composition of the oxide. The sample was rapidly introduced (flash heating) and sustained there for a period of time (30-60 min) under controlled 0.6 l min^{-1} O₂ flow and finally it was rapidly removed from the furnace (quenching) to cool down to room temperature.

Construction of a tailor-made ALD reactor

A part of this thesis has been to build a new ALD reactor, see **Figure 2.11**. The ALD system design has been developed from scratch being inspired by the reactor developed by Dr. Massimo Tallarida at ALBA-Synchrotron. The system was designed trying to respond to the needs of the research work done in the lab and includes:

1. Ozone generator and analyzer to work with highly reactive ozone as oxidizer for the synthesis of oxides.
2. Multi-precursor system for the deposition of complex oxides and heterostructures of multiple oxides.
3. Valving system for the specific control of each precursor and to do pressure-boost pulsing

when required.

4. Heater with wide range of temperature which includes the typical ALD temperature window (150-250°C) but also have the possibility to go up to 1000°C.

5. Easy access and more frequent use compared to the other ALD reactor which is found in the cleanroom of ICMAB.

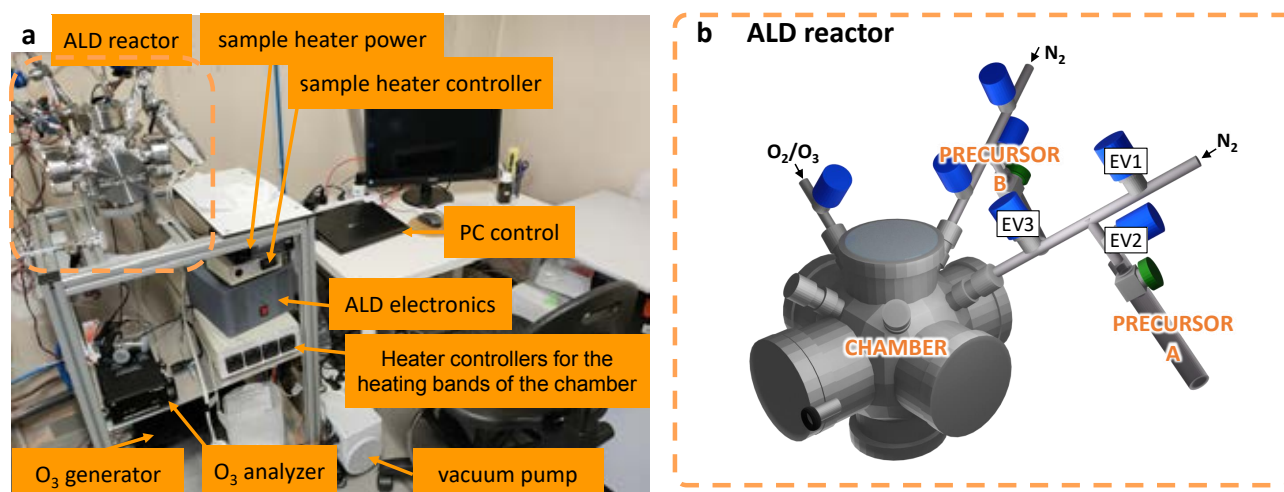


Figure 2.11: ALD: home-built equipment. (a) ALD equipment comprising the ALD reactor, O₃ generator and analyzer, vacuum pump and electronic controlling system through home-made software. (b) Sketch of the ALD reactor configured with three inlets: precursor A, precursor B and O₂/O₃.

Fig. 2.11a shows the complexity of the whole ALD system composed of the different parts that were required to have control of determining process parameters such as temperature, pressure, gas flow and valving system, among others. The temperature system consisted of separated heating power and controllers for the different parts of the ALD system including sample holder, chamber, precursor cylinders and dosing lines. The sample holder was heated with a HeatWave Labs button heater, which is capable of heating up to 1000 °C,¹⁵⁴ the heating of the chamber and precursor dosing lines was done with heating wires (up to 250 °C) wrapped with heat resistant aluminum tape and the precursor cylinders were heated with heating jackets (up to 180 °C). The vacuum was done using a Edwards RV5 two stage rotary vane pump connected to the chamber with a stop valve in-between, and it was monitored using an Edwards Pirani gauge located at the vacuum chamber (base pressure $P_0 \sim 3 \cdot 10^{-2}$ mbar). The reactor is equipped with an oxygen dosing line connected to a BMT 803 N ozone generator coupled with a BMT

965 BT ozone analyser to provide a stronger oxidising agent. On the other hand, ultrapure N_2 is used as carrier gas and its flow is regulated through a mass flow controller. All these parameters were electronically controlled by a home-made software developed by an electronic engineer (X. Sintas).

Fig. 2.11b shows the ALD reactor chamber, which can be equipped with up to 5 precursor dosing lines (in the sketch only 3 are occupied: O_2 , precursor A and precursor B). Each precursor dosing line consists of a three-valving system which allows to work with either flow mode or pressure-boost mode. Moreover, compared to the commercial Savannah 100 ALD system where all the precursors were connected in series sharing the same dosing line, here the precursors are connected in parallel avoiding possible cross-contaminations. The sample holder is located in the center of the vacuum chamber held over its heater and monitored with a thermocouple that is put inside it.

The construction of this ALD reactor has been done step by step and it has proved to be very challenging, highlighting the importance of an accurate control of each of the parameters mentioned above to obtain a reproducible and controlled ALD process. Its optimization and understanding are still ongoing during the writing of this thesis and, therefore, this manuscript does not include oxides developed under this new reactor.

2.1.3 Pulsed Laser Deposition (PLD)

PLD is a physical vapor deposition technique where a high-power laser beam is pulsed to a target made of the material that wants to be deposited in such a way that the material is vaporized in a plasma plume getting deposited as thin film on a substrate, see **Figure 2.12**. This process occurs in a vacuum chamber either in ultra high vacuum or in the presence of a gas such as O_2 which helps oxygenating the film when oxides are deposited.¹⁵⁵

In this thesis, PLD was used to deposit thin films of LSMO. The PLD depositions were carried out by the scientific services of ICMAB in a PLD system equipped with reflection high-energy electron diffraction (RHEED) and a 248 nm KrF excimer laser. 60 nm thick LSMO films were deposited at 725 °C under 0.1 mbar of PO_2 . Limited depositions of CFO were also performed

by PLD at 450 °C with 0.1 mbar PO₂.

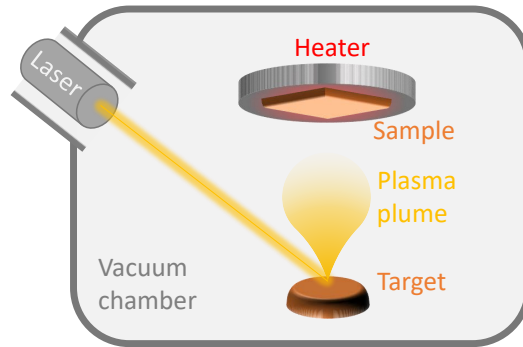


Figure 2.12: Configuration of a PLD deposition chamber

2.2 Sacrificial etching and membrane lift-off

The procedure to etch the sacrificial layer and subsequent exfoliation is extremely challenging and it was a new research field in the group. It was investigated the optimal processing conditions to achieve a high transfer yield diminishing the amount of cracks and defects and preserving the integrity of the membrane.

Sacrificial layer etching. The etching of bare SAO//STO was investigated with different solvents (water, acetone, acetic acid...) as described in Chapter 3. The SAO film is instantly etched when in contact with a drop of water, and the same was observed for the other SC_xAO films with different Ca contents. However, when an oxide is grown on top of the sacrificial, the water penetration is limited only to the edges slowing the etching rate. Heterostructures with SAO sacrificial had to be immersed in water for at least 2 days to obtain a complete etching, while the time of immersion was increased up to 1-2 weeks to ensure the complete etching of the less-soluble SC_xAO sacrificials consistent with the change in the chemistry^{75,80} (Chapters 5 and 6).

Transfer process. The transfer of faultless freestanding oxides from a sacrificial layer is a complex step as there are several parameters that one needs to consider. In this thesis, the transfer was either done with the help of a polymer support adhered to the sample prior to its immersion in water, here named *polymer transfer process*, or with no support, here named

floating transfer process and explained in detail in Chapter 4. Regarding the polymer transfer process, an adequate polymer support should present a force of adhesion strong enough to ensure the preferential adhesion of the released oxide membrane on the polymer rather than on the STO substrate and, on the other hand, the adhesion should be weak enough to enable the posterior transfer of the oxide membrane to the final support of interest. In this thesis, polydimethylsiloxane (PDMS), polyethylene terephthalate (PET), and liquid polymers that are then cured on the oxide such as polypropylene carbonate (PPC) or poly(methyl methacrylate) (PMMA) have been tested and compared. Finally, the polymer support that allowed us to obtain reproducible and good quality membranes was a PET foil being basically a screen-protector composed of PET with a thin layer of silicone. Prior to its adhesion to the oxide film, a plastic protection film was removed from the PET surface and exposed to UV-ozone for 5 min. The oxide sample was exposed to UV-ozone as well to make its surface more reactive and similar between them. Finally, the oxide was placed on the PET foil and they were manually pressed to ensure a conformal intimate contact between them prior to immersing the entire stack in water. The adhesion conditions between PET and the sample were further studied and optimized in the framework of an EU-NFFA project with the Paul Scherrer Institut (PSI, Switzerland) using a hot-embossing machine with controlled pressure (100-500 N), time (1-10 min) and temperature (25-100 °C). The optimal conditions were found to be working at room temperature with 100 N pressure and it was not observed any significant differences with time of pressure.

The etching of the sacrificial layer was assessed by optical microscope to control when to proceed with the lift-off. Once the etching was completed, polymer and STO were separated manually to obtain the transferred membrane attached on the polymer support. This is a crucial step where a more accurate control could help minimizing membrane damages such as cracks improving as well the transfer yield.

The released membranes supported on a polymer stamp could be further transferred to any arbitrary substrate including silicon, glass or metallic-coated supports, among others. To do so, first the membrane and the new substrate were exposed to UV-ozone and the stack poly-

mer/membrane/new substrate was slightly pressed together to improve the contact. When PET was used as stamp, by heating the sample at 90 °C for about 5 min (70 °C for PDMS), the PET could be removed and the membrane transferred to the other substrates.^{81,156}

STO recycling. After recovering the STO substrate from the SC_xAO etching, it was subsequently treated to reuse it. First, 10 min sonication in H_2O was used to remove any remaining traces, and then 30 s immersion in buffered HF solution (30%) and post-annealing for 1 h at 950 °C was carried out to recover the terrace-like morphology¹⁵⁷ as shown in Chapter 3. Nevertheless, recently, 80 °C hot water soaking and rinsing treatments of STO after SAO etching have demonstrated to give similar results.⁹¹

2.3 Characterization

In this chapter all the characterization techniques used in the different chapters to characterize solution, films and membranes are described. However, note that the specific characterizations used in each chapter can also be find there as this thesis is a compendium of articles. The characterization techniques have been classified according to the specimen to characterize: solution or films/membranes. Regarding the latter, the techniques presented are divided for structure, morphology, thickness and composition as well as their physical properties including magnetic, electric, optic, ferroelectric and photoresponse properties.

- Solution: rheometer, thermogravimetric analysis (TGA), differential scanning calorimetry (DSC) and infrared spectroscopy (IR).
- Structure: X-ray diffraction (XRD), reflection high-energy electron diffraction (RHEED) and scanning transmission electron microscopy (STEM-EELS).
- Morphology: atomic force microscopy (AFM) and scanning electron microscopy (SEM).
- Thickness: spectroscopic ellipsometry (SE) and X-ray reflectometry (XRR).

- Chemical composition: X-ray photoelectron spectroscopy (XPS) and energy-dispersive X-ray spectroscopy (EDX).
- Physical properties: superconducting quantum interference device (SQUID), ultraviolet-visible spectroscopy (UV-vis), four-point probes (4PP) and physical property measurement system (PPMS), piezoresponse force microscopy (PFM) and photoresponse characterization.

In some cases, both the data acquisition and data analysis was done by the author, as it is for rheology, SEM-EDX, SE, IR, UV-vis and 4PP. In other cases, the measurements were carried out by technicians and the author was the responsible of the data analysis, as it is the case for TGA, DSC, XRD, RHEED, AFM, XRR, XPS and SQUID. Some measurements were realized in collaboration with experts in the field, as it is for STEM, PPMS, PFM, macroscopic ferroelectric and the photoresponse characterization.

2.3.1 Solution characterization

Rheology

A rheometer was used to study the viscosity of the precursor solutions used in CSD. All the measurements were done at a controlled temperature of 22°C using a Rheometer HAAKE RheoStress RS600 from Thermo Electron Corp at NANOQUIM cleanroom - ICMAB. The resulting value is the average of three different measurements, all of them done with 1 ml of precursor solution just after filtering it.

Thermogravimetric analysis (TGA) and differential scanning calorimetry (DSC)

Thermogravimetric analysis (TGA) is an analytical technique in which the mass of a sample is measured over time as it is heated at a constant rate and in specific atmosphere. TGA allows to determine a material's thermal stability and its fraction of volatile components lost as a function of temperature. When combined with differential scanning calorimetry (DSC) which

determines the variation in the heat expected to increase the temperature of the sample, one could determine which decomposition process is occurring at each temperature and use it to optimize the annealing process of the studied material.

In this thesis, TGA and DSC were done with a thermal analyzer METTLER TOLEDO model TGA/DSC 1 equipped with a oven HT1600 and microbalance MX5 at University of Málaga, with a range of temperatures from 30 to 1000 °C, heating rate of 10 °C·min⁻¹, and O₂ gas flow of 50 mL·min⁻¹. In order to carry out this study, the precursor solutions were previously dried to a gel by a rotary evaporator (R-100)

Infrared spectroscopy (IR)

IR spectroscopy is an analytical technique used to identify and study the chemical composition of materials based on the interaction of infrared radiation with molecular vibrations in a sample, which results in the absorption or transmission of specific wavelengths of light.

In this thesis an IR equipment Spectrophotometer Jasco 4700 at ICMA B was used to study the composition of precipitates coming from non-optimized precursor solutions.

2.3.2 Structure characterization

X-ray diffraction (XRD)

XRD is a technique used to determine the crystallographic structure of a material. By irradiating a crystalline material with incident X-rays of monochromatic wavelength comparable to the atomic spacing (i.e. Cu-K α $\lambda = 1.5406 \text{ \AA}$), these are scattered into different directions because of their interactions with the electron clouds within the material. When this material is crystalline and so its atoms are arranged in a crystal lattice, the scattered X-rays interact through constructive/destructive interference at specific incident angles resulting in a diffraction pattern. **Figure 2.13** illustrates two beams with identical wavelength and phase scattered by two different atoms of a crystalline solid. Constructive interference only occurs when the

path difference between the scattered X-rays ($2d \sin\theta$) is equivalent to an integer number of the wavelength. This diffraction comes defined by the Bragg's law (Equation 2.2) where n is

$$n\lambda = 2d(hkl)\sin\theta \quad (2.2)$$

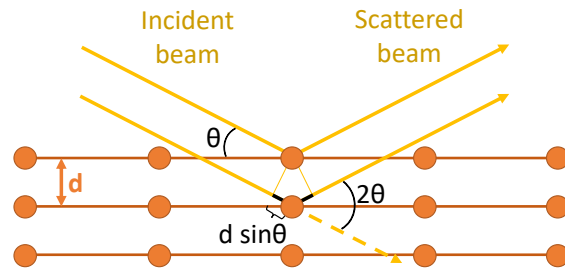


Figure 2.13: Bragg diffraction. Schematic diagram of two beams scattered by two atoms of a crystalline solid.

an integer, λ is the wavelength of the incident X-ray, $d(hkl)$ is the interplanar spacing and θ is half the angle between the incident and the scattered X-rays. Note that the incident angle θ is inversely related to the interplanar spacing $d(hkl)$. Therefore, each set of crystal planes will produce a diffraction spot at a different position as a function of $d(hkl)$, and the whole set of spots in a diffraction pattern will determine the crystal cell structure. Regarding the relative intensity of these spots, it comes determined by the chemical nature and atomic positions of the structure. Additionally, the sharpness, area, and shape of these spots provide additional structural details about the sample analyzed, such as the strain and the size of the crystallites. Experimentally, the X-ray diffraction patterns can be acquired moving the sample and/or the detector with different angles, as depicted in **Figure 2.14a**. Specifically, ω is the angle at which the incident beam intersects the sample surface, usually changed by keeping the X-ray source fixed and moving the sample. The rotation of the sample in the other two directions is described by the angles ϕ and χ . On the other hand, the rotation of the detector is described by the 2θ angle. Depending on the angle varied, the scan mode provides different information about the crystallinity of the sample, such as the mean position of the atoms in the crystal, crystallographic disorder, strain, and others. The XRD analysis performed in this thesis include: θ - 2θ scan, rocking curve (ω scan), ϕ scan, Pole figure, grazing incidence X-ray diffraction (GIXRD) and reciprocal space maps (RSM).

θ - 2θ scan. This is the most used scan mode to study the crystallinity of thin films. In this

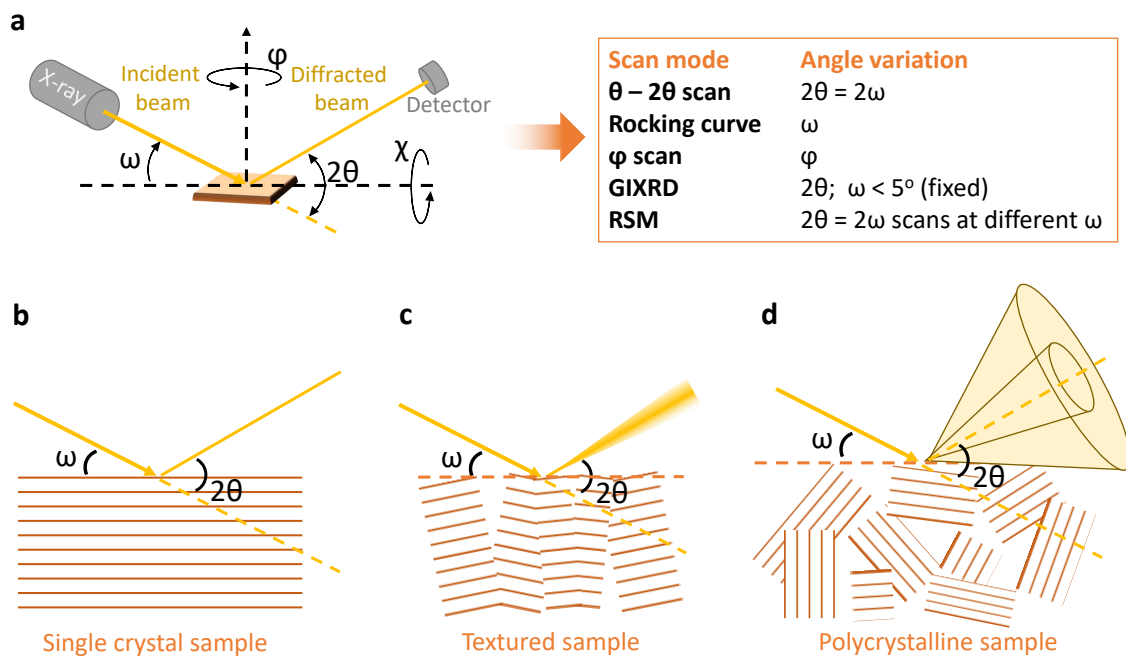


Figure 2.14: XRD scan modes (a) Schematic diagram of a XRD setup and the corresponding different scan modes that can be run by varying the angles 2θ , ω , ϕ and χ . Diffraction phenomena observed for (b) single crystal, (c) textured, and (d) polycrystalline sample.

case, during the measurement the sample and detector are rotated with an angular ratio of 1:2, so that $2\omega = 2\theta$. This scan mode allows to detect only the atomic planes parallel to the sample surface. Therefore, for thin films which possess preferential orientation, the peaks observed will depend not only on the phases present, but also on their orientation.

Two-dimensional (2D) θ - 2θ patterns can be measured using a 2D areal detector which acquires a large 2θ and χ range simultaneously. Such measurement allows on one hand much faster data collection and on the other hand the measured pattern is not limited to a diffraction plane (specific χ) but within a diffraction cone. Therefore, depending on the crystallinity of the sample, 2D measurements allow to differentiate between diffraction rings for polycrystalline samples and isolated spots for single-crystal samples. Nevertheless, the resolution in 2D patterns tends to be worse than in a conventional θ - 2θ scan.

GIXRD. Grazing incidence X-ray diffraction (GIXRD) is a useful surface-sensitive technique to characterize polycrystalline thin films. In conventional θ - 2θ scans with large incidence angles, the weak diffraction contribution of a thin film could be hindered by that of the substrate

because of the μm -order penetration depth of X-rays. On the other hand, if the angle of incidence ω is kept fixed small enough ($<5^\circ$), collecting the spectrum by only moving the detector along 2θ , the diffraction contribution of the film is maximized. For randomly-oriented polycrystalline films, the diffraction pattern should follow the intensities of the reference powder spectrum. Note that this configuration is not suitable for epitaxial films.

Rocking curve. Also named ω scan, the detector is set at a specific 2θ corresponding to an out-of-plane diffraction peak, for example (00l) for films grown on (001) STO substrate, and the sample is tilted along ω . This scan mode allows to measure the diffraction from planes that are not perfectly parallel to the surface, as in textured films like the one shown in Fig. 2.14c. A perfect crystal should produce a very sharp peak which width comes determined by the instrument broadening and the intrinsic width of the crystal material. On the other hand, if the sample contains defects like dislocations or tilting of the crystalline grains, the peak will be broadened giving information about the out-of-plane crystalline order of the sample. Note that this mode is not suitable to detect in-plane twisting of the crystallites, as it will have no influence on the out-of-plane reflections.

ϕ scan. Also named azimuthal scan, consists on rotating the sample along ϕ while keeping ω and 2θ constant. If this rotation is done while measuring the intensity of a diffracted spot with in-plane contribution, for example (110), any in-plane twisting of the crystallites will involve a change of diffraction in ϕ , giving information about the in-plane crystalline order of the sample. Similarly, 360° ϕ scans in 2D measurements, also known as Pole Figure, are used to determine the in-plane orientation of the film related to the substrate.

Reciprocal space maps (RSM) Also known as Q-plots, consists on mapping a 2D region of the reciprocal space by carrying out several θ - 2θ scans ($2\omega = 2\theta$) at successive ω values. Therefore, a 2D diffraction pattern along 2θ and ω is obtained, which can be converted into reciprocal space units, Q_x and Q_z , using the following equations:

$$Q_x = \frac{2\pi}{\lambda} [\cos(2\theta - \omega) - \cos(\omega)] \quad (2.3)$$

$$Q_z = \frac{2\pi}{\lambda} [\sin(2\theta - \omega) + \sin(\omega)] \quad (2.4)$$

where λ is the X-ray wavelength. Q-plots are a powerful tool to obtain information related to the lattice parameters of a textured film as well as other defect-related broadening factors. For example, while a conventional θ - 2θ can only be used to obtain the out-of-plane lattice parameters, here both in-plane and out-of-plane lattice parameters can be extracted from the Q_x and Q_z of a diffraction spot. Regarding the broadening of a diffraction spot, broadening along Q_x could correlate to tilting of planes while a broadening along Q_z could be related to the strain of a film epitaxially grown on a mismatched substrate.

The diffractometers employed in this study were a Bruker D8 Discover A25 diffractometer for high resolution θ - 2θ scans, rocking curve, ϕ scans and Q-plots; a Siemens D5000 diffractometer for fast θ - 2θ scans and GIXRD; and a Bruker-AXS, model D8 Advance diffractometer equipped with a bidimensional detector Vantec-500 (GADDS) for 2D θ - 2θ scans and pole figures, all of them located in the scientific services at ICMAB.

Reflection high-energy electron diffraction (RHEED)

RHEED is a technique used to characterize the crystallinity of the surface of a material.

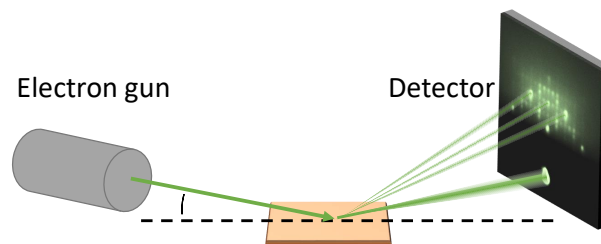


Figure 2.15: RHEED. Sketch of a typical setup for RHEED measurements

As shown in **Figure 2.15**, RHEED is based on the use of a high-energy electron beam (10-50 keV) which arrives at the surface under a grazing incident angle (0.1 - 5°) and the scattered

electrons are gathered on a photoluminescent detector screen. Because of the small angle of incidence, the electrons penetrate only the first layers of atoms, making the technique very surface-sensitive (penetration depth $\sim 1-5$ nm). These electrons form a diffraction pattern that is a picture of the reciprocal lattice of the surface's crystal structure and also provide information on the surface morphology and roughness.¹⁵⁷ Similar to XRD, the diffraction patterns obtained by RHEED are spots for single-crystal, circles for polycrystalline and no diffraction for amorphous sample surfaces. Nevertheless, the shape of the diffracted spots can vary from circular spots to streaks depending on the smoothness of the sample. Thanks to its high sensitivity to variations in morphology, this technique is often used during the epitaxial growth of oxides by PLD and MBE to monitor thickness in real time.

In this thesis, high-pressure RHEED has been used to study the evolution of the surface crystallinity of the sacrificial layer under different conditions, as well as to study the crystallinity of as-deposited LSMO and CFO films by PLD at ICMAB. RHEED analysis of the SC_xAO films ambient stability was performed at ICN2. RHEED measurements were performed with incidence of electrons along the $[100]$ STO at a glancing angle of $1-2^\circ$.

Scanning transmission electron microscopy (STEM)

STEM is a microscopy technique where an electron beam is transmitted through a sufficiently thin sample to then form an image. Thanks to a complex system of condenser lenses, objective lense and aberration correcting lenses, TEM can achieve images with atomic-scale resolution. Unlike conventional TEM, in STEM the electron beam is focused to a fine spot (< 0.2 nm spot size) and then scanned over the sample point by point to finally construct the image. In this scanning mode, the signals from interaction of the sample with the electrons can be obtained simultaneously and spatially correlated, making the technique suitable for analytical modes such as high-angle annular dark-field (HAADF) imaging, spectroscopic mapping by EDX, and electron energy loss spectroscopy (EELS).

To allow the pass of the beam of electrons through the sample, this must be ultrathin (< 100 nm) limiting the technique to either nanosized specimens dispersed on a TEM grid or a thin slice

of a larger sample. As shown in **Figure 2.16**, in this thesis two different sample preparation pathways were followed to either study the cross-section of the entire heterostructure or study the top view of a freestanding oxide. For the cross-section, Fig. 2.16a, specimens were prepared using the standard focused ion beam (FIB) lift-out process in a Thermo Fisher Scientific FIB system. Protective amorphous carbon and thin Pt layers were applied over the region of interest before milling. For the top view, Fig. 2.16b, first the sacrificial layer was etched in water without adding any support and then the freestanding oxide floating on the water surface was picked directly with a TEM grid.

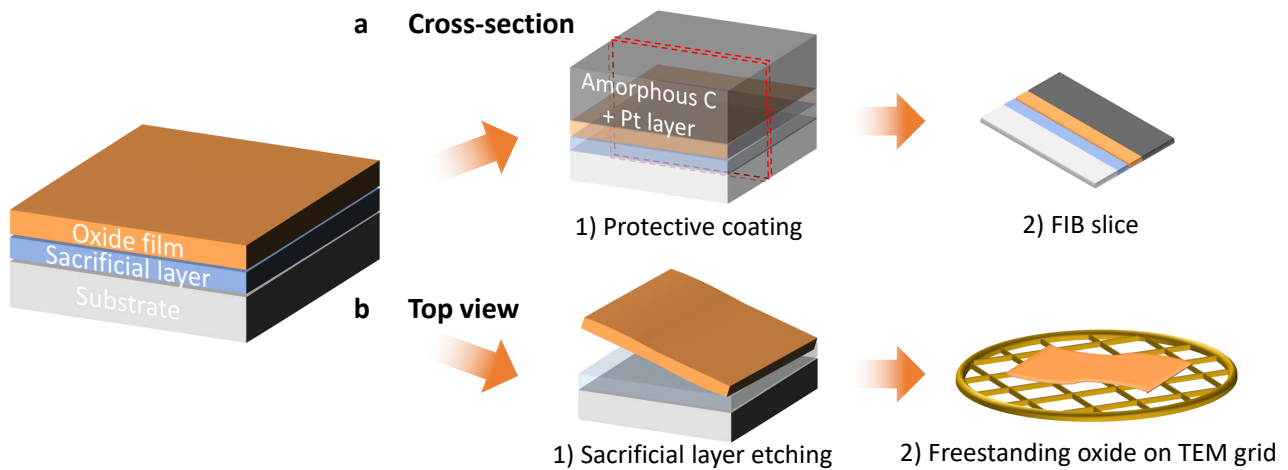


Figure 2.16: Sample preparation for STEM. (a) Cross-section analysis by applying first a protective coating and then using FIB to prepare a lamella; (b) Top view analysis of freestanding oxides released after the SAO etching.

In this thesis, aberration-corrected STEM imaging was performed using a Nion HERMES-100 operated at 60-100 kV. High-angle annular dark-field (HAADF) images were acquired using an annular detector with collection semi-angle of 75-210 mrad. Electron energy loss spectroscopy (EELS) measurements were performed using a collection semi-angle of 75 mrad, an energy dispersion of 0.9 eV per channel, and a probe current of ~ 20 pA. To minimize the possible beam-induced structural damage on the SAO films, images were acquired with reduced beam current (10 pA) and pixel dwell time ($2 \mu\text{s}\cdot\text{px}^{-1}$). The cross-section sample preparation, all the measurements and data analysis was performed by our collaborators Dr. R. Guzman and Prof.

Wu Zhou at the University of Chinese Academy of Sciences, Beijing, China.

2.3.3 Surface morphology characterization

Scanning electron microscopy (SEM) and energy-dispersive X-ray spectroscopy (EDX)

SEM is a type of microscope used to obtain high-resolution images of surfaces and structures at the sub-micron level by scanning the surface of the material with a focused beam of electrons. The primary electron beam is generated by an electron gun, typically a hot filament or a cold cathode material. Then, the electron beam is focused into a narrow spot using a series of electromagnetic lenses, and the spot is then scanned across the surface of the sample in a raster pattern.

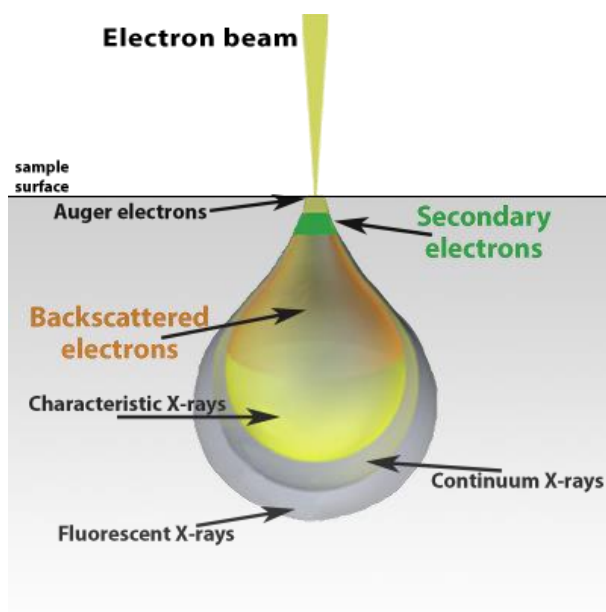


Figure 2.17: Scanning electron microscopy (SEM-EDX). Illustration of different kinds of interactions between the incident electrons and the sample. *Figure adapted from Ref.¹⁵⁸*

When the electrons interact with the atoms on the surface of the sample, they emit various signals, including secondary electrons (SE), backscattered electrons (BSED), and X-rays (EDX), as illustrated in **Figure 2.17**. These signals are detected and converted into an image of the

surface of the sample, each one providing different information of the sample. The SE, produced by inelastic interaction with the sample surface or near-surface regions, provide morphological information. The BSED, on the other hand, come from deeper interaction region of the sample and are originated from elastic scattering with energy dependence on the atomic number in the sample, thus providing compositional information (the larger the atomic number, the brighter the detected signal).

Energy-dispersive X-ray spectroscopy (EDX) is based on the characteristic X-rays emitted from the sample atoms as a result of the interaction with the electron beam. By analyzing the intensities and energies of these X-rays, one can obtain qualitative or semi-quantitative compositional information.

In this study, the SEM-EDX characterization was carried out using a QUANTA FEI 200 FEG-ESEM equipped with a EDX detector by EDAX Inc at ICMAB. The working conditions were 15 kV working voltage and 3.0 spot size under high vacuum.

Atomic force microscopy (AFM)

AFM is a type of scanning probe microscopy used to study the surface properties of materials at the nanoscale level. It uses a cantilever to scan the surface of a sample and measure its topography and physical properties, such as hardness and elasticity. A variant of AFM is piezoelectric force microscopy (PFM) that allows imaging and manipulation of piezoelectric/ferroelectric materials, as further explained in section 2.3.6.

Herein, surface morphology and roughness were analyzed from topographic images acquired using tapping mode with an AFM Keysight 5100 instrument in the scientific services at ICMAB. The acquired images were processed with Mountains Software.

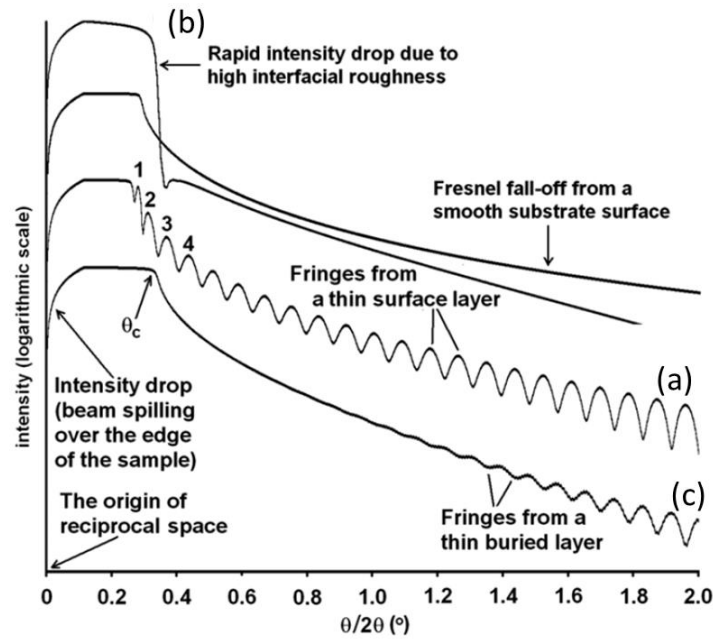


Figure 2.18: X-Ray reflectometry (XRR). Simulated θ - 2θ reflectivity scans obtained from different kind of samples where typical phenomena observed in XRR scans are signaled. *Figure adapted from Ref.¹⁵⁹*

2.3.4 Thickness analysis

X-Ray reflectometry (XRR)

XRR is a non-destructive surface-sensitive analytical technique where the reflected X-rays when interact with a flat surface can be used to measure thickness, density, and roughness of layered thin film materials both in crystalline and amorphous form.¹⁵⁹ In XRR, the diffractometer mechanism is the same than for XRD but at very low angles ($2\theta \sim 1^\circ$) higher than the critical angle (θ_c). The X-rays are reflected at the surface of the sample and at the interfaces between different layers due to the discontinuity in the reflective indexes of each material. The interference between the reflected lights from different interfaces generates the so called Kiessig fringes, as illustrated in **Figure 2.18a** and the spacing between fringes ($\Delta\theta$) is inversely related to the film thickness (d) by the following equation:

$$d = \lambda/2\Delta\theta \quad (2.5)$$

where λ is the X-ray wavelength. As shown in Fig. 2.18b, in XRR high surface roughness is detected from the rapid intensity drop of the curve, thus smooth surfaces and interfaces are required to be able to identify nice Kiessig fringes. For buried layers, fringes arise at higher angles (Fig. 2.18c), while for superlattice structures a more complex pattern arises with the weaker (closely spaced) fringes arising from the total thickness and the stronger (more widely spaced) fringes from the smaller bilayer repeat.

In this study, XRR was used to measure the thickness of the deposited thin films. The measurements were done with a Siemens D5000 diffractometer at ICMAB in the $0.5\text{-}5^\circ$ 2θ range with a 0.002° step size.

Spectroscopic ellipsometry (SE)

Spectroscopic ellipsometry (SE) is a non-destructive optical technique used to measure the complex refractive index and thickness of thin films and multilayers. A linearly polarized light beam is directed to the sample at an angle of incidence and the changes in polarization of the reflected light are measured. The measured data is then analyzed using computational models to extract information about the optical properties of the sample, including the refractive index, thickness, and the extinction coefficient.

Herein, SE was only used to measure the thickness of thin films. The measurements were carried out with a GES5E Ellipsometer from SOPRA Optical Platform located in the NANOQUIM platform at ICMAB. It was used in reflection mode with a light beam focused on the sample with a microspot mode. The spectral range studied was 200-900 nm with a variant light incident angle of $65\text{-}75^\circ$. Data analysis was done by Winelli Software fitting the data to a multi-layered structural model.

2.3.5 Chemical composition characterization

X-ray photoelectron spectroscopy (XPS)

XPS is a surface-sensitive analytical technique used to study the elemental composition, chemical state, and electronic structure of materials. In XPS, a sample is bombarded with X-rays, which causes the emission of photoelectrons from the sample surface (penetration depth ~ 10 nm). By measuring the kinetic energy and number of these emitted photoelectrons, it allows to determine the binding energy of the electrons and from there identify and quantify the elements present in the sample. As the binding energy is influenced by the chemical environment of the atom from which they originate, XPS can also provide information about the chemical state of the atoms in the sample.¹⁶⁰

In this study XPS measurements were performed with a SPECS PHOIBOS 150 hemispherical analyzer (SPECS GmbH, Berlin, Germany) using a monochromatic Al $K\alpha$ radiation (1486.74 eV) source at 300 W at ICN2, Barcelona, Spain. The samples were analyzed with a spot size of $3.5 \text{ mm} \times 0.5 \text{ mm}$ at a base pressure of $4 \cdot 10^{-10}$ mbar. Pass energies of 20 and 50 eV and step sizes of 0.05 and 1 eV were used for the high-resolution and survey spectra, respectively. In Chapter 4 in-situ annealing to study the surface chemical composition with temperature (room temperature up to 800 °C) was performed in an annexed XPS chamber. The acquired spectra were processed with CasaXPS software using Shirley background subtraction. Binding energies were calibrated using C 1s (stipulated at 285 eV) except for the study with temperature where Al 2p was used instead.

2.3.6 Physical properties characterization

Magnetic characterization

A SQUID, or Superconducting Quantum Interference Device, is a highly sensitive magnetic sensor used to measure extremely subtle magnetic fields in thin films.¹⁶¹ **Figure 2.19** shows

the principles of a SQUID magnetometer setup. The sample is placed in a drinking straw holder which moves vertically in a second-order gradiometer used to suppress external magnetic fields. By mechanically moving the sample through a superconducting pick-up coil, changes of magnetic flux created are detected, it is converted to voltage V_{SQUID} and finally with a software it can be extracted the magnetic moment as a function of the applied magnetic field. Note that the high sensitivity of this technique makes it susceptible to artifact contributions and thus special precautions are required when preparing the sample.¹⁶² In this thesis, the mag-

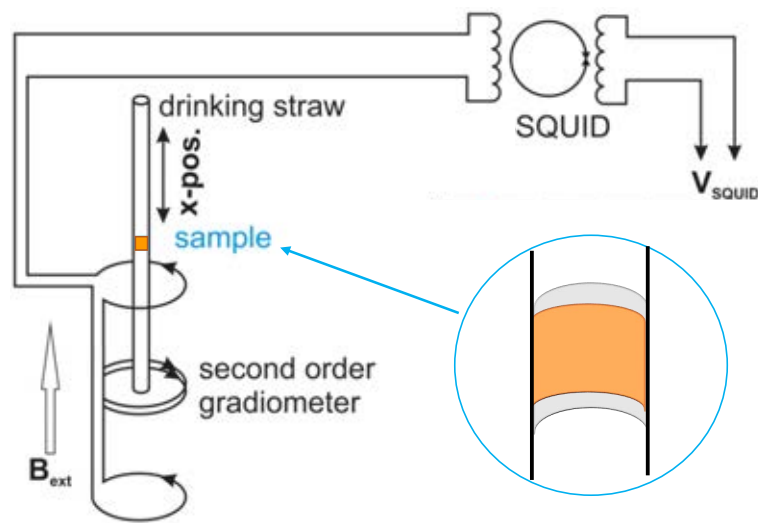


Figure 2.19: SQUID setup for magnetic measurements *Figure adapted from Ref.¹⁶¹*

netic properties of CFO thin films and membranes were probed employing a MPMS3 SQUID magnetometer from Quantum Design with a VSM mode (vibration sample motion) located in the scientific services at ICMAB. In-plane magnetic hysteresis loops, $M(H)$, were acquired at 300 K with a maximum applied field of 15 kOe. To study the effect of the bending on the magnetic behavior of the CFO membranes, these were transferred to Kapton and clamped on plastic holders with different outward bending radii (r).

Optical characterization

Ultraviolet-visible spectroscopy (UV-vis) is a technique where a beam of light (ultraviolet and visible range) is passed through a sample and its interaction is studied by measuring the in-

tensity of the transmitted or absorbed light as a function of wavelength. Herein, UV-vis was used to measure the transmittance of ALD deposited AZO films. Transmittance spectra were collected by means of UV-Visible/NIR spectrophotometer Jasco V780 at ICMAB in the wavelength range of 250–1000 nm with continuous scan and transmission mode. Glass substrate was used as a reference and air was subtracted as background.

Electrical characterization

The analysis of resistivity (ρ) of thin films and membranes has been done using the Van der Pauw configuration.¹⁶³ Assuming that the sample is homogeneous and that the current flows uniformly through the material, this technique enables to measure the sheet resistance (R_s) of thin films of any arbitrary shape. With film thickness (t) established by XRR or ellipsometry, ρ can be calculated from $\rho = R_s \cdot t$.

For room temperature resistivity measurements, the ρ was calculated from lineal I-V curves obtained by applying current with an alternating power source from Kethley Atertronik Company (current range of 0.25-0.9 mA) and measuring the voltage with a SR850 Lock-In Amplifier Model at ICMAB in a collaboration with Dr. Sebastian Reparaz. Silver contacts made from silver paste were prepared manually on the corners of the sample.

For temperature-dependent resistivity curves, $\rho(T)$ was measured in a Physical Properties Measurement System (PPMS) from Quantum Design. 50 nm thick gold contacts were prepared by standard photolithography combined by lift-off. In this case the contacts preparation and the measurements by PPMS were performed in collaboration with A. Barrera and Dr. A. Palau at ICMAB.

Ferroelectric characterization

Piezoelectric force microscopy (PFM) is a scanning probe microscopy technique used to investigate the piezoelectric properties of materials at the nanoscale. In PFM, a sharp conductive tip is brought into contact with the sample surface, and a voltage is applied to the tip. Based on the piezoelectric effect, when the voltage applied results in a sample deformation this

is detected by the resulting deflection of the probe cantilever. However, the static change of domain dimensions is typically in the picometer range. Thus, to increase the signal-to-noise ratio PFM applies an AC voltage which results in a surface oscillation with the same frequency and specific amplitude and phase. The phase contrast between AC excitation and the sample's piezoelectric response directly relates to the polarization orientation of the domain below the tip, while the amplitude of the piezoelectric response resolves the position of domain walls. When used on a ferroelectric material, the applied bias voltage can also be used to switch regions of ferroelectric domains being a unique tool for the ferroelectric characterization at micro and nano length scales.¹⁶⁴

In this study, PFM measurements were performed with an MFP-3D ASYLUM RESEARCH microscope (Oxford Instrument Co.), using the BudgetSensors silicon (n-type) probes with Pt coating (Multi75E-G). To enhance sensitivity, the dual AC resonance tracking (DART) method was employed. Scanned areas were either $10 \times 10 \text{ mm}^2$ or $5 \times 5 \text{ mm}^2$ and the electrically written regions were $6 \times 6 \text{ mm}^2$ or $3 \times 3 \text{ mm}^2$, respectively. PFM voltage hysteresis loops were always performed at remanence, using a dwell time of 100 ms. These measurements were performed by PhD student H. Tan and Dr. Ignasi Fina in our collaboration with MULFOX group at ICMAB.

Macroscopic ferroelectric characterization. Another experimental technique for studying the switching behaviour of a ferroelectric film is by sweeping an electric field (E) to the film at a specific frequency and measuring the polarization hysteresis loop ($P(E)$). From the loop obtained, one can find out the coercive field (E_c) and the remnant polarization (P_r); hence the switching characteristics of the film. Nonetheless, non-ferroelectric contributions may alter the polarization loop leading to fictitious values of the ferroelectric parameters.¹⁶⁵ Thus, the current loop as a function of the electric field ($I(E)$) is usually also displayed to facilitate the differentiation between ferroelectric contributions and leakage current.

In this thesis, the ferroelectric analyses were performed at room temperature and in dark conditions, applying an electric field of up to 2000 kVcm^{-1} to the top electrode (either AZO or ITO) at a constant rate with a frequency of 2 kHz, using an aixACCT TFAalyzer2000

system with a virtual ground method. Also, dielectric leakage current compensation was used to minimize leakage current effects.¹⁶⁵ The photolithography process carried out to prepare the AZO contacts and all these measurements were performed by P. Machado, member of our research group. The ITO deposition by RF magnetron sputtering was done in collaboration with Dr. G de Luca in ICN2. We would also like to acknowledge Prof. Josep Fontcuberta for providing access to his experimental facilities at ICMAB.

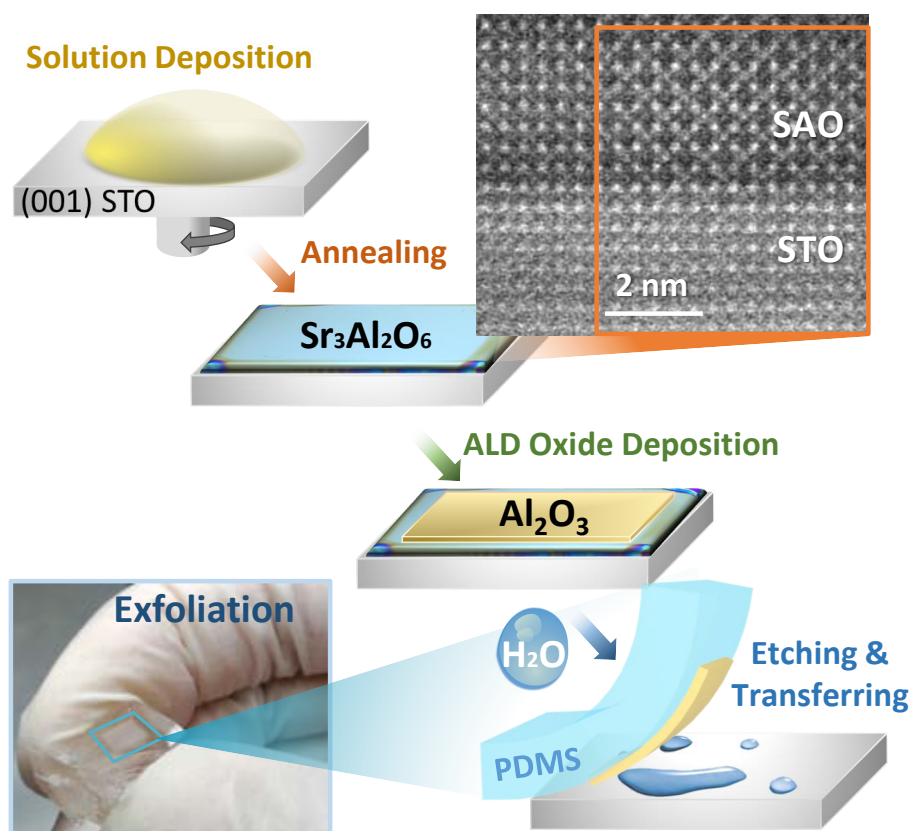
Photoresponse characterization

In this study we refer to photoresponse characterization as those techniques that allow us to study the electrical response of a material when it is illuminated. Here two different approaches were used to measure the photoresponse of our material. On one hand, the measurement of short-circuit current (no applied voltage) as function of time under light pulses is used to study if photocurrent is generated and whether it is stable and repeatable. On the other hand, I-V curves are a representation of the current generated by the material under constant illumination (or in dark) while the voltage across the material is varied. The I-V curve can be used to determine properties of the material such as its open-circuit voltage (V_{oc}), short-circuit current I_{sc} , and fill factor (FF), which will ultimately determine the power conversion efficiency (PCE) of the device.

To perform the photoresponse characterizations the sample was first prepared with appropriate top and bottom contacts for measuring the electrical response and it was installed in a setup with controlled illumination which consisted of a blue monochromatic laser with a wavelength of 405 nm and irradiance of 350 mW cm^{-2} . The time dependent short circuit current density under illumination was measured using an aixACCT TFAalyzer2000 platform and the I-V characteristic curves were collected in dark and under illumination applying a sweeping voltage of $\pm 0.8 \text{ V}$ at the top of $3 \cdot 10^{-3} \text{ mm}^2$ flake with ITO top electrode and grounding the Nb-STO bottom contact, using a Keithley 6517B sourcemeter. These measurements were performed by P. Machado, member of our research group. Here again, we would like to acknowledge Prof. Josep Fontcuberta for providing access to his experimental facilities at ICMAB.

Chapter 3

Facile chemical route to prepare water soluble epitaxial $\text{Sr}_3\text{Al}_2\text{O}_6$ sacrificial layers for free-standing oxides



Facile Chemical Route to Prepare Water Soluble Epitaxial $\text{Sr}_3\text{Al}_2\text{O}_6$ Sacrificial Layers for Free-Standing Oxides

Pol Salles, Ivan Caño, Roger Guzman, Camilla Dore, Agustín Mihi, Wu Zhou, and Mariona Coll*

The growth of epitaxial complex oxides has been essentially limited to specific substrates that can induce epitaxial growth and stand high temperature thermal treatments. These restrictions hinder the opportunity to manipulate and integrate such materials into new artificial heterostructures including the use of polymeric and silicon substrates and study emergent phenomena for novel applications. To tackle this bottleneck, herein, a facile chemical route to prepare water-soluble epitaxial $\text{Sr}_3\text{Al}_2\text{O}_6$ thin films to be used as sacrificial layer for future free-standing epitaxial complex oxide manipulation is described. Two solution processes are put forward based on metal nitrate and metalorganic precursors to prepare dense, homogeneous and epitaxial $\text{Sr}_3\text{Al}_2\text{O}_6$ thin films that can be easily etched by milli-Q water. Moreover, as a proof of concept, a basic heterostructure consisting of $\text{Al}_2\text{O}_3/\text{Sr}_3\text{Al}_2\text{O}_6$ on SrTiO_3 is fabricated to subsequently exfoliate the Al_2O_3 thin film and transfer it to a polymer substrate. This is a robust chemical and low-cost methodology that could be adopted to prepare a wide variety of thin films to fabricate artificial heterostructures to go beyond the traditional electronic, spintronic, and energy storage and conversion devices.

1. Introduction

Complex oxides are of great interest for their rich variety of chemical and physical properties including magnetism, ferroelectricity, multiferroicity, catalytic behavior, and superconductivity.^[1] Up to date, the preparation of crystalline complex oxide thin films has been mainly limited on substrates that can stand high temperature thermal treatments and on single

crystal substrates when epitaxial growth is pursued. These requirements dramatically limit their applicability excluding the possibility to prepare many artificial multilayered architectures to investigate emergent phenomena that arise in thin films and at their interfaces,^[2] as well as the fabrication of flexible devices and monolithic integration into silicon.^[3–5] Many efforts have been devoted to develop procedures to detach the functional oxide film from the growth substrate in order to be able to freely manipulate it. They include mechanical exfoliation,^[6] dry etching,^[7,8] and wet-chemical etching.^[9,10] Among the chemical etching procedures, the use of a sacrificial layer, which is incorporated between the substrate and the functional oxide, appears as a fast and relatively low-cost process. For this approach to be successful, the sacrificial layer should transfer the epitaxy from the substrate to the desired oxide, stand the deposition

process of the functional oxide and be selectively removed by a chemical treatment, which allows to retrieve the original single-crystal substrate. $(\text{La,Sr})\text{MnO}_3$ has been proved effective to be selectively etched by an acid blend allowing the transfer of single epitaxial $\text{Pb}(\text{Zr,Ti})\text{O}_3$ layers^[11] and more complex architectures such as $\text{SrRuO}_3/\text{Pb}(\text{Zr,Ti})\text{O}_3/\text{SrRuO}_3$.^[12] Recently, the use of water-soluble $\text{Sr}_3\text{Al}_2\text{O}_6$ (SAO) sacrificial layer enlarged the family of free-standing epitaxial perovskite oxide layers (SrTiO_3 , BiFeO_3 , BaTiO_3)^[13–15] and multilayers ($\text{SrTiO}_3/(\text{La,Sr})\text{MnO}_3$)^[16] that can be manipulated opening a whole new world of opportunities.^[5,10,17] The deposition techniques to prepare such structures is also a key factor to be considered not only for film quality but also for process scalability. While high vacuum deposition techniques such as molecular beam epitaxy and pulsed laser deposition are well established techniques to produce high quality films,^[1,18–20] alternate procedures that can deliver low-cost production such as solution processing and atomic layer deposition are gaining interest.^[21,22]

Chemical solution deposition (CSD) is considered a mature technique for the preparation of oxide films. The synthesis of ternary and quaternary oxides is not a trivial task but the pioneering work done in ferroelectric lead zirconate titanate inspired many researchers to extend it to other compositions and broaden the application fields.^[23,24] Nonetheless, there is still a myriad of compositions to be explored, including SAO,

P. Salles, I. Caño, C. Dore, Dr. A. Mihi, Dr. M. Coll
ICMAB-CSIC
Campus UAB 08193, Bellaterra, Barcelona, Spain
E-mail: mcoll@icmab.es

Dr. R. Guzman, Prof. W. Zhou
School of Physical Sciences and CAS Key Laboratory of Vacuum Physics
University of Chinese Academy of Sciences
Beijing 100049, China

 The ORCID identification number(s) for the author(s) of this article can be found under <https://doi.org/10.1002/admi.202001643>.

© 2021 The Authors. Advanced Materials Interfaces published by Wiley-VCH GmbH. This is an open access article under the terms of the Creative Commons Attribution-NonCommercial License, which permits use, distribution and reproduction in any medium, provided the original work is properly cited and is not used for commercial purposes.

DOI: 10.1002/admi.202001643

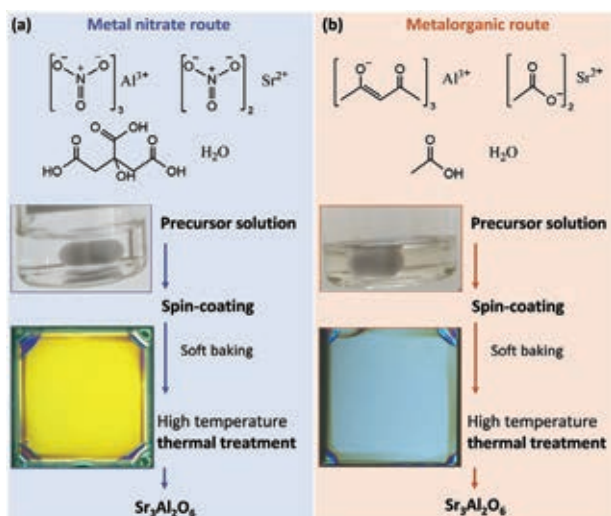


Figure 1. Solution processing scheme to prepare SAO thin films from a) metal nitrate route and b) metalorganic route.

which brings new synthetic challenges that requires a better understanding on the role of the solution-precursor chemistry on the film properties.

Here we will tackle the synthesis of SAO prioritizing the use of environmentally benign solvents assessing the influence of precursor chemistry on the film structure and morphology. Among the plethora of salt precursors suitable for the synthesis of metal oxides, metal nitrate and metalorganic precursors are here examined. Although these are two popular routes to prepare metal-oxides,^[21,25] a procedure to prepare epitaxial SAO is unexplored. We demonstrate that using metal nitrate and metalorganic precursors, homogeneous solutions can be stabilized and spin-coated on single crystal substrates. Upon high thermal treatment optimization, epitaxial SAO is successfully obtained by both routes. Etching selectivity using common solvents such as water, methanol, acetone, and acetic acid is here presented. Ultimately, to test the viability of SAO as sacrificial layer, thin films of amorphous Al₂O₃ are deposited by atomic layer deposition (ALD) on SAO and transferred to a polymeric support.

2. Results and Discussion

The development of the synthesis of SAO by CSD encompassed three main steps: stabilization of the precursor solution, homogeneous deposition by spin-coating and thermal treatment to convert the precursor gel to pure-phase and epitaxial films, as will be discussed in detail below, see **Figure 1**.

2.1. Solution Chemistry

Metal nitrate precursors are often soluble in water, they have a relatively low decomposition temperature and the high-volatility of the decomposition products minimizes the presence of residual contaminants in the final film.^[25] In this work, SAO films prepared from the metal nitrate route were carried out by mixing aluminum nitrate (Al(NO₃)₃) and strontium nitrate

(Sr(NO₃)₂) in water. The chelating agent citric acid (CA) was employed to minimize hydrolysis and condensation reactions and ensure the SrTiO₃ (STO) substrate wettability to obtain a homogeneous gel after spin-coating.

On the other hand, the use of mixed metalorganic compounds (carboxylates and alkoxides or β -diketonates) is a common route for the preparation of perovskite oxides and there is a plethora of commercially available precursors. Nonetheless, finding a suitable solvent for a system that includes several metalorganic compounds might be an arduous task.^[26] The combination of strontium acetate (Sr(CH₃COO)₂) and aluminum acetylacetonate (Al(CH₃COCH=C(O)CH₃)₃) enables the preparation of a relatively simple solution by being dissolved in acetic acid. To improve solution stability and avoid acetylacetonate precipitation, 0–10% of water was added.^[26,27] However, the precursor solution ages after few days revealed by the precipitation of aluminum acetylacetonate, see **Figure S1**, Supporting Information.

To ensure a controlled transformation process from the precursor salts to the formation of pure phase SAO, thermal decomposition of both precursor solutions need to be investigated.

2.2. Thermal Decomposition and Phase Formation

The thermogravimetric analysis (TGA) of the derived gel from the metal nitrate route is shown in **Figure 2a–c**. The TGA and derivative (DTG) curves show four-step mass losses, **Figure 2a,b**. The first step between 100 °C and 270 °C is the most pronounced with a mass loss of 53%, followed by a subtle but long second step between 270 and 550 °C with a 20% mass loss. The third step occurs between 550 and 670 °C (5%) and the last one between 740 and 930 °C (5%). Along with the first and second mass loss, several exothermic peaks can be seen in the differential scanning calorimetry (DSC) curve (**Figure 2c**). According to the thermogravimetric analysis reported for the individual metal nitrates and CA,^[28,29] simultaneous phenomena can take place in this range of temperature. It involves the CA decomposition through intermediates such as aconitic acid,^[30] the dehydration and condensation of Al(NO₃)₃, and the elimination of NO_x and CO₂ gases as reaction products. The third and fourth mass loss could be related to the decomposition of Sr(NO₃)₂ through the formation of SrCO₃ and the release of gases such as H₂O, NO_x, and CO₂.^[31] From 740 to 930 °C, final decomposition of the intermediates, elimination of gases, probably CO₂ and O₂,^[32] and crystallization of Sr₃Al₂O₆ may occur,^[33] consistent with the large endothermic peak present in the DSC curve. Note the fact that our starting gel contains a mixture of nitrates and organics (CA), therefore, the formation of intermediates and their decomposition can moderately differ from that reported for the respective nitrates and CA. Mass spectroscopy coupled to TGA could supply additional information on the specific decomposition products of our gels, however, this detailed study is out of the scope of this work. Nonetheless, the TGA study here presented is valuable to define a tentative thermal profile consisting of a soft baking at 120 °C in air to tackle the major mass loss and then a high temperature treatment at temperatures >700 °C to promote the SAO crystallization.

The thermal decomposition analysis for the acetate and acetylacetonate precursors is shown in **Figure 2d–f**. Here, three

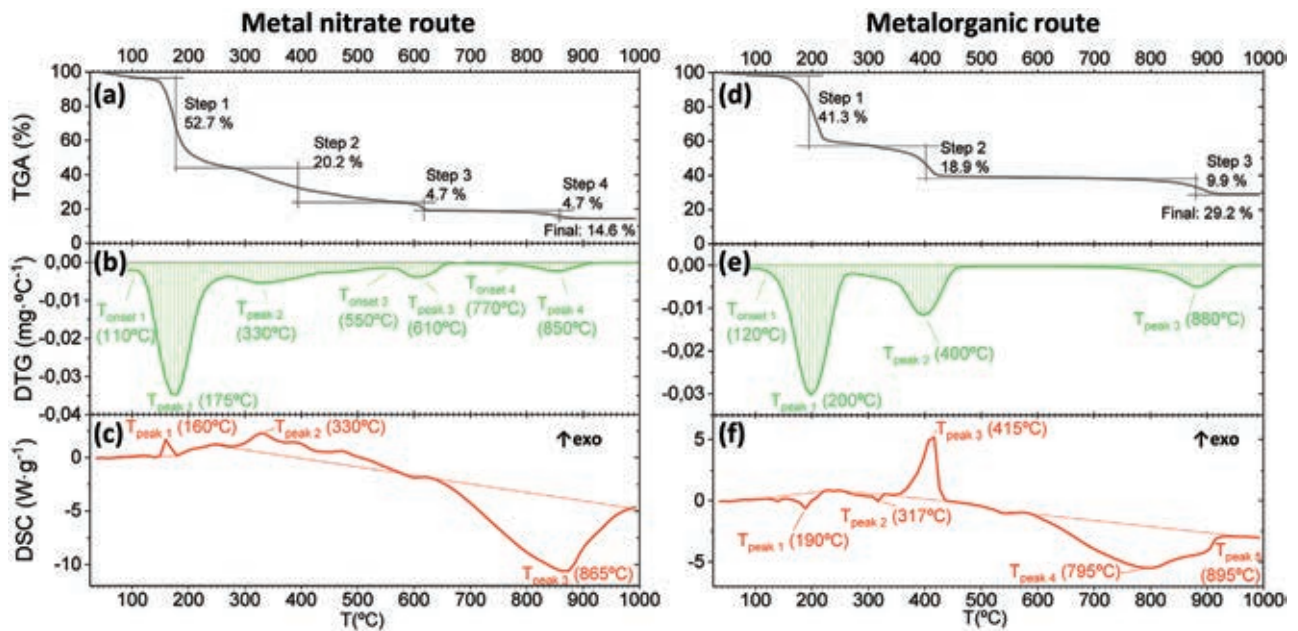


Figure 2. Thermal analysis of SAO precursor solutions. The metal nitrate solution analysis on the left side, with the corresponding a) thermogravimetric analysis, TGA, and its derivative b) DTG and c) the differential scanning calorimetry, DSC. The metalorganic route on the right, with its d) TGA, e) DTG, and f) DSC.

mass loss steps are identified. From 100 to 270 °C (41%), from 270 to 480 °C (19%) and from 710 to 960 °C (10%). The first mass loss mainly involves two-three endothermic peaks. At this temperature range, dehydration of the two reagents followed by melting and decomposition of $\text{Al}(\text{CH}_3\text{COCH}=\text{C}(\text{O})\text{CH}_3)_3$ to Al_2O_3 can occur.^[34,35] A small endothermic peak and a sharp exothermic peak occurs in the second step of mass loss that could be assigned to the melting of $\text{Sr}(\text{CH}_3\text{CO}_2)_2$ and conversion to carbonate, SrCO_3 , respectively, with the release of CO_2 , H_2O , and acetone.^[32,36] The final decomposition process occurs between 800–950 °C, where carbonates are expected to decompose to the oxide forming the $\text{Sr}_3\text{Al}_2\text{O}_6$ phase with the release of CO_2 . Note that the decomposition of the metalorganic precursors takes place below 500 °C whereas for the metal nitrate route is enlarged to higher temperature (≈ 700 °C) in well agreement with previous reports on the synthesis of complex oxides from acetates versus nitrates.^[32] Based on that, the thermal profile defined for the metalorganic route consists of a two-step soft-baking (5 min at 150 °C and 5 min at 230 °C in air) and then expose the sample at high temperatures >700 °C.

According to the above thermal decomposition analysis, fine tuning of the processing parameters have been carried out: temperature (700–900 °C), time (10–90 min), heating/cooling ramps (5–660 °C min^{-1}) in oxygen atmosphere, and the structural evolution of the films has been investigated by X-ray diffraction (XRD), see Figure S2, Supporting Information. Figure 3a shows a representative XRD θ - 2θ scan of the optimized 70 nm film from the metal nitrate route. The presence of Bragg reflections at 22.5°, 45.8°, and 71.7° appearing as a shoulder of the (00l) STO Bragg reflections (see inset Figure 3a), can be assigned to the epitaxial growth of SAO on STO. Moreover, no crystalline secondary phases are detected in the analyzed θ - 2θ range. The XRD pole figure measurements around the (110)

STO and (660) SAO reflections reveal a cube on cube growth with fourfold symmetry, see Figure S3, Supporting Information. The crystalline quality of the SAO film was further characterized by XRD rocking curve (ω) around the (008) SAO reflection with a full width at half maximum (FWHM) value of 0.13° (FWHM = 0.02° for STO), Figure 3b. In-plane XRD ϕ -scan measurement around the (660) SAO results in FWHM values of 0.71° (FWHM = 0.10° for STO), Figure 3c, confirming the biaxial texture. Reported texture analysis for physical deposited SAO films, molecular beam epitaxy (MBE), show rocking curve FWHM values slightly smaller, that is, FWHM = 0.015° (FWHM = 0.013° for STO).^[20] Cross-sectional Z-contrast high angle annular dark field (HAADF) using scanning transmission electron microscopy (STEM), Figure 3d,e, further confirms the epitaxial growth of SAO film on the STO (001) substrate. The HAADF-STEM images show high crystal quality and sharp interface. The typical rhombic motifs of the Sr atoms in $\text{Sr}_3\text{Al}_2\text{O}_6$ observed in higher resolution images (Figure 3c) confirms the growth of the $\text{Sr}_3\text{Al}_2\text{O}_6$ phase viewed along the [001].

SAO films prepared from the metalorganic route also led to highly epitaxial films showing sharp and intense (00l) Bragg reflections, with out-of-plane and in-plane texture of $\Delta\omega = 0.09^\circ$ and $\Delta\phi = 0.84^\circ$, respectively, see Figure S4, Supporting Information. Note that the intensity of the SAO peaks is higher than the films from the metal nitrate route because the films are thicker, 120 nm, in good agreement with a more viscous precursor solution (8.8 $\text{mPa}\cdot\text{s}$ versus 4.1 $\text{mPa}\cdot\text{s}$).

Both routes lead to a homogeneous and crack free film, see optical microscope images from Figure 1. Further surface morphology analysis carried out by atomic force microscopy (AFM) reveals a granular surface with an root mean square (rms) roughness of 2.5 and 5.3 nm for the metal nitrate and metalorganic routes, respectively, Figure S5, Supporting Information.

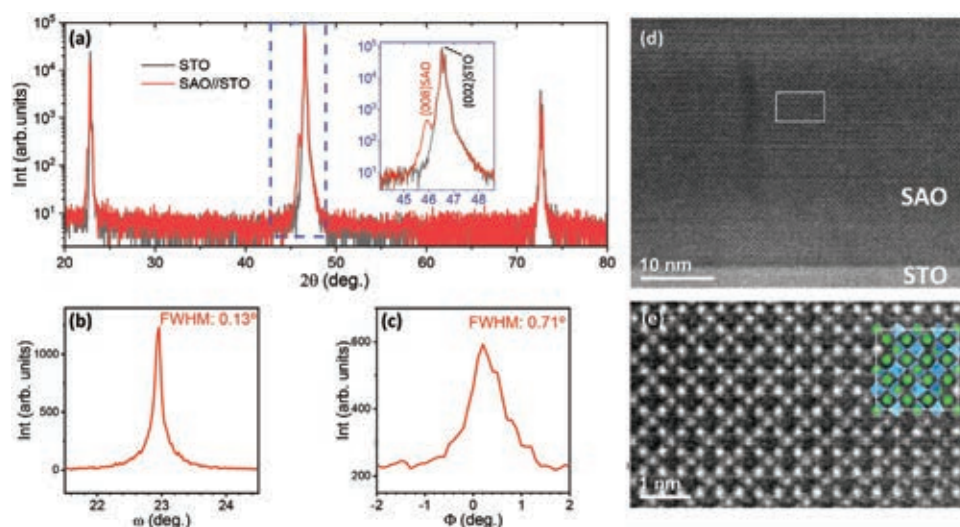


Figure 3. SAO thin film structural characterization. a) XRD θ - 2θ scan of a SAO thin film on STO substrate prepared from the metal nitrate route compared to bare STO substrate. Inset corresponding to the θ - 2θ range of the (008) SAO peak and (002) STO peak. b) Rocking curve around the (008) SAO reflection and c) Phi-scan around the (660) SAO reflection. d) Z-contrast HAADF-STEM cross-section of SAO//STO interface and e) Higher magnification Z-contrast image of the SAO film showing crystallographic order at the atomic level. A single $\text{Sr}_3\text{Al}_2\text{O}_6$ unit cell atomic structure is overlaid, where green atoms are Sr and blue atoms Al. Oxygen atoms are omitted for clarity.

Note that MBE and pulsed laser deposition films of thickness ranging from 8 unit cells to 20 nm show a step-and-terrace surface morphology (with rms <0.7 nm), replicating the STO surface.^[15,16,20] Importantly, SAO exposure to ambient moisture can severely degrade the surface morphology.

2.3. Etching of Sacrificial Layer

The purpose to study the effect of solvents on the integrity of SAO is twofold. First, to identify the solvents that effectively remove SAO and second, to investigate which solvents do not degrade the SAO being of interest if the heterostructure is aimed to be prepared from all-solution methodology.

It has been investigated four different common solvents used in CSD: acetic acid/methoxyethanol blend, methanol, acetone, and water. Figure S6, Supporting Information shows the optical micrograph images of the samples exposed 1 min to the different solvents and compared to an as-prepared SAO. The results indicate that the SAO thin film is not affected by the immersion in the solvent blend acetic acid/methoxyethanol. On the other hand, its immersion in methanol and acetone deteriorates the sample. Finally, the use of milli-Q water completely etches the SAO film in a few seconds, proving its effectiveness as etching solvent, in well agreement with previous studies performed on high-vacuum deposited films.^[9,13,16,37] Importantly, the latter STO substrates can be recycled and used for subsequent film growth studies.

2.4. Free-Standing Al_2O_3 Films

The capability of SAO to act as a sacrificial layer for transferring free-standing oxides is here examined by depositing a 40 nm Al_2O_3 thin film by ALD on SAO//STO and transferring it to a

polydimethylsiloxane (PDMS) support. Atomic layer deposition has been chosen as the deposition technique for Al_2O_3 , using ozone as co-reactant, stimulated by its low-temperature and chemical gas-phase characteristics, which is expected to minimize interface diffusion, but also for the rapid pickup of the technique in industry which would facilitate the integration of this approach in already existing industrial processes.^[38] From AFM analysis it has been investigated the surface morphology of the as-deposited Al_2O_3 on SAO//STO and compared to the bare SAO//STO. Both samples show smooth and continuous surface defined by fine grain size resulting in an rms of 2.5 nm, **Figure 4**. Therefore, the deposition of Al_2O_3 does not introduce surface defects on SAO thanks to the low-temperature and conformal coating nature of the ALD. Note that when Al_2O_3 is deposited on freshly cleaned STO substrates, the typical step-and-terrace morphology is identified, Figure S7, Supporting Information.

The deposition and exfoliation process followed in this work is schematized in **Figure 5**.

First, the SAO thin film is prepared by CSD on a STO substrate following the metalorganic route described above. Then, the Al_2O_3 film is deposited on the SAO//STO whose edges have been previously covered by tape to assure that the can penetrate and etch the SAO film after the Al_2O_3 coating, Figure 5c,d.

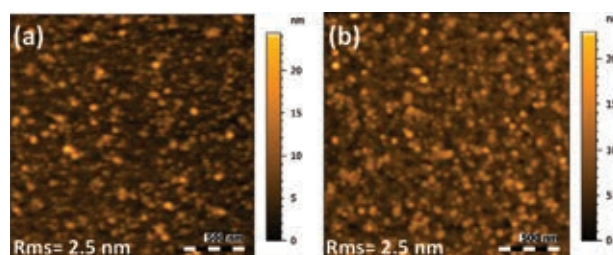


Figure 4. $2\ \mu\text{m} \times 2\ \mu\text{m}$ AFM topographic images of a) SAO//STO film and b) 40 nm ALD- Al_2O_3 /SAO//STO.

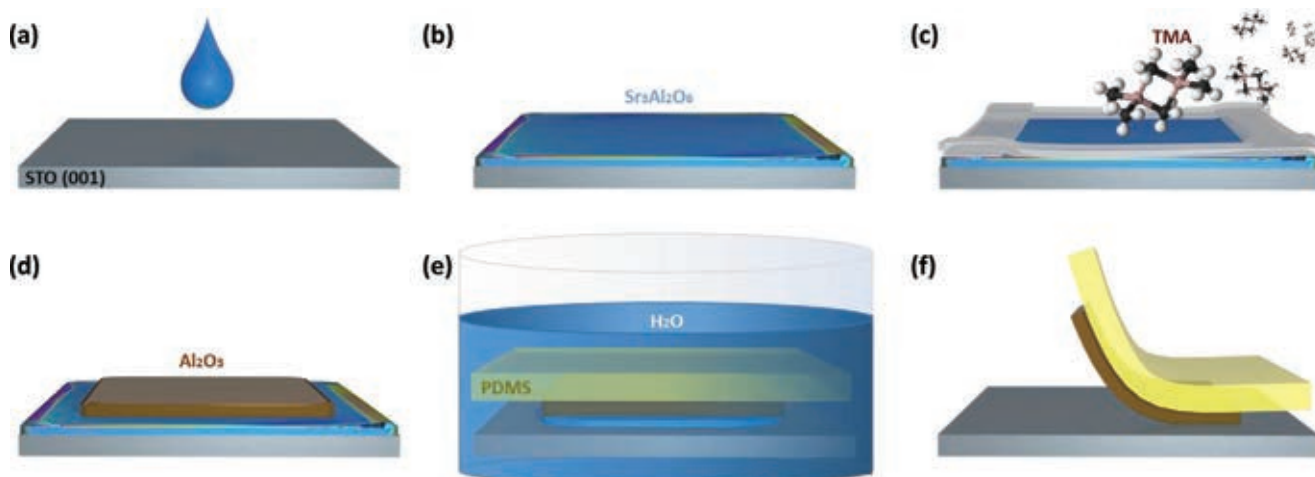


Figure 5. Scheme of the process followed to obtain Al_2O_3 films on a polymer support. a) spin-coating of SAO solution on STO substrate and processing to obtain b) SAO epitaxial film; c) atomic layer deposition of Al_2O_3 on SAO//STO, with edges masked, to obtain d) Al_2O_3 film; e) immersion in milli-Q water of PDMS supported Al_2O_3 /SAO//STO system for SAO etching; f) PDMS/ Al_2O_3 detachment from STO substrate.

Next, the PDMS is adhered to the heterostructure and the system is immersed in milli-Q water where the etching of SAO takes place, Figure 5e. Finally, the PDMS/ Al_2O_3 can be exfoliated from the STO, Figure 5f.

Following this procedure it has been possible to transfer a continuous $0.4 \times 0.4 \text{ cm}^2$ piece of 40 nm of Al_2O_3 on PDMS, see Figure 6a. This PDMS/ Al_2O_3 architecture has been subsequently characterized by scanning electron microscopy-energy-dispersive X-ray spectroscopy (SEM-EDX) upon transferred on a conductive carbon tape identifying the presence of aluminum on the transferred piece, Figure 6b,c.

Therefore, the combination of CSD-SAO and ALD- Al_2O_3 allowed to demonstrate the potential of CSD-SAO as sacrificial layer to transfer oxide films opening the door to future studies on freestanding epitaxial oxides by an all-chemical route.

3. Conclusions

In this study we have developed a new procedure to prepare epitaxial $\text{Sr}_3\text{Al}_2\text{O}_6$ thin films on STO by solution deposition. Metal nitrate and metalorganic precursors can be used as precursor sources upon optimization of film decomposition and crystallization. Etching of $\text{Sr}_3\text{Al}_2\text{O}_6$ is effective with water,

whereas methanol and acetone partially degrades the film. Finally, free-standing ALD- Al_2O_3 films can be obtained from SAO//STO and transferred to a PDMS stamp under mild conditions. Therefore, we present a low-cost, scalable platform that can enable further exploration of the preparation of self-supporting (epitaxial) oxides, offering another alternative to detach the synthesis of oxides from the rigid lattice matched substrate. It is envisaged many new opportunities to prepare artificial oxide heterostructures and devices offering a whole new dimension for microelectronics, photovoltaics, spintronics, and optoelectronics.

4. Experimental Section

Thin Film Preparation: $\text{Sr}_3\text{Al}_2\text{O}_6$ thin films were prepared by chemical solution deposition using two different routes named by the chemistry of the precursors, metal nitrate and metalorganic route. For the metal nitrate route, stoichiometric amounts of strontium nitrate, $\text{Sr}(\text{NO}_3)_2$ (>99%) and hydrated aluminum nitrate, $\text{Al}(\text{NO}_3)_3 \cdot 9\text{H}_2\text{O}$ (>98%) were dissolved as purchased in milli-Q water with citric acid (CA), $\text{C}_6\text{H}_8\text{O}_7$ (>99%). The precursor solution was stirred for 3 h at 90°C in a reflux condenser to obtain a 0.25 M solution. The molar ratio of CA to total metal cations CA:M was 2:1, obtaining a viscosity of 4.1 mPa·s. The solution was filtered with a PTFE hydrophilic filter of $0.45 \mu\text{m}$ pore size previous to deposition. For the metalorganic route, stoichiometric amounts of strontium acetate, $\text{Sr}(\text{C}_2\text{H}_3\text{O}_2)_2$, and aluminum

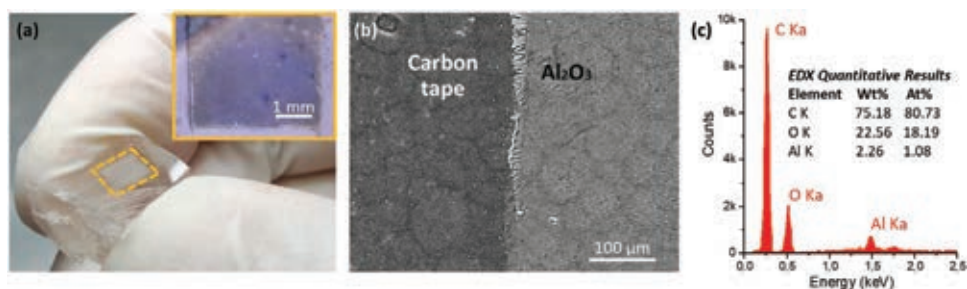


Figure 6. Transferring of Al_2O_3 films. a) Exfoliated ALD- Al_2O_3 film on a PDMS support. Inset: magnified image of the transferred Al_2O_3 film. b) SEM and c) EDX of Al_2O_3 film transferred from the PDMS support to a carbon tape.

acetylacetonate, $\text{Al}(\text{C}_5\text{H}_7\text{O}_2)_3$ (>99%), were dissolved in a solvent blend of acetic acid (>99.8%) and milli-Q water to obtain a 0.25 M solution. The precursor solution was stirred for 3 h at 60 °C. The percentage of water in solution was varied between 0–10 %, obtaining a viscosity of 8.8 mPa·s when 5 % water is used. The solutions were filtered with a PTFE filter of 0.22 μm pore size.

The solutions were spin-coated by disposing 15 μL on a $5 \times 5 \text{ mm}^2$ monocrystalline SrTiO_3 (STO) (001) substrate. For the metal nitrate route, the STO substrate was exposed to a UV–ozone pre-treatment for 5 min to improve wettability. The samples were spun at 6000 rpm for 30 s and then exposed to a soft baking. The nitrate samples at 120 °C for 10 min and the metalorganic 5 min at 150 °C + 5 min at 230 °C (according to the thermogravimetric analysis, Figure 2). Finally, the samples were introduced in a tubular furnace, where annealing temperature (700–900 °C), time at that temperature (10–90 min) and heating/cooling rate (5–25 °C min^{-1} - flash heating (660 °C min^{-1})) were optimized, Figure S3, Supporting Information. The optimal conditions were a heating ramp of 25 °C min^{-1} from room temperature to 800–900 °C and cooled down at 25 °C min^{-1} , all under 0.6 $\text{l}\cdot\text{min}^{-1}$ O_2 flow. Annealing time was optimized according to film thickness. The samples, specially those prepared from the metal nitrate route, are very sensitive to moisture. Solution deposition process and sample manipulation until it is exposed to soft backing (230 °C) should be handled in relative humidity <30%.

The transfer of the deposited Al_2O_3 thin film was done using polydimethyl siloxane PDMS Sylgard 186 as support. Both the PDMS support and the heterostructure $\text{Al}_2\text{O}_3/\text{SAO}/\text{STO}$ were exposed to a UV–ozone treatment for 5 min to improve adhesion, before mild pressing them, and then the structure was immersed in milli-Q water for etching. Finally, PDMS and STO were mechanically separated, obtaining on one side the PDMS with the Al_2O_3 thin film on it and, on the other side, a clean STO. After recovering the STO substrate, it was further treated for a better recycling. First, 10 min sonication in H_2O was used to remove any remaining traces, and then 30 s immersion in buffered HF solution (30%) and post-annealing for 1 h at 950 °C was proceeded to recover the terracelike morphology,^[39] see Figure S5d, Supporting Information.

Al_2O_3 thin films have been deposited by ALD using a commercial reactor from Savannah–Cambridge Nanotech 100 in flow mode. Trimethylaluminum and ozone were alternatively pulsed/purged for 0.05 s/5 s and 0.1 s/7 s, respectively under a 20 sccm N_2 carrier gas. The reactor temperature was set at 150 °C for 400 cycles. Under these conditions, we obtained 40 nm films of amorphous Al_2O_3 .

Thermogravimetric Characterization: TGA and DSC were done with a thermal analyzer METTLER TOLEDO model TGA/DSC 1 equipped with an oven HT1600 and microbalance MX5 at University of Málaga, with a range of temperatures from 30 to 1000 °C, heating rate of 10 °C $\cdot\text{min}^{-1}$, and O_2 flow of 50 $\text{mL}\cdot\text{min}^{-1}$. In order to carry out this study, the precursor solutions were previously dried to a gel by a rotary evaporator (R-100).

Surface Morphology Characterization: Magnified images of the thin films were taken by optical microscope (Leica S9 i and Leica DM1750 M). Surface morphology and roughness were analyzed from topographic images acquired with an AFM Keysight 5100 instrument and analyzed using Mountains Software. Surface morphology was also analyzed by SEM, together with chemical analysis by EDX, with a SEM QUANTA FEI 200 FEG-ESEM.

Structure Characterization: Phase and crystalline structure of the SAO films were studied by XRD using a Siemens Diffractometer D-5000 along a scan range of 2θ 20–80°. Texture analysis has been performed by XRD pole figure measurements using a Bruker-AXS, model D8 Advance diffractometer equipped with a bidimensional detector Vantec-500 (GADDS). Out-of-plane and in-plane texture analysis have been performed by XRD rocking curve and phi scan, respectively, using Bruker-AXS, model A25 D8 Discover diffractometer. All three diffractometers are with $\text{Cu-K}\alpha = 1.5418 \text{ \AA}$.

Aberration-corrected STEM imaging were performed using a Nion HERMES-100, operated at 100 kV. HAADF images were acquired using an annular detector with collection semi-angle of 92–210 mrad. Cross-sectional STEM specimens were prepared using the standard focused ion beam (FIB) lift-out process in a Thermo Fisher Scientific FIB system.

Protective amorphous carbon and thin Pt layers were applied over the region of interest before milling. To minimize the sidewall damage and sufficiently thin the specimen for electron transparency, final milling was carried out at a voltage of 5 kV. To reduce possible beam-induced structural damage on the SAO films, images were acquired with reduced beam current (10 pA) and pixel dwell time (2 $\mu\text{s}\cdot\text{px}^{-1}$)

Thickness of the SAO films was studied by profilometry on samples with a side cleaned with water, using a Profilometer P16+ from KLA Tencor. (Measurement made as an average of three consecutive scans, analysed using Mountains Software)

Supporting Information

Supporting Information is available from the Wiley Online Library or from the author.

Acknowledgements

This research was supported by the Spanish Ministerio de Ciencia, Innovación y Universidades (“Severo Ochoa” Programme for Centres of Excellence in R&D FUNFUTURE CEX2019-000917-S and MAT2017-83169-R(AEI/FEDER, EU)). The project that gave rise to these results received the support of a fellowship from “la Caixa” Foundation LCF/BQ/DI19/11730026. M.C. acknowledges Becas Leonardo fundación BBVA. I.C. acknowledges the JAE Intro fellowship, JAEINT1901918. This work was done in the framework of the doctorate in material science of the Autonomous University of Barcelona. This work received financial support from the National Key R&D Program of China (2018YFA0305800), and the Beijing Outstanding Young Scientist Program (BJJWZYJH01201914430039).

Conflict of Interest

The authors declare no conflict of interest.

Keywords

atomic layer deposition, free-standing oxides, sacrificial layer, solution processing, $\text{Sr}_3\text{Al}_2\text{O}_6$

Received: September 18, 2020

Revised: December 1, 2020

Published online:

- [1] M. Coll, J. Fontcuberta, M. Althammer, M. Bibes, H. Boschker, A. Calleja, G. Cheng, M. Cuoco, R. Dittmann, B. Dkhil, I. E. Baggari, M. Fanciulli, I. Fina, E. Fortunato, C. Frontera, S. Fujita, V. Garcia, S. Goennenwein, C.-G. Granqvist, J. Grollier, R. Gross, A. Hagfeldt, G. Herranz, K. Hono, E. Houwman, M. Huijben, A. Kalaboukhov, D. Keeble, G. Koster, L. Kourkoutis, et al., *Appl. Surf. Sci.* **2019**, *482*, 1.
- [2] M. Bibes, J. E. Villegas, A. Barthélémy, *Adv. Phys.* **2011**, *60*, 5.
- [3] D. Dubbink, Ph.D. Thesis, University of Twente, Netherlands **2017**.
- [4] S.-H. Baek, C.-B. Eom, *Acta Mater.* **2013**, *61*, 2734.
- [5] W. Gao, Y. Zhu, Y. Wang, G. Yuan, J.-M. Liu, *J. Materiomics* **2020**, *6*, 1.
- [6] J. Liu, Y. Feng, R. Tang, R. Zhao, J. Gao, D. Shi, H. Yang, *Adv. Electron. Mater.* **2018**, *4*, 1700522.
- [7] L. P. Lee, M. J. Burns, K. Char, *Appl. Phys. Lett.* **1992**, *61*, 2706.

- [8] C. K. Jeong, S. B. Cho, J. H. Han, D. Y. Park, S. Yang, K.-I. Park, J. Ryu, H. Sohn, Y.-C. Chung, K. J. Lee, *Nano Res.* **2017**, *10*, 437.
- [9] Y. Zhang, C. Ma, X. Lu, M. Liu, *Mater. Horiz.* **2019**, *6*, 911.
- [10] H. S. Kum, H. Lee, S. Kim, S. Lindemann, W. Kong, K. Qiao, P. Chen, J. Irwin, J. H. Lee, S. Xie, S. Subramanian, J. Shim, S.-H. Bae, C. Choi, L. Ranno, S. Seo, S. Lee, J. Bauer, H. Li, K. Lee, J. A. Robinson, C. A. Ross, D. G. Schlom, M. S. Rzchowski, C.-B. Eom, J. Kim, *Nature* **2020**, *578*, 75.
- [11] S. R. Bakaul, C. R. Serrao, M. Lee, C. W. Yeung, A. Sarker, S.-L. Hsu, A. K. Yadav, L. Dedon, L. You, A. I. Khan, J. David Clarkson, C. Hu, R. Ramesh, S. Salahuddin, *Nat. Commun.* **2016**, *7*, 10547.
- [12] S. R. Bakaul, C. R. Serrao, O. Lee, Z. Lu, A. Yadav, C. Carraro, R. Maboudian, R. Ramesh, S. Salahuddin, *Adv. Mater.* **2017**, *29*, 1605699.
- [13] D. Ji, S. Cai, T. R. Paudel, H. Sun, C. Zhang, L. Han, Y. Wei, Y. Zang, M. Gu, Y. Zhang, W. Gao, H. Huyan, W. Guo, D. Wu, Z. Gu, E. Y. Tsybal, P. Wang, Y. X. Pan, *Nature* **2019**, *570*, 87.
- [14] R. Guo, L. You, W. Lin, A. Abdelsamie, X. Shu, G. Zhou, S. Chen, L. Liu, X. Yan, J. Wang, J. Chen, *Nat. Commun.* **2020**, *11*, 2571.
- [15] K. Gu, T. Katayama, S. Yasui, A. Chikamatsu, S. Yasuhara, M. Itoh, T. Hasegawa, *Adv. Funct. Mater.* **2020**, *30*, 2001236.
- [16] D. Lu, D. J. Baek, S. S. Hong, L. F. Kourkoutis, Y. Hikita, H. Y. Hwang, *Nat. Mater.* **2016**, *15*, 1255.
- [17] W. Liu, H. Wang, *J. Materiomics* **2020**, *6*, 385.
- [18] D. G. Schlom, *APL Mater.* **2015**, *3*, 062403.
- [19] M. Brahlek, A. S. Gupta, J. Lapano, J. Roth, H.-T. Zhang, L. Zhang, R. Haislmaier, R. Engel-Herbert, *Adv. Funct. Mater.* **2018**, *28*, 1702772.
- [20] H. Sun, C. Zhang, J. Song, J. Gu, T. Zhang, Y. Zang, Y. Li, Z. Gu, P. Wang, Y. Nie, *Thin Solid Films* **2020**, *697*, 137815.
- [21] T. Schneller, R. Waser, M. Kosec, D. Payne, *Chemical Solution Deposition of Functional Oxide Thin Films*, Springer, Berlin **2013**.
- [22] M. Coll, M. Napari, *APL Mater.* **2019**, *7*, 110901.
- [23] J. M. Vila-Fungueiriño, B. Rivas-Murias, J. Rubio-Zuazo, A. Carretero-Genevri, M. Lazzari, F. Rivadulla, *J. Mater. Chem. C* **2018**, *6*, 3834.
- [24] M. Coll, J. Gàzquez, R. Huhne, B. Holzapfel, Y. Morilla, J. Garcia-Lopez, A. Pomar, F. Sandiumenge, T. Puig, X. Obradors, *J. Mater. Res.* **2009**, *24*, 1446.
- [25] E. A. Cochran, K. N. Woods, D. W. Johnson, C. J. Page, S. W. Boettcher, *J. Mater. Chem. A* **2019**, *7*, 24124.
- [26] D. Levy, M. Zayat, *The Sol–Gel Handbook: Synthesis, Characterization, and Applications*, Wiley, New York **2015**.
- [27] A. J. C. Nixon, D. R. Eaton, *Can. J. Chem.* **1978**, *56*, 1928.
- [28] M. M. Barbooti, D. A. Al-Sammerrai, *Thermochim. Acta* **1986**, *98*, 119.
- [29] P. Melnikov, V. A. Nascimento, I. V. Arkhangelsky, L. Z. Zanoni Consolo, *J. Therm. Anal. Calorim.* **2013**, *111*, 543.
- [30] D. Wyrzykowski, E. Hebanowska, G. Nowak-Wiczak, M. Makowski, L. Chmurzyński, *J. Therm. Anal. Calorim.* **2011**, *104*, 731.
- [31] S. Culas, A. Surendran, J. Samuel, *Asian J. Chem.* **2013**, *25*, 3855.
- [32] L. Pardo, J. Ricote, *Multifunctional Polycrystalline Ferroelectric Materials: Processing and Properties*, Springer, Berlin **2011**.
- [33] P. Ptáček, E. Bartoníčková, J. Švec, T. Opravil, F. Šoukal, F. Frajkorová, *Ceram. Int.* **2015**, *41*, 115.
- [34] Y. Duan, J. Li, X. Yang, X. M. Cao, L. Hu, Z. Y. Wang, Y. W. Liu, C. X. Wang, *J. Therm. Anal. Calorim.* **2008**, *94*, 169.
- [35] T. Maruyama, S. Arai, *Appl. Phys. Lett.* **1992**, *60*, 322.
- [36] B. Malič, M. Kosec, K. Smolej, S. Stavber, *J. Eur. Ceram. Soc.* **1999**, *19*, 1345.
- [37] S. S. Hong, J. H. Yu, D. Lu, A. F. Marshall, Y. Hikita, Y. Cui, H. Y. Hwang, *Sci. Adv.* **2017**, *3*, eaao5173.
- [38] K. Erwin, M. Bart, *NEVAC* **2020**, *58*, 2.
- [39] G. Koster, B. L. Kropman, G. J. H. M. Rijnders, D. H. A. Blank, H. Rogalla, *Appl. Phys. Lett.* **1998**, *73*, 2920.

Supporting Information for

Facile chemical route to prepare water soluble epitaxial $\text{Sr}_3\text{Al}_2\text{O}_6$ sacrificial layers for free-standing oxides

Pol Salles,[†] Ivan Caño,[†] Roger Guzmán,[‡] Camilla Dore,[†] Agustín Mihi,[†] Wu Zhou,[‡] and Mariona Coll^{*,†}

[†]*ICMAB-CSIC, Campus UAB 08193, Bellaterra, Barcelona, Spain*

[‡]*School of Physical Sciences and CAS Key Laboratory of Vacuum Physics, University of Chinese Academy of Sciences, Beijing 100049, China*

E-mail: mcoll@icmab.es

Phone: +34 93 5801853

Stability of SAO precursor solution from metalorganic route

In the metalorganic route, the solution stability depends on the percentage of H_2O present in the solution. When the solvent used is pure acetic acid, small crystals appear in solution in a few hours. These crystals were filtered and analysed by IR, see Figure S1. The IR spectrum reveal the formation of $\text{Al}(\text{CH}_3\text{COCH}=\text{C}(\text{O})\text{CH}_3)_3$ crystals¹. When 5-10% of H_2O is added in the solution, it is very likely that the ketonic-enolic-bidentate internal exchange in beta-diketones is shifted² and the formation of this precipitate is avoided.

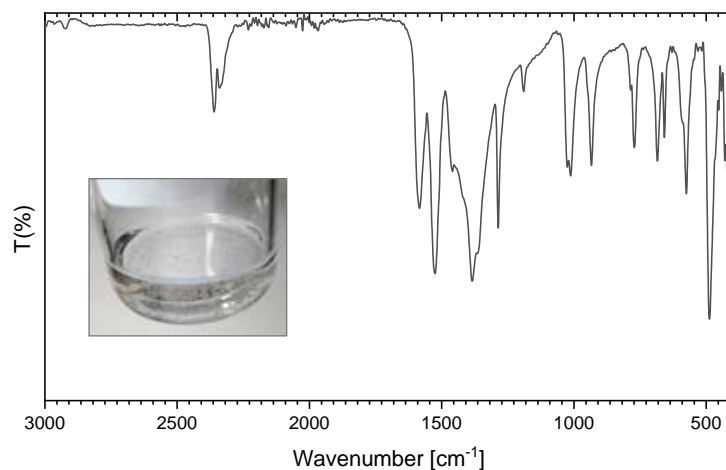


Figure S1: IR spectrum of the filtered precipitate obtained from the metalorganic solution when no water is added (photo inset).

Optimization of Thermal treatment

To investigate the influence of the annealing parameters on the crystalline quality of the SAO thin film, a XRD θ - 2θ study was performed as shown in Figure S2. All the samples were fabricated with the metal nitrate solution with the same thickness and only varying an specific annealing parameter at a time. The more crystalline the film is, the higher its XRD Bragg reflection intensity is. In this case, the (008) SAO Bragg reflection at 45.8° , which appear as a shoulder of the (002) STO, was used to compare the effect of maximum temperature (700 - 900°C), heating rate (5°C min^{-1} , $25^\circ\text{C min}^{-1}$ and $660^\circ\text{C min}^{-1}$) and time at maximum temperature (10 - 90 min). The study of the effect of temperature (Figure S2a) indicates that phase formation starts at 750°C but maximum intensity is achieved at 800 - 900°C . Regarding the heating rate (Figure S2b), the flash heated sample presents the lowest intensity whereas slower heating ramps favor the development of crystalline SAO films. Since 5°C min^{-1} and $25^\circ\text{C min}^{-1}$ conditions show similar results, $25^\circ\text{C min}^{-1}$ is chosen to avoid extensive processing times.

Finally, the optimization of the annealing time for 70 nm films indicates that 30 min is the minimum time required, Figure S2c. The thicker the films, the longer the time required.

Regarding the optimization of the film crystallinity prepared from the metalorganic route, analogous optimization process has been carried out identifying similar processing conditions. Note that the metalorganic solutions, for the same molarity, are more viscous than the metal nitrate solutions and therefore, thicker films are obtained. Therefore, annealing time has been adjusted according to the final film thickness. Figure S4 shows the XRD θ - 2θ scan for a SAO film prepared from a 0.25 M metalorganic solution.

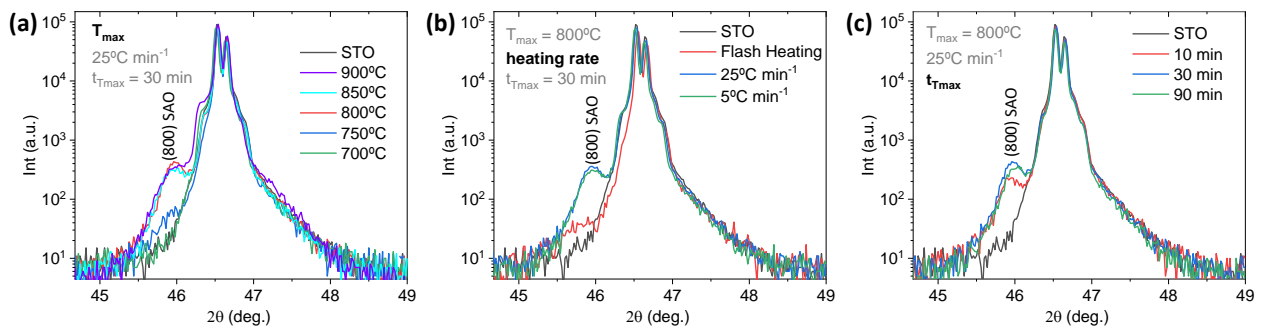


Figure S2: XRD θ - 2θ scans of SAO thin films grown on (001) STO substrate from the metal nitrate route under different annealing conditions. The parameters studied here are (a) temperature, (b) heating rate and (c) time at maximum temperature.

Texture analysis

The in-plane orientation of the SAO film on a STO substrate has been investigated by means of a ϕ -scan in the 2θ range close to the (110) STO reflection, Figure S3a. Both (110) STO and (660) SAO diffract at ϕ of 90, 180, 270 and 360° as shown in both Figure S3a and b, which proves the cube on cube orientation of the SAO film. Small differences in ϕ are attributed to instrumental error.

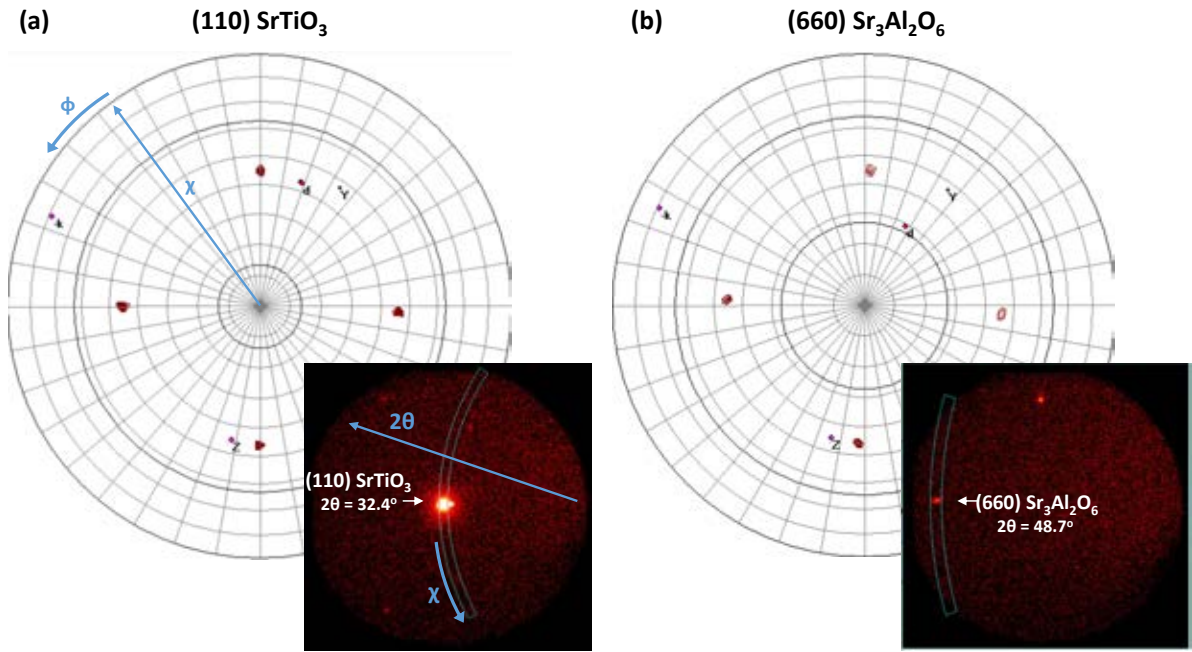


Figure S3: XRD Pole Figures along ϕ for (a) (110) SrTiO₃ and (b) (660) Sr₃Al₂O₆ reflections. Inset: bidimensional frame at a specific ϕ where the corresponding reflection appears.

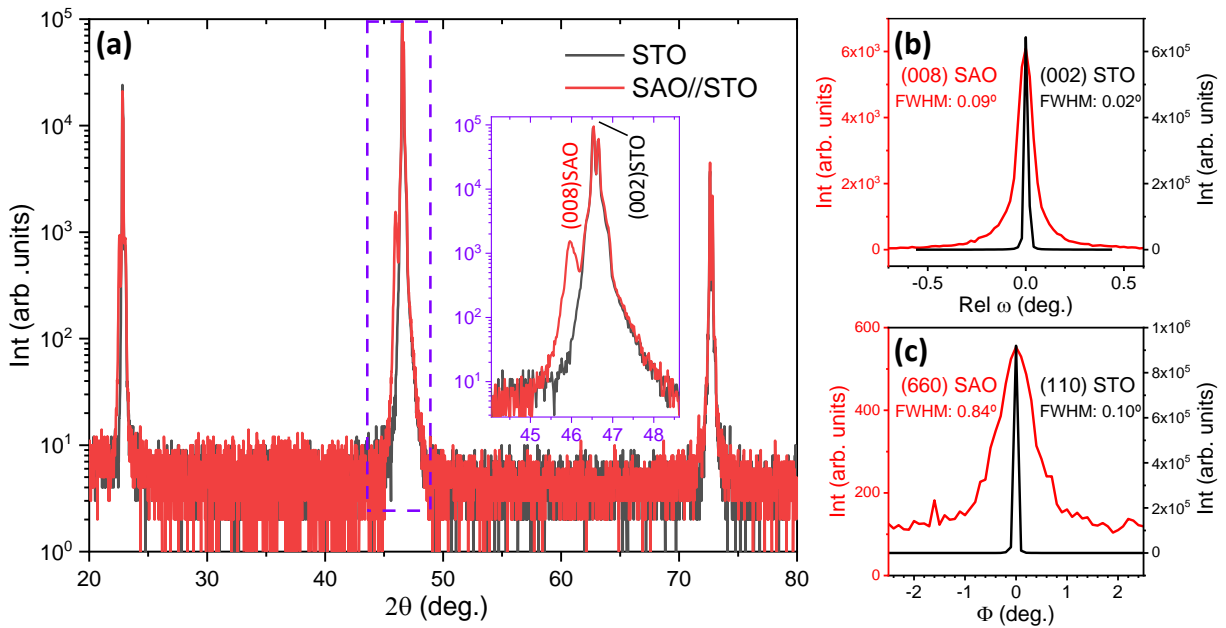


Figure S4: XRD analysis of SAO thin film grown on (001) STO substrate from a 0.25 M metalorganic solution with 5 % H₂O. (a) θ - 2θ scan, with inset corresponding to magnification of (008) SAO shoulder and (002) STO peak. (b) Rocking Curve around the (008) SAO and (002) STO reflections. (c) ϕ -scan around the (660) SAO and (110) STO reflections.

Surface morphology

Atomic force microscopy was used to investigate the surface morphology of the SAO films and explore the surface of the substrate after etching the sacrificial layer. In Figure S5 it is observed the topographic image and the corresponding optical microscope images of the films prepared from the metal nitrate route (a) and metalorganic route (b). In both cases, the films are dense with surface roughness (rms) of 2.5 and 5.3 nm, respectively. Upon water exposure, the sample shows a very smooth surface (rms = 0.5 ± 0.2 nm) resembling that of a bare substrate, Figure S5c. Also, further acid etching ensures a step-like surface morphology to re-use the STO substrate, Figure S5d.

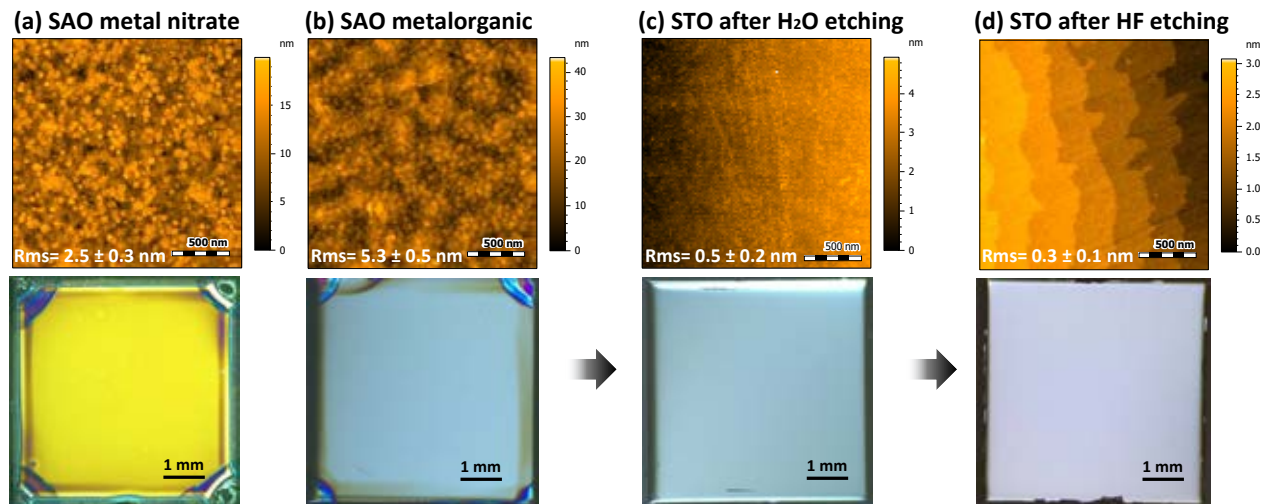


Figure S5: Top panel AFM topographic image and bottom panel optical microscope images of (a) SAO thin film on STO substrates from the metal nitrate-based and (b) metalorganic-based; (c) SAO//STO substrate after immersion in H₂O; and (d) STO substrate after immersion in HF.

Etching of sacrificial layer by different solvents

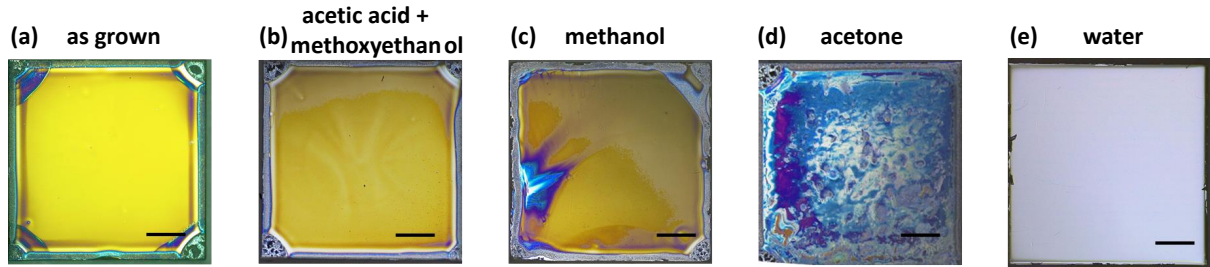


Figure S6: Magnified images of different SAO//STO samples (a) as grown and after immersion for 1 min in (b) solvent blend of acetic acid: methoxyethanol (1:3), (c) methanol, (d) acetone and (e) milli-Q water. Black scale bar = 1 mm

Al₂O₃ deposition by ALD

SAO's vulnerability to moisture could raise concerns about the suitability of using ex-situ techniques to deposit the functional oxide. We have compared in the main manuscript the surface topography of ALD- Al₂O₃ on SAO and as-deposited SAO thin films (figure 4). No further degradation is observed upon ALD-Al₂O₃. Also, we have included for comparison the surface topography of ALD-Al₂O₃ on STO substrate, see figure S7.

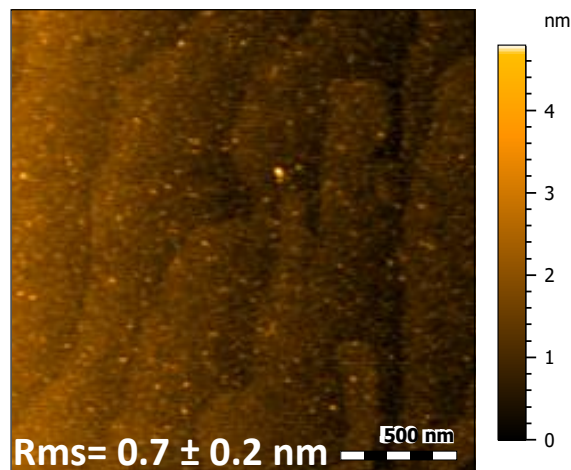


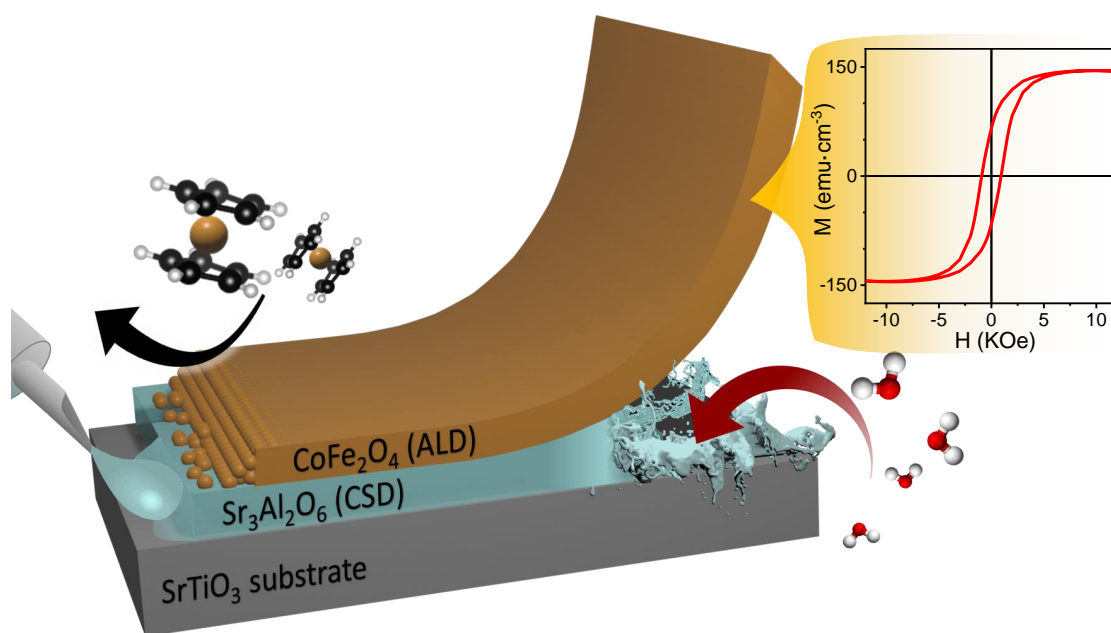
Figure S7: AFM topographic image of a 40 nm Al₂O₃ deposited by ALD on STO, where the step-like surface can still be appreciated.

(1) Spectral Database for Organic Compounds SDBS, <https://sdb.sdb.aist.go.jp>

(2) D. Levy, M. Zayat, The Sol-Gel Handbook: Synthesis, Characterization, and Applications, Wiley, 2015

Chapter 4

Bendable polycrystalline and magnetic CoFe_2O_4 membranes by chemical methods



Bendable Polycrystalline and Magnetic CoFe_2O_4 Membranes by Chemical Methods

Pol Salles, Roger Guzmán, David Zanders, Alberto Quintana, Ignasi Fina, Florencio Sánchez, Wu Zhou, Anjana Devi, and Mariona Coll*

Cite This: *ACS Appl. Mater. Interfaces* 2022, 14, 12845–12854

Read Online

ACCESS |

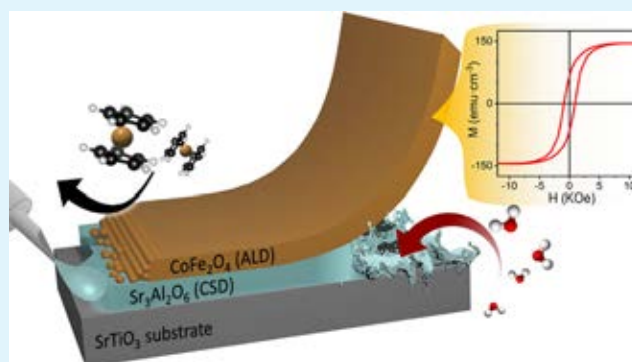
Metrics & More

Article Recommendations

Supporting Information

ABSTRACT: The preparation and manipulation of crystalline yet bendable functional complex oxide membranes has been a long-standing issue for a myriad of applications, in particular, for flexible electronics. Here, we investigate the viability to prepare magnetic and crystalline CoFe_2O_4 (CFO) membranes by means of the $\text{Sr}_3\text{Al}_2\text{O}_6$ (SAO) sacrificial layer approach using chemical deposition techniques. Meticulous chemical and structural study of the SAO surface and SAO/CFO interface properties have allowed us to identify the formation of an amorphous SAO capping layer and carbonates upon air exposure, which dictate the crystalline quality of the subsequent CFO film growth. Vacuum annealing at 800 °C of SAO films promotes the elimination of the surface carbonates and the reconstruction of the SAO surface crystallinity. Ex-situ atomic layer deposition of CFO films at 250 °C on air-exposed SAO offers the opportunity to avoid high-temperature growth while achieving polycrystalline CFO films that can be successfully transferred to a polymer support preserving the magnetic properties under bending. Float on and transfer provides an alternative route to prepare freestanding and wrinkle-free CFO membrane films. The advances and challenges presented in this work are expected to help increase the capabilities to grow different oxide compositions and heterostructures of freestanding films and their range of functional properties.

KEYWORDS: CoFe_2O_4 , $\text{Sr}_3\text{Al}_2\text{O}_6$, sacrificial layer, atomic layer deposition, solution processing, flexible device



INTRODUCTION

The rapid development of electronic devices, telecommunication systems, and sensors pushes new functional demands with increasingly stringent requirements like flexibility, light weight, and miniaturization.^{1,2} Transition metal oxides present the richest variety of functional properties due to the large diversity of chemical compositions and structures that they can offer.^{3–5} An important twist is the processing of such materials as high-temperature growth conditions and specific crystalline substrates are required to achieve a certain degree of crystallinity, limiting their application field. The scientific community is putting a huge effort on learning how to grow these films and heterostructures to meet the new requirements while keeping their functionality.^{5,6} Mechanical exfoliation^{7–9} and wet and dry etching release methods¹⁰ are the most common processes for fabricating pliable and freestanding functional membranes. One of the most attractive approaches is the use of a sacrificial layer which allows one to detach the functional complex oxide film from the substrate. The choice of the sacrificial layer is of paramount importance. Its crystal structure, chemical composition, surface morphology, and lattice parameter will affect the crystalline quality of the transferred film and the selective etching.^{11–14} $(\text{La,Sr})\text{MnO}_3$ (LSMO),¹⁵ SrRuO_3 (SRO),¹⁶ and $\text{Sr}_3\text{Al}_2\text{O}_6$ (SAO)¹⁷ are some

of the sacrificial layers used to prepare epitaxial perovskite oxide membranes such as SrTiO_3 ,¹⁸ BiFeO_3 ,^{19,20} BaTiO_3 ,²¹ BaSnO_3 ,¹² SRO,^{22,23} and LSMO¹⁷ or even nanocomposites $\text{BaTiO}_3\text{--CoFe}_2\text{O}_4$.²⁴ Among the above-mentioned sacrificial layers, SAO is especially suitable to prepare perovskite oxides, it can be easily dissolved in water, contributing to the sustainability of the process, and by scrupulous variation of its lattice constant via cation substitution permits easy lattice matching with the functional oxide and avoid further crack formation.^{12,14,25} Nonetheless, the soft and open structure of SAO has a strong sensitivity to air humidity and can also facilitate cation interdiffusion during the high-temperature growth of the targeted complex oxide film.^{11,17,26–28} These characteristics can jeopardize the quality of the oxide membrane. Finally, the use of SAO to fabricate membrane oxides with dissimilar crystal structure has remained barely explored.

Received: December 17, 2021

Accepted: February 21, 2022

Published: March 1, 2022



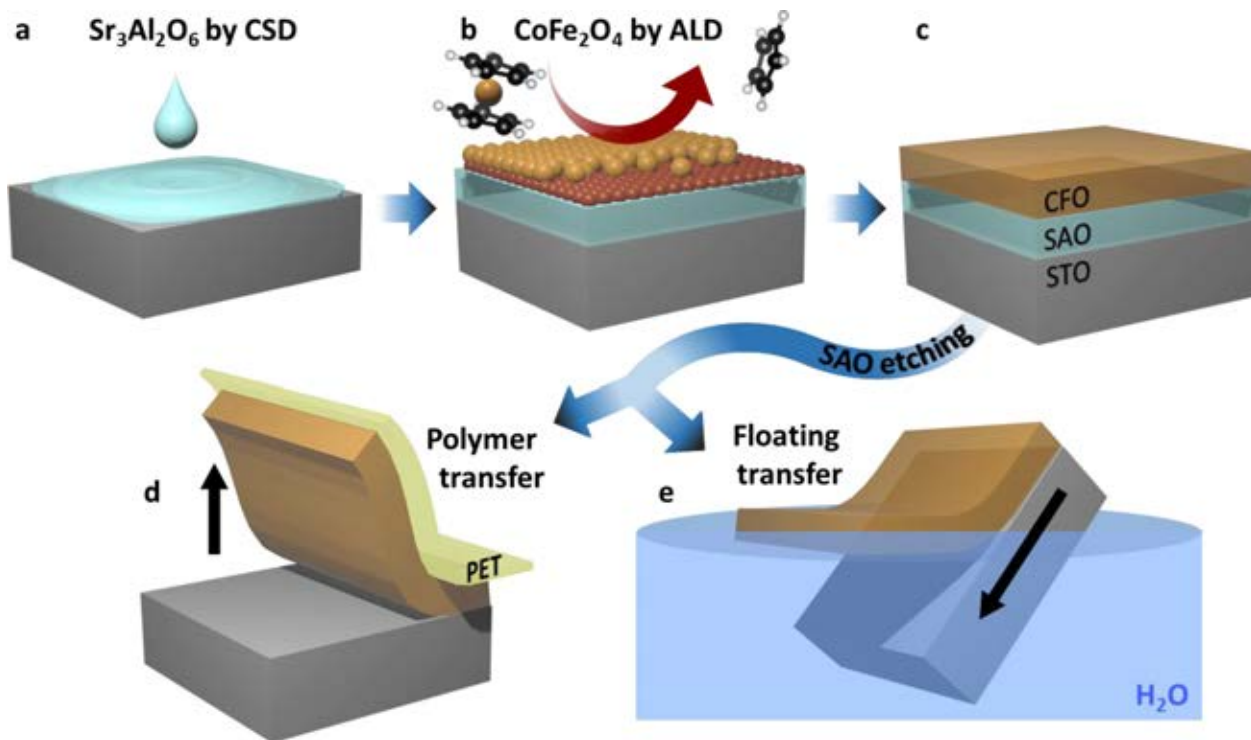


Figure 1. Sketch of the process followed to achieve CFO membranes. (a) SAO is deposited by chemical solution deposition on a (001) STO substrate. (b) CFO is deposited by ALD, achieving (c) a CFO/SAO//STO heterostructure. This heterostructure is immersed in water to finally transfer a CFO membrane following (d) the polymer support strategy and (e) the floating strategy.

Generally, reported complex oxide membranes are prepared at high temperature by high-vacuum deposition techniques,^{11,29} although many challenges still remain in the continuous search for an ubiquitous and green route to prepare them. Today, it is possible to grow a wide variety of complex oxide thin films by cost-effective low-vacuum deposition methods^{30–33} offering a great opportunity to go one step further and investigate the viability of such techniques to obtain complex oxide membranes.

CoFe₂O₄ (CFO) has stimulated considerable interest for its remarkable magnetic and electrochemical properties.^{24,34–38} The possibility to provide mechanical flexibility to this material could dramatically increase its application area, for example, in wearable products,³⁹ bendable magnetic sensors for diagnostics and medicine,^{5,40–42} and energy-related applications.⁴³ The preparation of CFO films on pliable substrates and as freestanding membranes by high-vacuum deposition techniques has been attempted by direct growth on muscovite substrates,^{44,45} mechanical lift off,⁷ and in-situ growth on the rock salt MgO sacrificial layer.⁴⁶ However, sustainable strategies to prepare a CFO freestanding membrane using water-soluble sacrificial layers and subsequent ex-situ and low-temperature growth to be further integrated in arbitrary substrates can open new areas of research.

In this exciting scenario, here we explore the ex-situ chemical synthesis of crystalline inverse spinel CFO bendable membranes using water-soluble SAO as a sacrificial layer. To reduce the typical high-temperature growth of these functional oxides and mitigate the cation interdiffusion at the CFO/SAO interface, low-temperature atomic layer deposition (ALD) is combined with solution processing. The critical effect of SAO air exposure on its surface structure and chemical composition has been assessed by reflection high-energy electron diffraction (RHEED), X-ray photoelectron spectroscopy (XPS), and scanning transmission electron microscopy (STEM). In-situ

vacuum annealing of SAO films has been proved successful to improve its surface quality. Finally, we studied the ex-situ grown ALD-CFO films and investigated the magnetic properties of the resulting bendable polycrystalline CFO membranes by superconducting quantum interference device (SQUID) magnetometry.

EXPERIMENTAL SECTION

The synthesis of the CFO membranes has been pursued following the sketch in Figure 1. The first step consists of the preparation of a SAO sacrificial layer on SrTiO₃ (STO) by chemical solution deposition (CSD), followed by the preparation of the CFO on SAO//STO by ALD (lattice mismatch 7%, Figure S1), and finally perform the selective etching and subsequent exfoliation by means of either the use of a polymer support or the floating approach, as described in detail below. ALD has been chosen over CSD to prepare the CFO films because the deposition of a metal–organic precursor solution on SAO contributes to its degradation according to the above-mentioned SAO characteristics and permits low-temperature growth (250 °C).⁴⁷

Synthesis of SAO Sacrificial Layer. The SAO epitaxial layer was prepared by CSD on (001) STO substrates using metal nitrate solutions of 0.1–0.25 M as described elsewhere.³³ Upon thermal treatment in a tubular furnace at 800 °C for 30 min with a heating/cooling rate of 25 °C·min^{−1} and under 0.6 L·min^{−1} O₂ flow, the samples were sealed under vacuum to minimize surface degradation.

Synthesis of CFO Films. CFO thin films were prepared by ALD with a Savannah 100 ALD system from Cambridge NanoTech Inc. Prior to film growth, the samples were exposed to ozone pulses to activate the surface forming a hydroxyl-terminated surface and facilitate the chemical reaction with the precursors. The deposition chamber was kept at 250 °C under a continuous N₂ flow of 50 sccm. The metal–organic precursors were handled under inert atmosphere. [Co(Cp)₂], bis(cyclopentadienyl)cobalt(II), was used as purchased and heated at 90 °C. [Fe(ⁱpki)₂], bis(*N*-isopropyl ketoiminate)iron(II), was synthesized as reported⁴⁸ and heated at 130 °C. The tailor-made [Fe(ⁱpki)₂] was chosen over other commercial Fe precursors because of the good reproducibility and deposition control identified in previous works.⁴⁹ The pulse of the metal–organic precursors was

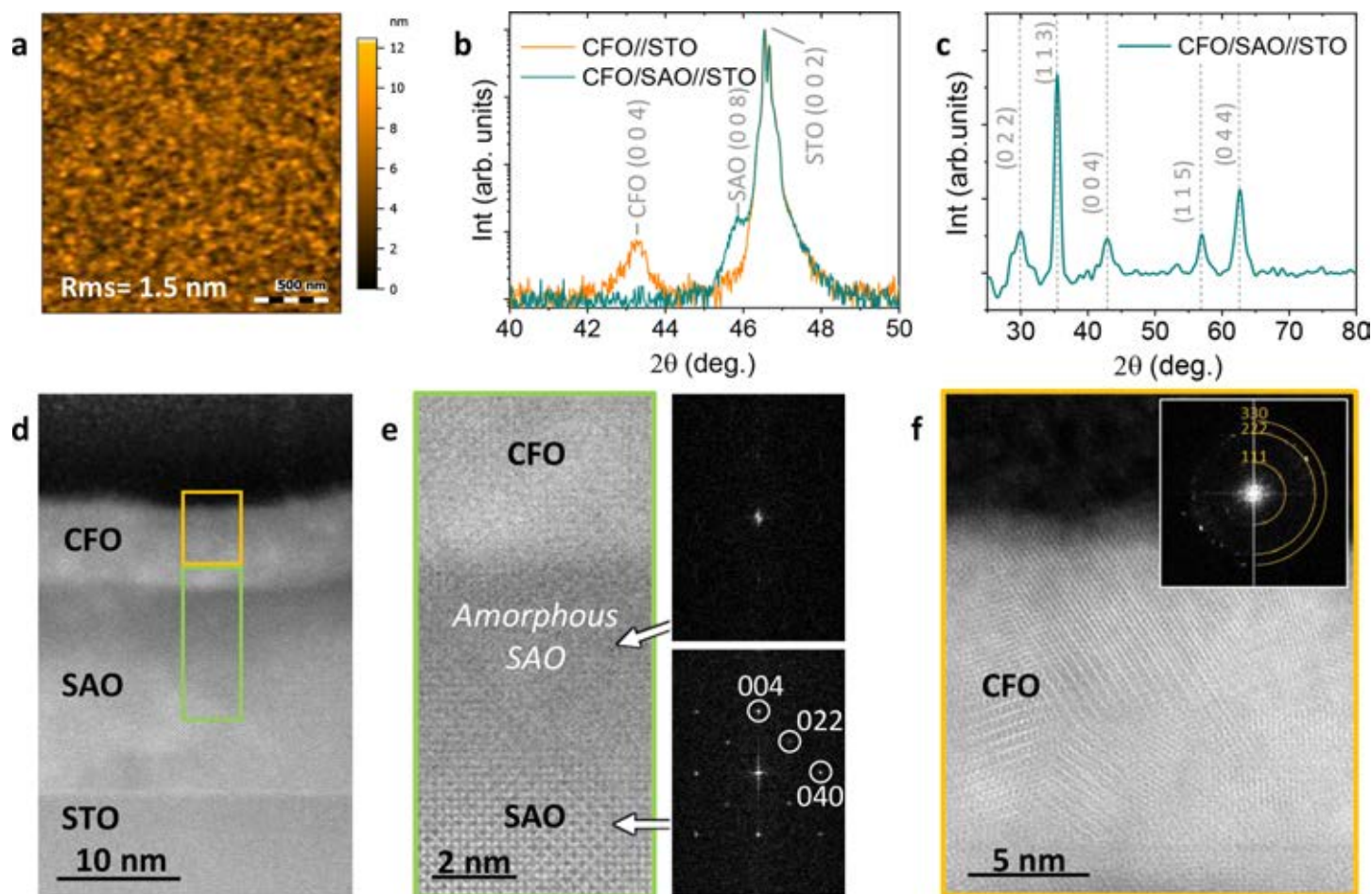


Figure 2. CFO/SAO//STO structure and surface morphology. (a) AFM topographic image of the CFO film. (b) XRD θ - 2θ scan of the as-deposited CFO thin film (250 °C) on SAO//STO compared to CFO grown directly on STO substrate, (004) CFO, (008) SAO, and (002) STO Bragg reflections are indicated. (c) GIXRD of the as-deposited CFO/SAO//STO heterostructure. Indexed peaks correspond to the CoFe_2O_4 crystalline phase. (d) Z-contrast HAADF-STEM cross-section of the CFO/SAO//STO films. (e) Magnification of the interface area with the corresponding FFT from the amorphous part and the crystalline part. (f) Magnification of the CFO film with its corresponding FFT pattern.

done in a pressure-boost mode as explained elsewhere.⁴⁹ Ozone, O_3 , was used as the oxygen source with a pulse/purge duration of 0.2 s/10 s. To achieve stoichiometric Co:Fe = 0.5 corresponding to CoFe_2O_4 , $[\text{Co}(\text{Cp})_2]$ and $[\text{Fe}(\text{pki})_2]$ were pulsed in a supercycle approach with 5 subcycles of Co-O for 13 subcycles of Fe-O; $[[\text{Co}(\text{Cp})_2]-\text{O}_3 \times 5 + [\text{Fe}(\text{pki})_2]-\text{O}_3 \times 13]] \times \text{supercycle}$. A growth incubation period was identified for films thinner than 40 nm. Films thicker than 40 nm show a constant growth rate of 0.8 nm·(supercycle)⁻¹ similar to what has been previously reported for ALD-CFO.^{47,50,51} A postannealing treatment was performed on some of the CFO thin films in a tubular furnace at 350–750 °C for 1 h under 0.6 L·min⁻¹ O_2 flow, as indicated in the text.

Transfer of CFO Membranes. The transfer of the CFO thin films deposited on SAO//STO was done following two different strategies, polymer support and float on,^{21,52} as shown in Figure 1d and 1e, respectively. In this work, the polymer support strategy consists of adhering a polyethylene terephthalate (PET) polymer film to the CFO/SAO//STO heterostructure by applying slight pressure before immersing it in Milli-Q water. Once the SAO is etched in water, polymer and STO are mechanically separated, achieving a CFO membrane on the polymer support. For specific analysis, the CFO membrane held on PET has been subsequently transferred to a second support including Kapton and silicon.

On the other hand, the floating strategy is based on direct immersion of the CFO/SAO//STO heterostructure in water with no support. Once the SAO is etched, the sample is removed, left to air dry, and slowly immersed again in water, which helps in separating the CFO from the STO substrate by capillary forces, achieving a CFO freestanding membrane floating on the water surface. The floating

CFO membrane can be directly fished with an arbitrary support (see Video S1 in the Supporting Information).

Characterization. Crystal Structure. X-ray diffraction (XRD) θ - 2θ and grazing incidence XRD (GIXRD) measurements were performed using a Siemens D-5000 and a Bruker-AXS (model A25 D8 Discover), respectively, both equipped with a Cu anode ($\text{Cu K}\alpha = 1.5418 \text{ \AA}$). The first one is adopted to study the epitaxial growth of the films and the second one to perform surface-specific phase analysis. Aberration-corrected scanning transmission electron microscopy (STEM) imaging was performed using a Nion HERMES-100, operated at 60 kV, at the University of Chinese Academy of Sciences, Beijing, China. High-angle annular dark-field (HAADF) images were acquired using an annular detector with a collection semiangle of 75–210 mrad. Cross-sectional STEM specimens were prepared using the standard focused ion beam (FIB) lift-out process in a Thermo Fisher Scientific FIB system. Protective amorphous carbon and thin Pt layers were applied over the region of interest before milling. To minimize the sidewall damage and sufficiently thin the specimen for electron transparency, final milling was carried out at a voltage of 2 kV. To reduce possible beam-induced structural damage on the SAO films, images were acquired with a reduced beam current (10 pA) and pixel dwell time (2 $\mu\text{s}\cdot\text{px}^{-1}$).

High-pressure reflection high-energy electron diffraction (RHEED) was performed with incidence of electrons along the [100] STO at a glancing angle of 1–2°. To study the crystalline evolution of SAO with temperature, RHEED patterns were acquired from as-deposited and in-situ-annealed films up to 825 °C at an oxygen partial pressure PO_2 of 0.1 mbar for 30 min.

Film Thickness. The CFO film thicknesses were extracted from X-ray reflectometry (XRR) measurements using a Siemens diffrac-

tometer D-5000, and it was further validated with spectroscopic ellipsometry measurements using a GESSE Ellipsometer from SOPRA Optical Platform. In both cases, the CFO//STO samples were used as the reference.

Surface Morphology. Magnified optical images of the thin films and the corresponding membranes were taken by a Leica DM1750 M optical microscope. The surface morphology and roughness were studied by topographic images acquired by a Keysight 5100 atomic force microscopy (AFM) instrument and analyzed by Mountains8 software. Surface analysis and qualitative chemical composition were further investigated by scanning electron microscopy (SEM) using a SEM QUANTA FEI 200 FEG-ESEM equipped with energy-dispersive x-ray spectroscopy (EDX).

Surface Chemical Composition. X-ray photoelectron spectroscopy (XPS) measurements were performed with a SPECS PHOIBOS 150 hemispherical analyzer (SPECS GmbH, Berlin, Germany) using a monochromatic Al K α radiation (1486.74 eV) source at 300 W at the Institut Català de Nanociència i Nanotecnologia (ICN2), Barcelona, Spain. The samples were analyzed with a spot size of 3.5 mm \times 0.5 mm at a base pressure of 4×10^{-10} mbar. Pass energies of 20 and 50 eV and step sizes of 0.05 and 1 eV were used for the high-resolution and survey spectra, respectively. In-situ annealing to study the surface chemical composition with temperature (room temperature up to 800 °C) was performed in an annexed XPS chamber. The acquired spectra were processed with CasaXPS software using Shirley background subtraction. Binding energies were calibrated using Al 2p.

Magnetic Properties. The magnetic properties of the CFO thin films and membranes were probed employing a MPMS3 SQUID magnetometer from Quantum Design. In-plane magnetic hysteresis loops, $M(H)$, were acquired at 300 K with a maximum applied field of 15 kOe. To study the effect of the bending on the magnetic behavior of the CFO membranes, these were transferred to Kapton and clamped on plastic holders with different outward bending radii (r), flat, 5 mm, and 2.5 mm. To calculate the strain (ϵ) generated from the outward bending of the CFO membranes on kapton, it was used the equation $\epsilon = (t_{\text{CFO}} + t_{\text{Kapton}})/2r$,^{45,46} where t is the thickness and r the curvature radius.

RESULTS AND DISCUSSION

Chemically Deposited Oxide Heterostructure. The ALD-deposited 40 nm CFO on SAO//STO at 250 °C shows a homogeneous and smooth surface in Figure 2a, replicating the same morphology of SAO films (Figure S2) as expected from the conformal nature of the ALD technique. The structure and crystalline quality of CFO on SAO//STO have been studied by XRD and compared to the model system CFO//STO (Figure 2b). From the XRD pattern it can be identified that the CFO//STO sample presents two main Bragg reflections at 43.2° and 46.5° which correspond to (004) CFO and (002) STO, respectively, revealing that c -axis-oriented CFO films are obtained on single-crystal STO (001) substrates. On the other hand, for the CFO/SAO//STO sample, Bragg reflections centered at 45.8° and 46.5° correspond to (008) SAO and (002) STO, respectively, confirming the c -axis-oriented growth of SAO on STO, in agreement with previous work.³³ However, the absence of the (004) CFO Bragg reflection in the latter indicates that no preferred (001) oriented growth is achieved in CFO. GIXRD analysis, which strengthens the signal from the first few nanometers of the film over the bulk/substrate, was done on CFO/SAO//STO films, see Figure 2b, disclosing that the CFO is crystalline and randomly oriented on SAO. The films do not present extra secondary phases as shown in Figure S3.

Z-contrast STEM imaging of a 10 nm ALD-CFO film on SAO//STO was selected to further study the heterostructure and interface quality with atomic resolution. From the low-

magnification Z-contrast image (Figure 2d) it is observed that the ALD-CFO film is homogeneous and conformal on the SAO film. A closer look at the CFO/SAO interface (Figure 2e) identifies two different regions in the SAO film. The upper part in contact with CFO shows an amorphous SAO “capping layer”, while the bulk of the film is highly crystalline, further confirmed by the respective fast Fourier transform (FFT) patterns. Turning to the CFO film, higher magnification Z-contrast imaging shows the presence of randomly oriented crystalline CFO grains (Figure 2f) in agreement with the GIXRD analysis shown above. Attempts to restore the SAO surface quality in as-prepared films by acid etching or by extended O₃ exposure at 250 °C in vacuum (10^{-2} Torr) before the ALD-CFO deposition were not successful.

In order to shed light on the formation and composition of this amorphous layer, RHEED and XPS analyses were carried out on bare as-deposited SAO films upon air exposure and after in-situ annealing in vacuum up to 825 °C, see sketch of the sample and thermal profile in Figure 3. Further details are

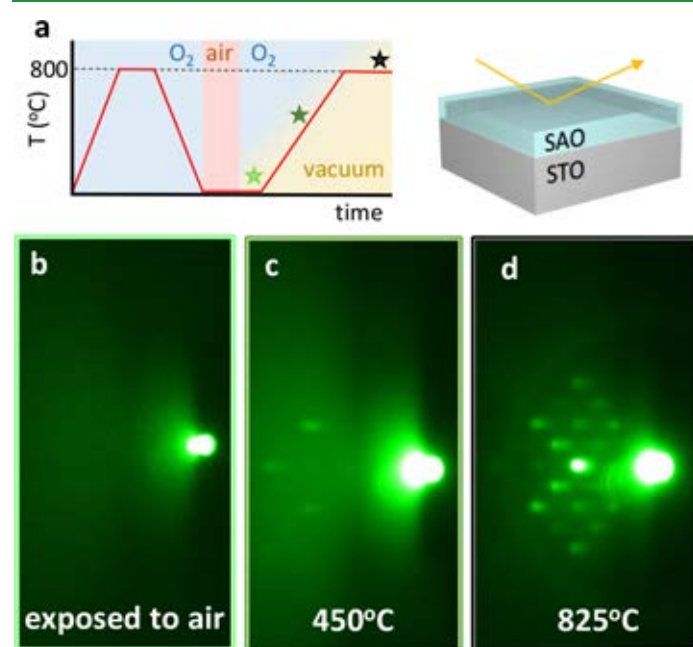


Figure 3. RHEED analysis of the SAO surface after air exposure. (a) Schematic of the followed thermal profile: SAO film is initially annealed in a tubular furnace at 800 °C with O₂ flow to obtain epitaxial SAO; then it is cooled down, exposed to air, and annealed again in the RHEED chamber under vacuum with PO₂. Colored stars in the temperature profile in (a) identify the temperature the measurements were performed: (b) at room temperature, (c) at 450 °C, and (d) at 825 °C.

provided in the Experimental Section. Figure 3b–d shows the high-pressure RHEED patterns from the as-deposited SAO film after air exposure and upon in-situ annealing taken along the [100] STO direction. From the pattern acquired from the as-deposited sample exposed to air, no diffraction spots are identified, revealing that the very first layers of the film are amorphous. Upon in-situ heating the sample at 450 °C in O₂, low-intensity spots appear, indicating some degree of crystallization. Further in-situ annealing to 825 °C shows a spotty diffraction pattern corresponding to a crystalline SAO surface. Therefore, in-situ annealing in O₂ causes the recrystallization of the SAO film surface.

In parallel, analogous XPS analyses were performed to elucidate the chemical composition of this amorphous top

surface and its in-situ evolution when heated in vacuum (no O₂ present in this case) following the thermal profile depicted in Figure 3a. From the overview spectrum (Figure S4) Sr, Al, C, and O can be identified. The Al 2p and Sr 3d core level spectra are not altered upon being exposed to the different in-situ annealing (not shown), from which the Sr:Al cation ratio can be easily calculated resulting in a stoichiometric ratio of 1.5. On the other hand, C 1s and O 1s core level spectra show significant differences, see Figure 4a and 4b, respectively. The

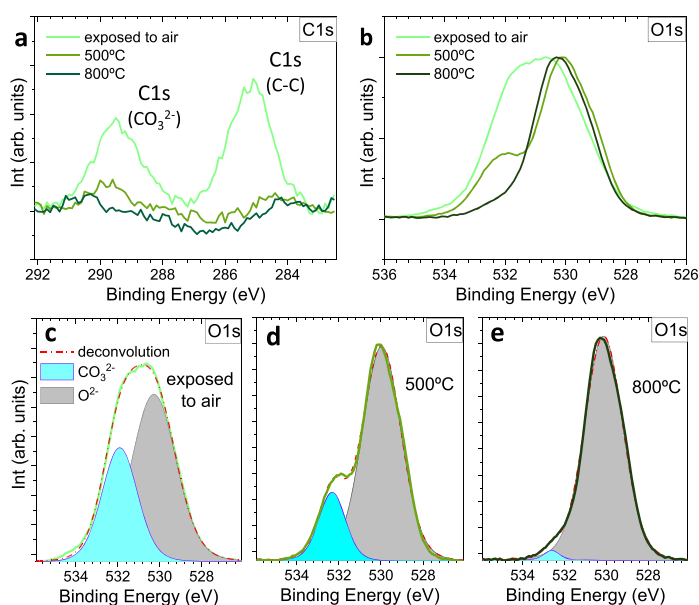


Figure 4. XPS analysis from a bare SAO surface. (a) C 1s and (b) O 1s core level spectra after air exposure and upon in-situ annealing in vacuum at 500 and 800 °C. O 1s spectra have been unbundled to clearly identify the different contributions (c) after air exposure, (d) at 500 °C, and (e) at 800 °C. Cyan area denotes carbonate species and gray area denotes lattice oxygen species.

C 1s core level spectrum from the as-deposited film shows two intense peaks, a broad one at 285 eV which extends up to 287 eV corresponding to the C–C with C–O–C contribution and another one at 289 eV assigned to the presence of the O–C=O moiety.^{53,54} When the sample is in-situ annealed in vacuum at 450 °C, the graphitic carbon vanishes and the C–O-related peak strongly decreases in intensity. A further in-situ annealing to 800 °C completely eliminates the C. The O 1s core level spectra in Figure 4b show a broad peak at 531 eV that gradually narrows upon annealing. Detailed analysis of the O 1s at each stage is shown in Figure 4c–e. The broad peak of the as-deposited sample centered at 531 eV can be deconvoluted into two main peaks at 530 and 532 eV (Figure 4c). The peak at 530 eV corresponds to metal oxide bond (529–530 eV), while the peak with lower intensity located in the range of 532–533 eV corresponds to carbonates.^{55,56} Upon heating, the O 1s carbonate contribution dramatically decreases with a small shift to higher energies being almost nonexistent at 800 °C, consistent with the C 1s trend. Therefore, according to this analysis, the SAO surface is covered with carbonates. It is very likely that they form within seconds when SAO samples are exposed to air before being sealed in vacuum for further manipulation. This surface reactivity is triggered by the affinity of the large Sr²⁺ ions for the hydration that could simultaneously hydrolyze few [Al₆–O₁₈]^{18–} rings.^{11,17} The formation of such carbonates together with the amorphous cap layer explain the growth of

polycrystalline CFO films. Nonetheless, performing an annealing in vacuum at 800 °C removes the presence of carbonates and restores the SAO surface crystallinity. It is envisaged that in-situ deposition of complex oxides on this restored SAO surface could enable epitaxial growth.

With the aim to study the effect of a postannealing temperature on the crystalline quality of CFO deposited on air-exposed SAO//STO, the heterostructure has been subjected to several ex-situ thermal treatments in a tubular furnaces from 350 to 750 °C under O₂ flow (Figure 5a). It is

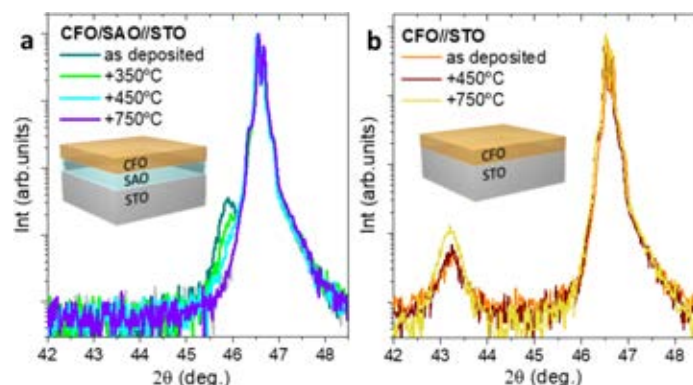


Figure 5. XRD θ – 2θ analysis of as-deposited (250 °C) and ex-situ postannealed CFO films from (a) CFO/SAO//STO and (b) CFO//STO.

observed that by increasing the postannealing temperature, the SAO (008) Bragg reflection decreases in intensity whereas no CFO (004) reflection appears. From GIXRD analysis, no significant changes are identified in the polycrystalline nature of CFO (Figure S5). An analogous study on the CFO//STO model system revealed that by increasing the postannealing temperature, the (004) CFO Bragg reflection increases in intensity, indicating that the crystalline quality does improve (Figure S6).^{51,57} Therefore, it is very likely that the CFO/SAO interface plays a key role in the CFO/SAO//STO crystallinity. According to reported STEM analysis on the LSMO/SAO//STO system, which demonstrated the susceptibility of SAO for interface cation diffusion when exposed to high temperature,^{26,27} it is suggested that the observed decrease in intensity of the SAO (008) reflection could be due to interface cation diffusion between CFO and SAO. In addition, XPS studies performed on exfoliated ALD-CFO films revealed the presence of Sr and Al traces (Figure S6), which would reinforce the hypothesis of cation diffusion during the postannealing. Baek et al.²⁶ overcame this issue by in-situ growing a few unit cells of the SrTiO₃ buffer layer.

CFO-Transferred Membranes. Upon Milli-Q water immersion of the CFO/SAO//STO heterostructure, two routes have been investigated to obtain CFO membranes: the use of a PET polymer support and the floating approach, as shown in Figure 1 d and 1e, respectively. Importantly, after CFO exfoliation, the STO substrate can be reused for subsequent experiments, contributing to the sustainability of the process.

Polymer Transfer. To achieve successful exfoliation of the entire CFO membrane, it is necessary to identify the optimal conditions to etch the sacrificial layer for the CFO/SAO//STO system. Note that the very thin film thickness of CFO makes the potential membrane susceptible to cracking and generating micro- and nanoscale defects during the exfoliation

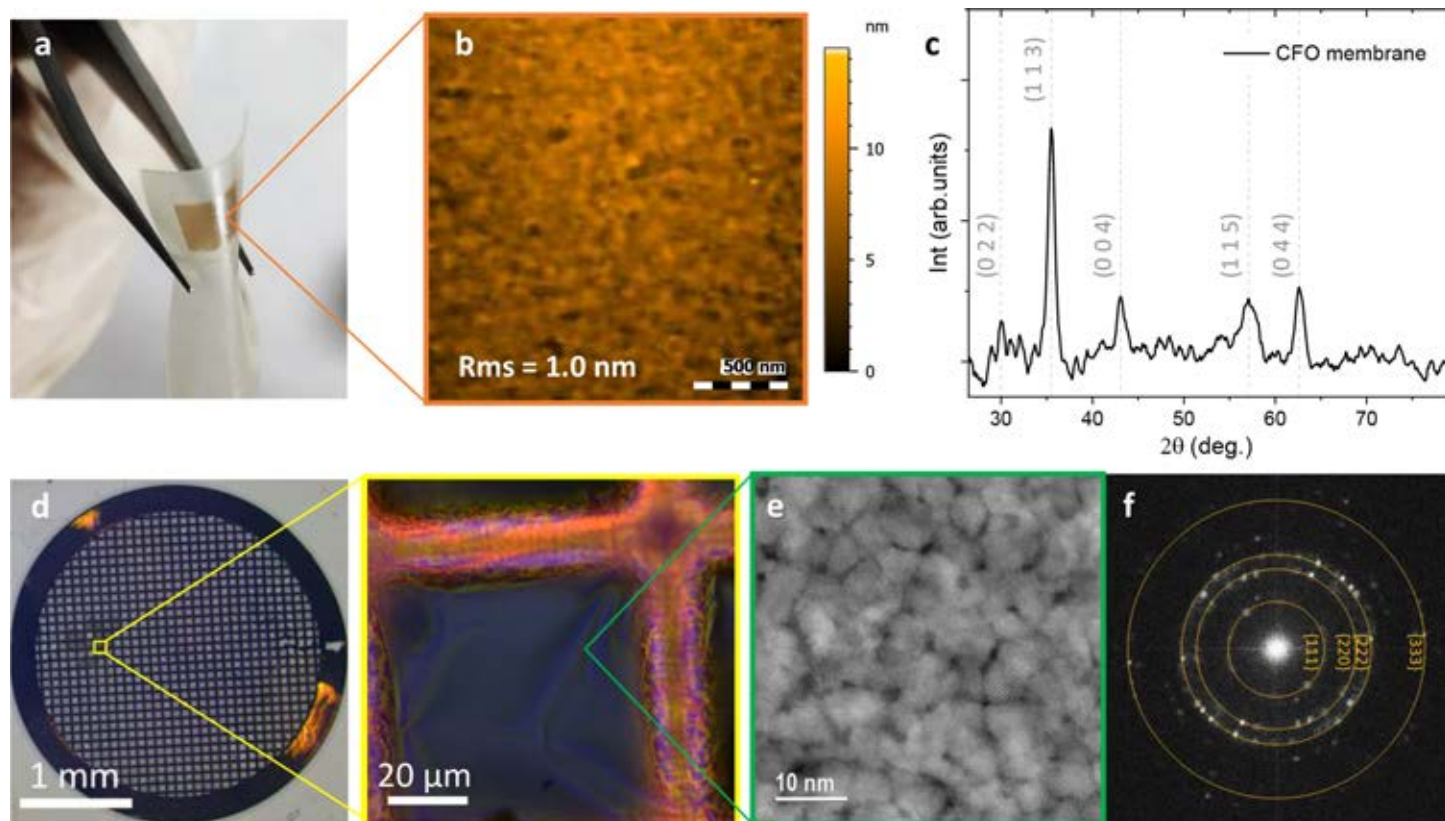


Figure 6. Structure and surface topographic characterization of 250 °C deposited CFO membranes and transferred by (a–c) a polymer support and (d–f) floating. (a) $5 \times 5 \text{ mm}^2$ CFO membrane on PET support with its corresponding (b) topographic analysis by AFM and (c) GIXRD analysis. (d) Optical microscope image of a Cu grid with a piece of CFO membrane picked directly from water with the corresponding magnification of the CFO membrane. (e) STEM top view of the CFO membrane and its corresponding (f) FFT pattern.

process.^{52,58} To improve the mechanical properties of the CFO membrane, attachment of a polymer support on the CFO prior to immersion of the heterostructure in water was first studied. Following this polymer strategy, CFO membranes of $5 \times 5 \text{ mm}^2$ have been successfully transferred to PET with no cracks, as shown in Figure 6a. The transferred CFO membranes remain strongly attached to the PET support by dispersive adhesion with good mechanical stability facilitating its manipulation and further characterization.⁵⁹ The surface topography and structure of a 60 nm CFO membrane was characterized by AFM and GIXRD. Figure 6b shows the surface morphology studied by AFM topographic images of the CFO membrane on PET, which is proved to be smooth and homogeneous with a root-mean-square surface roughness (rms) of $1.0 \pm 0.2 \text{ nm}$. GIXRD shows that the polycrystalline nature of the CFO film before exfoliation is preserved after the transfer (Figure 6c). We emphasize the feasibility of performing a second transfer of the CFO membranes from PET to another arbitrary substrate such as silicon wafers or kapton tapes, as shown in Figure S7.

Floating and Transfer. Another promising strategy that was studied to obtain freestanding CFO membranes is the floating transfer method, Figure 1e. In this case, the CFO/SAO//STO heterostructure is immersed in water with no additional support. Once the SAO has been completely etched, the remaining heterostructure is taken out to dry and then slowly immersed again in water with a given angle facilitating that the capillary forces of the water surface separate the CFO membrane from the STO substrate, leaving the CFO membrane floating; an example of the floating process is shown in Video S1. Finally, the CFO membrane can be picked

out with a support. Figure 6d–f shows an example where a CFO membrane of 14 nm was picked out from the water surface with a Cu grid. The freestanding CFO membrane remains unbroken over the Cu grid holes as shown in Figure 6d, which allowed us to perform HR-STEM analysis. The crystalline grains of the CFO membrane can be distinguished with a diameter size ranging from 5 to 15 nm (Figure 6e). Different atomic planes of the crystalline CFO are identified, and the crystallinity is further confirmed by the FFT pattern presented in Figure 6f. A more extensive study of the crystallinity of the CFO grains observed by STEM can be found in Figure S8. This strategy presents some benefits when compared to the polymer transfer. First, the CFO membrane wrinkles formed during etching can easily spread when the membrane remains floating on water. As a result, flat and smooth membranes can be obtained when picked up with a support. Another advantage is that when the CFO floating membrane is picked out by a support, the adhesion of the membrane with the support is mainly related to the gravity and the drying of water between them, leaving the interface energy between the support and the CFO membrane irrelevant. This independence from the interfacial forces implies the freedom of using virtually any type of support without limitations, which is not the case for the polymer transfer strategy. However, on the other hand, a drawback of the floating transfer is that because the CFO membranes are so fragile and in this case no support is used during the etching and separation, cracks can be formed easily, compromising the integrity of the CFO membrane.

Magnetic Properties. The magnetic properties of 60 nm CFO films and membranes at 300 K were assessed using

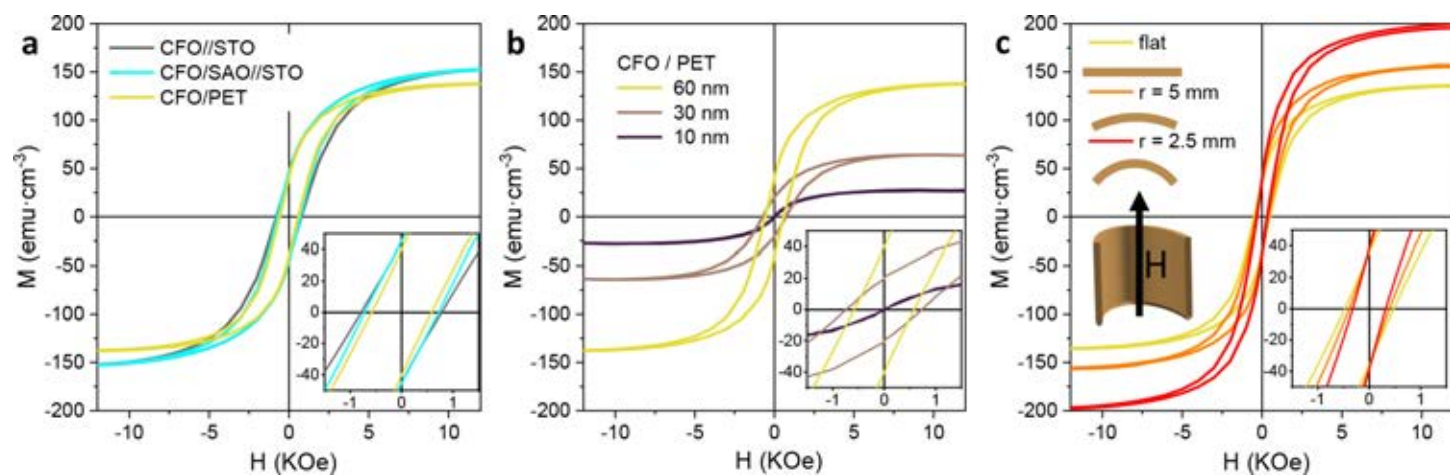


Figure 7. In-plane magnetic hysteresis loops, $M(H)$, performed at 300 K on CFO films and membranes. Inset shows $M(H)$ from -1.5 to 1.5 kOe. (a) CFO films grown on STO, SAO//STO, and transferred onto PET. (b) CFO membranes on PET for different thicknesses, 10, 30, and 60 nm. (c) CFO membranes under different radii of curvature.

SQUID magnetometry (Figure 7). In-plane $M(H)$ hysteresis loops corresponding to CFO//STO, CFO/SAO//STO, and transferred CFO on PET are shown in Figure 7a. From these measurements it can clearly be seen that the inclusion of the SAO layer does not significantly alter the magnetic properties of CFO, showing a similar saturation magnetization, M_s , of $150 \text{ emu}\cdot\text{cm}^{-3}$ and coercivities of 0.7 kOe. Moreover, after etching the SAO layer and CFO transfer to a PET substrate, the CFO/PET magnetic properties also remain unaltered as evidenced by the resemblance in the hysteresis shape and saturation magnetization. Note that the obtained magnetization values for the CFO membranes are congruous with earlier studies on epitaxial CFO membranes.^{7,44–46} These M_s values are lower than those for bulk CFO materials.⁶⁰ Variations in M_s could arise from many different factors including off-stoichiometry, strain, grain boundaries, and structural distortions.^{36,50,61} Considering that in our work both epitaxial films and polycrystalline membranes show similar M_s values, this decrease could be tentatively attributed to cation migration and redistribution in the tetrahedral and octahedral sites, as previously demonstrated in spinel ferrite samples.^{62–64}

Figure 7b shows the magnetic properties for transferred CFO membranes with thicknesses of 10, 30, and 60 nm onto PET substrates. The CFO thickness was tuned controlling the number of ALD cycles. The CFO membranes are homogeneous and continuous with no cracks. However, random wrinkles were observed (Figure S9). From the $M(H)$ hysteresis loops in Figure 7b, it is observed that M_s decreases by diminishing the CFO membrane thickness. Notoriously, the 10 nm CFO membranes show a paramagnetic behavior. Cation diffusion and doping in a spinel structure could distort its structure, altering the magnetization of saturation.⁶⁵ Therefore, it is very likely that the Al and Sr traces identified on the CFO membrane surface by XPS (Figure S6), probably due to the easy cation diffusion during the sample processing, could distort the CFO structure, diminishing M_s . Thus, the thinner the membrane, the larger the contribution of Sr and Al and thus the lower the M_s .

$M(H)$ hysteresis loops from 60 nm CFO membranes transferred on kapton tape and held at different outward bending radii, r (flat, 5 mm, and 2.5 mm) were acquired. These bending radii correspond to 0, 0.75%, and 1.5% tensile strains, respectively, see the Experimental Section for further details. Figure 7c shows the magnetic field-dependent magnetization

curves in the in-plane direction (parallel to the curvature axis) for the different bendings. The membranes show an increase in the M_s while H_c is barely modified by increasing the curvature radius, in agreement with previous reports on epitaxial CFO membranes.⁴⁶ Note that despite the large amount of research performed on the magnetic behavior of epitaxial-strained rigid CFO films, it is only recently that the first reports appeared exploring the anisotropy–strain scenario on epitaxial pliable CFO membranes.^{44–46} Therefore, more detailed analysis is required to elucidate the mechanism by which the magnetization varies with bending in polycrystalline membranes.

CONCLUSIONS

We investigated the synthesis of CFO membranes by combining atomic layer deposition and solution processing using a sacrificial layer of SAO. We shed light on the chemical preparation of oxide heterostructures under compatible thermodynamic conditions and the critical role of interface perfection on the crystalline quality of the CFO membranes. Surface-specific characterization on the structure (RHEED, STEM) and chemistry (XPS) of epitaxial SAO reveals the formation of an amorphous top layer and carbonates. In this study, we also unravel how to restore the SAO surface quality by annealing in vacuum. ALD-CFO growth at 250 °C on air-exposed solution-processed SAO is polycrystalline, and the CFO films can be easily transferred to a polymer support. Alternatively, CFO membranes have been prepared by floating, resulting in freestanding membranes. We demonstrated the formation of CFO membranes of various thicknesses (from 10 to 60 nm) with the possibility of being stretched or bent, showing robust magnetization at room temperature. This pliable system will allow future studies on the intrinsic effect of mechanical strain, which is of high interest for flexible magnetostrictive sensors or actuators but also for energy- and medicine-related applications. Therefore, this is a straightforward, sustainable, and cost-effective approach to prepare functional crystalline oxide membranes, opening the door for manufacturing a wide variety of oxide membranes and artificial architectures with less restricted and mild processing conditions. We also envisage new opportunities to produce oxide membranes with tuned degree of crystallinity when chemical methods are combined with high-vacuum deposition methods, broadening the study of physical and chemical

phenomena occurring at these novel and bendable oxide interfaces for enhanced functionalities.

■ ASSOCIATED CONTENT

SI Supporting Information

The Supporting Information is available free of charge at <https://pubs.acs.org/doi/10.1021/acsami.1c24450>.

Atomic representations of the STO, SAO, and CFO crystalline structures; AFM analysis of STO, SAO//STO, and CFO//STO; XRD θ - 2θ of CFO/SAO//STO; XPS overview of SAO//STO; GIXRD and AFM of CFO/SAO//STO after postannealing at 450 °C; XPS analysis of Sr and Al traces at CFO membranes; examples of second transfer of CFO membranes; XRR measurements of CFO//STO; optical microscopy images of CFO membranes of different thicknesses (PDF)

Video of the floating process of a CFO membrane (MP4)

■ AUTHOR INFORMATION

Corresponding Author

Mariona Coll – ICMAB-CSIC, Barcelona 08193, Spain;
orcid.org/0000-0001-5157-7764; Phone: +34 93 5801853; Email: mcoll@icmab.es

Authors

Pol Salles – ICMAB-CSIC, Barcelona 08193, Spain;
orcid.org/0000-0003-1426-611X

Roger Guzmán – School of Physical Sciences and CAS Key Laboratory of Vacuum Physics, University of Chinese Academy of Sciences, Beijing 100049, China; orcid.org/0000-0002-5580-0043

David Zanders – Inorganic Materials Chemistry, Ruhr University Bochum, Bochum 44801, Germany; orcid.org/0000-0001-5516-7738

Alberto Quintana – ICMAB-CSIC, Barcelona 08193, Spain;
orcid.org/0000-0002-9813-735X

Ignasi Fina – ICMAB-CSIC, Barcelona 08193, Spain;
orcid.org/0000-0003-4182-6194

Florencio Sánchez – ICMAB-CSIC, Barcelona 08193, Spain; orcid.org/0000-0002-5314-453X

Wu Zhou – School of Physical Sciences and CAS Key Laboratory of Vacuum Physics, University of Chinese Academy of Sciences, Beijing 100049, China; orcid.org/0000-0002-6803-1095

Anjana Devi – Inorganic Materials Chemistry, Ruhr University Bochum, Bochum 44801, Germany; orcid.org/0000-0003-2142-8105

Complete contact information is available at: <https://pubs.acs.org/doi/10.1021/acsami.1c24450>

Notes

The authors declare no competing financial interest.

■ ACKNOWLEDGMENTS

This work was funded by MICIN/AEI/10.13039/501100011033/FEDER through the projects Severo Ochoa FUNFUTURE CEX2019-00917-S and PID2020-114224RB-I00. We also acknowledge the financial support from the 2020 Leonardo Grant for Researchers and Cultural Creators BBVA Foundation, the i-link A20346-CSIC project, the National Key

RD Program of China (2018YFA0305800), and the Beijing Outstanding Young Scientist Program (BJJWZYJH01201914430039). The project that gave rise to these results received the support of a fellowship from the “la Caixa” Foundation LCF/BQ/DI19/11730026. D.Z. acknowledges the funding and financial support of the Fund of Chemical Industries (Kekulé fellowship) for his Ph.D. research. The authors are thankful to R. Solanas for his help with the RHEED measurements. This work has been done in the framework of the doctorate in material science of the Autonomous University of Barcelona.

■ REFERENCES

- (1) Rim, Y. S.; Bae, S.; Chen, H.; De Marco, N.; Yang, Y. Recent Progress in Materials and Devices toward Printable and Flexible Sensors. *Adv. Mater.* **2016**, *28*, 4415–4440.
- (2) Shi, Q.; Dong, B.; He, T.; Sun, Z.; Zhu, J.; Zhang, Z.; Lee, C. Progress in Wearable Electronics/Photonics—Moving Toward the Era of Artificial Intelligence and Internet of Things. *InfoMat* **2020**, *2*, 1131–1162.
- (3) Coll, M.; Fontcuberta, J.; Althammer, M.; Bibes, M.; Boschker, H.; Calleja, A.; Cheng, G.; Cuoco, M.; Dittmann, R.; Dkhil, B.; El Baggari, I.; Fanciulli, M.; Fina, I.; Fortunato, E.; Frontera, C.; Fujita, S.; Garcia, V.; Goennenwein, S.; Granqvist, C.-G.; Grollier, J.; Gross, R.; Hagfeldt, A.; Herranz, G.; Hono, K.; Houwman, E.; Huijben, M.; Kalaboukhov, A.; Keeble, D.; Koster, G.; Kourkoutis, L.; Levy, J.; Lira-Cantu, M.; MacManus-Driscoll, J.; Mannhart, J.; Martins, R.; Menzel, S.; Mikolajick, T.; Napari, M.; Nguyen, M.; Niklasson, G.; Paillard, C.; Panigrahi, S.; Rijnders, G.; Sánchez, F.; Sanchis, P.; Sanna, S.; Schlom, D.; Schroeder, U.; Shen, K.; Siemon, A.; Spreitzer, M.; Sukegawa, H.; Tamayo, R.; van den Brink, J.; Pryds, N.; Granozio, F. M. Towards Oxide Electronics: a Roadmap. *Appl. Surf. Sci.* **2019**, *482*, 1–93.
- (4) Chen, X.; Mi, W. Mechanically Tunable Magnetic and Electronic Transport Properties of Flexible Magnetic Films and their Heterostructures for Spintronics. *J. Mater. Chem. C* **2021**, *9*, 9400–9430.
- (5) Gao, W.; Zhu, Y.; Wang, Y.; Yuan, G.; Liu, J.-M. A Review of Flexible Perovskite Oxide Ferroelectric Films and Their Application. *J. Materiomics* **2020**, *6*, 1–16.
- (6) Kum, H.; Lee, D.; Kong, W.; Kim, H.; Park, Y.; Kim, Y.; Baek, Y.; Bae, S.-H.; Lee, K.; Kim, J. Epitaxial Growth and Layer-Transfer Techniques for Heterogeneous Integration of Materials for Electronic and Photonic Devices. *Nat. Electron* **2019**, *2*, 439–450.
- (7) Kum, H. S.; Lee, H.; Kim, S.; Lindemann, S.; Kong, W.; Qiao, K.; Chen, P.; Irwin, J.; Lee, J. H.; Xie, S.; Subramanian, S.; Shim, J.; Bae, S.-H.; Choi, C.; Ranno, L.; Seo, S.; Lee, S.; Bauer, J.; Li, H.; Lee, K.; Robinson, J. A.; Ross, C. A.; Schlom, D. G.; Rzechowski, M. S.; Eom, C.-B.; Kim, J. Heterogeneous Integration of Single-Crystalline Complex-Oxide Membranes. *Nature* **2020**, *578*, 75–81.
- (8) Wu, P.-C.; Chen, P.-F.; Do, T. H.; Hsieh, Y.-H.; Ma, C.-H.; Ha, T. D.; Wu, K.-H.; Wang, Y.-J.; Li, H.-B.; Chen, Y.-C.; Juang, J.-Y.; Yu, P.; Eng, L. M.; Chang, C.-F.; Chiu, P.-W.; Tjeng, L. H.; Chu, Y.-H. Heteroepitaxy of Fe₃O₄/Muscovite: A New Perspective for Flexible Spintronics. *ACS Appl. Mater. Interfaces* **2016**, *8*, 33794–33801.
- (9) Shi, X.; Wu, M.; Lai, Z.; Li, X.; Gao, P.; Mi, W. Bending Strain-Tailored Magnetic and Electronic Transport Properties of Reactively Sputtered γ -Fe₄N/Muscovite Epitaxial Heterostructures toward Flexible Spintronics. *ACS Appl. Mater. Interfaces* **2020**, *12*, 27394–27404.
- (10) Zhang, Y.; Ma, C.; Lu, X.; Liu, M. Recent Progress on Flexible Inorganic Single-Crystalline Functional Oxide Films for Advanced Electronics. *Mater. Horiz.* **2019**, *6*, 911–930.
- (11) Sun, H.; Zhang, C.; Song, J.; Gu, J.; Zhang, T.; Zang, Y.; Li, Y.; Gu, Z.; Wang, P.; Nie, Y. Epitaxial Optimization of Atomically Smooth Sr₃Al₂O₆ for Freestanding Perovskite Films by Molecular Beam Epitaxy. *Thin Solid Films* **2020**, *697*, 137815.
- (12) Singh, P.; Swartz, A.; Lu, D.; Hong, S. S.; Lee, K.; Marshall, A. F.; Nishio, K.; Hikita, Y.; Hwang, H. Y. Large-Area Crystalline

BaSnO₃ Membranes with High Electron Mobilities. *ACS Appl. Electron. Mater.* **2019**, *1*, 1269–1274.

(13) An, F.; Qu, K.; Zhong, G.; Dong, Y.; Ming, W.; Zi, M.; Liu, Z.; Wang, Y.; Qi, B.; Ding, Z.; Xu, J.; Luo, Z.; Gao, X.; Xie, S.; Gao, P.; Li, J. Highly Flexible and Twistable Freestanding Single Crystalline Magnetite Film with Robust Magnetism. *Adv. Funct. Mater.* **2020**, *30*, 2003495.

(14) Hong, S. S.; Gu, M.; Verma, M.; Harbola, V.; Wang, B. Y.; Lu, D.; Vailionis, A.; Hikita, Y.; Pentcheva, R.; Rondinelli, J. M.; Hwang, H. Y. Extreme Tensile Strain States in La_{0.7}Ca_{0.3}MnO₃ Membranes. *Science* **2020**, *368*, 71–76.

(15) Bakaul, S. R.; Serrao, C. R.; Lee, M.; Yeung, C. W.; Sarker, A.; Hsu, S.-L.; Yadav, A. K.; Dedon, L.; You, L.; Khan, A. I.; Clarkson, J. D.; Hu, C.; Ramesh, R.; Salahuddin, S. Single Crystal Functional Oxides on Silicon. *Nat. Commun.* **2016**, *7*, 10547.

(16) Pesquera, D.; Khestanova, E.; Ghidini, M.; Zhang, S.; Rooney, A. P.; Maccherozzi, F.; Riego, P.; Farokhipoor, S.; Kim, J.; Moya, X.; Vickers, M. E.; Stelmashenko, N. A.; Haigh, S. J.; Dhesi, S. S.; Mathur, N. D. Large Magnetoelectric Coupling in Multiferroic Oxide Heterostructures Assembled Via Epitaxial Lift-off. *Nat. Commun.* **2020**, *11*, 3190.

(17) Lu, D.; Baek, D. J.; Hong, S. S.; Kourkoutis, L. F.; Hikita, Y.; Hwang, H. Synthesis of Freestanding Single-Crystal Perovskite Films and Heterostructures by Etching of Sacrificial Water-soluble Layers. *Nat. Mater.* **2016**, *15*, 1255–1260.

(18) Hong, S. S.; Yu, J. H.; Lu, D.; Marshall, A. F.; Hikita, Y.; Cui, Y.; Hwang, H. Y. Two-Dimensional Limit of Crystalline Order in Perovskite Membrane Films. *Sci. Adv.* **2017**, *3*, No. eaao5173.

(19) Guo, R.; You, L.; Lin, W.; Abdelsamie, A.; Shu, X.; Zhou, G.; Chen, S.; Liu, L.; Yan, X.; Wang, J.; Chen, J. Continuously Controllable Photoconductance in Freestanding BiFeO₃ by the Macroscopic Flexoelectric Effect. *Nat. Commun.* **2020**, *11*, 2571.

(20) Ji, D.; Cai, S.; Paudel, T. R.; Sun, H.; Zhang, C.; Han, L.; Wei, Y.; Zang, Y.; Gu, M.; Zhang, Y.; Gao, W.; Huyan, H.; Guo, W.; Wu, D.; Gu, Z.; Tsymbal, E. Y.; Wang, P.; Nie, Y.; Pan, X. Freestanding Crystalline Oxide Perovskites down to the Monolayer Limit. *Nature* **2019**, *570*, 87–90.

(21) Gu, K.; Katayama, T.; Yasui, S.; Chikamatsu, A.; Yasuhara, S.; Itoh, M.; Hasegawa, T. Simple Method to Obtain Large-Size Single-Crystalline Oxide Sheets. *Adv. Funct. Mater.* **2020**, *30*, 2001236.

(22) Hu, C.-Z.; Zhang, Y.-S.; Niu, X.; Zhong, N.; Xiang, P.-H.; Duan, C.-G. Strain-Controlled Electrical and Magnetic Properties of SrRuO₃ Thin Films with Sr₃Al₂O₆ Buffer Layers. *Appl. Phys. Lett.* **2021**, *118*, 072407.

(23) Le, P. T. P.; ten Elshof, J. E.; Koster, G. Epitaxial Lift-off of Freestanding (011) and (111) SrRuO₃ Thin Films Using a Water Sacrificial Layer. *Sci. Rep.* **2021**, *11*, 12435.

(24) Zhong, G.; An, F.; Qu, K.; Dong, Y.; Yang, Z.; Dai, L.; Xie, S.; Huang, R.; Luo, Z.; Li, J. Highly Flexible Freestanding BaTiO₃-CoFe₂O₄ Heteroepitaxial Nanostructure Self-Assembled with Room-Temperature Multiferroicity. *Small* **2022**, *18*, 2104213.

(25) Xu, R.; Huang, J.; Barnard, E. S.; Hong, S. S.; Singh, P.; Wong, E. K.; Jansen, T.; Harbola, V.; Xiao, J.; Wang, B. Y.; Crossley, S.; Lu, D.; Liu, S.; Hwang, H. Y. Strain-Induced Room-Temperature Ferroelectricity in SrTiO₃ Membranes. *Nat. Commun.* **2020**, *11*, 3141.

(26) Baek, D. J.; Lu, D.; Hikita, Y.; Hwang, H. Y.; Kourkoutis, L. F. Ultrathin Epitaxial Barrier Layer to Avoid Thermally Induced Phase Transformation in Oxide Heterostructures. *ACS Appl. Mater. Interfaces* **2017**, *9*, 54–59.

(27) Baek, D. J.; Lu, D.; Hikita, Y.; Hwang, H. Y.; Kourkoutis, L. F. Mapping Cation Diffusion Through Lattice Defects in Epitaxial Oxide Thin Films on the Water-Soluble Buffer Layer Sr₃Al₂O₆ Using Atomic Resolution Electron Microscopy. *APL Materials* **2017**, *5*, 096108.

(28) Li, D.; Adamo, C.; Wang, B. Y.; Yoon, H.; Chen, Z.; Hong, S. S.; Lu, D.; Cui, Y.; Hikita, Y.; Hwang, H. Y. Stabilization of Sr₃Al₂O₆ Growth Templates for Ex Situ Synthesis of Freestanding Crystalline Oxide Membranes. *Nano Lett.* **2021**, *21*, 4454–4460.

(29) Xie, Z.; Li, Z.; Lu, H.; Wang, Y.; Liu, Y. Etching Sr₃Al₂O₆ Sacrificial Layer to Prepare Freestanding GBCO Films with High Critical Current Density. *Ceram. Int.* **2021**, *47*, 13528–13532.

(30) Schwartz, R. W.; Schneller, T.; Waser, R. Chemical Solution Deposition of Electronic Oxide Films. *C. R. Chim.* **2004**, *7*, 433.

(31) Coll, M.; Napari, M. Atomic Layer Deposition of Functional Multicomponent Oxides. *APL Materials* **2019**, *7*, 110901.

(32) Mackus, A. J. M.; Schneider, J. R.; MacIsaac, C.; Baker, J. G.; Bent, S. F. Synthesis of Doped, Ternary, and Quaternary Materials by Atomic Layer Deposition: A Review. *Chem. Mater.* **2019**, *31*, 1142–1183.

(33) Salles, P.; Caño, I.; Guzman, R.; Dore, C.; Mihi, A.; Zhou, W.; Coll, M. Facile Chemical Route to Prepare Water Soluble Epitaxial Sr₃Al₂O₆ Sacrificial Layers for Free-Standing Oxides. *Adv. Mater. Interfaces* **2021**, *8*, 2001643.

(34) Huang, W.; Zhu, J.; Zeng, H. Z.; Wei, X. H.; Zhang, Y.; Li, Y. R. Strain Induced Magnetic Anisotropy in Highly Epitaxial CoFe₂O₄ Thin Films. *Appl. Phys. Lett.* **2006**, *89*, 262506.

(35) Shirsath, S. E.; Liu, X.; Yasukawa, Y.; Li, S.; Morisako, A. Switching of Magnetic Easy-axis Using Crystal Orientation for Large Perpendicular Coercivity in CoFe₂O₄ Thin Film. *Sci. Rep.* **2016**, *6*, 30074.

(36) Gatel, C.; Warot-Fonrose, B.; Matzen, S.; Moussy, J.-B. Magnetism of CoFe₂O₄ Ultrathin Films on MgAl₂O₄ Driven by Epitaxial Strain. *Appl. Phys. Lett.* **2013**, *103*, 092405.

(37) He, Q.; Rui, K.; Chen, C.; Yang, J.; Wen, Z. Interconnected CoFe₂O₄ – Polypyrrole Nanotubes as Anode Materials for High Performance Sodium Ion Batteries. *ACS Appl. Mater. Interfaces* **2017**, *9*, 36927–36935.

(38) Mitra, S.; Veluri, P. S.; Chakraborty, A.; Petla, R. K. Electrochemical Properties of Spinel Cobalt Ferrite Nanoparticles with Sodium Alginate as Interactive Binder. *ChemElectroChem.* **2014**, *1*, 1068–1074.

(39) Gao, W.; Emaminejad, S.; Nyein, H. Y. Y.; Challa, S.; Chen, K.; Peck, A.; Fahad, H. M.; Ota, H.; Shiraki, H.; Kiriya, D.; Lien, D.-H.; Brooks, G. A.; Davis, R. W.; Javey, A. Fully Integrated Wearable Sensor Arrays for Multiplexed In-situ Perspiration Analysis. *Nature* **2016**, *529*, 509–514.

(40) Lizundia, E.; Maceiras, A.; Vilas, J.; Martins, P.; Lanceros-Mendez, S. Magnetic Cellulose Nanocrystal Nanocomposites for the Development of Green Functional Materials. *Carbohydr. Polym.* **2017**, *175*, 425–432.

(41) Wang, Z.; Wang, X.; Li, M.; Gao, Y.; Hu, Z.; Nan, T.; Liang, X.; Chen, H.; Yang, J.; Cash, S.; Sun, N.-X. Highly Sensitive Flexible Magnetic Sensor Based on Anisotropic Magnetoresistance Effect. *Adv. Mater.* **2016**, *28*, 9370–9377.

(42) Zheng, H.; Wang, J.; Lofland, S. E.; Ma, Z.; Mohaddes-Ardabili, L.; Zhao, T.; Salamanca-Riba, L.; Shinde, S. R.; Ogale, S. B.; Bai, F.; Viehland, D.; Jia, Y.; Schlom, D. G.; Wuttig, M.; Roytburd, A.; Ramesh, R. Multiferroic BaTiO₃-CoFe₂O₄ Nanostructures. *Science* **2004**, *303*, 661–663.

(43) Yuan, C.; Wu, H. B.; Xie, Y.; Lou, X. W. D. Mixed Transition-Metal Oxides: Design, Synthesis, and Energy-Related Applications. *Angew. Chem., Int. Ed.* **2014**, *53*, 1488–1504.

(44) Liu, H.-J.; Wang, C.-K.; Su, D.; Amrillah, T.; Hsieh, Y.-H.; Wu, K.-H.; Chen, Y.-C.; Juang, J.-Y.; Eng, L. M.; Jen, S.-U.; Chu, Y.-H. Flexible Heteroepitaxy of CoFe₂O₄ /Muscovite Bimorph with Large Magnetostriction. *ACS Appl. Mater. Interfaces* **2017**, *9*, 7297–7304.

(45) Oh, K. L.; Kwak, Y. M.; Kong, D. S.; Ryu, S.; Kim, H.; Jeon, H.; Choi, S.; Jung, J. H. Mechanical Stability of Ferrimagnetic CoFe₂O₄ Flexible Thin Films. *Curr. Appl. Phys.* **2021**, *31*, 87–92.

(46) Zhang, Y.; Shen, L.; Liu, M.; Li, X.; Lu, X.; Lu, L.; Ma, C.; You, C.; Chen, A.; Huang, C.; Chen, L.; Alexe, M.; Jia, C.-L. Flexible Quasi-Two-Dimensional CoFe₂O₄ Epitaxial Thin Films for Continuous Strain Tuning of Magnetic Properties. *ACS Nano* **2017**, *11*, 8002–8009.

(47) Coll, M.; Montero Moreno, J. M.; Gazquez, J.; Nielsch, K.; Obradors, X.; Puig, T. Low Temperature Stabilization of Nanoscale

Epitaxial Spinel Ferrite Thin Films by Atomic Layer Deposition. *Adv. Funct. Mater.* **2014**, *24*, 5368–5374.

(48) Peeters, D.; Sadlo, A.; Lowjaga, K.; Mendoza Reyes, O.; Wang, L.; Mai, L.; Gebhard, M.; Rogalla, D.; Becker, H.-W.; Giner, I.; Grundmeier, G.; Mitoraj, D.; Grafen, M.; Ostendorf, A.; Beranek, R.; Devi, A. Nanostructured Fe_2O_3 Processing via Water-Assisted ALD and Low-Temperature CVD from a Versatile Iron Ketoiminate Precursor. *Adv. Mater. Interfaces* **2017**, *4*, 1700155.

(49) Yu, P.; Beer, S. M. J.; Devi, A.; Coll, M. Fabrication of $\text{Gd}_x\text{Fe}_y\text{O}_z$ Films Using an Atomic Layer Deposition-Type Approach. *CrystEngComm* **2021**, *23*, 730–740.

(50) Chong, Y. T.; Yau, E. M. Y.; Nielsch, K.; Bachmann, J. Direct Atomic Layer Deposition of Ternary Ferrites with Various Magnetic Properties. *Chem. Mater.* **2010**, *22*, 6506–6508.

(51) Pham, C. D.; Chang, J.; Zurbuchen, M. A.; Chang, J. P. Magnetic Properties of CoFe_2O_4 Thin Films Synthesized by Radical-Enhanced Atomic Layer Deposition. *ACS Appl. Mater. Interfaces* **2017**, *9*, 36980–36988.

(52) Shen, L.; Wu, L.; Sheng, Q.; Ma, C.; Zhang, Y.; Lu, L.; Ma, J.; Ma, J.; Bian, J.; Yang, Y.; Chen, A.; Lu, X.; Liu, M.; Wang, H.; Jia, C.-L. Epitaxial Lift-Off of Centimeter-Scaled Spinel Ferrite Oxide Thin Films for Flexible Electronics. *Adv. Mater.* **2017**, *29*, 1702411.

(53) Del Toro, R. S.; Pinto-Castilla, S.; Cañizales, E.; Avila, E.; Díaz, Y.; Gutiérrez, B.; Sifontes, B. Synthesis of $\text{SrFe}(\text{Al})\text{O}_{3-d}-\text{SrAl}_2\text{O}_4$ Nanocomposites via Green Route. *Nano-Struct. Nano-Objects* **2020**, *22*, 100437.

(54) Al-Rawas, A.; Widatallah, H.; Al-Harhi, S.; Johnson, C.; Gismelseed, A.; Elzain, M.; Yousif, A. The Formation and Structure of Mechano-Synthesized Nanocrystalline $\text{Sr}_3\text{Fe}_2\text{O}_{6.4}$: XRD Rietveld, Mössbauer and XPS Analyses. *Mater. Res. Bull.* **2015**, *65*, 142–148.

(55) Vovk, G.; Chen, X.; Mims, C. A. In Situ XPS Studies of Perovskite Oxide Surfaces under Electrochemical Polarization. *J. Phys. Chem. B* **2005**, *109*, 2445–2454.

(56) Moulder, J.; Chastain, J. *Handbook of X-ray Photoelectron Spectroscopy: A Reference Book of Standard Spectra for Identification and Interpretation of XPS Data*; Physical Electronics Division, Perkin-Elmer Corp., 1992.

(57) Lie, M.; Barnholt Klepper, K.; Nilsen, O.; Fjellvåg, H.; Kjekshus, A. Growth of Iron Cobalt oxides by Atomic Layer Deposition. *Dalton Trans* **2008**, 253–259.

(58) Zhang, B.; Yun, C.; MacManus-Driscoll, J. L. High Yield Transfer of Clean Large-Area Epitaxial Oxide Thin Films. *Nano-Micro Lett.* **2021**, *13*, 39.

(59) Chen, X.-D.; Liu, Z.-B.; Zheng, C.-Y.; Xing, F.; Yan, X.-Q.; Chen, Y.; Tian, J.-G. High-Quality and Efficient Transfer of Large-Area Graphene Films onto Different Substrates. *Carbon* **2013**, *56*, 271–278.

(60) Eskandari, F.; Porter, S. B.; Venkatesan, M.; Kameli, P.; Rode, K.; Coey, J. M. D. Magnetization and Anisotropy of Cobalt Ferrite Thin Films. *Phys. Rev. Materials* **2017**, *1*, 074413.

(61) Bozorth, R. M.; Tilden, E. F.; Williams, A. J. Anisotropy and Magnetostriction of Some Ferrites. *Phys. Rev.* **1955**, *99*, 1788–1798.

(62) Fritsch, D.; Ederer, C. First-Principles Calculation of Magnetoelastic Coefficients and Magnetostriction in the Spinel Ferrites CoFe_2O_4 and NiFe_2O_4 . *Phys. Rev. B* **2012**, *86*, 014406.

(63) Hou, Y. H.; Zhao, Y. J.; Liu, Z. W.; Yu, H. Y.; Zhong, X. C.; Qiu, W. Q.; Zeng, D. C.; Wen, L. S. Structural, Electronic and Magnetic Properties of Partially Inverse Spinel CoFe_2O_4 : a First-Principles Study. *J. Phys. D: Appl. Phys.* **2010**, *43*, 445003.

(64) Yu, T.; Shen, Z. X.; Shi, Y.; Ding, J. Cation Migration and Magnetic Ordering in Spinel CoFe_2O_4 Powder: Micro-Raman Scattering Study. *J. Phys.: Condens. Matter* **2002**, *14*, L613–L618.

(65) Naveed-Ul-Haq, M.; Hussain, S.; Webers, S.; Salamon, S.; Ahmad, I.; Bibi, T.; Hameed, A.; Wende, H. On the Structure–Property Relationships of (Al, Ga, In)-doped Spinel Cobalt Ferrite Compounds: a Combined Experimental and DFT Study. *Phys. Chem. Chem. Phys.* **2021**, *23*, 18112–18124.

Supporting Information for

Bendable polycrystalline and magnetic

CoFe₂O₄ membranes by chemical methods

Pol Salles,[†] Roger Guzmán,[‡] David Zanders,[¶] Alberto Quintana,[†] Ignasi Fina,[†]
Florencio Sánchez,[†] Wu Zhou,[‡] Anjana Devi,[¶] and Mariona Coll^{*,†}

[†]*ICMAB-CSIC, Campus UAB 08193, Bellaterra, Barcelona, Spain*

[‡]*School of Physical Sciences and CAS Key Laboratory of Vacuum Physics, University of
Chinese Academy of Sciences, Beijing 100049, China*

[¶]*Inorganic Materials Chemistry, Ruhr University Bochum, Universitätsstraße 150,
Bochum 44801, Germany.*

E-mail: mcoll@icmab.es

Phone: +34 93 5801853

CFO on SAO//STO

Surface morphology and structure

CoFe_2O_4 (CFO) has a spinel ferrite structure AB_2O_4 (space group $Fd\bar{3}m$) with a lattice parameter of $a=8.39$ Å. SAO and STO are perovskites with $a=15.84$ Å and $a=3.91$ Å respectively. Therefore, epitaxial growth of CFO on these perovskites would imply a large-lattice mismatch of $\sim 6\text{-}7\%$, see **Figure S1**.

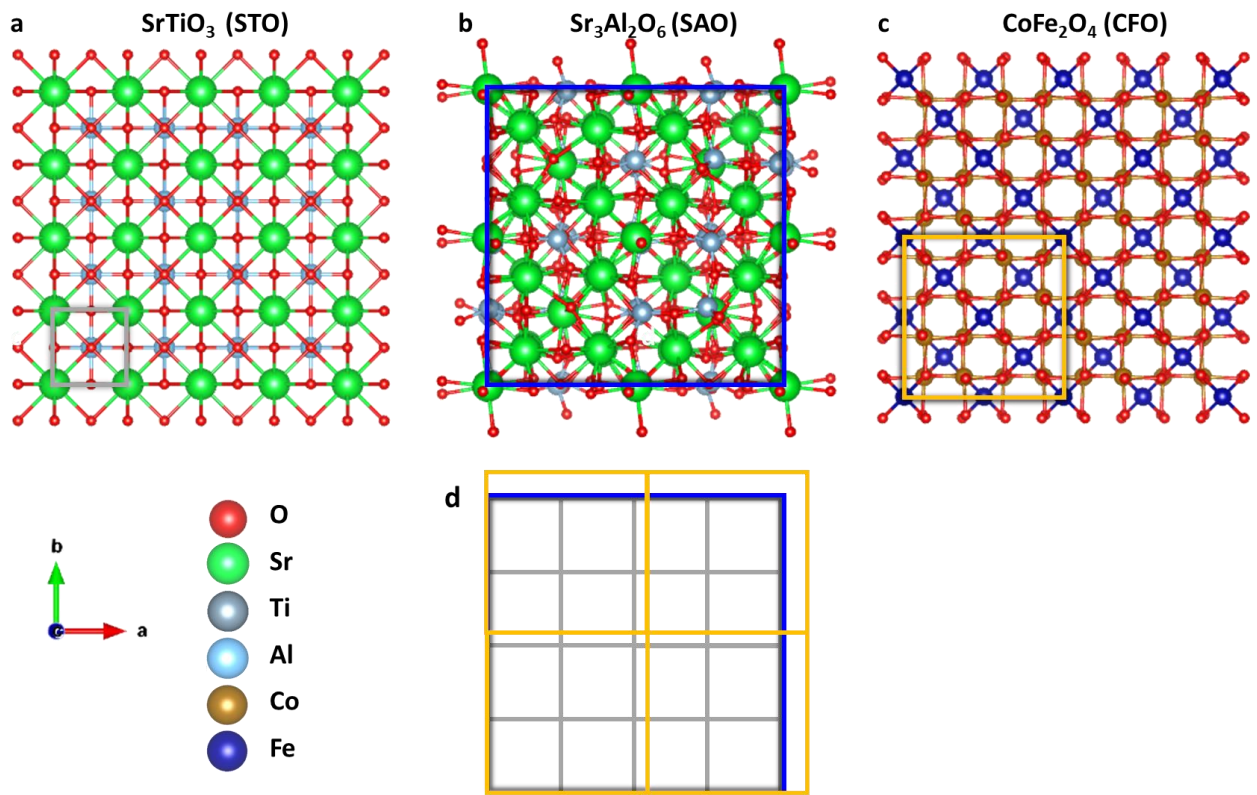


Figure S1: Atomic representation of (a) STO, (b) SAO and (c) CFO crystalline structures. (d) The cells are superposed to facilitate mismatch comparison.

The conformality of the CFO coatings made by Atomic Layer Deposition (ALD) can be confirmed with the surface morphology analyzed by Atomic Force Microscopy (AFM), see **Figure S2**. The monocrystalline (001) STO substrates are previously treated with HF and annealed at 950°C to achieve the terrace-like morphology (Figure S2a).^{1,2} When the SAO sacrificial layer is deposited by chemical solution deposition (CSD) a smooth surface is

achieved, but the terrace-like morphology of the STO is lost (Figure S2b). On the other hand, depositing the CFO films by ALD, because of the atomic precision of the technique and the surface reaction-based mechanism, the coating is completely conformal keeping the surface topography of the previous layer, even the terrace-like morphology of the STO substrate (Figure S2c).

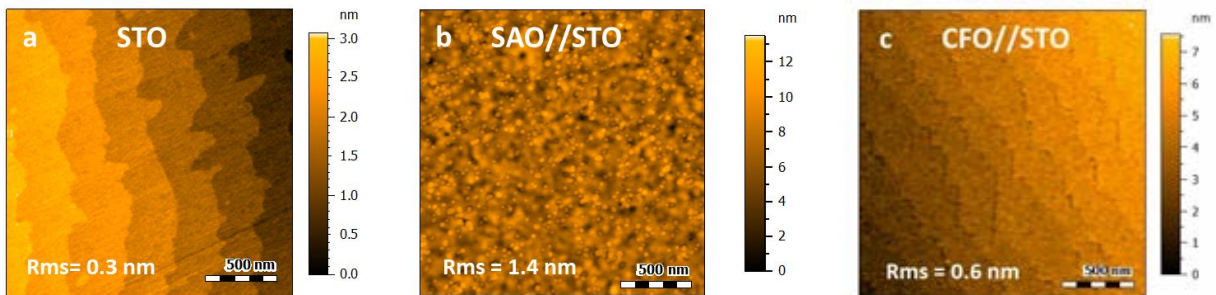


Figure S2: Surface morphology by AFM of (a) STO bare substrate, (b) SAO//STO and (c) CFO//STO.

The XRD analysis of the CFO film on SAO//STO and on bare STO show no secondary phases in the 2θ range of $20-80^\circ$, see **Figure S3**

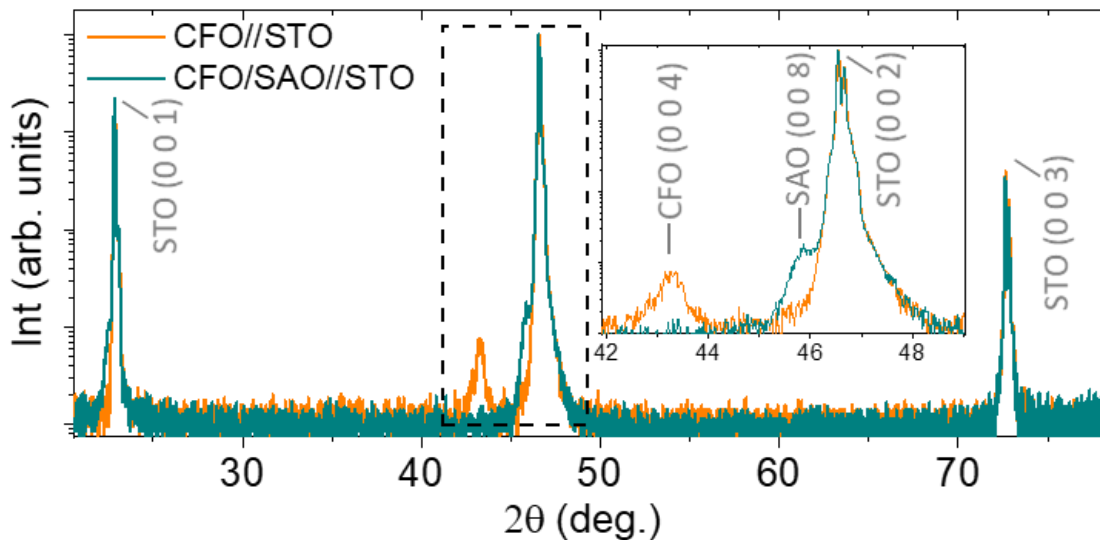


Figure S3: XRD θ - 2θ scan of the as deposited CFO thin film on SAO//STO compared to CFO grown directly on STO substrate. Inset corresponding to the θ - 2θ range of the (004) CFO, (008) SAO and (002) STO Bragg reflections.

Surface chemical composition

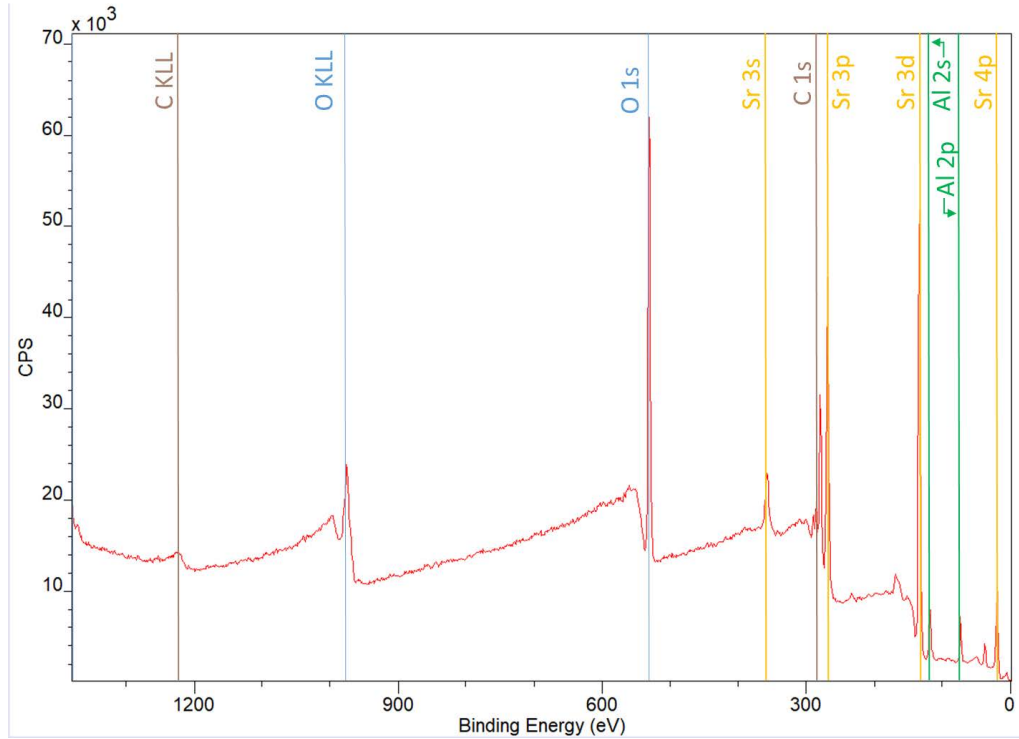


Figure S4: XPS overview analysis of SAO surface after air exposure

Post-annealing treatment on CFO/SAO//STO heterostructures

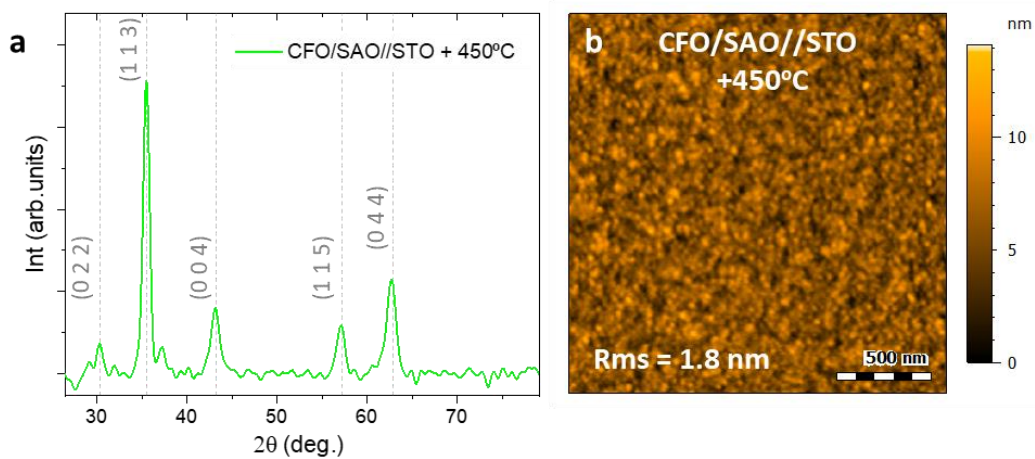


Figure S5: Effect of post-annealing treatment (1 h at 450°C) to CFO/SAO//STO heterostructures: (a) GIXRD 2θ scan, (b) AFM topographic image

CFO membranes

Surface chemical composition

As schematically shown in **Figure S6a**, the chemical composition of the CFO film at the CFO/SAO interface was studied after etching the SAO phase and transferring the CFO membrane to a PET support, thoroughly washed with DI water. In this way, the CFO membrane is turned upside down exposing the face previously in contact with SAO, which was characterized by X-Ray Photoelectron Spectroscopy (XPS) analysis. Note that XPS is a technique that allow to study the chemical composition of the very top surface of a material, with a depth profile lower than 10 nm. Therefore, analyzing the presence of Sr and Al would allow to determine if traces of SAO diffused into the first few nanometers of the CFO film. This characterization was done to two different CFO membranes to see the effect of the post-annealing treatment (as deposited *versus* 450°C post-annealing). Figure S6b shows the Sr3d spectra of the two samples, both with a peak at 134 eV confirming the presence of Sr in both of them, but with different intensities of the peak. The amount of Sr calculated in each case in percentage of the whole atomic contribution corresponds to 0.5 % for the as deposited and 1.5 % for the post-annealing. Figure S6c shows the Al2p spectra used to analyze the presence of Al in the CFO film. In this case both samples had similar peak intensities at 74 eV, corresponding to a 8 % of the atomic contribution. These results imply an accumulation of mainly Al at the CFO surface after SAO etching, which is independent of whether there was post-annealing or not. Sr, on the other side, tends to accumulate much less at the CFO film, and in this case it gets worsened by post-annealing the sample.

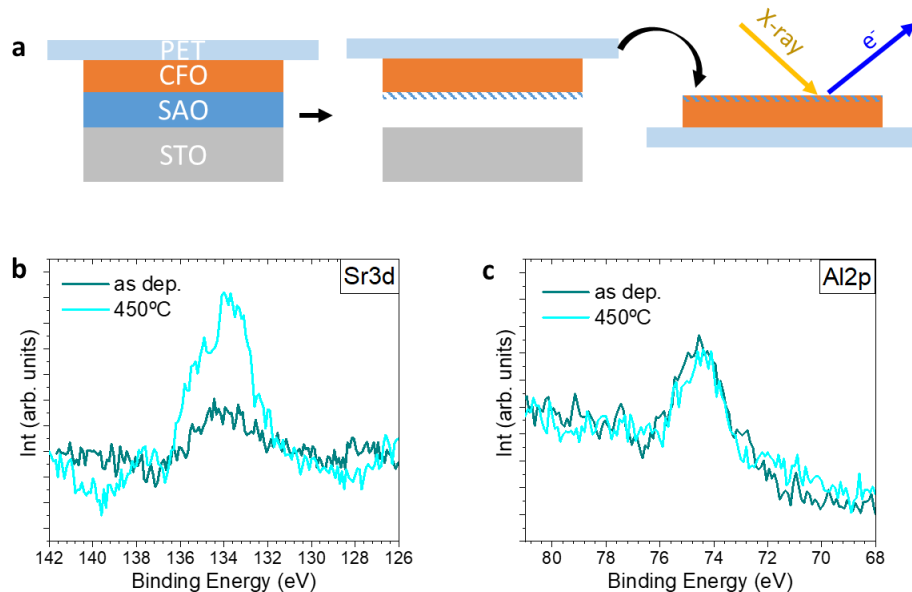


Figure S6: XPS analysis of the CFO surface after SAO etching. (a) Schematics of the process followed to study the CFO face that was initially in contact with SAO. (b) Sr3d core level spectra and (c) Al2p core level spectra of the CFO films as deposited and with a 450°C post-annealing in oxygen.

Double transfer CFO membranes

In the polymer support strategy, the transfer of CFO after SAO etching was done using a PET support. A PET support gives robustness and mechanical stability to the CFO membranes, while keeping flexibility and high optical transmittance to visible light.³ However it presents some limitations when it comes to a few characterization techniques. For example, GIXRD measurements on PET are not possible because the background signal of the PET support hides the relatively weak reflections of the thin CFO membranes. SEM analysis of CFO//PET is also compromised because of the charging of the insulating PET support. Therefore, for some specific characterization, subsequent transfer to another substrate was required.

The adhesion between the CFO membrane and the PET is based on dispersive adhesion with no involvement of a chemical reaction, therefore this attachment is reversible and allows to easily transfer the CFO membrane to other supports.³ **Figure S7** shows how CFO

membranes can be transferred twice, first to PET and then to another support, showing as examples a Si support with a SiO₂ layer on the top and a piece of Kapton tape. The smoothness of the CFO membrane (probed by AFM in Figure 6b, main manuscript), combined with the physical favorable interaction at the interface and some applied pressure, allow to successfully transfer most part of the CFO membrane to other supports. Schematics of the entire process from the initial CFO/SAO//STO heterostructure to the final CFO//Si or CFO//Kapton heterostructure are shown in Figure S7a. After transferring the CFO membrane to Si, it was characterized by SEM-EDX (Figure S7b,c). The membrane is dense and no cracks were identified in the area analyzed. From the EDX analysis, O, Si, Fe and Co were identified. Another example of a successful second transfer is Kapton tape. As shown in Figure S7d a 5 x 5 mm² CFO film can be entirely transferred from PET to Kapton.

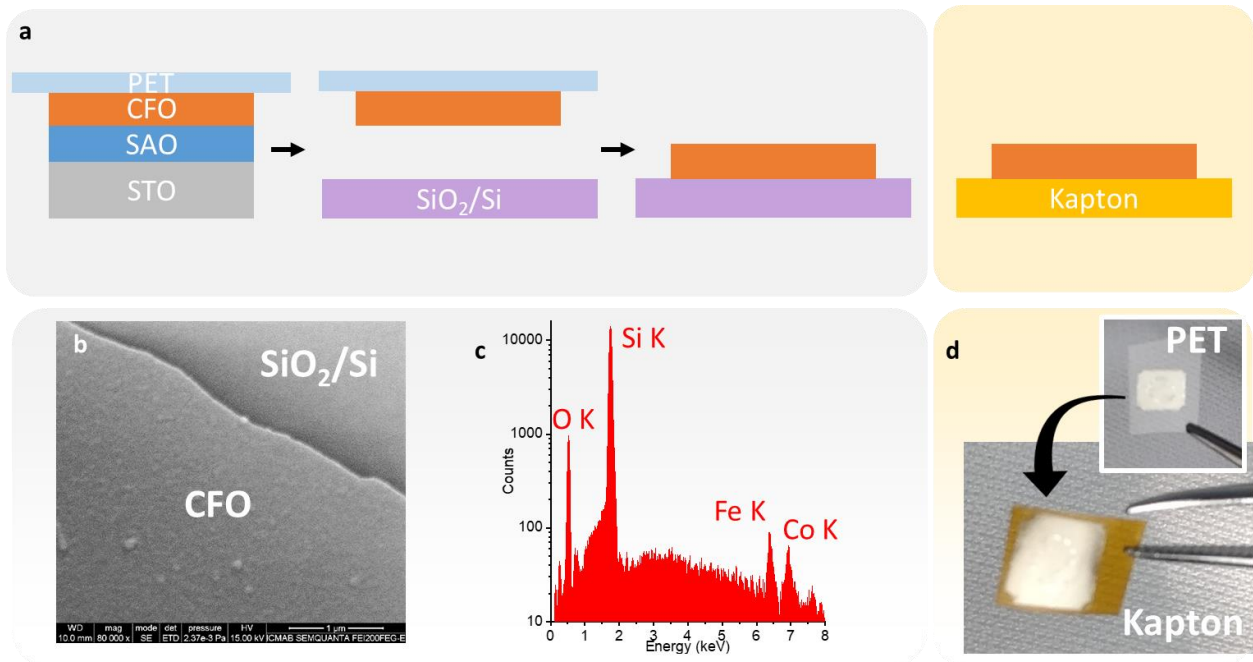


Figure S7: Second transfer of CFO membranes: (a) Scheme of the procedure to perform the second transfer of a CFO membrane from PET to either a SiO₂/Si or Kapton tape. The transferred CFO membrane to Si was analysed by (b) SEM and (c) EDX. (d) Picture of the CFO membrane entirely transferred to Kapton (5x5 mm²).

Microstructure of freestanding CFO membranes

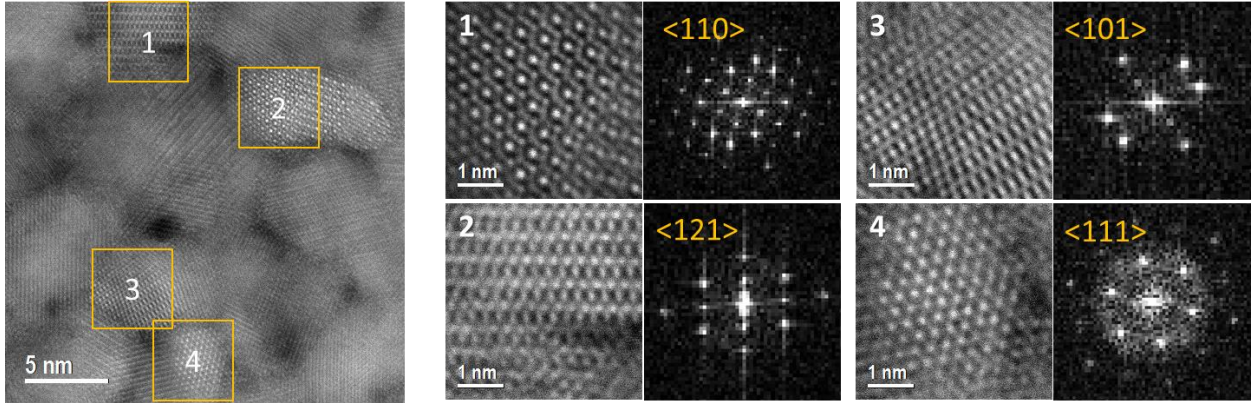


Figure S8: HR-TEM top-view analysis of a 14 nm freestanding CFO membrane. Identification of different crystallographic orientations of four grains with the corresponding fast fourier transform patterns.

CFO membranes with different thicknesses

Simultaneous ALD-CFO depositions on SAO//STO and on bare STO, allowed to use samples on STO as reference for thickness measurements. X-ray reflectivity (XRR) measurements were carried out on all the samples to confirm their thickness. **Figure S9a** shows the XRR spectra of the CFO//STO samples with 10, 30 and 60 nm thin, analogous to the CFO membranes analyzed in Figure 7 main manuscript. Kiessig fringes, used for thickness determination from XRR measurements, are well-defined and more easily analyzed for very low roughness thin films allowing to confirm the expected thickness according to the ALD cycles performed.

Figure S9b-d shows optical microscopy images of the transferred CFO membranes on PET for different CFO thicknesses. In all three cases, ripples along all the surface are observed. The size of these ripples appear to be directly related to the thickness of the membrane, as proportionally schematized under the optical microscope images. The appearance of these features could be related to a relaxation of the film after substrate declamping.^{4, 5}

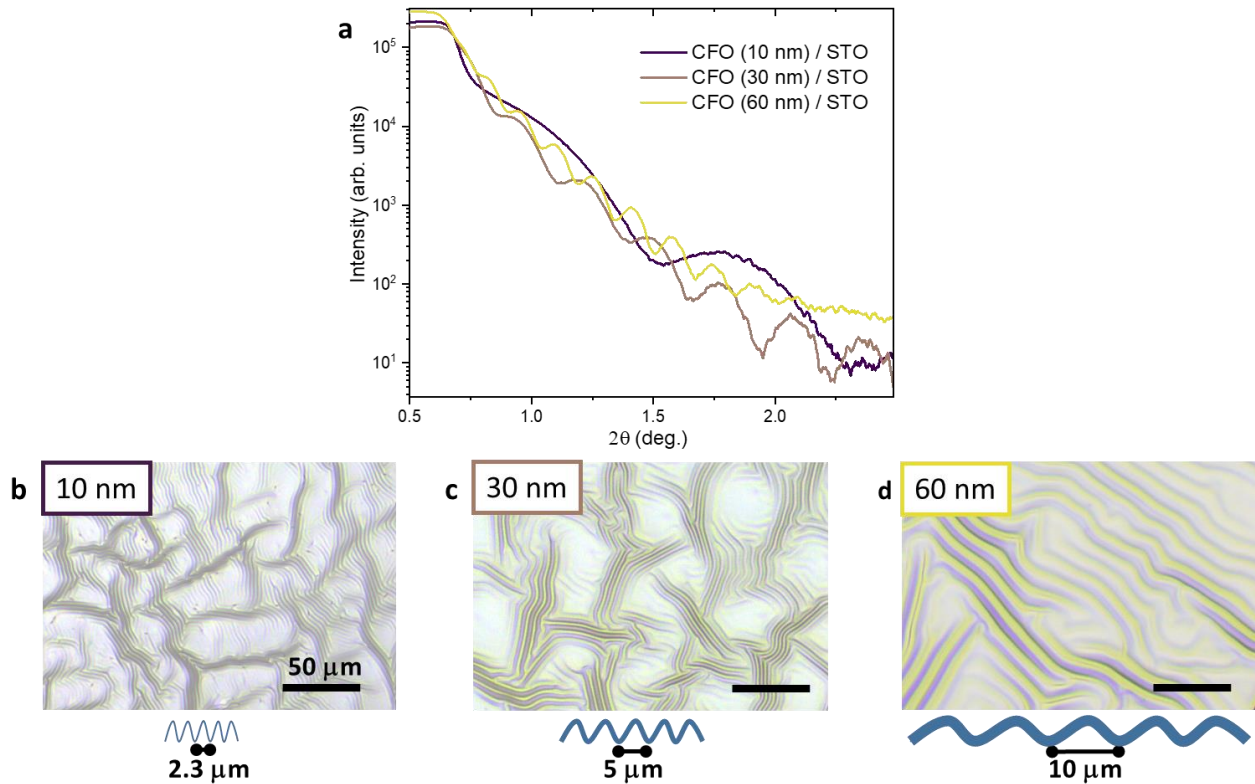


Figure S9: CFO membranes of different thicknesses. (a) XRR measurements for thickness determination of CFO film grown on STO. (b-d) Optical microscopy images of rippled CFO membranes of different thickness on PET polymer, scale bar of $50 \mu\text{m}$. Schematic proportional representation of the ripples are made for comparison.

References

- (1) Salles, P.; Caño, I.; Guzman, R.; Dore, C.; Mihi, A.; Zhou, W.; Coll, M. Facile Chemical Route to Prepare Water Soluble Epitaxial $\text{Sr}_3\text{Al}_2\text{O}_6$ Sacrificial Layers for Free-Standing Oxides. *Adv. Mater. Interfaces*, **2021**, *8*, 2001643.
- (2) Koster, G.; Kropman, B. L.; Rijnders, G. J. H. M.; Blank, D. H. A.; Rogalla, H. Quasi-ideal Strontium Titanate Crystal Surfaces Through Formation of Strontium Hydroxide. *Appl. Phys. Lett.*, **1998**, *73*, 2920–2922.
- (3) Chen, X.-D.; Liu, Z.-B.; Zheng, C.-Y.; Xing, F.; Yan, X.-Q.; Chen, Y.; Tian, J.-G. High-quality and Efficient Transfer of Large-Area Graphene Films Onto Different Substrates.

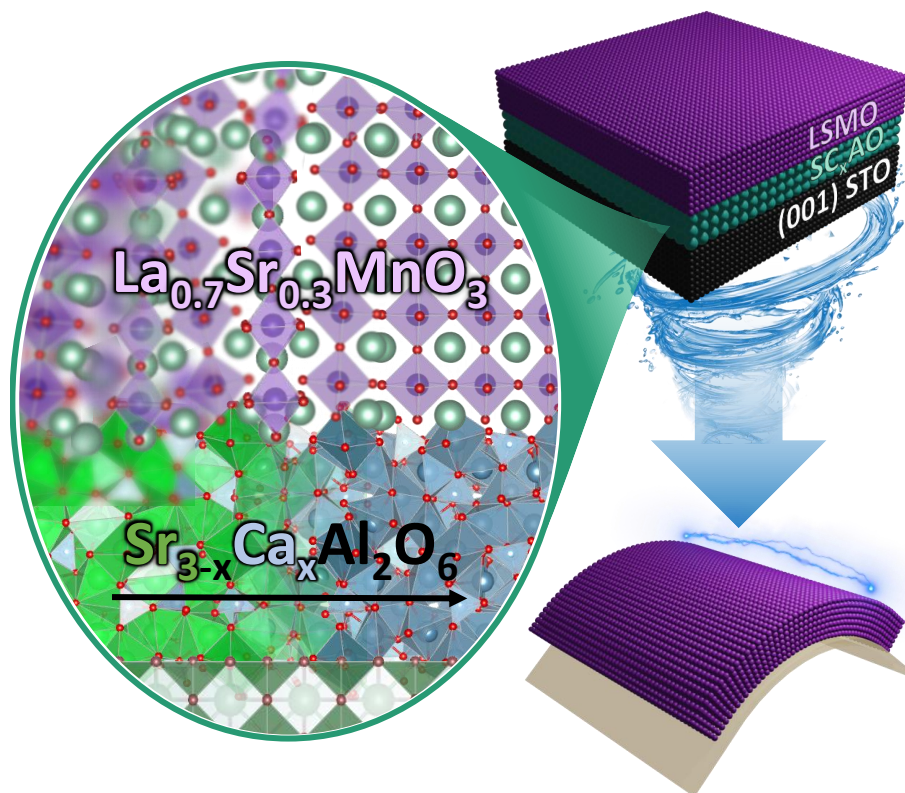
Carbon **2013**, *56*, 271–278.

(4) Cendula, P.; Kiravittaya, S.; Mei, Y. F.; Deneke, C.; Schmidt, O. G. Bending and Wrinkling as Competing Relaxation Pathways for Strained Free-Hanging Films. *Phys. Rev. B* **2009**, *79*, 085429.

(5) Melzer, M.; Lin, G.; Makarov, D.; Schmidt, O. G. Stretchable Spin Valves on Elastomer Membranes by Predetermined Periodic Fracture and Random Wrinkling. *Adv. Mater.*, **2012**, *24*, 6468–6472.

Chapter 5

On the role of the $\text{Sr}_{3-x}\text{Ca}_x\text{Al}_2\text{O}_6$ sacrificial layer composition for epitaxial $\text{La}_{0.7}\text{Sr}_{0.3}\text{MnO}_3$ membranes



Abstract

The possibility to fabricate freestanding single crystal complex oxide films has raised enormous interest to be integrated in next-generation electronic devices envisaging distinct and novel properties that can deliver unprecedented performance improvement compared to traditional semiconductors. This step demands for ease material heterointegration in mature semiconductor device technology. The use of the sacrificial layer approach to detach the complex oxide film from the growth substrate, and in particular water-soluble $\text{Sr}_3\text{Al}_2\text{O}_6$ (SAO) sacrificial, has significantly expanded the complex oxide perovskite membranes library. Nonetheless, the extreme water sensitivity of SAO hinders its manipulation in ambient conditions and restricts the deposition approaches to those using high vacuum. Here it is presented a pioneering study on the role of Ca-substitution in solution processed SAO ($\text{Sr}_{3-x}\text{Ca}_x\text{Al}_2\text{O}_6$ with $x \leq 3$) identifying a noticeable improvement on film crystallinity preserving a smooth surface morphology while favoring the manipulation in a less-restricted ambient conditions. Then, the study focuses on the effect of the sacrificial composition on the subsequent ex-situ deposition of $\text{La}_{0.7}\text{Sr}_{0.3}\text{MnO}_3$ (LSMO) by pulsed laser deposition to obtain epitaxial films with slightly different degree of strain. Finally, epitaxial and strain-free LSMO membranes with metal-insulator transition at 290 K are delivered. This work offers an hybrid and versatile approach to prepare and easily manipulate crystalline perovskite oxide membranes to design new artificial heterostructures that can be of use to study novel physical phenomena at the nanoscale for high-performance oxide electronic devices.

5.1 Introduction

Next generation electronic devices are facing a rapidly advancing technological development to respond the evolving needs of today's society and its future expected challenges. Within these technological advances, novel and multifunctional device concepts are starting to attract interest.^{1,166,167} Complex transition-metal oxides, in particular ABO_3 perovskite oxides, are a promising family of materials that offer a wide range of properties including ferroelectricity,³

multiferroicity,¹⁰³ metal-insulator transitions,¹⁶⁸ magnetism, and superconductivity,² to name a few.¹⁶⁹ These properties are affected by the oxide structure, crystalline quality and presence of defects requiring the growth of such materials to be precise, constrained on specific crystalline substrates and to be processed at high temperature^{170–173} which limit significantly their unprecedented opportunities. Nonetheless, in the last few years this field is experiencing a major turn boosted by the development of synthetic approaches to detach these epitaxial oxides from the growth substrate and freely manipulate them.^{38,174} In fact, the fabrication of new artificial heterostructures by assembling very dissimilar materials, their integration in conventional materials such as silicon, plastics and 2D semiconductors,^{28,31,175} and the possibility to obtain spontaneous shaped structures¹⁷⁶ is becoming a reality opening the possibility to study novel interface phenomena, nanoengineer their properties and unlock strain states that might not be available by traditional epitaxial growth.^{22,27,177}

The use of a sacrificial layer is an appealing approach to fabricate and manipulate freestanding epitaxial complex oxides membranes.⁵⁸ This method consists of adding a buffer layer between the substrate and the complex oxide that ensures epitaxial growth and the subsequent detachment upon selective etching. Recently, Sr₃Al₂O₆ (SAO) has been proved successful to be used as water-soluble sacrificial layer.^{81,84,178} SAO has a pseudoperovskite structure (Pa-3) with a cubic unit cell ($a = 15.844 \text{ \AA}$; $a/4 = 3.961 \text{ \AA}$)⁷⁸ which is close to 4 times the lattice constant of SrTiO₃ (STO, $a = 3.905 \text{ \AA}$), a typical monocrystalline substrate used for the growth of different perovskite oxides.¹⁷⁹ The SAO structure consists of discrete Al-O networks based on rings of six AlO₄ tetrahedra (Al₆O₁₈¹⁸⁻) with two nonbridging oxygens bonds with Sr²⁺ ions. Because Al³⁺ is more electronegative than Sr²⁺, Sr-O bonding has a more ionic character than Al-O. When exposed to water, the easy protonation of this Sr-O ionic bonding is the responsible of the fast hydrolysis of the structure, which makes SAO a suitable sacrificial layer to be etched with water.^{79,80} However, despite these wealthy properties, SAO still presents some challenges that need to be overcome to exploit its full potential.

First, while its high reactivity with water makes it almost the perfect candidate for selective

etching against many perovskite oxides,⁵⁸ it also helps the fast development of an amorphous capping layer when exposed to air.¹⁸⁰ This reactivity hinders the subsequent epitaxial growth of the perovskite oxide. The use of a protective SrTiO₃ layer¹⁸¹ can partially help fixing the sacrificial instability issue, although it brings some limitations to prepare stacked membrane heterostructures with pristine interfaces.²⁰ Also, the softness of the SAO structure can give rise to cation interdiffusion at the interface during the high temperature growth of the complex oxide, as it was reported for the La_{0.7}Sr_{0.3}MnO₃/SAO system,⁴⁸ which can hinder the membrane exfoliation and alters its functional properties. Finally, the growth of complex oxides on mismatched SAO can produce cracked and wrinkled membranes upon exfoliation as a mechanism for strain release.²² It is worth noting that the detachment of a faultless membrane, regardless of the nature of the sacrificial layer, remains a key challenge in the preparation of freestanding films.^{70,76}

A simple way to modify the properties of SAO is to engineer the metal-oxygen bond through cation substitution. The lower the M²⁺ electronegativity (Ba²⁺ < Sr²⁺ < Ca²⁺), the higher its bonding ionicity with the nonbridging oxygens of the structure and thus it is easier to hydrolyse. Consequently, Ba₃Al₂O₆ is dissolved much faster in water than Ca₃Al₂O₆.⁷⁵ Additionally, the difference in cation size (Ba²⁺ > Sr²⁺ > Ca²⁺) enables tuning the SAO lattice parameter ranging from $a/4 = 4.125 \text{ \AA}$ for Ba₃Al₂O₆ to $a/4 = 3.816 \text{ \AA}$ for Ca₃Al₂O₆⁸⁰ providing a platform of sacrificial layers that can accommodate many different perovskite oxides with different strain states being a powerful tool to modulate the physical properties of the epitaxial oxide membrane.^{22,66,68,75}

La_{0.7}Sr_{0.3}MnO₃ (LSMO) is an attractive perovskite oxide with extraordinary electrical and magnetic properties making the material an appealing candidate for spintronics and memory devices.^{168,182–184} The growth of high quality LSMO membranes is also of crucial importance where slight variation in strain,^{185–187} crystal orientation,¹⁸⁸ oxygen stoichiometry^{189,190} and Sr doping¹⁹¹ can significantly affect its properties. The preparation of flexible and epitaxial LSMO has already been attempted by high-vacuum deposition processes using mica substrates^{192,193} and sacrificial layers such as YBa₂Cu₃O₇¹⁹⁴ and SAO.^{48,67,81,85,195} Here we go one step further

developing an hybrid and versatile synthetic approach for LSMO membranes, based on solution-processed $\text{Sr}_{3-x}\text{Ca}_x\text{Al}_2\text{O}_6$ with $x \leq 3$ (SC_xAO) sacrificial layers in which ambient stability and crystallinity is dramatically improved upon Ca-substitution with preserved smooth surface morphology demonstrated by means of reflection high energy electron diffraction (RHEED), scanning transmission electron microscopy (STEM), x-ray diffraction (XRD) and atomic force microscopy (AFM). Then it is discussed how SC_xAO composition affects the ex-situ deposition of pulsed laser deposited (PLD) LSMO films on their crystallinity, strain, interface cation diffusion and electrical properties. Finally, it is presented the properties of the exfoliated LSMO membranes demonstrating the feasibility to integrate high quality epitaxial LSMO-PLD flakes on arbitrary substrates with a metal-insulator transition as high as 290 K.

5.2 Results and Discussion

5.2.1 Structural analysis

Figure 5.1(a-d) shows the schematic process that has been followed for the fabrication of epitaxial LSMO membranes. First, the $\text{Sr}_{3-x}\text{Ca}_x\text{Al}_2\text{O}_6$ (SC_xAO , $x \leq 3$) sacrificial layer is deposited and grown on a (001) SrTiO_3 (STO) substrate by solution processing (CSD), Figure 5.1a (Details on the synthesis process can be found in Chapter 2). Then, the film is brought into a PLD chamber where an in-vacuum high-temperature re-crystallization process is performed, Figure 5.1b, followed by the LSMO-PLD deposit, Figure 5.1c. Finally, the sacrificial layer is water-etched to obtain millimeter sized LSMO membranes supported on a polyethylene terephthalate (PET) sheet, Figure 5.1d. These membranes can be subsequently transferred to other substrates such as glass and silicon (See Experimental Section for further details).

The surface crystallinity of the films at each stage of the growth process has been monitored by RHEED. Figure 5.1(e-g) shows the evolution of the surface crystallinity for the system with SAO sacrificial layer. The SAO film as-grown at 800°C and exposed to air shows no spots indicating an amorphous surface. The film after vacuum thermal annealing at 825°C results

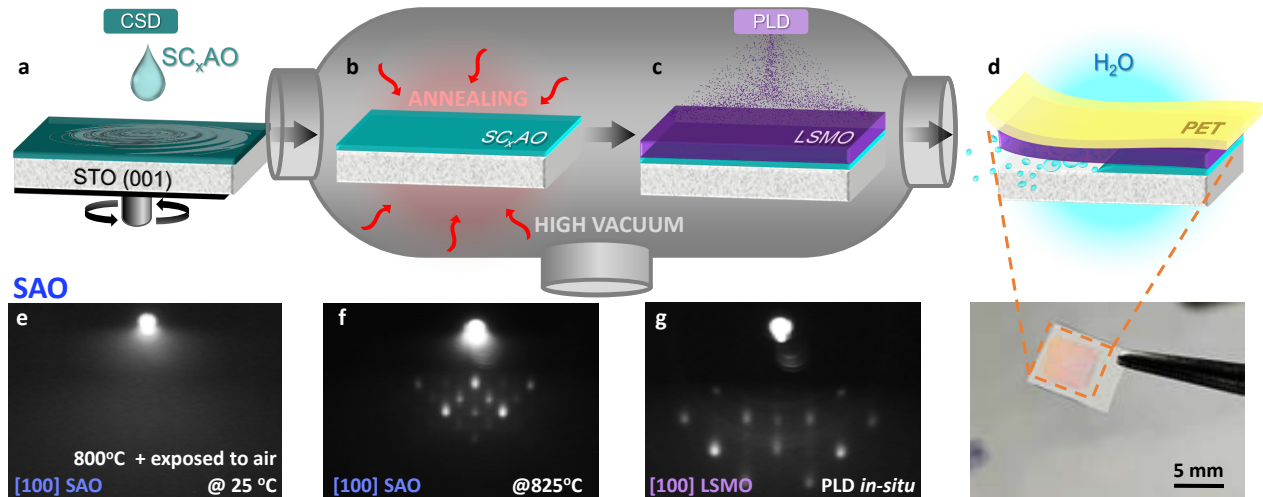


Figure 5.1: (a-d) Sketch of the process followed to fabricate LSMO membranes: (a) SC_xAO is grown by CSD on a (001) STO substrate at 800 °C and exposed to air. Then, it is brought to the PLD chamber where (b) an annealing treatment up to 825 °C is performed to achieve re-crystallization of the SC_xAO surface and (c) LSMO is grown by PLD. (d) Finally, the LSMO film can be attached on a polymer support and separated from its original substrate by etching the SC_xAO sacrificial layer in water. Image of a $5 \times 5 \text{ mm}^2$ LSMO membrane on a PET support after etching the sacrificial layer. (e-g) In-situ RHEED analysis of (e) SAO after air exposure, (f) SAO after vacuum annealing and (g) LSMO deposited by PLD.

in a spotty pattern revealing that the surface recrystallizes, as previously reported.¹⁸⁰ Then, the LSMO film is deposited by PLD on the reconstructed SAO obtaining a new spotty pattern that discloses the formation of an oriented LSMO film, Figure 5.1g.

The same process has been followed to study the behavior of the SC_xAO series with $x \leq 3$ and the subsequent growth of the LSMO. From the acquired RHEED patterns (**Figure 5.2**) it is observed that crystalline films are obtained for all sacrificial layer composition after the vacuum annealing and the crystallinity is transferred to the LSMO films. The periodicity and intensity of the spots identified in the sacrificial layer pattern moderately change as Ca is incorporated in SC_xAO , anticipating changes in the crystallinity and lattice parameter. Slight differences are also appreciated in the shape of the diffraction spots of the LSMO films which could be attributed to a change in the surface morphology.¹⁹⁶ From the AFM topographic images it is observed that, prior to the LSMO depositions, all SC_xAO films are dense, smooth and homogeneous with a root-mean-square (rms) roughness of $\sim 1 \text{ nm}$ (**Figure S1(a-d)**, Supporting Information). After the LSMO deposition, Figure S1(e-h), the films are homogeneous with smooth surfaces of rms $\sim 2 \text{ nm}$ and the size of the grains moderately increases for the LSMO

grown on CAO, which is in agreement with the shape of the RHEED pattern.

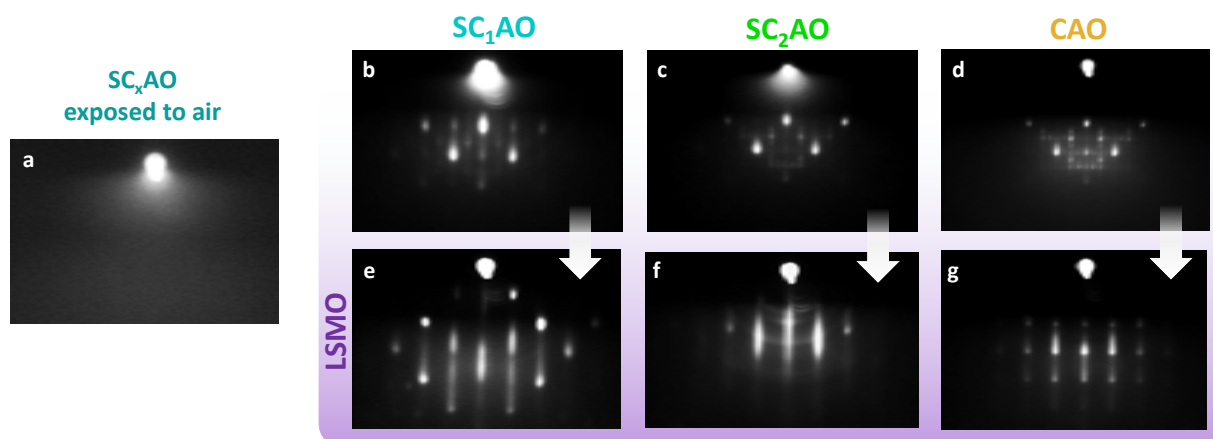


Figure 5.2: RHEED analysis along the [100] STO of the different SC_xAO sacrificial layers (a) after air exposure, (b-d) after vacuum annealing and (e-g) LSMO deposited by PLD.

A separate study was performed to investigate the influence of Ca substitution on the SC_xAO ambient stability. As a case example it is discussed the evolution for SC_2AO composition (see **Figure S2**). The as-prepared SC_2AO films after being annealed in vacuum were exposed to air and sealed in plastic bags. RHEED analysis were performed every 7, 16 and 30 days and the samples were stored in a sealed plastic bag between experiments. Using this procedure, the surface quality of the samples containing Ca was preserved up to 16 days, Figure S2a. Longer storage time (i.e. 30 days) results in sample degradation as the spots in the RHEED pattern are significantly less intense and the surface morphology roughens dramatically. Remarkably, epitaxial LSMO films are obtained on the SC_2AO sacrificial layers after being stored 16 days in sealed plastic bags (Figure S2b). Note that by investigating the RHEED pattern of the whole series of vacuum-annealed SC_xAO films after 7 days it is found a clear trend in surface crystallinity. The higher the Ca concentration, the more intense the RHEED spots and therefore, more stable (Figure S2c), in agreement with the expected water sensitivity according to the Ca doping.^{75,80} This study opens the possibility to work in a less-strict environment for the sacrificial layers and combine ex-situ and in-situ deposition techniques.

Further structural analysis to study the influence of the sacrificial layer composition on the film crystallinity and subsequent growth of LSMO, was carried out by X-ray diffraction analysis

(XRD). **Figure 5.3a** shows the XRD θ - 2θ analysis for the four SC_xAO systems comparing the bare STO contribution, the $\text{SC}_x\text{AO}/\text{STO}$ and the $\text{LSMO}/\text{SC}_x\text{AO}/\text{STO}$. The most intense peak at $2\theta = 46.5^\circ$ corresponds to the (002) STO Bragg reflection and the shoulders appearing next to the STO after growing the different layers can be identified as (008) SC_xAO and (002) LSMO, indicated with ∇ and $*$, respectively, in Figure 5.3a. Focusing on the $\text{SC}_x\text{AO}/\text{STO}$ system, it is observed that by increasing the Ca concentration, the 2θ values of the (008) SC_xAO reflection shifts to higher angles. The shifts in 2θ agree with a change in the $c_{\text{SC}_x\text{AO}}$ lattice parameter from $c_{\text{SAO}}/4 = 3.96 \text{ \AA}$ ($x = 0$) to $c_{\text{CAO}}/4 = 3.81 \text{ \AA}$ ($x = 3$).

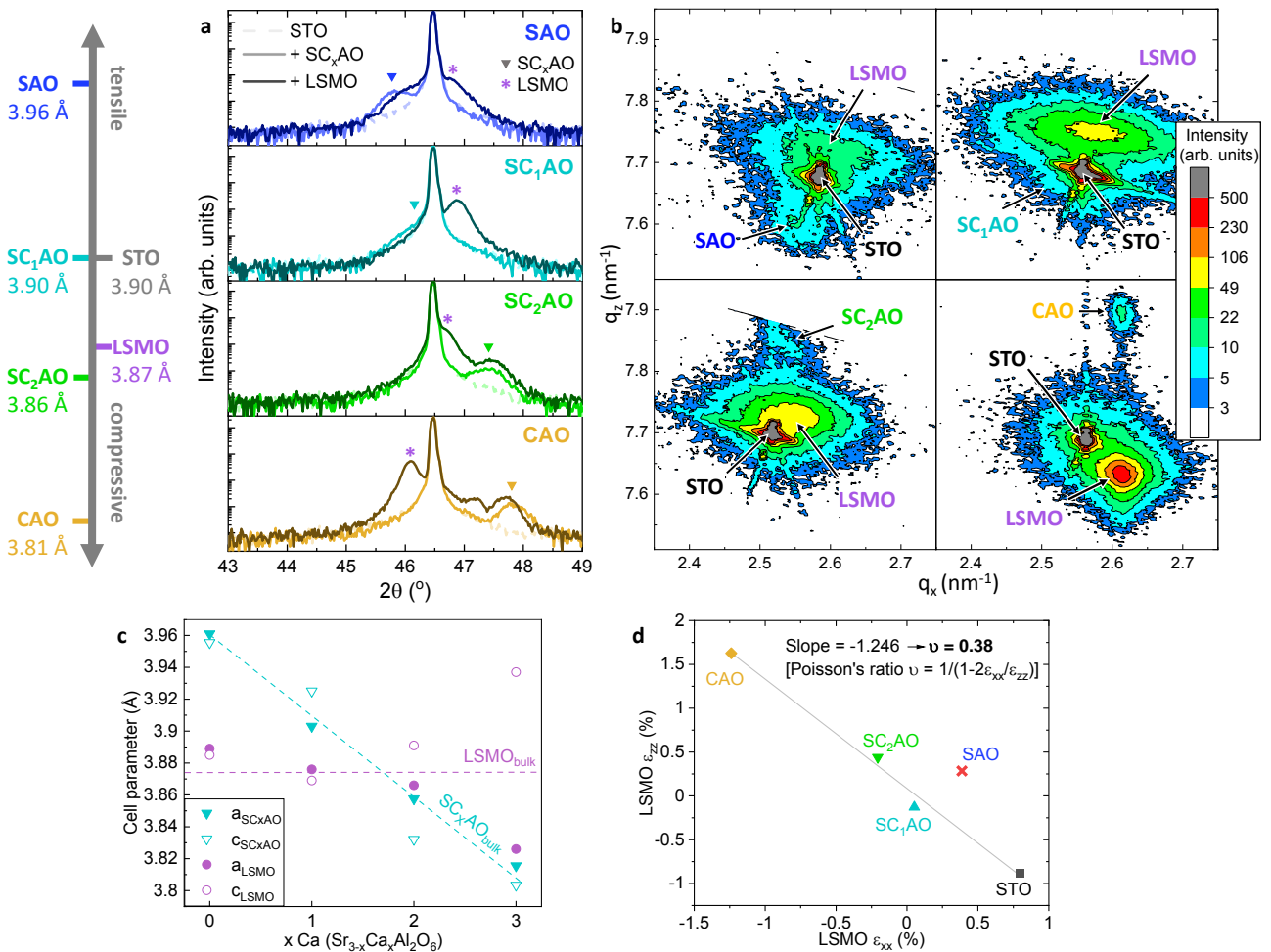


Figure 5.3: (a) XRD θ - 2θ scans for the LSMO/SC_xAO/STO heterostructures at each step of the process. ∇ indicates the (008) SC_xAO diffraction peak and $*$ indicates the main (002) LSMO diffraction peak in each case. (b) Reciprocal space map around (103) STO reflection for the different LSMO/SC_xAO/STO heterostructures. (103) LSMO and (4 0 12) SC_xAO reflections, indicated in each case, have been used to extract (c) the lattice parameters of the SC_xAO and LSMO films. (d) Strain in-plane ϵ_{xx} vs. strain out-of-plane ϵ_{zz} plot for Poisson's ratio calculation of LSMO films.

After the deposition of the LSMO layer on the in-situ vacuum annealed $\text{SC}_x\text{AO//STO}$, the (002) LSMO Bragg reflection is observed for all the samples indicating that c-axis oriented growth has been achieved regardless of the Ca composition in the sacrificial, in well agreement with the spotty-streaky RHEED patterns shown in Figure 5.2(e-g). It is noted that the intensity of the (002) LSMO Bragg reflection in the SAO system is slightly lower than the rest. Also, the (008) SAO Bragg reflection for the same system shows a moderate shift towards higher 2θ values. This could indicate that reactivity at the LSMO/SAO occurred which is in agreement with previous studies on all-vacuum deposited LSMO/SAO system.⁴⁸ Also, the heterostructure LSMO/CAO//STO shows an additional peak that appears at $2\theta = 47.2^\circ$ which might be attributed to the formation of a thin layer of a mixed perovskite La-Sr-Mn-Ca-Al-O at the interface.¹⁹⁷ Texture analysis of the LSMO films reveals an improvement of crystalline quality when deposited on Ca-doped SAO (Table S1 and **Figure S3a**) and no further secondary phases are observed in extended XRD θ - 2θ scans (Figure S3b). Remarkably, the 2θ position of the (002) LSMO reflection shifts as a function of the SC_xAO composition suggesting a variation in the LSMO lattice parameter. In order to shed light on these 2θ shifts and the ones observed for the (008) SC_xAO Bragg reflections, high-resolution XRD reciprocal space maps (RSM) have been carried out, see Figure 5.3b. The most intense peak corresponds to the (103) STO Bragg reflection whereas less intense and defined peaks appear for (103) LSMO and (4 0 12) SC_xAO . It is noted that the higher the Ca concentration in the sacrificial layer, the more resolved the (4 0 12) SC_xAO and (103) LSMO reflections, strengthening the results of the texture analysis that already indicated an increase in crystalline quality. From the RSM it has been extracted the in-plane (a_{LSMO} and $a_{\text{SC}_x\text{AO}}$) and out-of-plane (c_{LSMO} and $c_{\text{SC}_x\text{AO}}$) lattice parameters and compared to the respective bulk values, shown in Figure 5.3c. For the SC_xAO films (cyan symbols) both a and c lattice parameters decrease by increasing the Ca concentration consistent with the change observed from Figure 5.3a and in well agreement with Vegard's Law.¹⁹⁸ On the other hand, the lattice parameters of LSMO films (purple symbols) follow a different trend. The lattice parameters of LSMO on SAO and SC_1AO are close to those of the LSMO bulk whereas those of LSMO on SC_2AO and CAO, diverge. Figure 5.3d depicts the experimental

in-plane and out-of-plane strain measured from the LSMO films on the different SC_xAO . The perpendicular strains (ϵ_{xx} , ϵ_{zz}) from LSMO grown on SC_xAO with $x=1-3$ and from LSMO on STO, follow a linear dependence according to the Poisson effect. This linear trend permits to extract the corresponding Poisson's ratio, $\nu=0.38$, consistent with the values reported for other strained LSMO films.¹⁸⁶ Note that the LSMO grown on SAO does not follow the same strain tendency (Figure 5.3c). In order to gain insights into this discrepancy and elucidate the possible cation interdiffusion identified from the XRD θ - 2θ analysis, cross-sectional Z-contrast high angle annular dark field (HAADF) using scanning transmission electron microscopy (STEM) was carried out for the systems grown on the two extreme compositions: SAO and CAO, **Figure 5.4**.

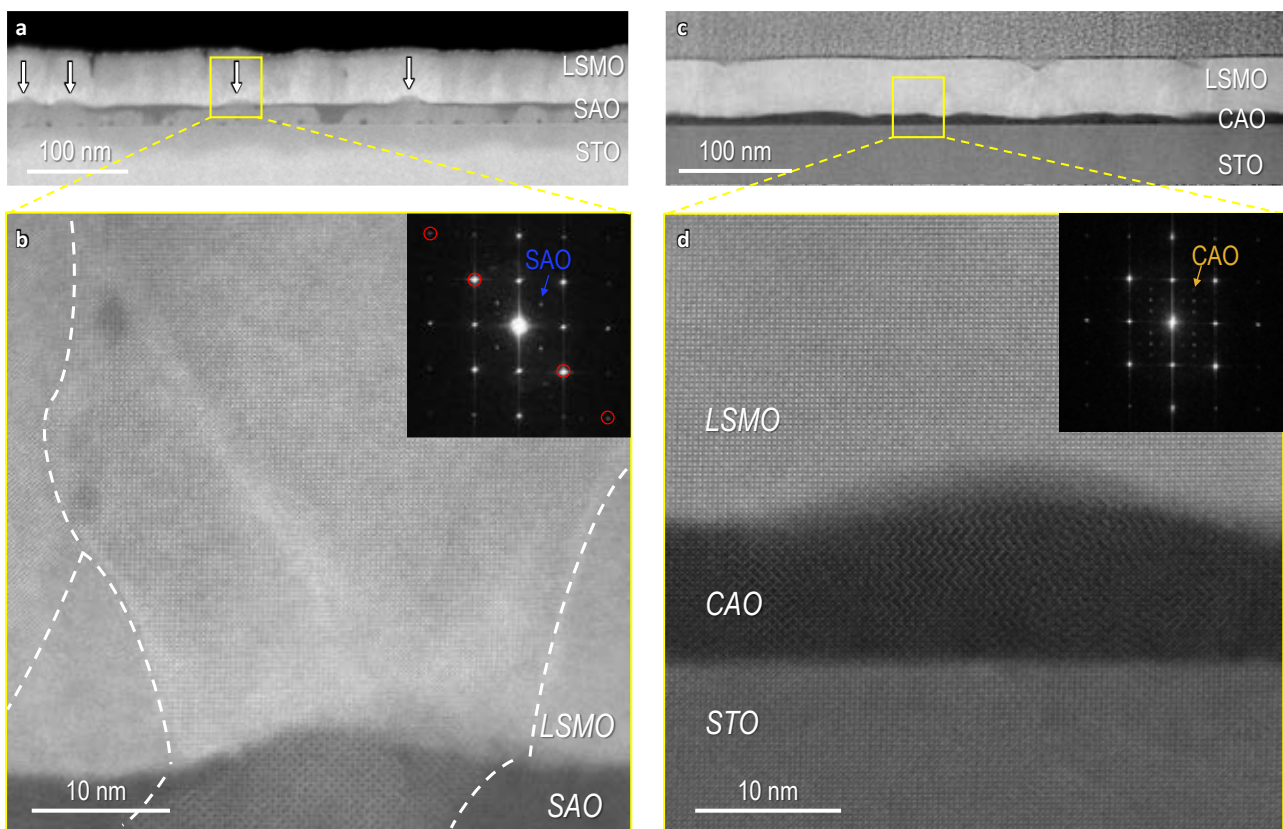


Figure 5.4: Z-contrast HAADF-STEM cross-sections. (a) LSMO/SAO//STO low magnification image. White arrows are used to indicate the formation of outcrops. (b) Higher magnification image of one of the outcrops with its corresponding FFT as inset. The LSMO grain boundaries with misoriented grains are marked and their corresponding FFT spots highlighted. (c) LSMO/CAO//STO low magnification image. (d) Higher magnification image with its corresponding FFT as inset.

First, it is investigated the LSMO/SAO//STO heterostructure, Figure 5.4a. The low magnification HAADF-STEM image allows identifying the LSMO and SAO layers on STO. The 60 nm LSMO film shows columnar grains, typical of the PLD growth.¹⁹⁹ The SAO film has a thickness of 20 nm with a rough interface with LSMO. It can be identified areas with dark contrast which corresponds to amorphous SAO and areas with outcrops (white arrows). Regarding the existence of amorphous SAO regions, it reveals that the post-annealing in vacuum performed on SAO films¹⁸⁰ prior to LSMO deposition does not completely reconstruct the surface crystallinity although the spotty RHEED pattern showed in Figure 5.3f. A closer look at one of these outcrops, Figure 5.4b, shows the atomic ordering of SAO and LSMO, confirming that it corresponds to epitaxial (001) SAO and it acts as nucleation site for epitaxial (001) LSMO. From the same magnification image it is also detected the formation of an antiphase boundary (APB) in the center of the (001) LSMO and few (101) oriented LSMO grains whose grain boundaries are identified by dashed white lines. This is further confirmed by fast fourier transform (FFT), red-marked in the inset image in Figure 5.4a. The nucleation of (101) LSMO grains could be favored by the rough and not completely (001) epitaxial SAO surface. Electron energy loss spectroscopy (EELS) analysis carried out in this region, Figure S4, indicates that there is also slight cation interdiffusion between LSMO and SAO, as anticipated from XRD. It is very likely that these two factors, misoriented LSMO grains and cation diffusion at the interface, favor the growth of an strain-free LSMO film with lower degree of crystallinity,²⁰⁰ explaining the deviation identified in Figure 5.3d.

The LSMO/CAO//STO system displays a different landscape. The low magnification image, Figure 5.4c, confirms the presence of 60 nm LSMO and 10 nm CAO layers on STO. The nature of the Z-contrast HAADF imaging evidence the successful full chemical substitution of Sr by Ca, as the image contrast in the CAO layer is remarkably lower respect to the SAO layer. Note that the CAO layer is thinner than SAO (20 nm) and it is attributed to different wettability of the precursor solution with the STO substrate. Higher magnification HAADF-STEM image at the LSMO/CAO interface, Figure 5.4d, confirms the growth of only (001) oriented films and it is supported by the FFT (inset). The LSMO layer has significantly less amount of structural de-

fects compared to LSMO/SAO (Figure 5.4b) probably because of the better crystalline quality of the CAO underneath. Therefore, full substitution of Sr by Ca in SC_xAO has an undeniable effect on improving the crystalline quality of the sacrificial and enables the epitaxial growth of moderately strained LSMO films. Nevertheless, it is worth noting that in some areas of the film the LSMO/CAO interface is not sharp which would be in line with the previous identification of interfacial reaction. Remarkably, the microstructure of the LSMO/ SC_1AO system is very similar to the one presented for the LSMO/CAO, **Figure S5**. Therefore, the incorporation of Ca with $x=1$ in SC_xAO is already causing a significant improvement in epitaxial quality and no amorphous interface is devised. Overall, from a structural standpoint, the incorporation of Ca in SAO allows tuning the cell parameter while improving the crystalline quality and ambient stability. The epitaxy is transferred to the LSMO generating films with different strain according to the lattice mismatch and surface quality of the SC_xAO underneath. Cation intermixing is spotted in some areas at the LSMO/ SC_xAO interface.

5.2.2 Electrical properties

To evaluate the electrical properties of LSMO, temperature-dependent resistivity measurements have been carried out on LSMO/ SC_xAO //STO heterostructures from 400K to 10K and compared to LSMO//STO. As shown in **Figure 5.5a**, all LSMO films show a metallic behavior, however, the resistivity of the LSMO on SAO is significantly higher than the rest. This performance is not surprising considering the LSMO/SAO microstructure unraveled from Figure 5.4 and in agreement with previous reports on the impact of microstructure on the electrical transport properties.^{188,201} Focusing on LSMO on Ca-doped SAO heterostructures and LSMO//STO, they all show similar resistivity values at room temperature. Nonetheless, the temperature dependence of the resistivity show variations being more pronounced for LSMO//STO. Also, changes in the metal to insulator transition, T_{MI} , can be appreciated from the resistance derivative curve in Figure 5.5b. These changes could be attributed to the presence of different degree of epitaxial strain, calculated in Figure 5.3d, although no clear trend is

observed for the heterostructures. The interfacial reactivity is also expected to produce changes on the electrical properties. Indeed, it has been widely reported the important role of ion stoichiometry in LSMO (oxygen deficiency, cation off-stoichiometry, Sr-segregation, interdiffusion) on the temperature-dependent resistivity.^{202–204} Thus, further STEM-EELS analysis would be useful to probe the interface of our LSMO heterostructures with atomic precision to elucidate its possible role.

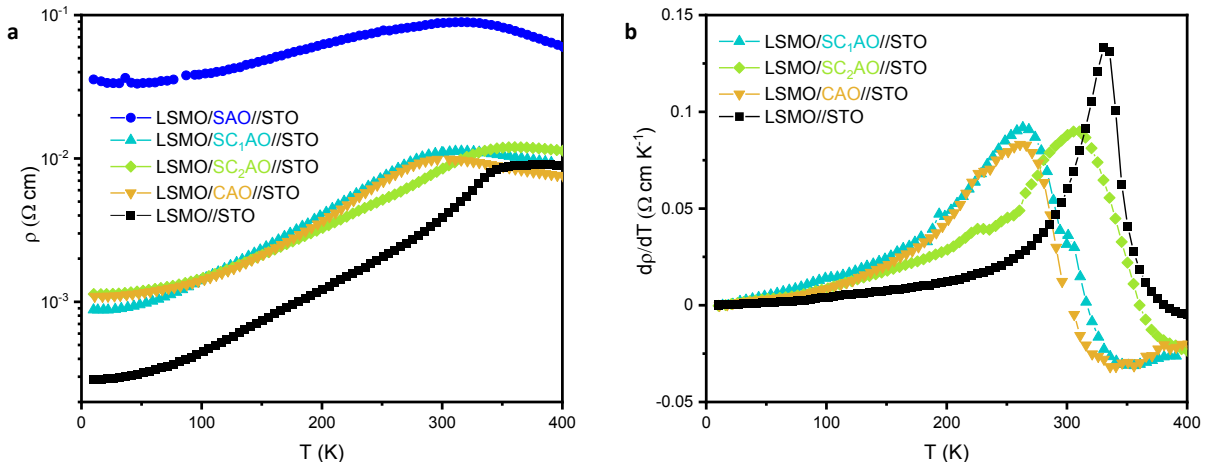


Figure 5.5: (a) Temperature-dependent resistivity of different LSMO/SC_xAO//STO and LSMO//STO heterostructures and (b) temperature derivative of the resistivity $d\rho/dT$.

5.2.3 Freestanding epitaxial LSMO

The last step to obtain freestanding epitaxial LSMO films requires adhering a support layer, in our case PET, to easily manipulate the membrane upon the sacrificial etching in water, **Figure 5.6a**. Also, the PET can be used as stamp to further transfer the LSMO released membranes to other substrates with no epitaxial relationship, *e.g.* glass or Si wafer. Importantly, we verified that the concentration of Ca in SC_xAO affects the immersion time in water of the heterostructure being SAO the fastest (2 days) and CAO the slowest (2 weeks), as expected.⁷⁵

The LSMO//PET stacks obtained from the different SC_xAO compositions show smooth and homogeneous surface morphology (Figure S1 (i-l)) and only show the (002) LSMO Bragg reflection, Figure 5.6b, which is centered at the 2θ value of LSMO-bulk. Therefore, all membranes on PET are fully relaxed. Optical inspection of the different LSMO membranes disclosed the

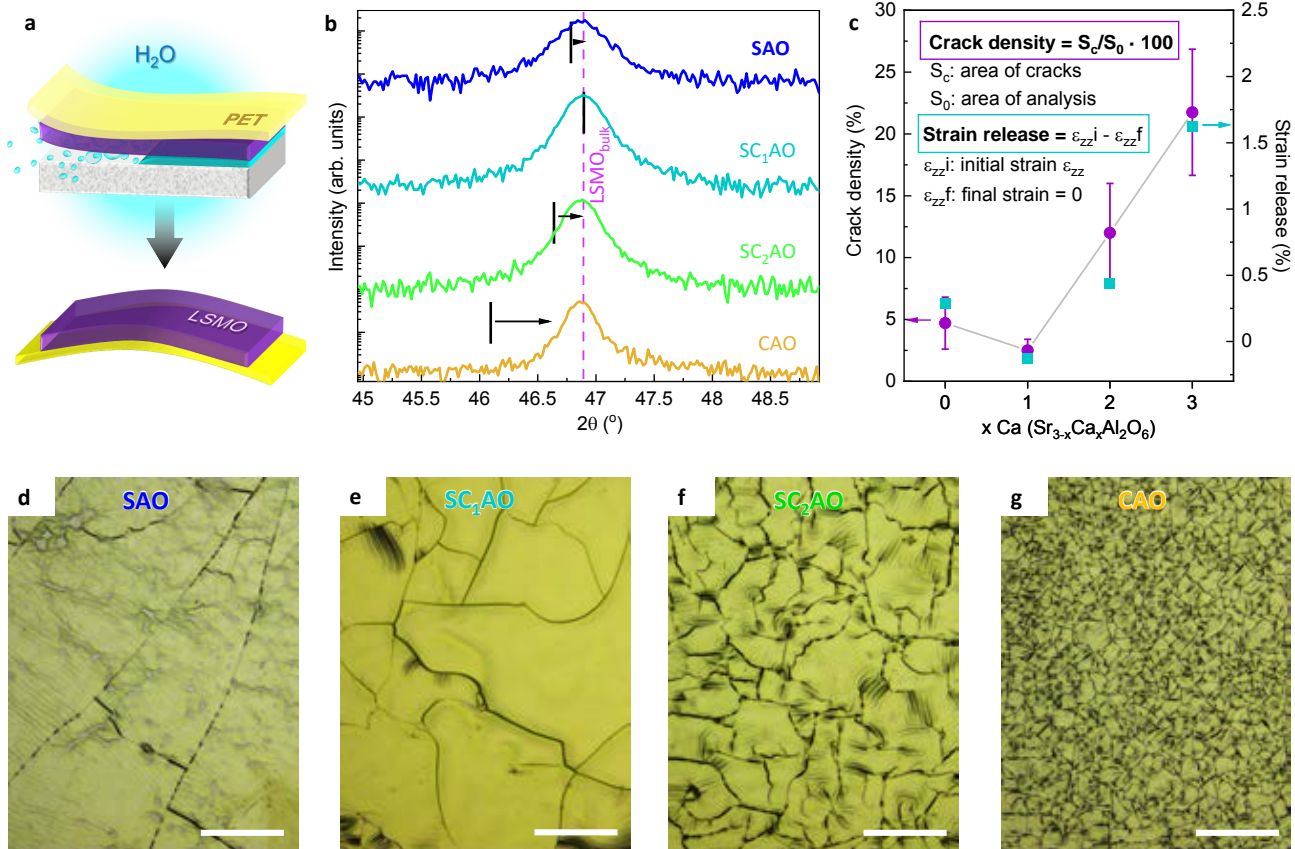


Figure 5.6: Freestanding LSMO on PET after the selective etching of the SC_xAO sacrificial layers. (a) Sketch of the process followed to transfer LSMO membranes to a PET support. (b) XRD θ - 2θ scans of the LSMO membranes supported on PET. The black bar indicates the position of the (002) LSMO Bragg reflection before the lift-off. (c) Crack density and strain release of LSMO membranes as a function of the Ca concentration of the SC_xAO sacrificial layer. Magnified images of the corresponding LSMO membranes on PET by etching (d) SAO, (e) SC_1AO , (f) SC_2AO and (g) CAO. White scale bars correspond to 200 μm .

formation of cracks. The density of cracks increases with the content of Ca in SC_xAO , Figure 5.6(e-g) and it can be quantified (details in **Figure S6**) and compared to the strain release for each LSMO/ SC_xAO system.⁶¹ From figure 5.6c it can be observed that the least strained LSMO on SC_xAO , *i.e.* on SC_1AO , generated least cracks. By increasing the amount of Ca in the sacrificial, the LSMO films show moderate compressive strain and they also show more cracks. It is suggested that the strain relaxation during the lift-off can be responsible for the formation of cracks,²⁰⁵ as previously reported in BaSnO_3 membranes.⁷⁵ Nevertheless, there are other factors that could be investigated to further reduce the crack density of the released membranes, including the sacrificial layer and membrane thicknesses,²² the use of additional

capping layers^{61,76} and modify the lift-off procedure.^{60,70} Indeed, the exfoliation process is one of the most critical steps in the preparation of membranes.²⁰⁶

Additional membrane analysis was performed on the LSMO obtained from SC₂AO which was selected based on a compromise between crystallinity, electrical performance ($T_{MI}=310$ K), moderate crack density and can be faster released than from CAO. X-ray photoelectron spectroscopy (XPS) survey spectrum revealed the presence of Al species on the LSMO membrane that was further verified from Al2p core level spectrum (**Figure S7**). This chemical analysis reaffirmed the cation intermixing at the interface LSMO/SC_xAO.

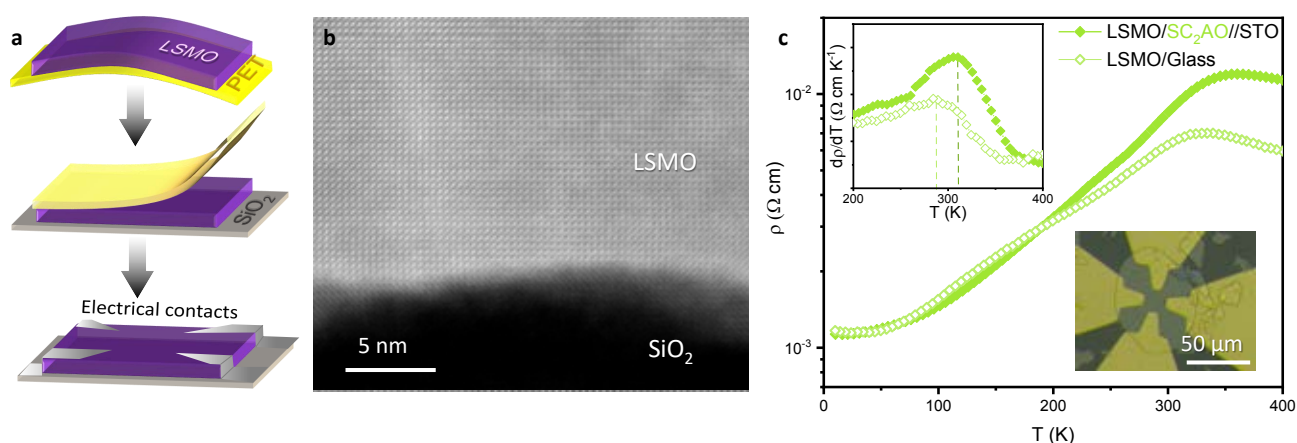


Figure 5.7: (a) LSMO membranes transferred from a PET support to other substrates such as SiO₂ (300 nm)/Si or glass which were used to make the electrical contact of the transferred LSMO. (b) Z-contrast HAADF-STEM cross-section of LSMO//SiO₂ interface. (c) Temperature-dependent resistivity of the released LSMO membrane. Upper inset shows the temperature derivative of the resistivity $d\rho/dT$. Lower inset corresponds to a magnified image of a LSMO flake with the contacts for the resistivity measurements.

Then, this LSMO membrane was double-transferred onto a rigid Si substrate, **Figure 5.7a**, to perform HAADF-STEM studies. Figure 5.7b proves the high crystallinity of the LSMO membrane integrated into silicon, a highly pursued goal to widen the possibilities of silicon-based electronics.^{101,207–209} The temperature-dependent resistivity of the LSMO membrane prepared from SC₂AO was also evaluated by transferring it to a glass substrate. Electrical measurements were performed by patterning gold contacts on top of a flake with no cracks. The resistivity curves obtained before and after the transferring (Figure 5.7c) are very similar indicating that there is almost no degradation of the film during the transferring process.

Finally, it is important to note that the hybrid process here presented that combines solution processed SC_xAO sacrificial layers with PLD to prepare epitaxial freestanding LSMO could be easily extended to other perovskite systems and beyond, such as spinels. In Figure S8 it is shown a RHEED study analogous to that presented in Figure 5.2 for the preparation of CoFe_2O_4 -PLD on solution processed SC_xAO confirming the growth of crystalline oriented CoFe_2O_4 films.

5.3 Conclusion

In this study we put forward a simple hybrid synthesis procedure combining solution processing and pulsed laser deposition to easily prepare epitaxial complex oxide membranes. First, it is investigated the influence of gradual Ca-substitution in solution processed SAO films (SC_xAO with $x \leq 3$) to effectively engineer its crystallinity, structure and robustness preserving a smooth surface. Moreover, it has been demonstrated that vacuum annealing of SC_xAO after air exposure reconstructs the surface crystallinity and increase their stability in air offering a less-strict environment to prepare and manipulate the sacrificial layers. The composition of SC_xAO influences the properties of the subsequent epitaxial LSMO film. Ca substitution in SC_xAO favors better crystallinity inducing slight compressive strain that is totally released upon LSMO exfoliation generating cracks. Improving the interface quality between functional complex oxide/sacrificial and improving the lift-off process is still required but epitaxial LSMO membranes can be obtained maintaining the metallic behavior identified prior the lift-off. Therefore, this work provides an innovative and versatile platform to synthesize complex oxide freestanding films and heterostructures that can be integrated in a wide variety of substrates in the search for novel and enhanced properties envisaging many technological benefits.

5.4 Supporting Information

AFM Surface morphology analysis

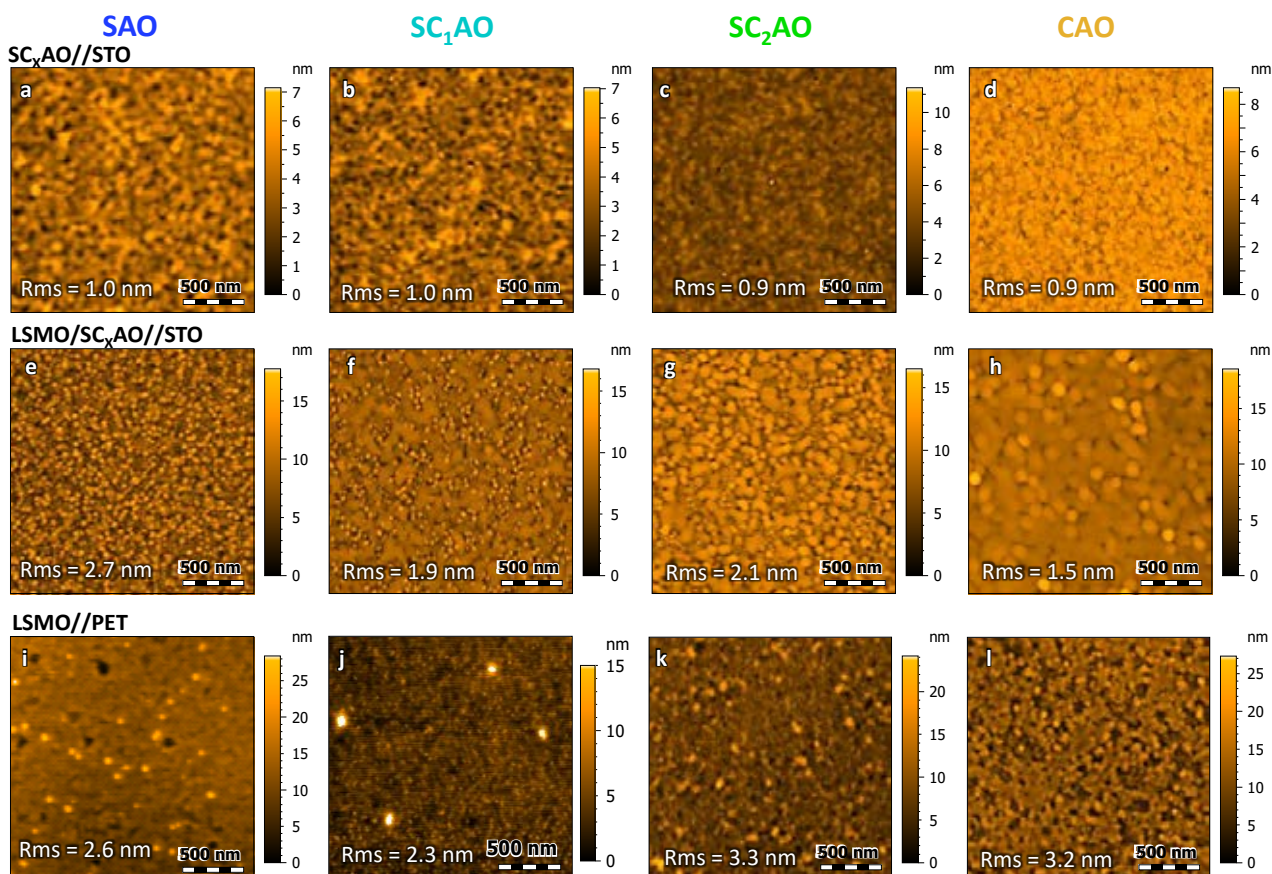


Figure S1: $2\mu\text{m} \times 2\mu\text{m}$ AFM topographic images of (a-d) SC_xAO sacrificial layers grown on (001) STO; (e-h) LSMO grown on top of them and (i-l) the same LSMO membrane transferred on a PET support.

SC_xAO air stability - RHEED and AFM analysis

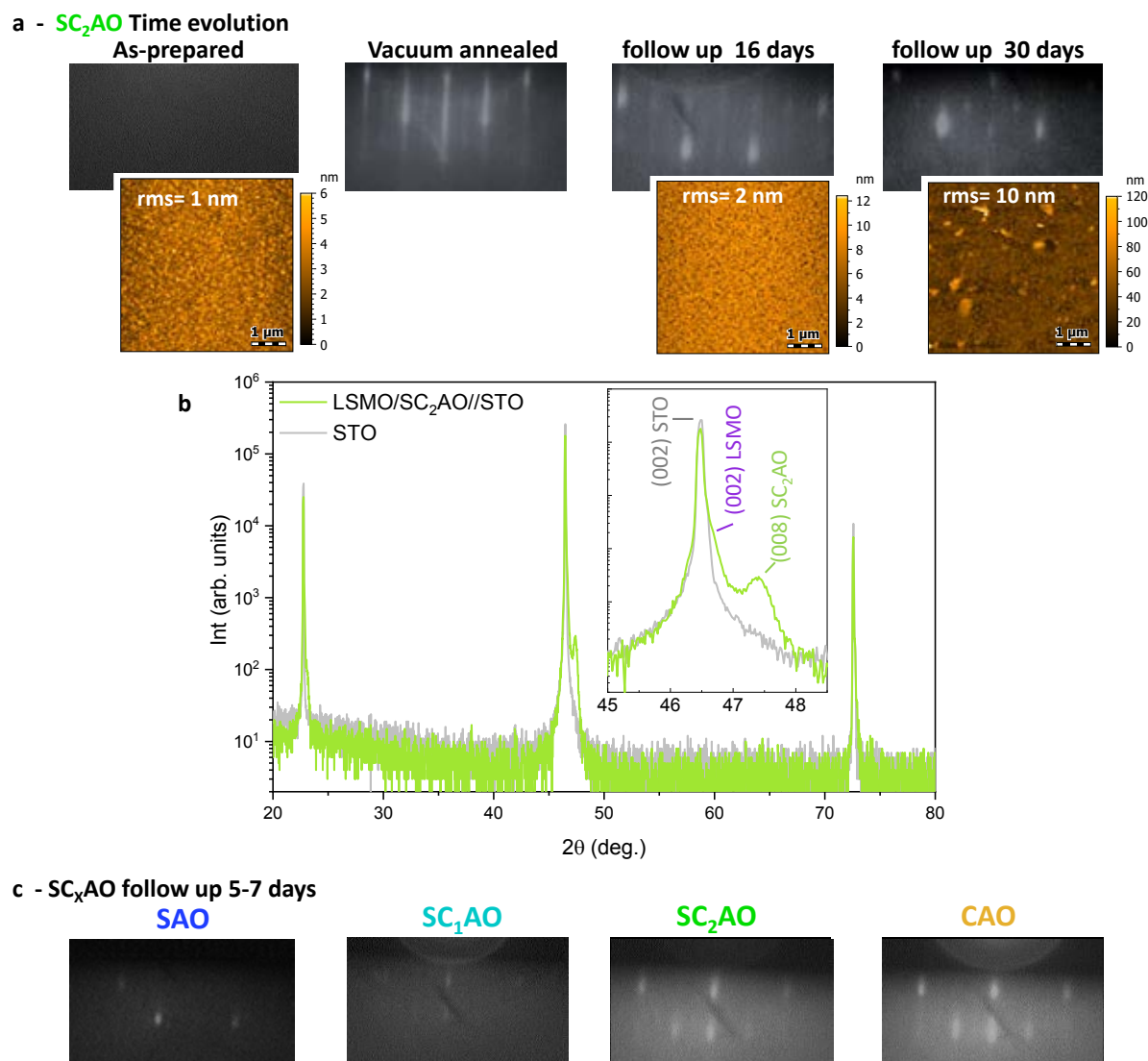


Figure S2: (a) RHEED and AFM characterization at room temperature of SC₂AO film grown at 800 °C and exposed to air, after in-vacuum annealing at 825 °C and after sealed in a plastic bag for 16 days and 30 days. (b) XRD θ - 2θ scan of a LSMO film grown on SC₂AO 16 days after the vacuum annealing and being exposed to air. (c) RHEED characterization at room temperature of SC_xAO films with different Ca concentration grown at 800 °C, vacuum-annealed at 825 °C and sealed for 5-7 days before characterization.

XRD analysis of LSMO/SC_xAO//STO heterostructures

Table S1: Texture analysis of SC_xAO films and LSMO on SC_xAO from rocking curve (ω) and phi scan (ϕ). In parenthesis it is indicated the reflection from which ω and ϕ have been calculated.

sample	ω	ϕ	sample	ω	ϕ
STO	0.02 (002)	0.10 (110)	LSMO//STO	0.09 (002)	0.39 (103)
SAO//STO	0.13 (008)	0.71 (660)	LSMO/SAO	-	-
SC ₁ AO//STO	-	-	LSMO/SC ₁ AO	0.51 (002)	1.66 (103)
SC ₂ AO//STO	0.15 (008)	0.33 (440)	LSMO/SC ₂ AO	-	-
CAO//STO	0.11 (008)	0.68 (440)	LSMO/CAO	0.13 (002)	0.79 (204)

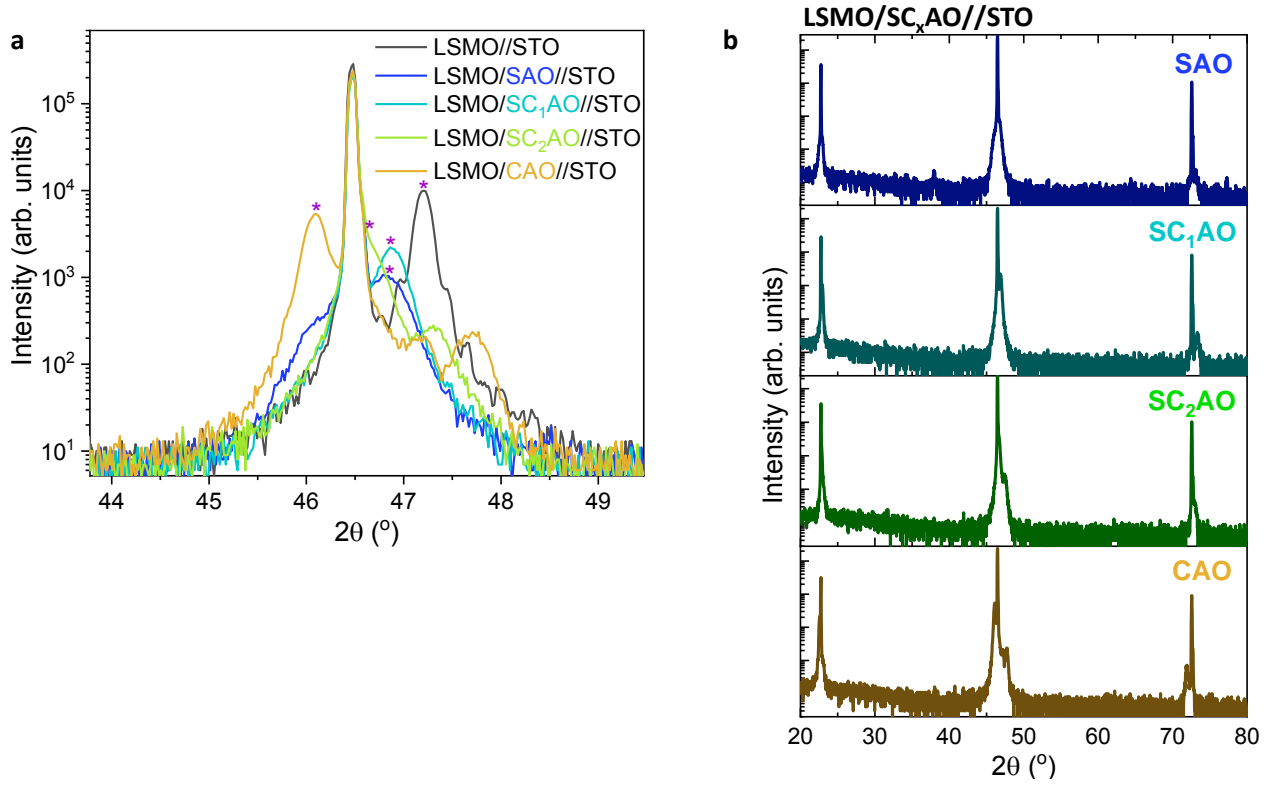


Figure S3: XRD θ - 2θ scans for the LSMO/SC_xAO//STO heterostructures (a) compared to LSMO//STO (* indicate (002) LSMO Bragg reflection) and (b) in a longer 2θ range

STEM-EELS characterization

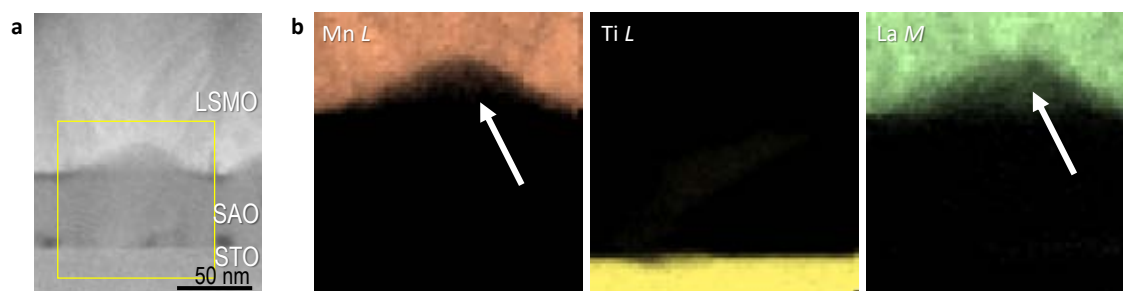


Figure S4: STEM-EELS map showing the distribution of La, Mn and Ti in a LSMO/SAO//STO heterostructure

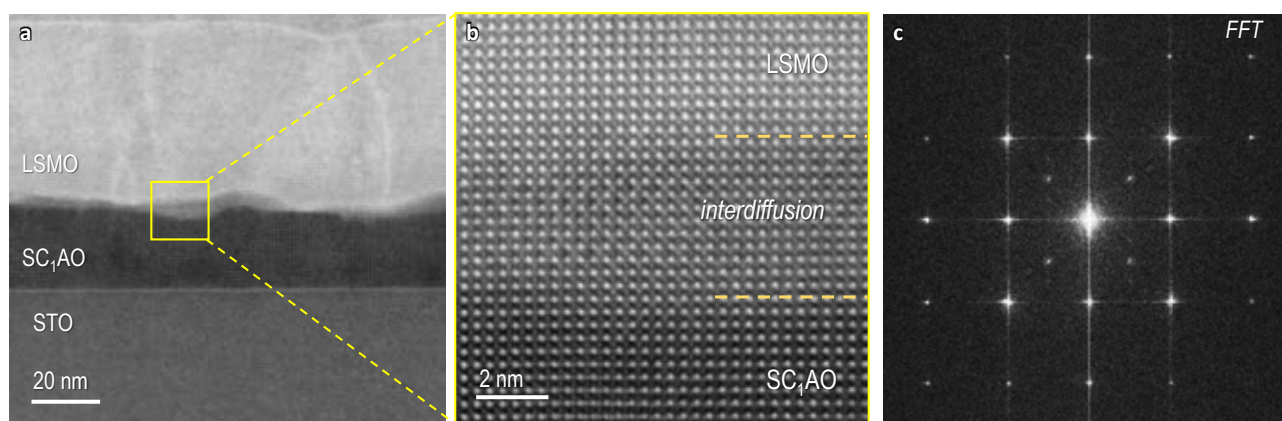


Figure S5: Z-contrast HAADF-STEM cross-section. (a) LSMO/SC₁AO//STO low magnification image. (b) Higher magnification image of LSMO/SC₁AO interface. (c) FFT of the heterostructure

LSMO membranes

Example
Crack density calculation

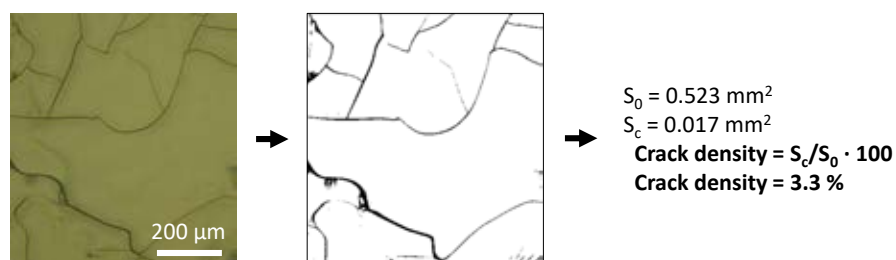


Figure S6: Crack density calculation. Example for a magnified image of a LSMO membrane on PET after etching SC₁AO. S_c is the area of the crack and S_0 the total area.

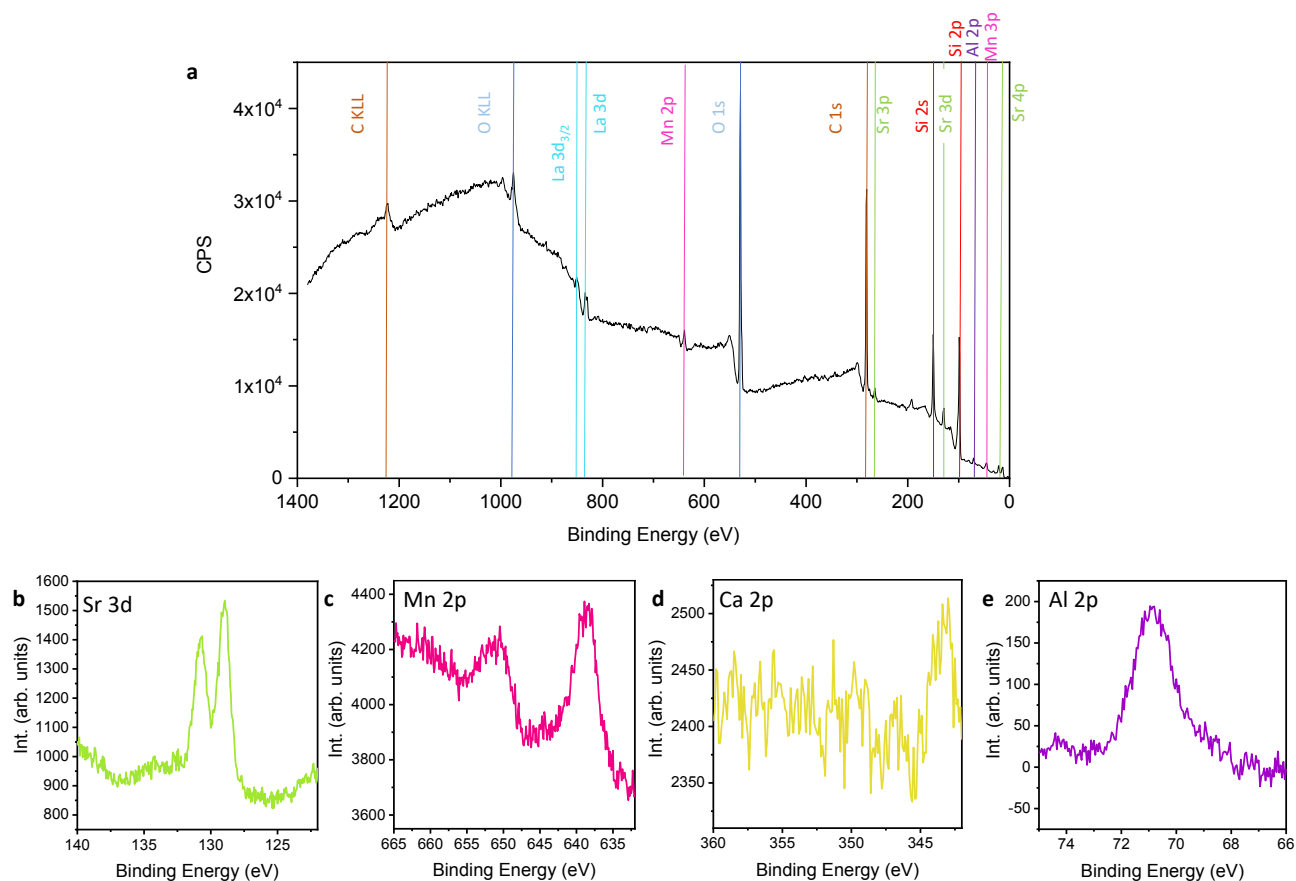


Figure S7: XPS analysis of a LSMO membrane after being released from SC_2AO . Note that the surface measured is the surface previously in contact with SC_2AO . (a) XPS overview spectrum and the corresponding (b) Sr 3d, (c) Mn 2p, (d) Ca 2p and (e) Al 2p core level spectra.

CoFe_2O_4 grown by PLD on SAO

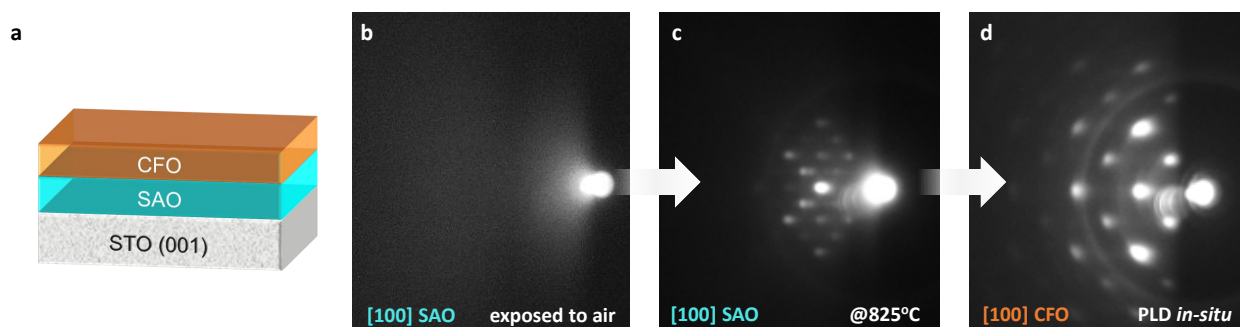


Figure S8: (a) Growth of epitaxial CoFe_2O_4 on SAO sacrificial layer. RHEED analysis of a SAO film (b) after air exposure, (c) after annealing in vacuum with PO_2 and (d) after depositing CoFe_2O_4 by PLD.

Chapter 6

Towards freestanding BiFeO₃ heterostructures for all-oxide photovoltaics

Among the family of complex oxides, BiFeO₃ (BFO) is a very attractive material being a room temperature, single-phase multiferroic material.²¹⁰ More recently, a plethora of research is focusing on its use in non-conventional photovoltaics specially because of its direct band gap of 2.6-2.7 eV and abnormal ferroelectric photovoltaic effect. Nonetheless, heteroepitaxial growth of BFO is most of the times desired in order to tune and enhance its properties and the growth on single crystal, expensive and fragile substrates hinders the exploitation of many of its interesting properties when integrated in flexible devices, artificial stacked heterostructures or Si-based technologies.

In this chapter we aim to merge the knowledge generated in the previous chapters on the use of Sr_{3-x}Ca_xAl₂O₆-CSD (SC_xAO) sacrificial layer to prepare chemical deposited epitaxial BFO membranes to ultimately fabricate a ferroelectric and photovoltaic multilayer device. The envisaged device consists of BFO photoabsorber deposited on LSMO bottom contact, using a ZnO electron transport layer and a top transparent electrode (Al-ZnO, In-SnO₂) to complete the heterostructure.

First, the study focus on the optimization of the ALD processes for BFO, ZnO and AZO. As a proof of concept, these components have been integrated in a device that shows ferroelectric and photoresponse behavior. Then, moving towards the preparation of freestanding BFO-based devices it has been explored the use of CSD versus ALD to deposit BFO on SC_xAO. It turns out

that direct deposit of BFO on as-prepared SC_xAO hinders the achievement of epitaxial films. Finally, BFO deposition by CSD has been attempted on LSMO/ SC_xAO system to investigate the heteroepitaxial film crystallinity and interface diffusion. The successful release of BFO/LSMO bilayer membranes was used to complete a freestanding ITO/ZnO/BFO/LSMO device where ferroelectricity and photoresponse were identified. This study unfolds the challenges to prepare a BFO-based membrane device using chemical methods providing an attractive platform to build on and prepare freestanding membranes opening many exciting possibilities for epitaxial complex oxides.

6.1 Introduction

Conventional silicon-based solar cells are reaching their theoretical power conversion efficiency (PCE) limit and there has been a lot of research interest to find alternative materials as light harvesters. One appealing alternative is employing photoabsorbers that are stable, non-toxic, do not rely on a p-n junction and would be able to provide efficiencies beyond the traditional Shockley-Queisser limit.⁷

In particular, ferroelectric perovskite oxides have attracted great attention as stable components presenting a unique photovoltaic mechanism named bulk photovoltaic effect (BPE).^{211,212} Also, ferroelectric materials carry a reversible spontaneous electric polarization that can be switched by an external electric field, temperature, pressure or strain. Importantly, to make the most of the BFO ferroelectric properties it is required to grow it with a preferred crystalline order, i.e., epitaxy, which adds complexity and restrictions in the preparation process of the device. When coupled with photoabsorption, such electric polarization found throughout the bulk of the material leads to a polarization-related charge separation mechanism, in contrast to conventional silicon-based solar cells where the built-in electric field is only present in the p-n junction.²¹³ In addition, the photovoltage generated is not limited by the band gap energy, but can be orders of magnitude larger.²¹⁴ Unfortunately, most ferroelectric perovskite oxides have a relatively large band gap, *i.e.* 3–4 eV, being able to harvest only 8–20% of the solar spectrum, and present

poor charge transport properties, so their actual PCE gets compromised.²¹¹

BiFeO₃ (BFO) is among the most attractive ferroelectric perovskite oxides to be used as photoabsorber because of its relatively narrow band gap of 2.7 eV and its high saturation polarization of up to 90 $\mu\text{C}\cdot\text{cm}^{-2}$ at room temperature.^{215,216} Moreover, BFO is a multiferroic that simultaneously show magnetic (antiferromagnetic), ferroelastic and ferroelectric properties at room temperature.^{210,217} Such features can even provide further exotic phenomena when combined with other functional oxides, making this material interesting not only for photovoltaics but also for other applications. For example, BFO combined with the ferrimagnetic magnetostriuctive CoFe₂O₄ (CFO) in a BFO-CFO nanocomposite could be used for magnetic sensors, memories, or flexible energy harvesting systems where the combination of magneto-mechano-electric effect is exploited.^{218,219}

Despite the promising features of BFO, there is still uncertainty about how the cross-coupling mechanism between light and ferroelectricity works and further understanding and optimization would be required before bringing this photovoltaic technology into a feasible alternative.²¹² Because the PCE of pristine BFO based devices is still low, it is essential to further increase short-circuit current density while keeping a high open-circuit voltage for improving the device performance. To move towards this direction, there are several strategies that are being studied. For example, cation engineering allows modifying the bandgap towards the visible. Bi₂FeCrO₆ multilayer devices have demonstrated to enhance the PCE up to 8.1%, the highest value reported up to now for a BFO-based device.²²⁰ In the device fabrication, the use of cost-effective methods is also a key aspect to consider.¹¹⁸ In this regard, BiFe_{1-x}Co_xO₃ ($x\leq 0.3$) epitaxial thin films prepared by chemical solution deposition have demonstrated to shift the bandgap while showing enhanced ferroelectricity compared to pristine BFO.¹⁰³ Another strategy to further engineer the properties of BFO could rely on strain engineering.^{221,222} In fact, growing epitaxial BFO thin films clamped on different substrates can induce changes on the polarization direction from [111] to [001] due to strain-driven phase modification.²²³ Last but not least, the efficiency of a photovoltaic device depends not only on the photoabsorber but also on the whole heterostructure in which chemical and structural compatibility of the different

components and band alignment²²⁴ need to be considered. Note that the ideal architecture for a BFO-based device is not well understood.

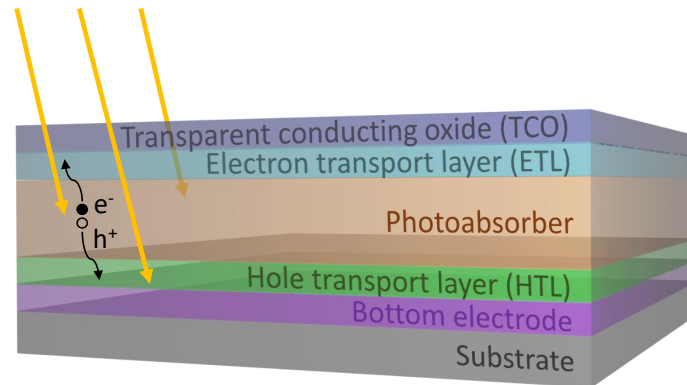


Figure 6.1: Example of a thin film photovoltaic heterostructure.

All-oxide photovoltaics has emerged as an attractive approach referring to solar cells that are entirely based on oxide thin films. The chemical, mechanical and thermal stability, as well as the abundance and non-toxicity of many multifunctional oxides and the possibility of preparing them by low-cost chemical methods is what makes this concept so appealing.²²⁵ A typical photovoltaic device architecture is shown in **Figure 6.1**, including the photoabsorber, which generates the photo-excited carriers, the charge transport layers, that help the selective transport of the photogenerated carriers to the electrodes and minimize recombination, and the electrodes, that collect the generated charges. The wide versatility of structures and compositions of transition metal oxides offer a broad range of physical properties that could fulfill the different functionalities of all the components needed in a photovoltaic device, some of them already used in traditional photovoltaic technologies. For example, potential **top electrode** oxides for BFO-based solar cells include transparent conducting oxides (TCO) such as is In-SnO₂ (ITO), which is the most popular because of its high conductivity and transmittance. Nevertheless, the scarcity of indium and the high processing cost implies demands for new compositions.²²⁶ In this scenario, Al-doped ZnO (AZO) appears to be an attractive alternative with abundant and non-toxic components.^{227, 228} Regarding the **bottom electrode**, the necessity to ensure epitaxial BFO growth, reduces significantly the variety of suitable candidates because

it will determine the epitaxial quality and strain of the grown BFO film, which can have a major role on its physical properties.²²⁹ SrRuO₃, LaNiO₃ and La_{0.7}Sr_{0.3}MnO₃ (LSMO) are some compositions that have already been tested.^{51,103} For the **selective transport layers**, a few examples of electron transport layers (ETLs) would be TiO₂, SnO₂ and ZnO. Among them, ZnO is of interest for its wide direct band gap with high transparency in visible and near-ultraviolet spectral regions, tunable n-type electrical conductivity and high chemical and thermal stability.²³⁰ On the other hand, hole transport layers (HTLs) that have already been studied in traditional photovoltaics are NiO, MoO₃, V₂O₅ or WO₃ all of them presenting high chemical stability and the possibility to be prepared by low cost processing.²³¹ Note that the selective layer to be placed between the bottom electrode and the BFO photoabsorber should also ensure epitaxial BFO growth. Nonetheless, these synthetic constraints could be minimized if the BFO epitaxial film was manipulated separately as freestanding and stacked in versatile and artificial heterostructures.

Freestanding BFO-based membranes. Freestanding epitaxial BFO membranes as thin as a single monolayer have been demonstrated using the SAO sacrificial layer.⁸⁴ Interestingly, the released ultrathin BFO spontaneously changes its structure from cubic to tetragonal with a large c/a ratio without applying any strain and it presents abnormally large polarization ($140 \mu\text{C}\cdot\text{cm}^{-2}$). Moreover, BFO membranes have demonstrated to present superior flexibility enduring cyclic 180° folding with good recovery and allowing bending strains larger than 5%.²⁶ This improved elasticity can be used to tune its physical properties through strain engineering. For example, applying uniaxial strain on freestanding BFO allows to induce anisotropic band gap engineering,²³² and bending a BFO/LSMO freestanding multilayer allows to control the photoconductance thanks to the BFO flexoelectric properties.²³³ Even without applying any external strain, the simple release of the BFO film from the clamping substrate can provide distinct ferroelectric response with ~ 40 % reduction of the switching voltage and a consequent ~ 60 % improvement in the switching speed.²³⁴ The possibility to prepare complex oxides on Sr_{3-x}Ca_xAl₂O₆-CSD sacrificial layers and deliver epitaxial membranes allows us to envisage the preparation of a chemical deposited epitaxial BFO membrane-based heterostructure to probe

the ferroelectric and photovoltaic performance.

On this basis, this chapter has been divided into two major parts as shown in **Figure 6.2**:

The first part is devoted to study the preparation of ZnO, Al-doped ZnO (AZO) and BFO by ALD-type approach (see Chapter 2.1.2) as potential electron transport layer, transparent conducting oxide and photoabsorber, respectively, as part of an all-oxide photovoltaic heterostructure (Fig. 6.2a).

- ZnO and AZO processing conditions can slightly differ in each ALD reactor.²³⁰ Here it has been adapted the optimal deposition conditions for our specific ALD reactor.¹³⁶
- Special effort has also been devoted on developing a synthesis process to prepare epitaxial BFO by a novel precursor combination.
- All the ALD developed oxides are integrated in an all-oxide heterostructure as a proof-of-concept functional device.

The second part of this chapter is focused on the challenging task to prepare freestanding epitaxial BFO membrane-based heterostructures from $\text{Sr}_{3-x}\text{Ca}_x\text{Al}_2\text{O}_6$ (SC_xAO) sacrificial layer, prioritizing the use of chemical methods as much as possible (Fig. 6.2b). In this section, the aimed device architecture is ITO/ZnO/BFO/LSMO. Here, special focus is placed to achieve high quality heteroepitaxial growth with minimal cation interdiffusion at the interface to ultimately characterize the photoferroelectric properties of the released membranes.

- The use of ALD *versus* CSD is investigated to direct deposit BFO on the sacrificial layer SC_xAO to prepare BFO membranes.
- Study the heterostructure quality of BFO-CSD film deposited on LSMO-PLD buffered SC_xAO //STO system.
- The lift-off of the BFO/LSMO membranes and their integration on flexible and conductive substrates to ultimately complete the ferroelectric and photovoltaic device.

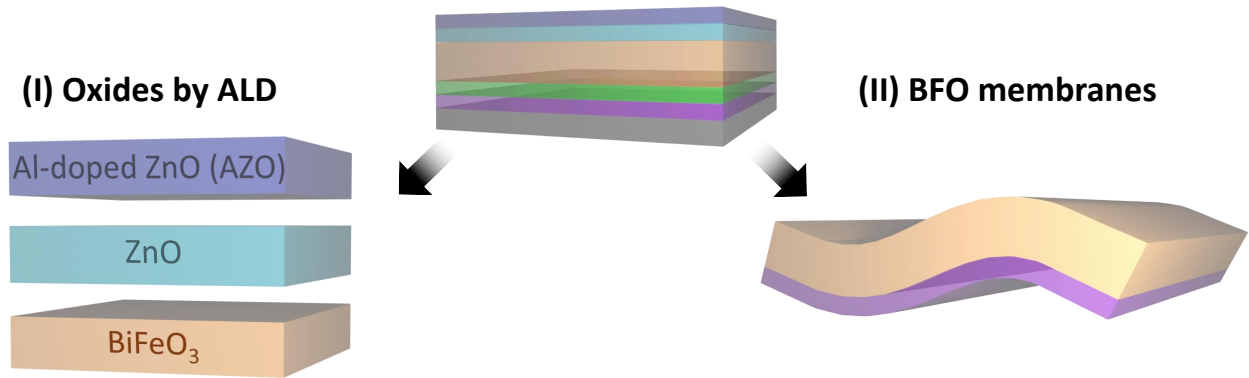


Figure 6.2: Towards all-oxide photovoltaics. Approaches followed: (I) Study the preparation by ALD of thin films of AZO as TCO, ZnO as ETL and BFO as photoabsorber. (II) Study the preparation of freestanding BFO-based heterostructures using the SC_xAO sacrificial layer.

6.2 ZnO, Al-doped ZnO and BiFeO₃ by ALD-type approach towards all-oxide photovoltaics

6.2.1 ZnO electron transport layer

In this study, ZnO is aimed to be integrated as electron transport layer in the BFO-based all-oxide device and it is pursued by ALD to achieve good uniformity and conformal growth, which can help minimizing recombination.¹¹⁸ The growth of ZnO was performed on SiO₂/Si substrates at 160 °C following the optimized processing conditions described in Chapter 2. The as-prepared 20 nm ZnO films crystallized in the hexagonal phase with a lattice parameter of $a=3.2 \text{ \AA}$ and $c=5.2 \text{ \AA}$.²³⁵ Note from the θ -2 θ GIXRD scan, **Figure 6.3a**, the relatively high intensity of the (002) diffraction peak differing from ZnO bulk (relative bragg reflections intensity represented as red lines) which indicates a preferential orientation along [001] direction.²³⁶ The topography of the ZnO film was analysed by AFM as shown in Fig. 6.3b, proving that the films are homogeneous, dense and smooth with a root mean square (rms) surface roughness of $1.8 \pm 0.3 \text{ nm}$. The film show small grains with an average size of $18 \pm 4 \text{ nm}$.²³⁷ The thickness dependence with the number of cycles (from 50 to 900) shows a linear dependence resulting in a growth per cycle (GPC) of $1.1 \pm 0.2 \text{ \AA cycle}^{-1}$ (Fig. 6.3c), which demonstrates that the

ZnO follows the ALD regime, i.e., self-limiting growth, except for an initial incubation period for < 50 cycles. The ZnO characteristics found here are consistent with what is described in the literature.^{230,236,237}

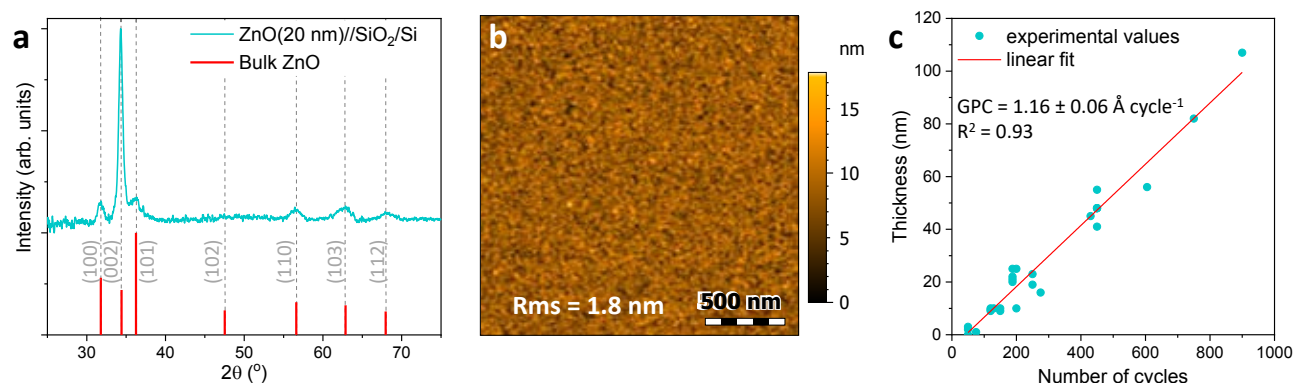


Figure 6.3: Characterization of ZnO deposits at 160 °C. (a) GIXRD pattern, (b) AFM topographic image, (c) Thickness dependence *vs.* number of deposition cycles.

6.2.2 Al-doped ZnO (AZO) transparent conducting oxide

In order to use Al-doped ZnO (AZO) as TCO, the optimal Al doping is usually found around 2-5% depending on the deposition conditions.²³⁰ By ALD, the Al doping can be controlled varying the cycle ratio of Zn:Al (ALD process schematized in Fig. 1.11c, Chapter 1.2, Introduction) However, its implementation is not straight-forward as the AlO_x layers have been observed to etch the underlying layer and hinder the growth of ZnO on them during the following cycles.²³⁸ Moreover, the ALD conditions to obtain an optimal AZO composition slightly differ depending on the ALD reactor used.¹³⁶ In order to identify the starting conditions to extrapolate the AZO deposition in our reactor, a literature research was performed including deposition temperature, cycle ratio and total number of cycles, as well as the resulting thickness and resistivity, listed in Table S1, Supporting Information. It was found that the optimal ranges would be a deposition temperature of 120-220 °C, a cycle ratio Zn:Al of 15:1-31:1, and a total number of cycles of 200-700.

According to that, fine tuning of Al-doping in ZnO with different Zn:Al ratios (15:1 - 35:1) was performed at 160°C for 500 cycles by alternately pulsing DEZ (diethylzinc) and TMA

(trimethylaluminum) precursors and water as oxidizer on SiO₂/Si and glass substrates. The influence of doping was investigated on crystallinity, surface morphology, light transmittance and electrical resistivity. All films regardless of the doping content were 63 ± 7 nm thick, according to XRR measurements, and had a smooth surface with rms roughness of 2-3 nm and an average grain size of 20 nm (AFM measurements in Figure S1) demonstrating that Al-doping does not modify the surface morphology. GIXRD analysis corroborated the formation of the hexagonal phase for all the compositions, as described in **Figure S2**.

To determine the suitability of using the developed AZO-ALD films as TCO for applications in solar cells and other optoelectronic devices, the optical and electrical properties have been evaluated. The optical transmittance of 60 nm AZO films deposited on glass was measured by UV-vis spectrophotometer, see **Figure 6.4a**. The bare glass shows $\sim 90\%$ transmittance in the 300-1000 nm wavelength range. After the deposition of the AZO films, the transmittance shifts to 70-80%, being still highly transparent in the visible region in well agreement with previous reports.²³⁹ Note that the UV absorption edge shifts with increasing Al doping level, which is related to a decrease of the AZO refractive index as a consequence of an increase of the free carrier concentration.²⁴⁰

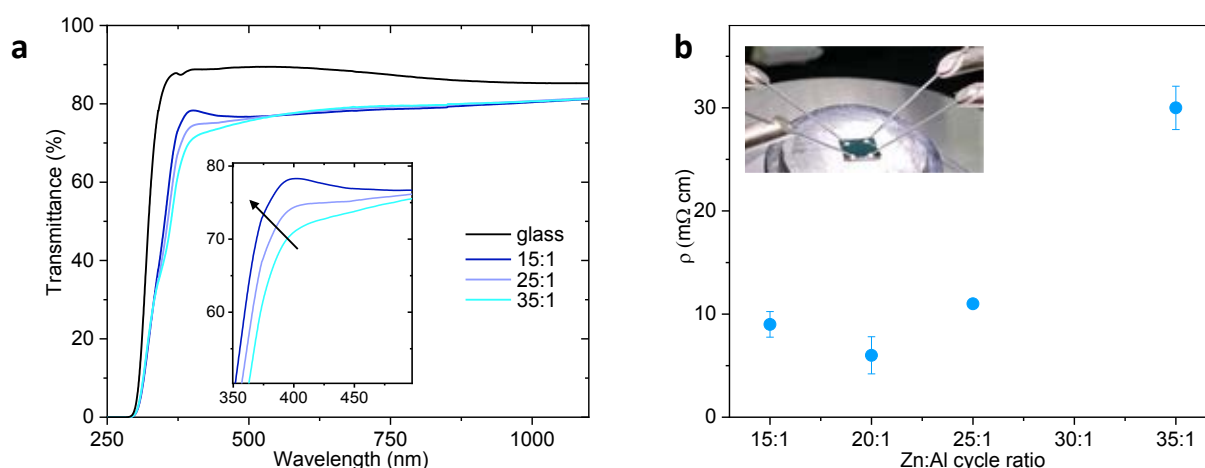


Figure 6.4: Optical and electrical characterization of AZO films deposited at 160°C. (a) UV-vis transmittance spectra of AZO films with different Zn:Al ratios deposited on glass substrates. Inset corresponding to the wavelength range where the UV absorption edge shifts. (b) Resistivity of AZO films as a function of the Zn:Al cycle ratio. Inset image corresponds to the setup used for the electrical characterization of the AZO films.

The resistivity of the AZO films at room temperature for the different Al-doping was measured using the Van der Pauw method²⁴¹ and listed in Fig. 6.4b. The resistivity varies from 6 m Ω ·cm to 30 m Ω ·cm in the range of Zn:Al ratios studied, obtaining the optimal resistivity properties for 20:1 Zn:Al cycles (6 m Ω ·cm). For higher Zn:Al ratios (lower Al% concentrations) there is an increase of resistivity which is attributed to the decrease of electron donors contributing to the n-type conductivity of the ZnO film.²⁴² On the other hand, for lower Zn:Al ratio (higher Al%) the resistivity increases again and it could be attributed to the formation of secondary phases for the poor solubility of Al into ZnO.²⁴³ The optimal doping level found in our study (20:1 Zn:Al cycle ratio) is within the range of what is reported in the literature (Table S1), although some of the reported AZO films show lower resistivity (<10⁻³ Ω ·cm) for a similar optical transmittance suggesting that there is still room for improvement. Engineering the Zn:Al ratio is the most obvious way to tune the resistivity through the electron donor concentration, but there are several other ALD operating parameters that could be optimized as well. For example, we identified that by doing the deposition at 200 °C instead of 160 °C, the optimal Zn:Al ratio changes (**Figure S3**), and some reports have demonstrated better performance for AZO films deposited at T > 200 °C.^{228,244}

Another way to fine tune the AZO optoelectronic properties would be optimizing the Al homogeneity throughout the film thickness. It is well known that typical AZO-ALD is composed of a multilayer arrangement of periodic Al₂O₃ and ZnO uniform layers instead of an homogeneous intermixing of the cations.²⁴⁵ In our work, the multilayer arrangement could be identified from the superstructure in XRR (**Figure S4**). To obtain more homogeneous distribution of Al along the thickness, some approaches try to decrease the density of Al₂O₃ deposited on a single cycle so the same Al% can be achieved with more "partially deposited" Al₂O₃ cycles. Some examples are performing unconventional cycling sequences in which no oxidizer is pulsed right after DEZ,²⁴⁶ or in-situ surface functionalization with organic molecules to better control the density of reactive sites.²⁴⁷

6.2.3 BiFeO₃ (BFO) photoabsorber

The deposition of BFO by ALD has been previously studied and developed by different research groups including in our team, as summarized in Table S2. The selection of Fe and Bi precursors is not straightforward and some particular difficulties related to BFO-ALD are the chemical compatibility and reactivity of the precursors, as well as their relatively low volatility, which makes the deposition homogeneity challenging. In this work we investigated how to prepare BFO using a new combination of precursors based on a tailor-made precursor, Fe(ⁱpki)₂,¹⁵¹ and the commercially available Bi(tmhd)₃, which although the compatibility is not optimal, with the Fe(ⁱpki)₂ we aim to improve the process reproducibility and robustness compared to our previous Fe complex (FeCp₂) according to recent work of our group performed in the systems Gd_xFe_yO_z and CoFe₂O₄.^{139,180} As previously introduced (Chapter 1.2, Introduction), preparing ternary oxides by ALD is a challenging process where cycles of binary oxides are usually combined into supercycles following a multilayered structure. During the deposition, multitude of parameters must be precisely controlled including precursors temperature window, GPC, chemical compatibility and cycling sequence, among others. In this chapter we focus on presenting the influence of the cycling sequence between Fe and Bi and the post-annealing temperature on BFO film crystallinity, phase purity and surface roughness, as these are key characteristics for the application of BFO as photoabsorber.¹⁰³ Importantly, the deposition of BFO has been done following an ALD type approach, i.e. the deposition of BFO has been carried out by alternate pulsing of precursors using an ALD tool although the deposition mechanism does not meet the strict ALD regime. The operating conditions are described in Chapter 2.1.2 including precursor volatilization temperature (Fe(ⁱpki)₂ at 130°C and Bi(tmhd)₃ at 150°C), deposition temperature (250°C) and pulse mode (pressure-boost mode), which were adapted from a previous work done in the group on BFO-ALD by a different combination of precursors.¹⁵³ Note that since we pursue epitaxial BFO films, all the depositions were performed on (001) STO single crystal substrates to induce the preferred (001) orientation. However, up to date no epitaxial BFO has been directly achieved by ALD in the as-deposited stage (T < 300°C) and a post-annealing

treatment at higher temperatures is necessary to induce its epitaxial growth. Here, it was applied a post-annealing treatment at 650 °C for 30 min in 0.6 l·min⁻¹ O₂ gas flow.¹⁵³

Cycling sequence. Here, the deposition of BFO by ALD has been done following a multilayer arrangement of the corresponding FeO_x and BiO_x binary oxides as schematized in Fig. 1.11b (Chapter 1) and described here:



which can also be written in a simplified manner as $N \times (a \text{ Fe} + b \text{ Bi})$, where N is the number of supercycles that determines the final thickness, and a and b are the number of Fe-based and Bi-based subcycles, respectively, that determine the stoichiometry of the film. Note that all the BFO-ALD depositions finish with 10 Fe-based subcycles to limit the Bi outdiffusion and volatilization during the post-annealing.^{141,248} **Figure 6.5a** contains the different cycling sequences studied for BFO films deposited at 250°C and then post-annealed. It is important to mention that for the deposition of complex oxides like BFO where several precursors are combined in an alternate manner and the surface chemistry varies for each cycle, its final stoichiometry will not only depend on the cycle ratio Fe:Bi but it will also be subjected to the subcycle sequence within a same ratio.^{249,250} Therefore, first, it has been studied the influence of subcycle sequence (3:3, 9:9, 18:18) for films prepared with a fixed Fe:Bi cycle ration of 1:1 (Fig. 6.5a). Then, the cycle ratio has been adjusted on the basis of the results obtained.

The crystallinity of the resulting BFO films on (001) STO substrates was analyzed by XRD θ - 2θ scans in the 2θ range 20-80°, as shown in **Figure 6.6**. For all the conditions studied, it can be identified three high intense sharp peaks at 22.7°, 46.5° and 72.5° which correspond to the (00l) Bragg reflections of the single crystal STO substrate (marked with grey lines), and the less intense peaks that appear as shoulders are identified as (00l) BFO Bragg reflections (marked with orange *), confirming the c-axis oriented growth. To compare the crystalline quality of

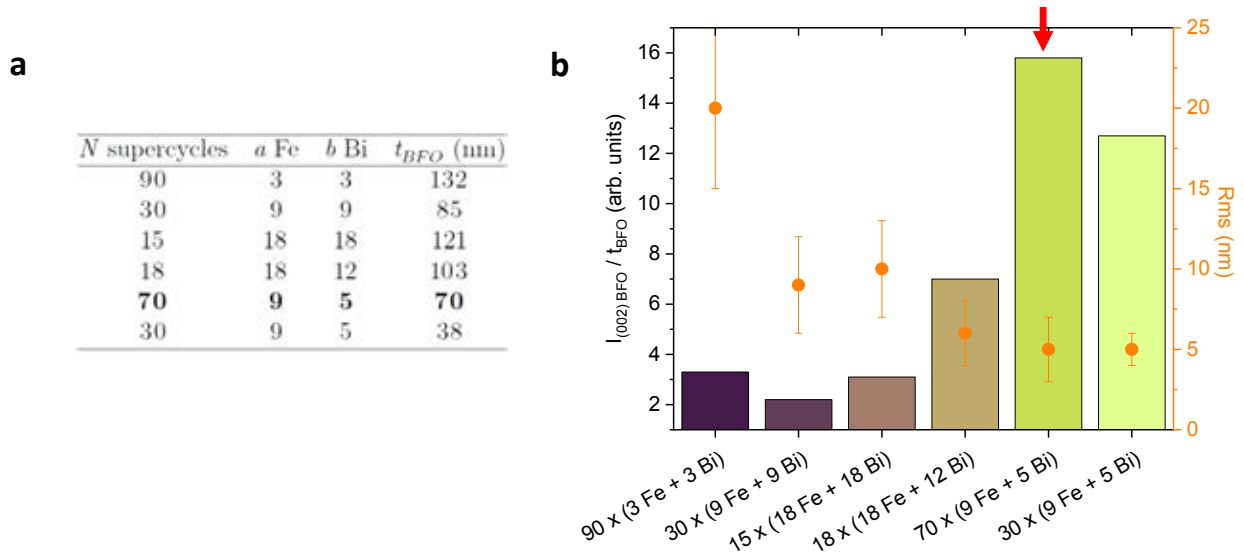


Figure 6.5: Cycling sequences used to prepare BFO-ALD on (001) STO substrates. (a) Conditions studied including the number of supercycles, N , the number of Fe-based subcycles, a , the number of Bi-based subcycles, b , and the resulting film thickness, t_{BFO} . (b) The resulting BFO crystalline quality defined by $I_{(002)BFO}/t_{BFO}$ and roughness Rms are represented for each BFO film. The red arrow indicates the optimal subcycle arrangement conditions to obtain a BFO with higher crystalline quality and lower roughness.

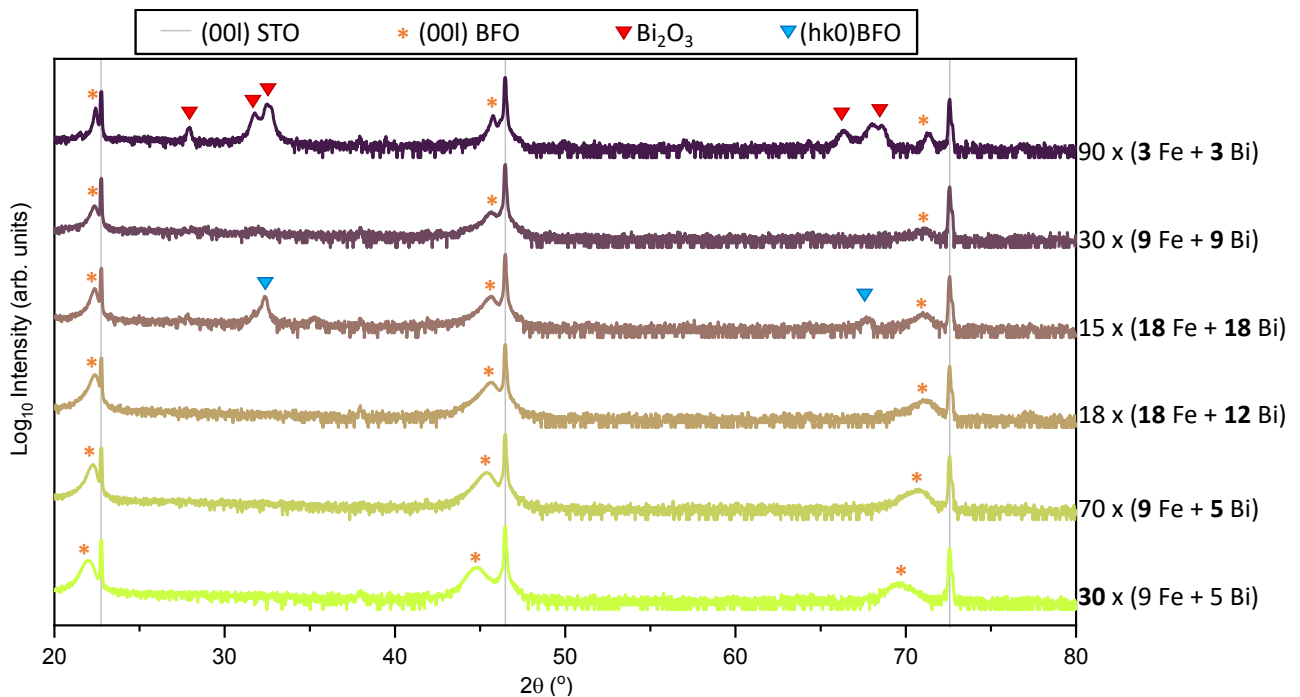


Figure 6.6: Cycling sequence effect on BFO-ALD film: XRD θ - 2θ scans of BFO//STO heterostructures deposited by ALD with different subcycle arrangements and post-annealed at 650°C.

the BFO films obtained at different conditions, the intensity of the (002) BFO Bragg reflection, $I_{(002)BFO}$, has been normalized by the BFO film thickness, t_{BFO} , and the resulting values are presented in Fig. 6.5b. Focusing on the BFO films prepared by Fe:Bi cycle ratio 1:1 (3:3, 9:9, 18:18), these are the ones that present the lowest (001) BFO intensity and some additional peaks appear at the region 25-35° and 65-70° for the (3:3) and (18:18) cycling sequences which can be attributed to Bi_2O_3 (indicated by red ∇) and $(hk0)\text{BiFeO}_3$ (indicated by blue ∇), respectively. These results show, on one hand, that too short subcycles (3:3) imply the formation of the Bi_2O_3 secondary phase which, together with the relatively high thickness, suggests that the growth of BiO_x is out of the ALD regime and it might follow a chemical vapor deposition CVD-type growth mode. Indeed, the chosen precursors $\text{Fe}(\text{ipki})_2$ and $\text{Bi}(\text{tmhd})_3$ present relatively different chemistry and their reactivity could vary depending on how they are combined, with different GPC when deposited on FeO_x or on BiO_x .²⁵¹ Note also that $\text{Bi}(\text{tmhd})_3$ is a typical precursor in CVD processes²⁵² and it is not optimal for the ALD operating conditions.²⁵³ On the other hand, long subcycles (18:18) lead to the coexistence of two preferred orientations, (001) and (hk0), a behaviour reported also in other BFO-ALD deposits.¹⁵³ Therefore, note that even having the same cycle ratio 1:1, the phases obtained are different in each case showing how the subcycle arrangement of the alternating FeO_x and BiO_x layers plays a key role to obtain pure-phase (001) BFO.^{132,249} When the cycle ratio Fe:Bi is carried out with an excess of Fe, (18:12 and 9:5), no secondary phases are detected (Fig. 6.6) and it is observed an improvement of the (001) BFO crystalline quality, specially for a Fe:Bi subcycle arrangement of 9:5 resulting a thickness of 70 nm (Fig. 6.5). This same cycle ratio (9:5) but with less number of supercycles N (from 70 to 30) results in films with 38 nm thickness. In this case, the (001) BFO Bragg reflections are also observed, with a small shift towards lower angles which is related to a more strained film.²¹⁰

The surface morphology of the BFO films deposited with different cycling sequences and post-annealed at 650°C was studied by AFM (**Figure S5**) and the rms values are presented in Fig. 6.5b. It is observed that the BFO films with a cycle ratio Fe:Bi 1:1 are composed of large grains, with diameter size ranging from 70 to 600 nm depending on the subcycle arrangement,

and all of them present very rough surface morphology with rms = 9-20 nm which could be related to the CVD-type growth. On the other hand, when the cycle ratio is modified with an excess of Fe, smoother BFO films with rms = 5 ± 1 nm and grains of 52 ± 15 nm diameter size are achieved, in agreement with other BFO-ALD reported films where by increasing the Fe content, it was obtained a transition from larger grains to closely packed smaller particles.²⁴⁹ Such surface roughness is still moderately high for ALD, which could reinforce that we are not following an ideal ALD growth mode. Based on the structural and morphological study, the cycling sequence $70 \times (9 \text{ Fe} + 5 \text{ Bi})$ has been selected as the optimal as it presents the highest (00l) BFO crystallinity with no secondary phases and a smoother surface. Moreover, note that BFO has an absorption depth of around 35 nm, therefore, this configuration is appropriate to prepare the minimum thickness required to be a suitable candidate for photoabsorber.²⁵⁴ With the optimal cycling sequence selected, we proceeded to study the influence of post-annealing temperature on the quality of the BFO film.²⁵¹

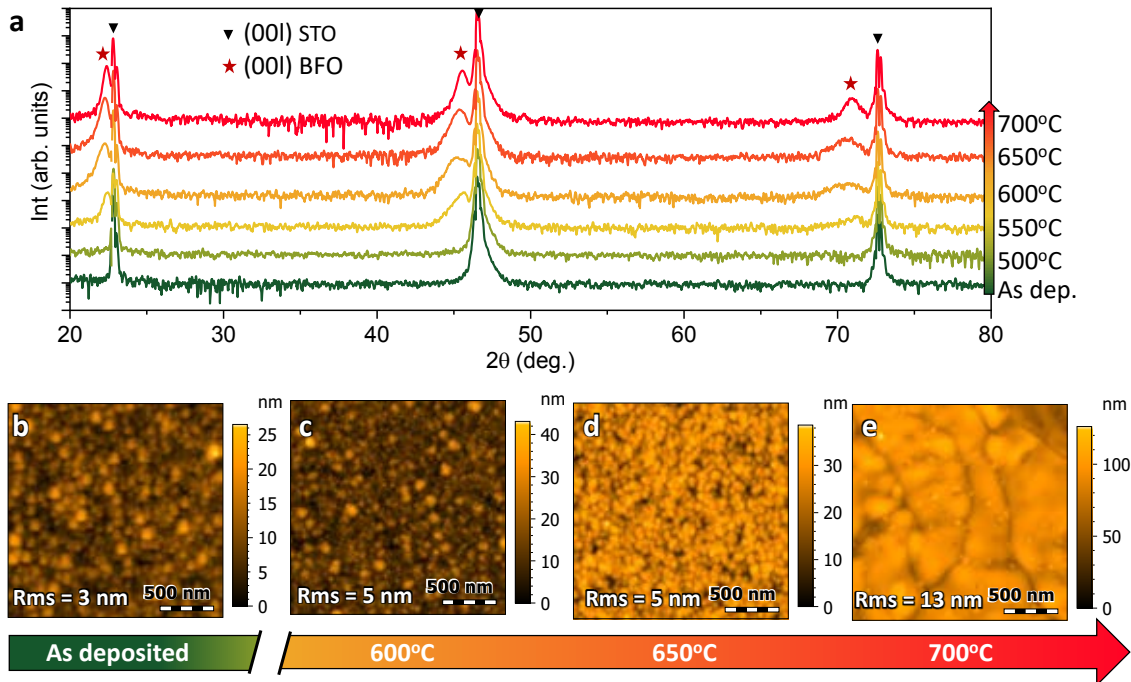


Figure 6.7: Post-annealing temperature effect on BFO-ALD films. (a) XRD θ - 2θ scans of a BFO//STO heterostructure as deposited by ALD and after treating it at different temperatures in O₂ flow. AFM topographic images of the same BFO film (b) as deposited and post-annealed at (c) 600°C, (d) 650°C and (e) 700°C.

Post-annealing temperature. The optimal post-annealing temperature to induce the epi-

taxial growth of BFO-ALD can differ depending on several factors including the substrate,²⁵⁵ the precursors used and the subcycle arrangement²⁴⁹ so it can range from 500 to 700°C (See Table S2). Here, the effect of the post-annealing temperature was investigated for the optimized 70 nm films deposited at 250°C as identified above and then post-annealed in a tubular furnace at 500°C, 550°C, 600°C, 650°C and 700°C for 30 min under 0.6 l·min⁻¹ O₂ gas flow. The resulting crystallinity and morphology of the BFO films after the post-annealing were analyzed by XRD and AFM, respectively, as shown in **Figure 6.7**. The XRD θ - 2θ scans in the range 20-80°, Fig. 6.7a, indicate that the formation of crystalline-oriented BFO growth starts at 550°C, temperature at which the (001) BFO Bragg reflections are revealed (indicated with a red star in the graph). Once nucleation started, the (001) BFO peaks become more defined and intensities increase gradually up to 700°C, indicating an improvement of the BFO crystallinity.²⁵⁶ On the other hand, the AFM topographic images of the BFO films, Fig. 6.7b-e, show that as the temperature increases, the surface roughness increases as well. Starting from a relatively smooth as-deposited BFO film with rms = 3 nm, it increases to 5 nm for the film processed at 650°C, while preserving similar grain size. However, by further increasing the temperature up to 700°C, there is a sudden change in the roughness of the layer to rms = 13 nm due to the sintering of the grains to bigger particles.^{257,258} As our interest is to use BFO as ferroelectric photoabsorber, high crystallinity and smooth surface morphology are pursued. Therefore, the optimal post-annealing treatment is chosen to be 650°C. Moreover, too high annealing temperatures could induce Bi volatilization¹⁴⁰ and increased interdiffusion when integrated in a heterostructure.⁴⁸

XPS analysis has been investigated on the BFO film prepared with the optimal crystallinity and surface morphology to verify cation ratio and oxidation states. Details on the spectra calibration and analysis are described in Chapter 2.3. High resolution Fe (2p) and Bi (4f) core levels are shown in **Figure 6.8** (a) and (b), respectively. From the Fe (2p) core level, binding energies from Fe 2p_{3/2} (724 eV), Fe 2p_{1/2} (710 eV) and the satellite peak (718 eV) were extracted indicating that Fe ions are in the valence 3+ as expected for BFO.¹⁵³ The Bi (4f) spectrum shows the Bi 4f_{5/2} and Bi 4f_{7/2} contributions centered at 164 eV and 159 eV respec-

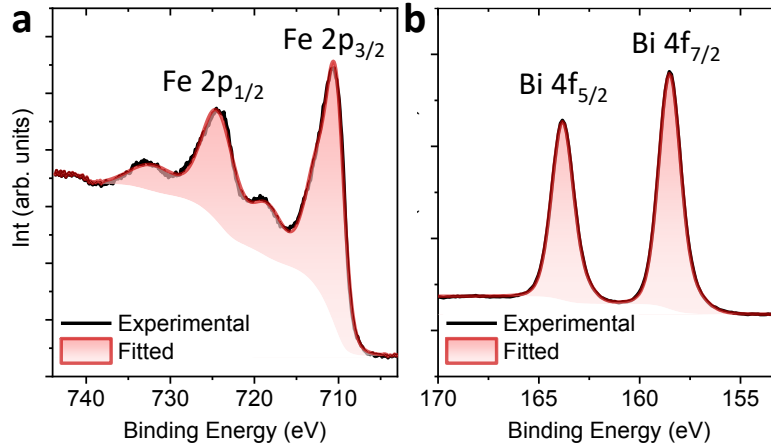


Figure 6.8: XPS spectra of a BFO-ALD film deposited on STO substrate: (a) Fe (2p) and (b) Bi (4f) core levels.

tively, characteristic of Bi³⁺ such as in Bi₂O₃ and BFO.^{153,259} From these spectra it has been obtained a cation ratio Fe:Bi of 1.1:1 indicating that the BFO-ALD presents a stoichiometry close to ideal.

6.2.4 All-oxide heterostructure

Once the ALD procedure to prepare ZnO, AZO and BFO was optimized, the next step was to study the integration of the different materials in a single all-oxide heterostructure. According to our experience in the group on the preparation of solution processed all-oxide BFO-based heterostructures for photovoltaics, the aimed device is: AZO-ALD 60 nm (transparent conducting oxide), ZnO-ALD 20 nm (electron transport layer), BFO-ALD 75 nm (photoabsorber) and LSMO-CSD 20 nm (bottom electrode) grown on a (001) STO substrate, as shown in **Figure 6.9a**. Therefore all the oxides were prepared solely by chemical methods (LSMO-CSD preparation details are explained elsewhere¹⁰³) and in this case no hole transport layer has been included. Importantly, to have access to both contacts and perform the ferroelectric and photoresponse characterization, a part of the LSMO//STO sample was masked during the ALD depositions to be later contacted. However, this process left inhomogeneities on the deposition due to a shadowing effect as shown in Fig. 6.9b. On the other hand, photolithography of the AZO contacts were prepared with sizes ranging from 40 x 40 to 300 x 300 μm², see Fig. 6.9c.

In this case we observed that the electric properties of the AZO contacts were not as good as those measured for a continuous film and it has been tentatively attributed to carbon remaining at the interface from the photolithography process. Further details of these encountered drawbacks during the preparation of the device are presented in **Figure S6**.

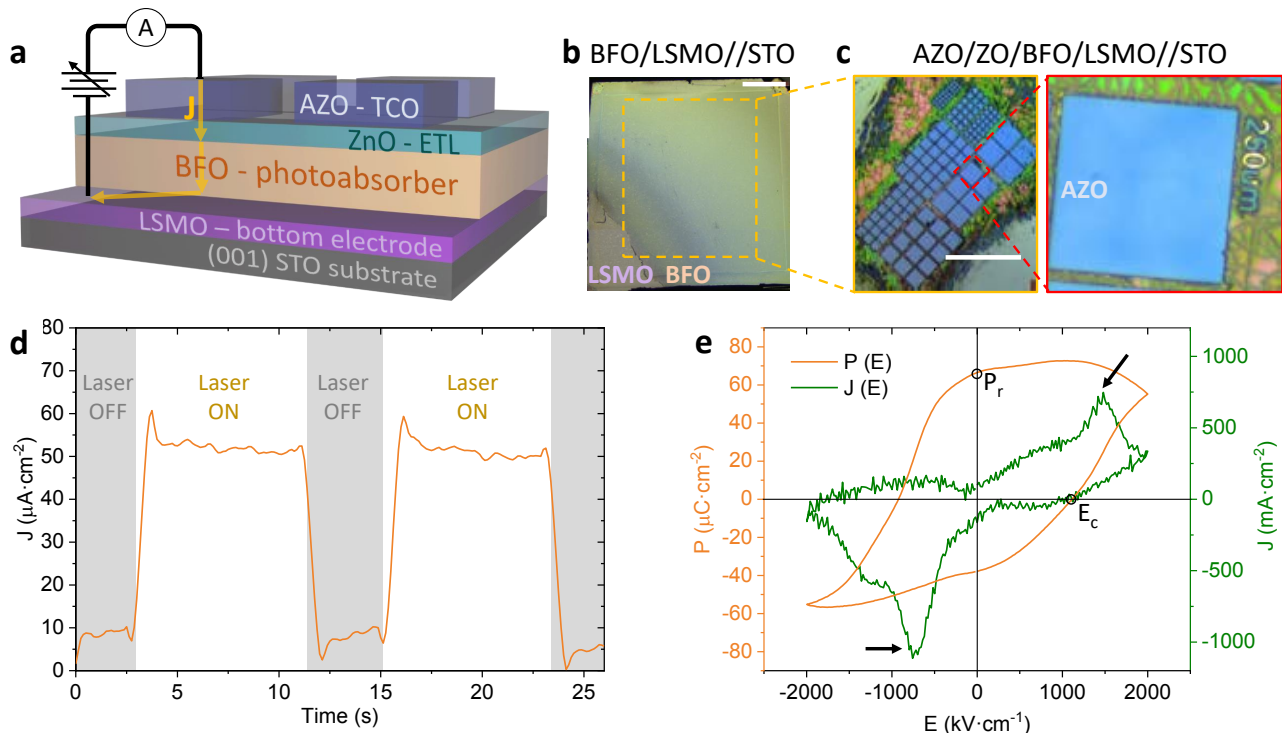


Figure 6.9: All-oxide photovoltaic device. (a) Schematic of the heterostructure prepared to test the photo- and ferroelectric responses of the device; (b) Magnified image of the heterostructure after BFO-ALD deposition, with the bottom left corner corresponding to the LSMO previously masked with polytetrafluoroethylene (PTFE) tape; (c) magnified images of the array of AZO contacts of different sizes made by photolithography. Scale bars correspond to 1 mm; (d) Photoresponse study: time dependence of the short circuit photocurrent. Light source: 405 nm laser with $380 \text{ mW}\cdot\text{cm}^{-2}$; (e) ferroelectric hysteresis $P(E)$ and current density $J(E)$ recorded at room temperature in dark at 2 kHz. The black arrows indicate the current switching peaks.

Photoresponse measurements were carried out with the contact configuration shown in Fig. 6.9a. Here, we define the positive sign of the current (J), where positive carriers flow from a $300 \times 300 \mu\text{m}^2$ AZO electrode to the bottom LSMO electrode, as indicated by the arrows. The photoresponse of the device is studied without being prepolarized by measuring the current density under laser pulses (Further details in Chapter 2, section 2.3). As shown in Fig. 6.9d, there is a significant change in current density when the laser is switched on and goes to zero

when it is switched off indicating that there is photoresponse. The response is reproducible and stable, although the magnitude of the current density is low compared to that obtained under similar conditions with BFO prepared from other deposition techniques.¹⁰³

Fig. 6.9e shows the ferroelectric hysteresis loop and the current loop of the device recorded under an applied electric field in dark on 80 x 80 μm^2 AZO contacts. The ferroelectric nature of the measured device is depicted from clear ferroelectric switching peaks (indicated by black arrows) in the current loop and the differences between the peaks could be mainly attributed to the asymmetric contacts. However, the shape of the ferroelectric loop at high applied electric fields is not well saturated and is due to residual contribution of leakage current.¹⁶⁵ The measured (P_r) and coercive field (E_c) for the BFO film are $\sim 60 \mu\text{C}\cdot\text{cm}^{-2}$ and $\sim 1000 \text{ kV}\cdot\text{cm}^{-1}$, respectively, although some residual contribution might remain.²⁶⁰ These values are in the range of what is typically obtained for BFO epitaxial films^{103,210} and it is the best macroscopic ferroelectric performance reported for an ALD-deposited BFO film in this architecture configuration.^{248,249} The ferroelectric character of the BFO-ALD film was also corroborated at the atomic scale by piezoelectric force microscopy (PFM) as shown in **Figure S7**.

Therefore, an all-chemical deposited all-oxide BFO-based photovoltaic device has been analysed for the first time, demonstrating photoresponse and ferroelectricity at room temperature. These results prove the potential of chemical methods to prepare complex oxide heterostructures. Nonetheless, further optimization would be required for the final device, starting from the process to integrate the different materials into a single device and fine tuning of the films thickness. This study will be continued in the framework of another PhD thesis recently started in the group.

6.3 Freestanding BFO-based heterostructures

This section aims to integrate the knowledge generated in the previous chapters including synthesis of sacrificial layers, preparation of epitaxial membranes and development of ALD oxide deposition processes to ultimately obtain freestanding epitaxial BFO membranes to be integrated in a photovoltaic device in the future. Three different heterostructure have been investigated to sequentially overcome the different challenges faced in the preparation of freestanding BFO as shown in **Figure 6.10**. First, it is investigated the influence of the BFO deposition technique (CSD vs ALD) on $\text{SC}_x\text{AO//STO}$, Fig. 6.10(a,b). Then, with the aim to better control interface reactivity and move towards an all-oxide heterostructure it is investigated the deposition of BFO-CSD on the previously studied system $\text{LSMO/SC}_x\text{AO//STO}$ (Chapter 5), Fig. 6.10c. Note that the study presented here was carried out in parallel to the development of Chapters 4 and 5. Consequently, when we started studying the systems represented in Fig. 6.10(a,b) (sections 6.3.1 and 6.3.2), we did not have a full understanding of the role of cation substitution and the presence of amorphous capping layer in SC_xAO sacrificials.

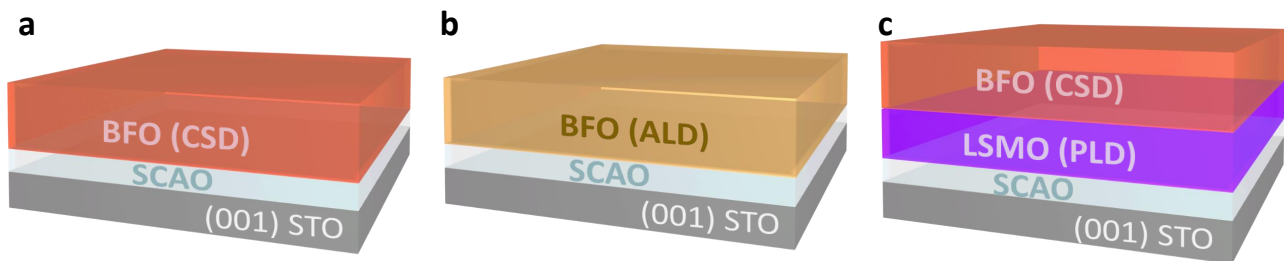


Figure 6.10: Towards freestanding BFO-based heterostructures. Sketchs of the heterostructures studied by a combination of CSD, ALD and PLD: (a) BFO-CSD on $\text{SC}_x\text{AO//STO}$, (b) BFO-CSD on $\text{SC}_x\text{AO//STO}$ and (c) BFO-CSD on $\text{LSMO-PLD/SC}_x\text{AO//STO}$.

6.3.1 BFO-CSD / SAO

To investigate the preparation of BFO membranes from SAO sacrificial layers, solution processed BFO (BFO-CSD) films were deposited on SAO//STO . The BFO precursor solution was casted by spin-coating on as-grown SAO//STO (Developed in Chapter 3) and the resulting BFO/SAO//STO heterostructure was treated up to 600 °C according to the previously opti-

mized process for BFO-CSD films¹⁰³ (BFO-CSD process described in detail in Chapter 2.1.1). In **Figure 6.11a**, XRD θ - 2θ patterns of the heterostructure at different stages of the process show the (00l) Bragg reflections of the STO substrate. First, when 20 nm thick SAO is deposited, (00l) SAO reflections appear confirming its c-axis textured growth. After the deposition of the BFO film, with expected thickness 100 nm, a group of (00l) Bragg reflections of higher intensity appears at the same region overlapping the SAO peaks. Such overlapping is predicted for (00l) BFO as its cell parameter ($a_{\text{BFO}} = 3.96 \text{ \AA}$)²⁶¹ is very close to that of SAO ($a_{\text{SAO}} = 3.96 \text{ \AA}$), but hinders an unambiguous identification of the formation of (00l) BFO films on (00l) oriented SAO film. The surface morphology of the sample after depositing the BFO-CSD layer was analyzed by AFM topographic images, see Fig. 6.11b. The analysis shows a surface roughness Rms of $\sim 8 \text{ nm}$ and an average grain diameter of $120 \pm 20 \text{ nm}$. Note that the surface roughness is higher than the BFO-CSD grown on bare STO (2-3 nm).¹⁰³

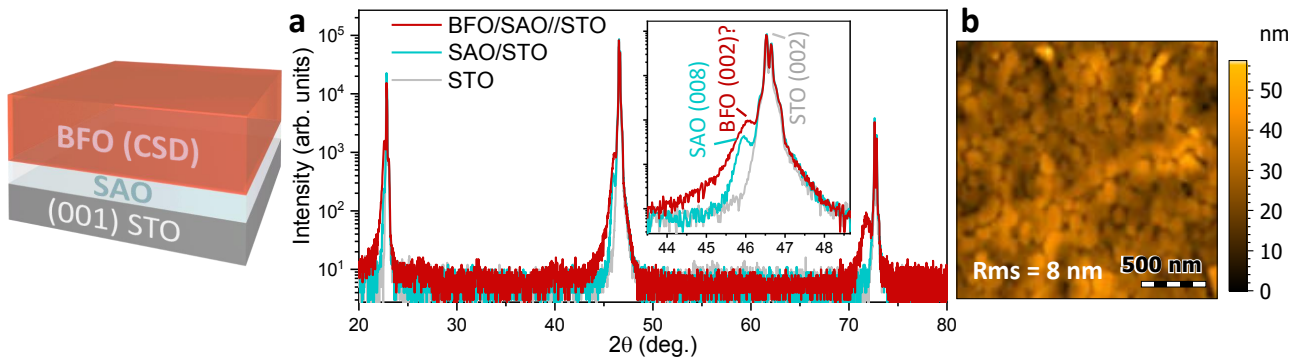


Figure 6.11: BFO-CSD / SAO //STO heterostructure. (a) XRD θ - 2θ scan of a BFO/SAO//STO heterostructure after the deposition and annealing of each layer. Inset corresponding to a magnification of the 2θ 44-48° range. (b) $2\mu\text{m} \times 2\mu\text{m}$ AFM topographic image of a BFO/SAO//STO heterostructure.

With the aim to obtain a freestanding BFO film from the BFO/SAO//STO heterostructure, this system was immersed in Milli-Q H_2O to etch the SAO sacrificial layer. However, no apparent SAO etching was achieved even after a long immersion time (several weeks). HAADF-STEM of the cross-section of the BFO/SAO//STO heterostructure, shown in **Figure 6.12a**, revealed the formation of a nanocomposite with squared-shape nanoparticles embedded in a matrix, instead of having discrete BFO/SAO layers. As shown by EELS elemental mapping in Fig.

6.12b, the composition of the nanoparticles is mainly Al and Sr, while the matrix is FeO_x rich and according to the XRD θ - 2θ scan it is very likely that the composition would be BiFeO_3 . Interestingly, as shown in Fig. 6.12c, both matrix and nanoparticles appears to be crystalline and oriented with perovskite structures. The formation of the nanocomposite would explain the impossibility to release the membrane upon immersing it in water. Therefore, the use of a solvent-based deposition process combined with a high temperature treatment to prepare an oxide on SAO results in an intermixing of cation species attributed to the previously described softness and easy hydrolysis of SAO (Chapter 3). According to these results, a solvent-free deposition approach for the deposition of BFO is assessed next.

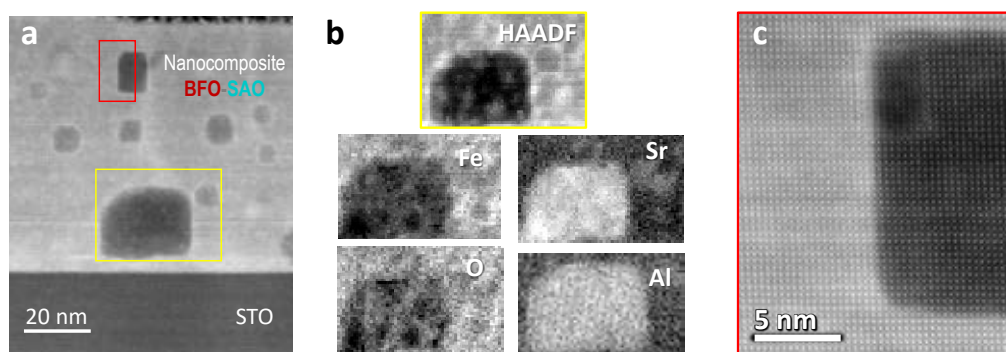


Figure 6.12: BFO-CSD/SAO nanocomposite. Z-contrast HAADF-STEM cross-section of the BFO/SAO//STO. (b) Magnification and corresponding EELS elemental mapping and (c) High resolution magnification of the BFO-SAO nanocomposite.

6.3.2 BFO-ALD / SC_2AO

The use of ALD instead of CSD to deposit BFO is attractive because (i) it uses gas phase precursors which is expected to prevent dissolution of SAO and (ii) low temperature deposition ($< 300^\circ\text{C}$) which should minimize cation interdiffusion. Both are expected to prevent the scenario described above (Section 6.3.1). However, note that a post-annealing treatment is needed after the BFO-ALD deposition to promote the epitaxial growth and here it will be investigated how it affects the system.

A 70 nm thick BFO film was deposited by ALD (BFO-ALD) on the sacrificial with the previ-

ously optimized conditions at 250 °C and then annealed in a tubular furnace at 650 °C for 30 min in a 0.6 l min⁻¹ O₂ gas flow (See section 6.2.3). Also, to further minimize reactivity of the BFO with the SAO here it is already implemented the knowledge generated in Chapter 5 and SrCa₂Al₂O₆ (SC₂AO) is used instead. It is important to remark that no vacuum annealing is performed before the ALD deposition.

Figure 6.13a shows the XRD θ - 2θ patterns of the heterostructure at different stages of the fabrication process. After depositing BFO on as-grown SC₂AO at 250°C, no extra Bragg reflections are identified besides the (001) SC₂AO and (001) STO. Therefore in this case, contrary to BFO-CSD, the integrity of the SC₂AO layer is preserved. However, after exposing the system at 650°C, the (001) SC₂AO reflections vanished and the expected (001) BFO reflections did not appear, which could indicate some reactivity may occur at the interface between the two phases. GIXRD revealed that the BFO films are polycrystalline with no traces of SC₂AO, see Fig. 6.13b. Note, that this is the same scenario previously identified for CoFe₂O₄-ALD on no-vacuum annealed SAO film (Chapter 4).

By immersing the BFO/SC₂AO//STO heterostructures with an adhered PET foil in Milli-Q water, entire BFO membranes of 5 x 5 mm² were successfully transferred with no cracks but with many wrinkles, see Fig. 6.13c. Indeed, freestanding BFO could be achieved even with no mechanical support (Freestanding BFO on Cu-grid shown in **Figure S8**). GIXRD confirmed the BFO membranes are polycrystalline as prior the lift-off (**Figure S9**). Note, on the other hand, that EDX analysis of the membrane (Fig. 6.13d) showed that along with Bi, Fe, O, the membrane also contains C, Sr, Ca and Al. The large contribution of C is attributed to the support. The presence of Sr, Ca, Al traces reinforce the previous hypothesis on cation inter-diffusion. The accomplished lift-off suggests that despite SC₂AO severely reacted during the post-annealing of BFO and probably favoring the polycrystalline growth, it did not jeopardize the release of the membrane. Therefore the use of ALD instead of CSD allows to overcome the dissolution issue. PFM analysis on BFO-ALD membranes was attempted but no ferroelectric response was detected most likely because of the lack of appropriate contact.

According to our previous studies on the presence of an amorphous capping layer and the use

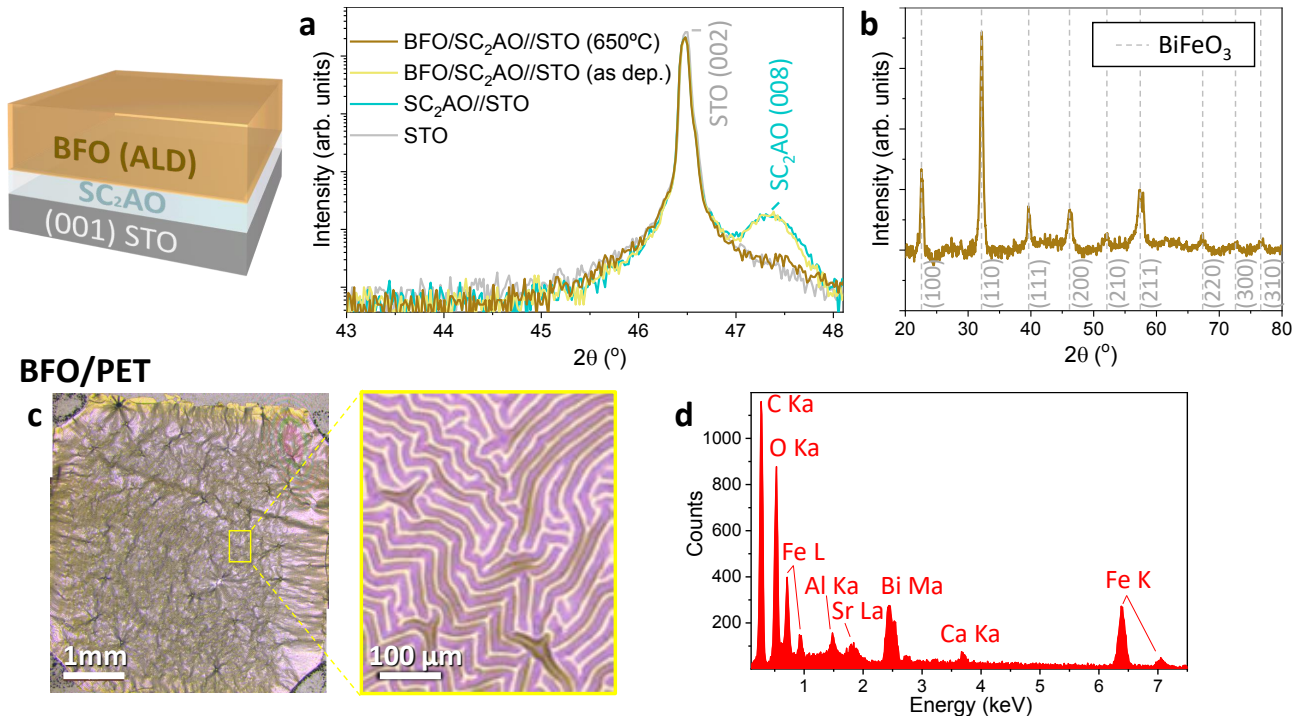


Figure 6.13: BFO-ALD / SC₂AO //STO heterostructure and subsequent membrane exfoliation. (a) XRD θ - 2θ scan of a BFO/SC₂AO//STO heterostructure at different steps of the preparation process. (b) GIXRD θ - 2θ scan of a BFO/SC₂AO//STO heterostructure after annealing at 650 °C. (c) Magnified optical microscope images of a transferred BFO membrane on a PET support and (d) EDX analysis.

of a vacuum annealing followed by in-situ deposition as a good strategy to promote epitaxial growth of the complex oxide (Chapters 4 and 5), we decided to upgrade our home-made ALD reactor to perform in-situ annealing prior the ALD deposit (details in Chapter 2). This is an ongoing work and beyond the scope of this thesis. Therefore, to progress on the preparation of epitaxial membrane-based devices, the work has been focused on the the use of the hybrid approach LSMO-PLD on SC_xAO-CSD to start building the device. Thus, the optimized LSMO-PLD/SC_xAO system was used to subsequently deposit BFO films by CSD. It is expected that using this architecture cation intermixing will be avoided and epitaxial growth promoted. I

6.3.3 BFO-CSD / LSMO / SC₂AO

Finally, the influence of solution processing of BFO on LSMO (60 nm)/SC_xAO//STO was studied by depositing 100 nm BFO-CSD film.¹⁰³ Note that in this case, SC₂AO is used as

sacrificial layer because we already identified that it leads to improved LSMO films in Chapter 5.

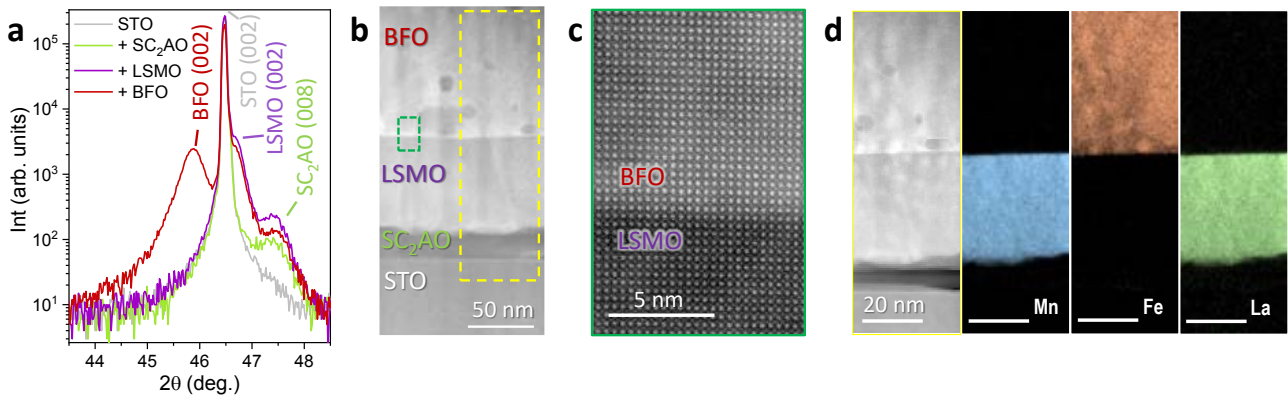


Figure 6.14: BFO-CSD/LSMO/ SC_2AO //STO heterostructure. (a) XRD θ - 2θ scan after the consecutive growth of SC_2AO , LSMO and BFO on a (001) STO substrate. (b) Z-contrast HAADF-STEM cross-section of the final heterostructure; (c) High resolution magnification of the BFO/LSMO interface; (d) EELS elemental mapping of Mn, Fe and La throughout the heterostructure cross-section.

The system was studied by XRD θ - 2θ scans after the deposition of each layer. **Figure 6.14a** shows that after the corresponding deposition, the (001) Bragg reflections for BFO, LSMO and SC_2AO are clearly identified being already a significant step forward compared to the previous approaches. It is identified an out-of-plane strain ϵ_{zz} of +0.3% for LSMO while relaxed BFO. Cross-section STEM further confirmed the fabrication of a multilayer oxide heterostructure where the three discrete layers are identified, Fig. 6.14b, although some small secondary phases are observed in the BFO film which seem to be Fe-rich. Further magnification at the BFO/LSMO interface shows the atomic structure of both phases confirming their epitaxial growth with an atomically sharp interface (Fig. 6.14c), which is confirmed by EELS elemental mapping as no cation interdiffusion is detected, see Fig. 6.14d. An analogous system consisting of BFO/LSMO/SAO//STO was also investigated in which dramatic cation interdiffusion was identified (**Figure S10**). Therefore, the synergetic contribution of LSMO-PLD layer on vacuum-annealed Ca-doped SAO helped the growth of epitaxial BFO films with sharp interface with LSMO and no cation interdiffusion.

To proceed with the release of the BFO/LSMO bilayer, the BFO/LSMO/ SC_2AO //STO het-

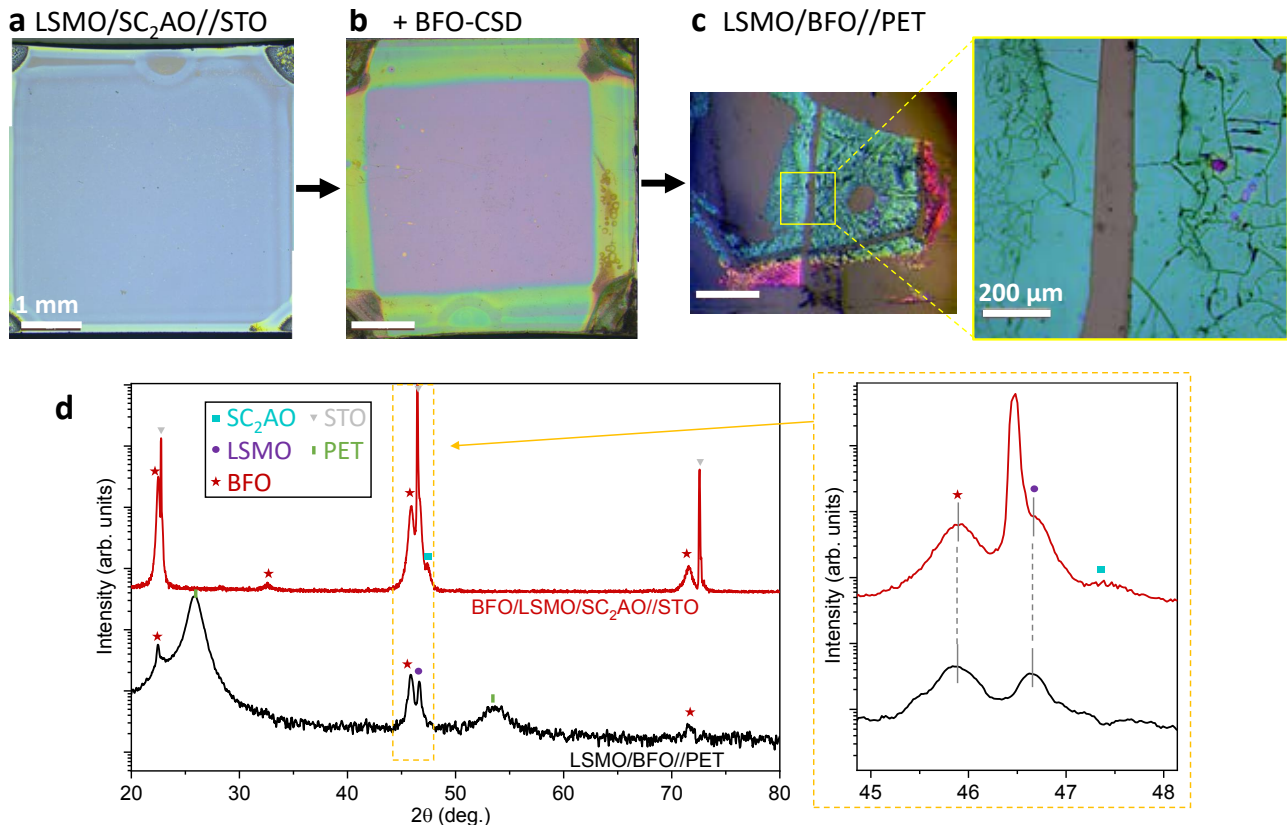


Figure 6.15: BFO-CSD/LSMO membrane on PET after SC_2AO etching. Magnified images of a LSMO/ SC_2AO //STO $5 \times 5 \text{ mm}^2$ sample (a) before and (b) after growing BFO-CSD, and (c) LSMO/BFO released membrane on PET after water immersion. (d) XRD θ - 2θ scan of a BFO/LSMO/ SC_2AO //STO heterostructure and the released BFO/LSMO membrane on a PET support. Inset corresponding to the 2θ range of the (002) STO peak.

eroheterostructure was adhered to a PET support and immersed in Milli-Q water. Although initially the lift-off was not achieved, it was found that by scratching the sample around the edges⁶¹ and increasing the Milli-Q water temperature to 85°C ,⁹¹ flakes of the released membrane could be finally adhered on a PET support. The fact that the water did not easily penetrate from the edges could be attributed to: (i) The edge effect of the BFO-CSD film, shown in **Figure 6.15a-b** and explained in Chapter 2, where the thick edge of the film could block the water penetration to dissolve the sacrificial. (ii) Also, the use of CSD could favor some solution penetration from the edges forming non-water soluble phases which do not jeopardize the formation of epitaxial BFO but it hinders the easy etching from the edges afterwards. As shown in Fig. 6.15c, the transfer yield of the released membrane is not complete and it presents several cracks. The released bilayer membrane transferred on PET shows the (001) BFO and LSMO

Bragg reflections, Fig. 6.15d, confirming that it corresponds to c-axis oriented BFO/LSMO bilayer membrane. As expected, the (008) SC₂AO reflection disappears indicating the complete etching of the sacrificial. Notably, no 2θ shifts of the BFO and LSMO Bragg reflections are observed after transfer indicating that no appreciable structural changes have occurred including no strain release. This is at odds to what observed for LSMO membranes in Chapter 5 which relaxed from its strained form to LSMO-bulk when released. The fact that here the LSMO lattice parameters do not apparently relax could be due to the fact that BFO acts as a capping layer sustaining the LSMO film partially strained.⁵¹

With the great achievement of preparing BFO/LSMO epitaxial membranes, the analysis of the ferroelectric response at the atomic scale was performed by PFM. The BFO/LSMO membranes were transferred from PET to Au/SiO₂/Si to have an available bottom contact, **Figure 6.16a**. Fig.6.16b shows the PFM-phase image of the as-prepared BFO/LSMO membrane. The observed contrast of some grains after poling at -6V and +6V indicates that these grains are ferroelectric but the film as a whole show almost no ferroelectric response. The same analysis was performed after post-annealing the BFO/LSMO membrane in oxygen (1 h at 600°C in 0.6 l·min⁻¹ O₂ flow) showing a sharp contrast in phase revealing ferroelectric behavior with better retention properties (Fig. 6.16c). The amplitude and phase signal loops of the thermally treated bilayer membrane show butterfly and 180° hysteresis loops, respectively, confirming the ferroelectric nature of the material, Fig. 6.16d.¹⁶⁴ The corresponding PFM topographic and amplitude images recorded simultaneously with the phase images are presented in **Figure S11**, demonstrating no surface degradation and suggesting that the electrochemical process at the tip-surface junction during the electric writing did not dominate the results. The improvement observed in the ferroelectric response after annealing in oxygen could be attributed to several factors including the samples surface clearing from organic contaminants, an improvement of the non-optimized ohmic contacts²⁶² or a variation of the oxygen vacancies in BFO/LSMO.^{189,190,263,264} Further analysis would be necessary to untangle the precise cause. Finally, to investigate the photoresponse of the BFO-CSD/LSMO bilayer, the device was completed with the deposition of the following device system: 70 nm ITO-RF magnetron sput-

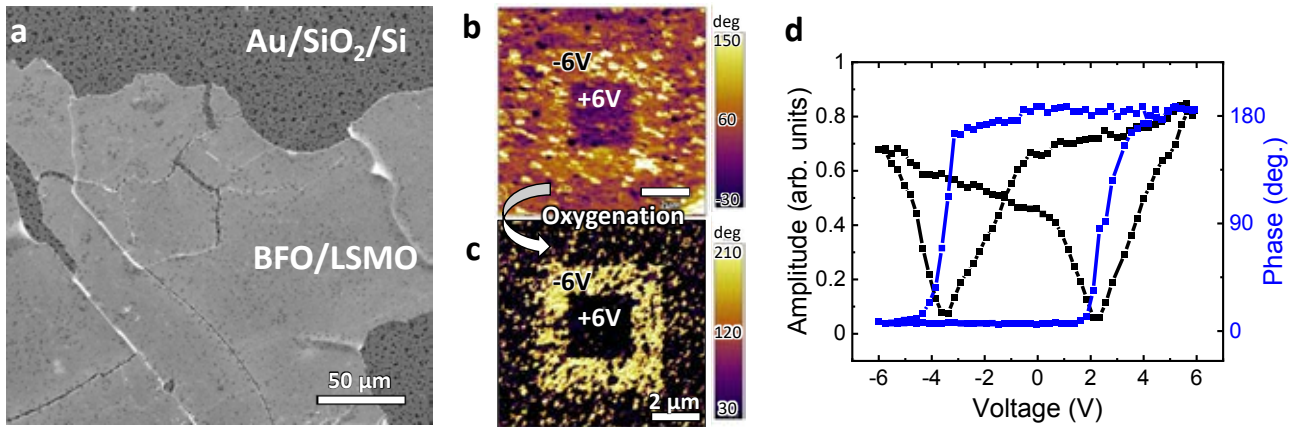


Figure 6.16: PFM analysis of BFO-CSD/LSMO membrane. (a) SEM image of a BFO/LSMO membrane on Au/SiO₂/Si substrate (b) Phase PFM images of a BFO/LSMO membrane as-transferred and (c) after oxygenation thermal treatment. (d) Amplitude and phase PFM loops for the oxygenation-treated membrane.

tering (transparent conducting electrode), 20 nm ZnO-ALD (selective layer), 100 nm BFO-CSD (photoabsorber) and 60 nm LSMO-PLD (bottom electrode) deposited on SC₂AO//STO. The system supported by a PET stamp was immersed in Milli-Q water and then transferred to a conductive substrate. As a proof of principle, although not optimal, the system was stamped on Nb-SrTiO₃ substrate. See scheme of the final device in **Figure 6.17a**. Note that ITO was used instead of the previously optimized AZO due to a break in stock of Al-precursor. Macroscopic ferroelectric characterization and photoresponse were studied from the above-mentioned membrane heterostructure upon post-annealing at 500 °C in oxygen (post-annealing temperature restricted to 500 °C to do not dramatically degrade ITO electrical properties²⁶⁵). The macroscopic ferroelectric characterization at room temperature, Fig. 6.17b, shows a distorted hysteresis loop suggesting that the ferroelectric response is merged with other phenomena such as resistance effects and leakage current which lead to an overestimated value of P_r .^{165,266} Indeed, the J peaks identified by red arrows further corroborates the high leakage current, which is likely related to the quality of the LSMO membrane compared to LSMO grown on bare STO (as demonstrated in Figure 5.5 in Chapter 5) as well as the interface quality with the other components. Therefore, here the P_r value is extracted from the ferroelectric switching peaks identified by black arrows instead (**Figure S12**).²⁶⁰ In this case, an average $P_r = 79 \mu\text{C}\cdot\text{cm}^{-2}$ is obtained which is in agreement with similar BFO films.¹⁰⁴ Regarding the $E_c \sim 220 \text{ kV}\cdot\text{cm}^{-1}$, this

value coincides with what is obtained for analogous BFO films clamped on LSMO//STO,¹⁰³ indicating that it was not affected by the release of the membrane.

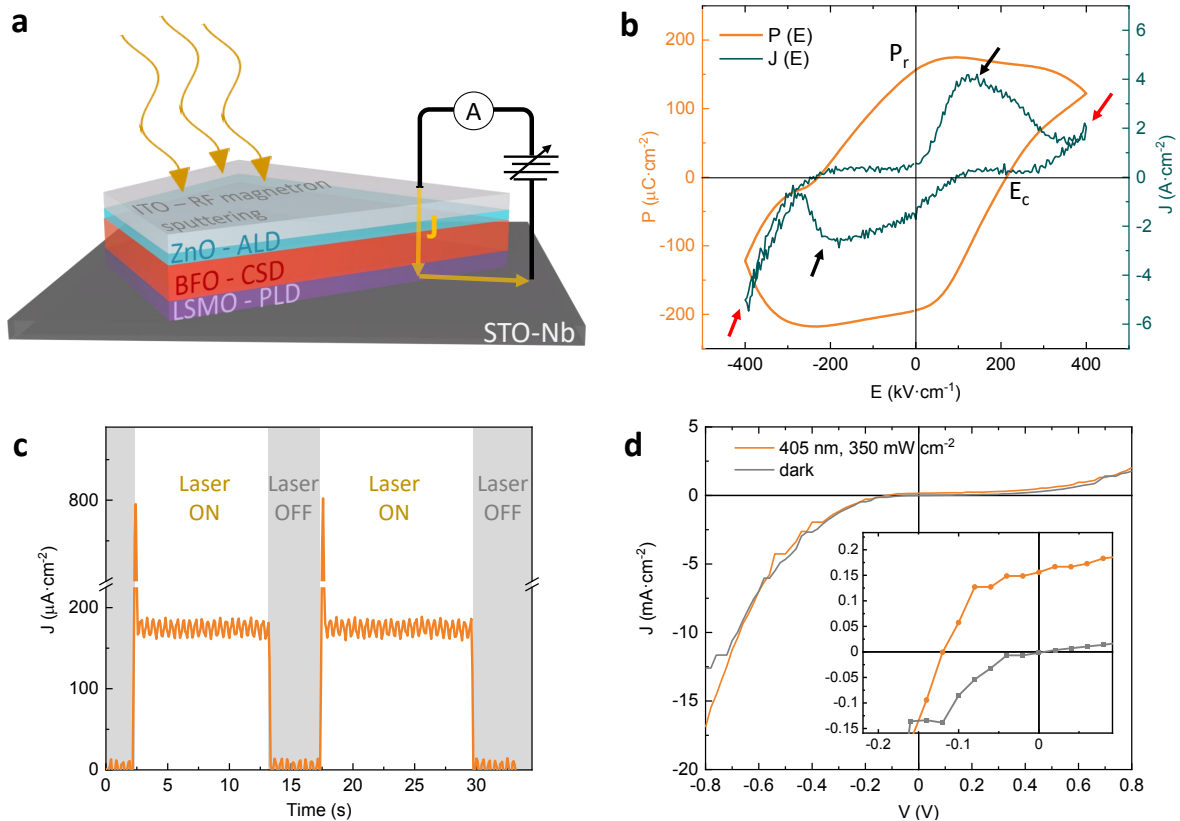


Figure 6.17: Photoferroelectric all-oxide heterostructure device from epitaxial BFO-CSD/LSMO membrane. (a) Schematic of the device prepared to test the ferroelectric and photovoltaic responses of a freestanding ITO/ZnO/BFO/LSMO flake transferred on Nb-STO; (b) Polarization hysteresis $P(E)$ and current density $J(E)$ recorded at room temperature, in dark at 2 kHz. The black arrows indicate the current switching peaks. The red arrows indicate leakage current; (c) Time dependence of the short circuit photocurrent under pulsed light. Light source: 405 nm laser with $350 \text{ mW}\cdot\text{cm}^{-2}$; (d) I-V curves for the heterostructure device in dark and under illumination (405 nm , $350 \text{ mW}\cdot\text{cm}^{-2}$).

Photoresponse measurements were carried out with the contact configuration shown in Fig. 6.17a using a laser wavelength of 405 nm and power of $350 \text{ mW}\cdot\text{cm}^{-2}$. Fig. 6.17c shows the variation of short-circuit current (J_{sc}) in dark and under illumination pulses. When the laser is off the current is zero, while under illumination fast photoresponse with stable and repeatable photocurrent is obtained. Note that the sharp increase in J_{sc} observed when the laser is switched is likely originated due to higher laser irradiance that stabilizes after ~ 50 ms. Finally, the photovoltaic response was studied with an I-V curve in dark and under

illumination as shown in Fig. 6.17d. A typical diode behavior is observed in dark, while there is a shift of the curve under illumination which indicates the generation of photoresponse. The resulting short-circuit current, open-circuit voltage and fill factor are $J_{sc} = 0.16 \text{ mA}\cdot\text{cm}^{-2}$, $V_{oc} = 0.12 \text{ V}$ and $FF = 55\%$, resulting in a power conversion efficiency (PCE) of $2\cdot 10^{-3}\%$ (Calculations detailed in **Figure S13**). Therefore, these results confirm the possibility of obtaining photoresponse from the freestanding BFO systems developed here. Future steps to maximize the performance of BFO-based photovoltaic devices might include fine tuning the BFO microstructure *e.g.* by cation substitution^{103,220} or strain tuning,^{84,232-234} optimizing the transfer process of the freestanding membrane,^{70,77} perform interface engineering to improve the contacts and decrease leakage current and ohmic contact resistances²⁶² and study different combinations of materials that compose the multilayered heterostructure.²²⁴ Currently it is under study the deposition of BFO-ALD on LSMO/SC_xAO which would be expected to further improve the properties of the system as BFO-ALD offers more homogeneous deposition and improved transfer yield.

6.4 Conclusions

This study is an important step forward towards the integration of complex oxide membranes on arbitrary substrates involving the use of chemical techniques. First it is investigated the feasibility to prepare an all-oxide photovoltaic heterostructure focusing on ALD as versatile thin film growth technique to prepare different types of simple, doped and complex oxides. Specifically, ZnO, AZO and BFO ALD processes were optimized by fine tuning the ALD operating parameters with special emphasis on the cycling sequence to finally identify and select the growth conditions to achieve optimal crystallinity, morphology and functional properties. The combination of these three ALD-developed oxides in an all-oxide rigid device with confirmed photoresponse and ferroelectricity was an unprecedented demonstration of the possibility to prepare and integrate such complex multilayer devices by all-chemical deposition techniques. In the second part of this study, all the know-how gathered in this thesis has been put together

with the goal to obtain freestanding epitaxial BFO-based heterostructures with an eye on its application in non-conventional photovoltaics. Here, CSD, ALD and PLD have been combined demonstrating the enormous impact of the deposition techniques on phenomena such as interdiffusion between phases, crystalline quality of the films and transfer yield. The growth of BFO-CSD on bare SAO has shown to form a nanocomposite because of the SC_xAO instability with solvents, while BFO-ALD allows obtaining polycrystalline BFO membranes although interdiffusion still occurs triggered by the possible amorphous capping layer of non-vacuum treated SC_xAO . Finally, growing a LSMO-PLD buffer layer on the in-situ vacuum annealed sacrificial has proven to be an effective approach to preserve the SC_xAO film from air degradation before the BFO deposition, thus partially avoiding the interdiffusion between BFO and SC_xAO and transferring epitaxy to the BFO layer grown on top. Indeed, it allowed to obtain epitaxial BFO-CSD/LSMO-PLD membranes, being the first reported freestanding epitaxial bilayer using these complementary deposition techniques. The bilayer membranes were integrated in the heterostructure ITO-sputtering/ZnO-ALD/BFO-CSD/LSMO-PLD presenting photoreponse and ferroelectricity.

In short, this study exposes the endless possibilities that lie behind the preparation of oxide heterostructures and epitaxial membranes introducing the use of chemical methods. These results envisage a broad range of possibilities of BFO allowing its integration in multilayers, including flexible devices or artificial heterostructures, strain engineering of the freestanding films to tune its physical properties and even exploit new phenomena like flexoelectricity.

6.5 Supporting Information

AZO-ALD films.

Table S1: Bibliographic summary of the optimal ALD growth conditions used to prepare AZO films as TCO.

Deposition temperature (°C)	Zn:Al cycle ratio	Total cycles / thickness (nm)	Resistivity (mΩ·cm)	Reference
200	15:1	450 / -	3 (glass)	242
200	19:1	- / 45	2.2	227
200	20:1	200 / 40	1	267
150	24:1	- / 90	0.57	246
300	5:1	180 / -	0.6	244
220	24:1	700 / 71	0.8	228
160	20:1	500 / 63	6	This work

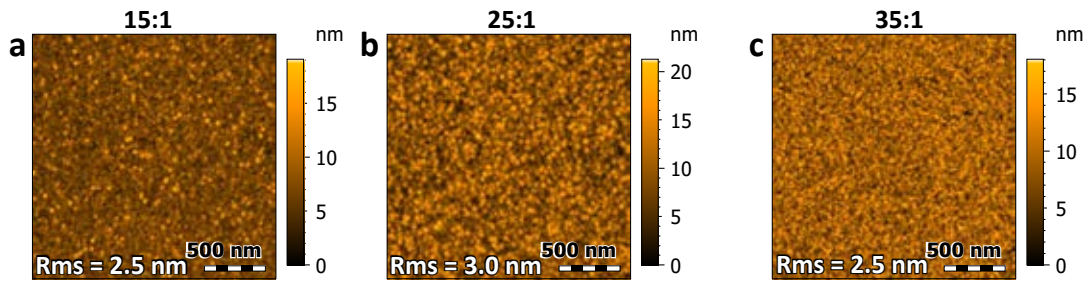


Figure S1: AFM topographic images of AZO films with different Zn:Al cycle ratio.

Figure S2 shows the GIXRD analysis of AZO films deposited with different Zn:Al cycle ratio corroborating the formation of the hexagonal phase for all the compositions. However, a slight 2θ shift of all the Bragg reflections to higher angles by increasing the Al-doping is identified, which indicates a change in the lattice parameters. As shown in Fig. S2b, the lattice parameter a and c were calculated from the (100) and (002) diffraction peaks, respectively, and it can be observed a decrease of both parameters by increasing the amount of Al in ZnO. This behavior can be attributed to the difference in ionic radius of Al^{3+} (0.53 Å) and Zn^{2+} (0.74 Å). Therefore, the incorporation of Al^{3+} leads to a reduction of the lattice parameter in the ZnO phase.²⁴² On the other hand, the relative intensity of (100)/(002) Bragg reflections changes with the content of Al, see S2b. It reveals that by increasing the Al content, the (100) orientation is

preferred. This trend agrees well with a change in the distribution of surface charges that in turn determines the surface energy of the crystal planes as reported in the literature.^{245,268} Nonetheless, small variations identified in the I_{100}/I_{002} could be also due to the fact that the 160°C is the threshold temperature at which there is a change in the preferential growth orientation.²³⁶

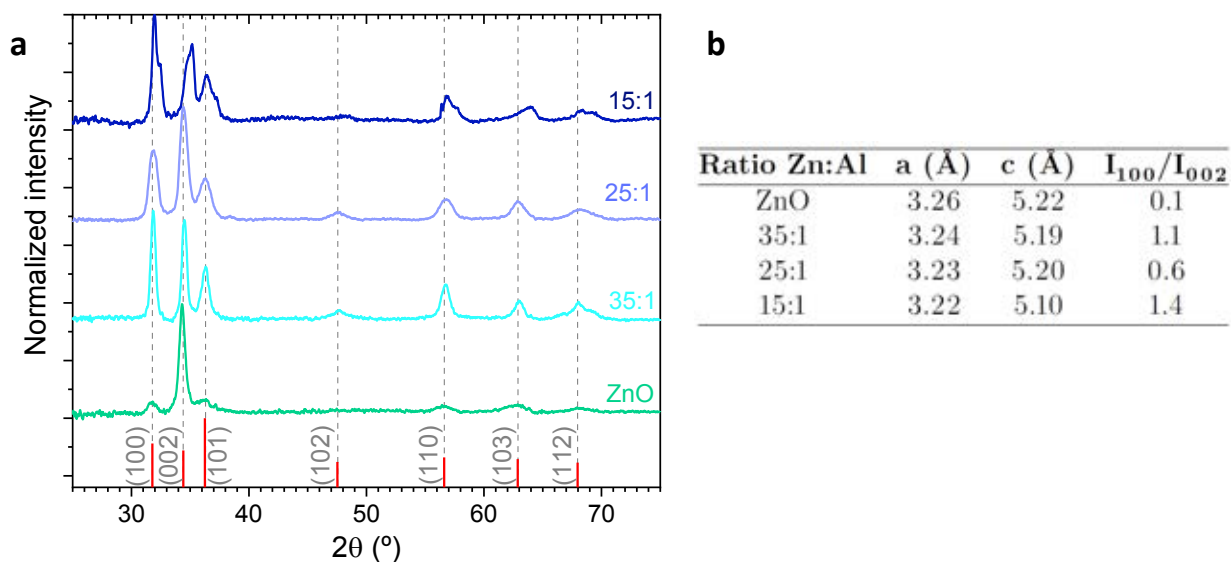


Figure S2: Influence of Al-doping in AZO crystallinity. (a) GIXRD pattern of AZO films with different Zn:Al ratio deposited on SiO₂/Si with 500 cycles at 160°C. Bulk ZnO Bragg reflections are indicated at the bottom (red). (b) Lattice parameters and intensity ratios of (100)/(002) Bragg reflections calculated from the GIXRD pattern.

Figure S3 shows the AZO films resistivity as a function of the Zn:Al ratio and the deposition temperature. For films deposited at 200 °C, the resistivity shows a different dependence with the Al concentration in ZnO showing the minimum value at 30:1 Zn:Al cycles (8 mΩ·cm). The fact that the film resistivity varies with temperature could be attributed to the different growth mechanisms²³⁶ and the variation of DEZ and TMA GPC with temperature.²⁶⁹

Figure S4a shows the XRR of AZO films deposited with different Zn:Al ratios. The Kiessig fringes identified at 2θ 1-3° are similar for all the AZO films indicating similar thickness. On the other hand, the superstructure peak (pointed with black arrow) shifts when varying the Zn:Al ratio. These superstructure peaks are useful to obtain the thickness of the multilayer separation, as presented in Fig. S4b. Note that the multilayer separation thickness decreases

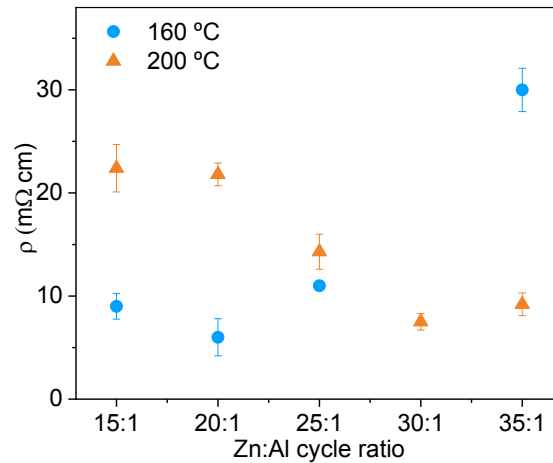


Figure S3: Deposition temperature effect on AZO films electrical properties. Resistivity of AZO films as a function of the Zn:Al cycle ratio and comparing the results obtained by films deposited at 160°C and 200°C.

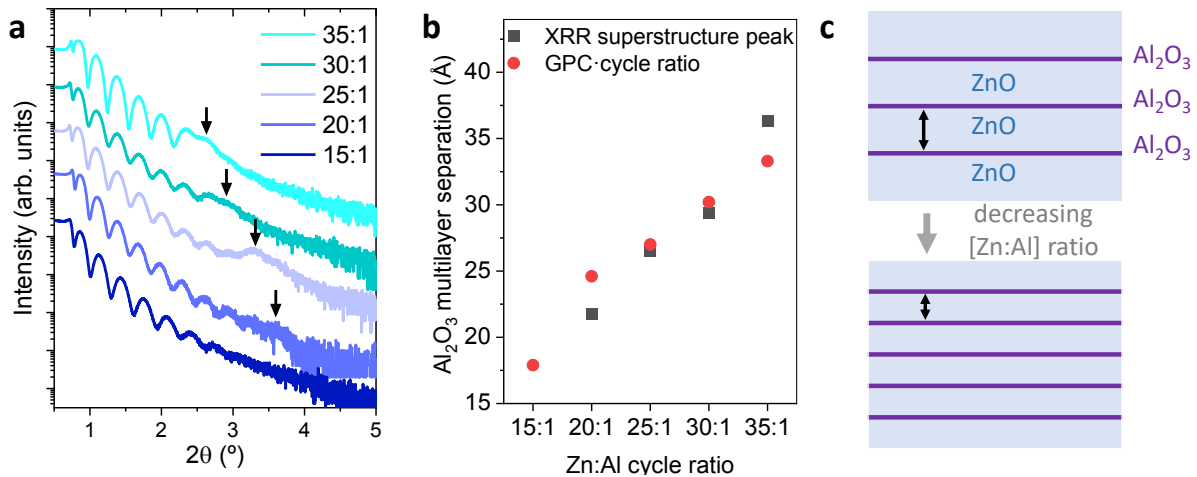


Figure S4: AZO multilayer arrangement. (a) XRR spectra of AZO films of similar thickness with different Zn:Al ratios deposited on SiO₂/Si substrates at 160°C. The arrows indicate the superstructure peak corresponding to the multilayered arrangement; (b) The Al₂O₃ multilayer separation thickness represented as a function of the Zn:Al cycle ratio according to the XRR superstructure peak and to the calculated estimated values from GPC-cycle ratio; (c) Sketches of two different ZnO:Al₂O₃ heterostructures obtained varying the Zn:Al cycle ratio. The black arrows indicate the the thickness of separation between the Al₂O₃ layers.

linearly with the cycle ratio, as expected since the number of ZnO cycles between each AlO_x cycle decreases, Fig. S4c. These values are compared to the estimated values calculated from the GPC (total thickness/total cycles) and cycle ratio (number of ZnO cycles between each AlO_x doping), showing a close resemblance and corroborating the AZO multilayer arrangement instead of an homogeneous distribution.

BFO-ALD films.**Table S2:** Bibliographic summary of BFO by ALD. Precursors used^a and their optimal Fe:Bi cycle ratio, deposition temperature and post-annealing temperature are specified.

Bi precursor	Fe precursor	Oxygen source	Fe:Bi cycle ratio	Deposition T (°C)	Post-annealing T (°C)	Reference
Bi(CH ₃) ₃	C ₆ H ₈ Fe(CO) ₃	H ₂ O	1:1	500	-	270
Bi(dmb) ₃	[Fe(OtBu) ₃] ₂	H ₂ O	1:1	150	500	271
Bi(mmp) ₃	Fe(cp) ₂	O ₃	3:5	250	660-700	256
Bi(mmp) ₃	Fe(cp) ₂	O ₃	12-22:2-3	200	600	255
Bi(tmhd) ₃	Fe(cp) ₂	O ₃	1:2	250	650	153
Bi(tmhd) ₃	Fe(tmhd) ₃	O ₃	7:2	210	650	251
Bi(dmb) ₃	[Fe(OtBu) ₃] ₂	H ₂ O	200:180	150	500	248
Bi(dmb) ₃	[Fe(OtBu) ₃] ₂	H ₂ O	200:180	140	550	272
Bi(dmb) ₃	[Fe(OtBu) ₃] ₂	H ₂ O	25-300:22-200	140	500	249
Bi(Ph) ₃	Fe(cp) ₂	O ₃	-	290	550	140
Bi(Ph) ₃	Fe(cp) ₂	O ₃	100:210	250	550	273
Bi(Ph) ₃	Fe(tmhd) ₃	O ₃	19:18	220	500	141
Bi(dmb) ₃	[Fe(OtBu) ₃] ₂	H ₂ O	-	150	600	274
Bi(tmhd) ₃	Fe(ⁱ pki) ₂	O ₃	9:5	250	650	This work

^a Bi(CH₃)₃ = Bi(III) trimethyl; Bi(dmb)₃ = Bi(III) 2,3-dimethyl 2-butoxide; Bi(mmp)₃ = Bi(III) 1-methoxy-2-methyl-2-propoxy; Bi(tmhd)₃ = Bi(III) Tris(2,2,6,6-tetramethyl-3,5-heptanedionato); Bi(Ph)₃ = Triphenyl Bi; C₆H₈Fe(CO)₃ = Cyclohexadiene Fe tricarbonyl; [Fe(OtBu)₃]₂ = Fe(III) tert-butoxide; Fe(cp)₂ = ferrocene; Fe(tmhd)₃ = Fe(III) Tris(2,2,6,6-tetramethyl-3,5-heptanedionato).

All-oxide photovoltaic device fabrication.

The fabrication of an all-oxide photovoltaic device combining different oxide-ALD layers required the use of polymeric materials as mask during the ALD preparation to make the electrical contacts and the drawbacks encountered during this process due to the use of these polymeric materials are described here. A high temperature resistant polytetrafluoroethylene (PTFE) tape was used to mask part of the LSMO during the BFO-ALD deposition and a photoresist resin was used to make AZO-ALD contacts of different sizes. As shown in Fig. 6.9b, a gradient in the color of the deposited BFO film with distance from the PTFE tape makes it clear that it had a shadowing effect on the BFO-ALD deposition. The XRD θ - 2θ scans of **Figure S6a** compare BFO/LSMO//STO with and without PTFE mask. Both scans present the (001) and

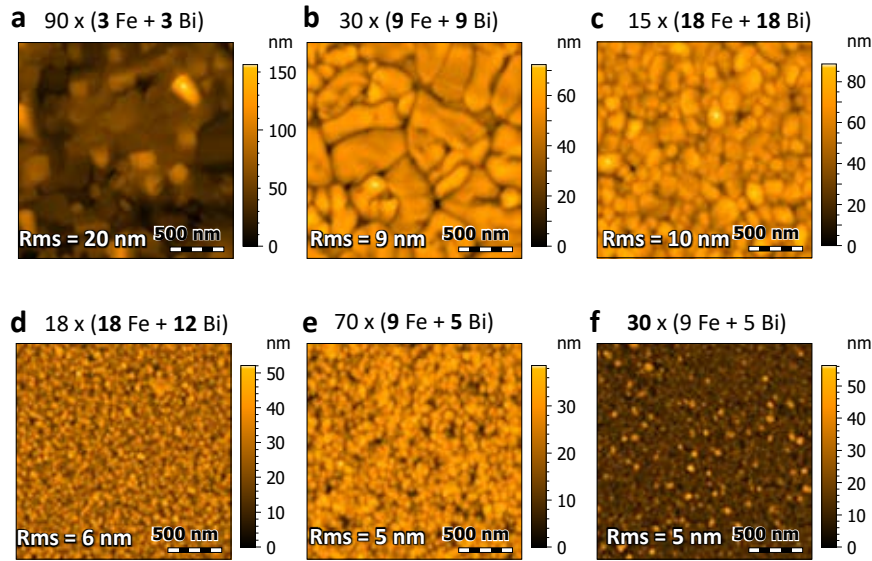


Figure S5: AFM topographic images of BFO-ALD thin films deposited on (001) STO substrates following different subcycle arrangements ($N \times (a \text{ Fe} + b \text{ Bi})$), and then annealed at 650°C .

(002) Bragg reflections of LSMO and BFO as shoulders of the (001)STO substrate, confirming that in both cases the textured growth of these oxides has been achieved. However, when the PTFE mask is present, the (001) BFO bragg reflections are less intense and a new peak appears at 35.2° which can be attributed to Fe_2O_3 , suggesting that PTFE somehow repels the BiO_x deposition making a FeO_x rich region in its vicinity and thus jeopardizing the desired Fe:Bi ratio 1:1. Regarding the AZO film, its resistivity was tested by Van der Pauw comparing the AZO deposited on a SiO_2/Si reference substrate and on the ZO/BFO/LSMO//STO heterostructure with the photolithography resin as mask. The results presented in Fig. S6b show an important increase of resistivity of the AZO film when deposited on the photovoltaic device ($38 \text{ m}\Omega\cdot\text{cm}$), compared to the expected resistivity usually obtained for the optimized AZO-ALD conditions ($6 \text{ m}\Omega\cdot\text{cm}$). This is tentatively attributed to carbon remaining from the photolithography process and requires optimization.

Towards freestanding epitaxial BFO-based heterostructures

Following the float-on approach explained in Chapter 4 for CoFe_2O_4 membranes, here after immersing the BFO/ SC_2AO //STO heterostructure a freestanding BFO membrane was obtained floating on the water surface. **Figure S8** shows a piece of the BFO membrane picked with a

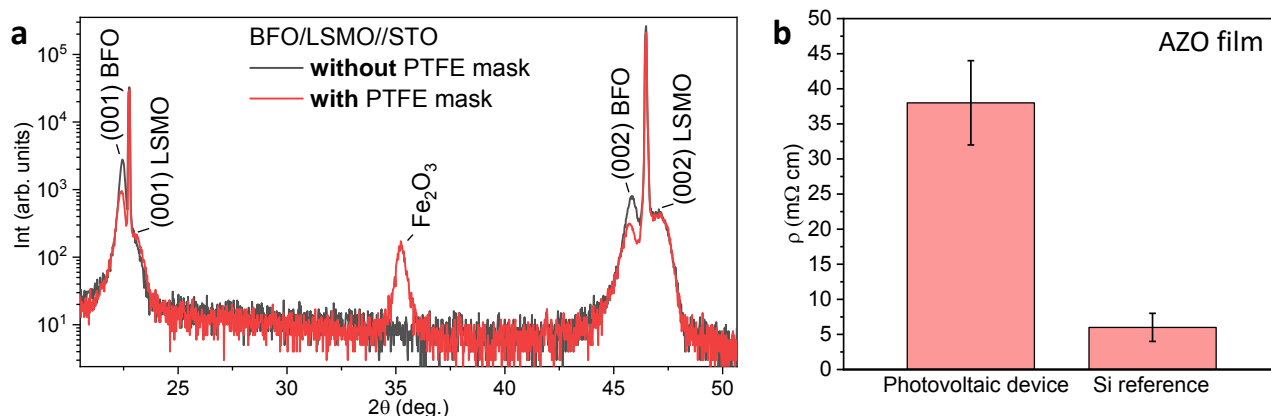


Figure S6: (a) XRD θ - 2θ scans of a BFO/LSMO//STO heterostructure with and without PTFE partially masking the LSMO film during the BFO deposition. (b) Resistivity measurements of AZO films deposited under the same ALD conditions on a SiO_2/Si substrate as reference and on the photovoltaic device composed of ZnO/BFO/LSMO//STO partially coated with photolithography resin as mask for contacts.

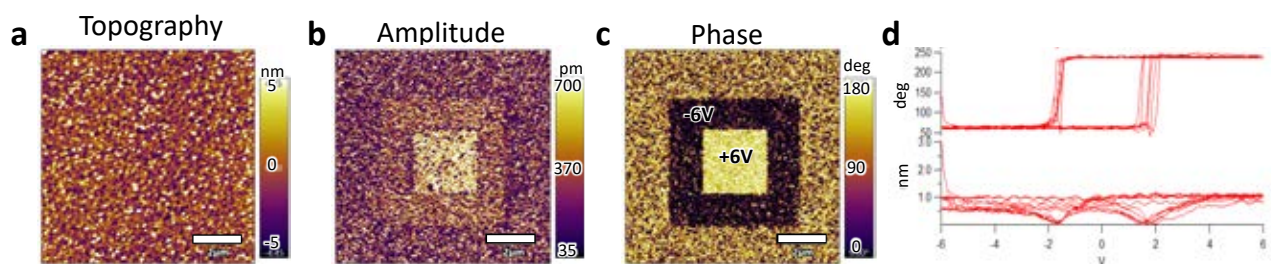


Figure S7: PFM analysis of a BFO-ALD film deposited and annealed at 650°C on LSMO-CSD//STO. (a) Topography, (b) amplitude and (c) phase images and (d) amplitude and phase PFM loops obtained after applying poling voltages of +6 and -6 V as indicated. All scale bars correspond to $2 \mu\text{m}$.

TEM Cu grid from the water surface to do further analysis.

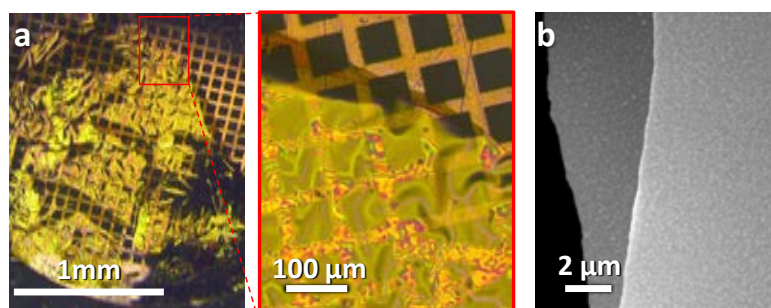


Figure S8: Float-on freestanding 70 nm BFO-ALD membrane on Cu grid (a) Magnified optical microscope images and (b) SEM image.

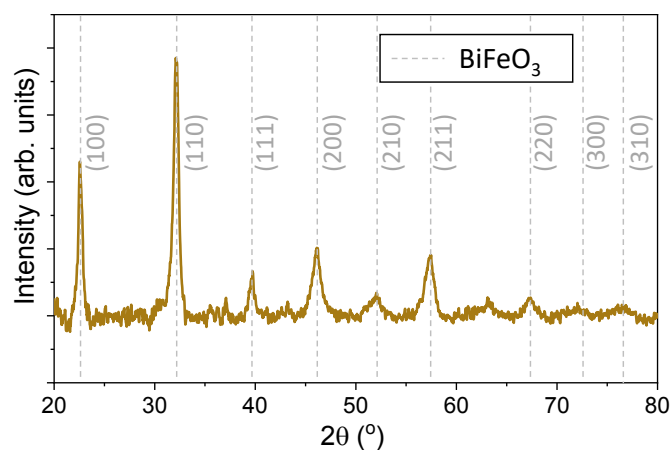


Figure S9: GIXRD analysis of 70 nm BFO-ALD membrane on PET

Figure S10 shows the structure analysis of a BFO-CSD/LSMO/SAO//STO heterostructure by XRD and STEM. An XRD θ - 2θ scan was done after the growth of each film, focusing at the region of the (002) STO Bragg reflection, Fig. S10a. The pattern obtained confirms first the textured growth of SAO and then LSMO as their (001) Bragg reflections appear as shoulders at 45.8° and 46.8° , respectively. The shift of the (008) SAO peak after growing LSMO is associated to a slight interdiffusion between them.²⁷⁵ Finally, when BFO is grown, a new intense peak at 45.8° appears, as expected for the (002) BFO Bragg reflection. Nevertheless, note that both (001) LSMO and BFO reflections are less intense than when grown on SC_2AO (Fig. 6.14, section 6.3.3), denoting a lower crystalline quality. The cross-section of the final heterostructure was analyzed by HAADF-STEM and presented in Fig. S10b-d. Fig. S10b shows a multilayer heterostructure where the SAO, LSMO and BFO films can be identified with different contrasts and a sharp interface between them. The LSMO/SAO surface is not completely homogeneous and LSMO vertical grains with different contrasts can be identified and related to different crystalline orientations.²⁷⁵ By further magnification (Fig. S10c), the atomic structure of BFO can be observed confirming its epitaxial growth. When compared to BFO-CSD directly grown on SAO, where a nanocomposite of BFO-SAO was obtained, here the LSMO successfully works as buffer layer protecting the SAO film from reacting with the BFO solution and as consequence it enables the epitaxial growth of BFO pure phase. Nevertheless, EELS elemental mapping reveals that mostly Fe but also small amounts of Mn and La cations

are found in the SAO film indicating that there has been interdiffusion of these cations during the processing. This reveals that the LSMO does not completely block the interaction between the SAO and the BFO films, as some Fe cations diffuse through the LSMO into the SAO film. The lift-off of the BFO/LSMO bilayer was attempted by immersing the entire heterostructure in Milli-Q water to etch the SAO film, but it was not achieved. The impossibility to etch the SAO film and obtain freestanding BFO/LSMO could be associated to the presence of Fe, Mn and La in the sacrificial layer, transforming it into a non-soluble phase.

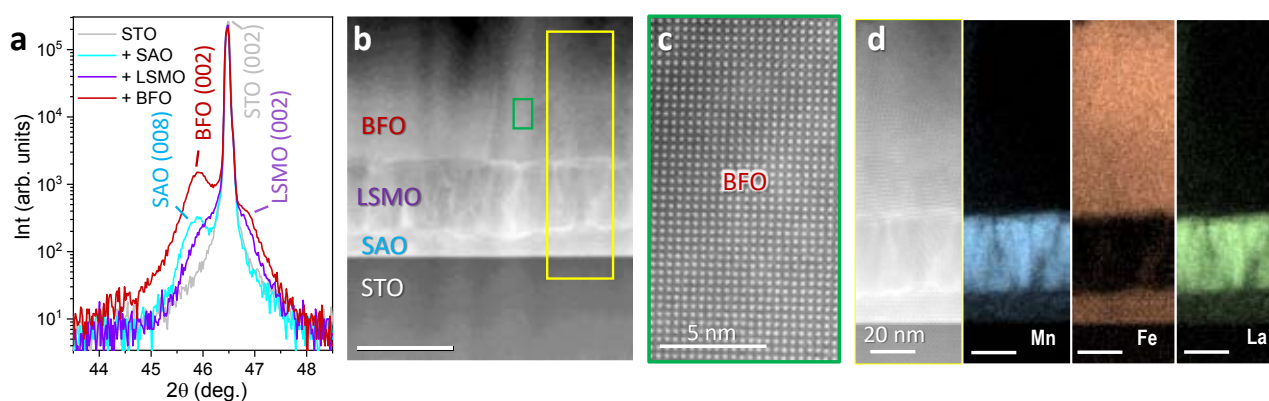


Figure S10: BFO-CSD/LSMO/SAO//STO heterostructure. (a) XRD θ - 2θ scan after the consecutive growth of SAO, LSMO and BFO on a (001) STO substrate. (b) Z-contrast HAADF-STEM cross-section of the final heterostructure. The green rectangle corresponds to (c) a high resolution magnification of the BFO film; and the yellow rectangle corresponds to (d) EELS elemental mapping of Mn, Fe and La along the heterostructure cross-section.

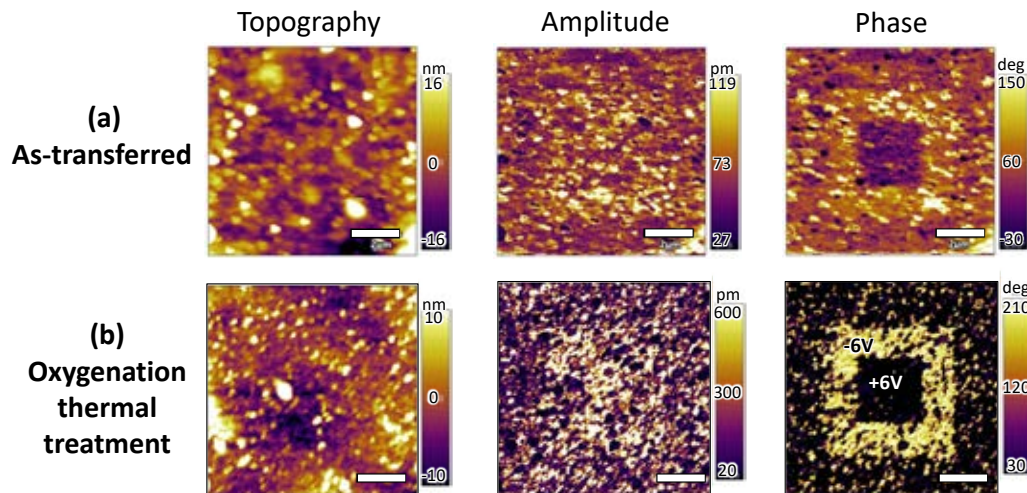


Figure S11: BFO-CSD/LSMO membrane: PFM analysis. AFM topography (left) and PFM amplitude (center) and phase (right) images obtained simultaneously from a BFO/LSMO membrane released from SC₂AO and stamped on Au/SiO₂/Si (a) as-transferred and (b) after an oxygenation annealing. All scale bars correspond to 2 μm .

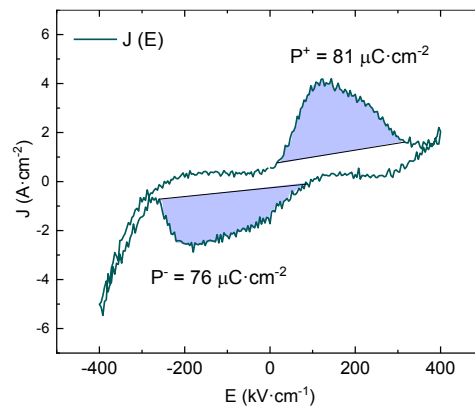
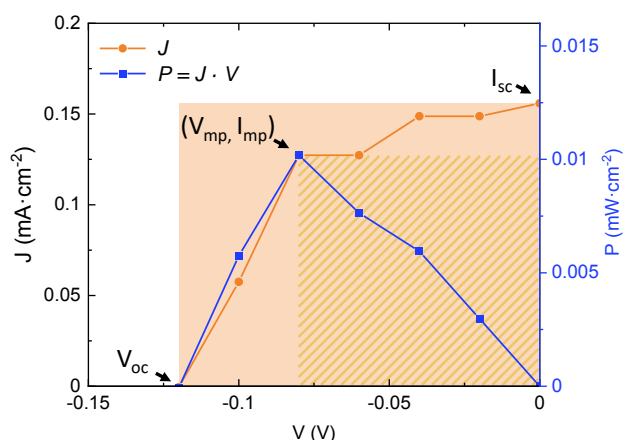


Figure S12: Macroscopic ferroelectric characterization: P_r calculation. J-E loop measured at room temperature, in dark at 2 kHz. Polarization values for positive and negative switching, evaluated from the area underneath the switching peak integrated with time ($\sim 2:P_r$, where P_r is the remanent polarization) are 81 $\mu\text{C}\cdot\text{cm}^{-2}$ and 76 $\mu\text{C}\cdot\text{cm}^{-2}$.

Figure S13 shows the quadrant of the I-V curve from Fig. 6.17d where the photovoltage takes place under illumination. The calculated power P shows a peak of maximum power P_{mp} which, together with the short-circuit current I_{sc} and the open circuit voltage V_{oc} , can be used to calculate the fill factor FF and power conversion efficiency PCE from the corresponding equations. The FF gives an idea of the "squareness" of the I-V curve which gets lowered by the different recombination mechanisms that can occur in a photovoltaic device.



$$FF = \frac{I_{mp} \cdot V_{mp}}{I_{sc} \cdot V_{oc}} = \frac{P_{mp}}{I_{sc} \cdot V_{oc}}$$

$$PCE = \frac{P_{mp}}{P_{in}} = \frac{I_{sc} \cdot V_{oc} \cdot FF}{P_{in}}$$

Figure S13: Photovoltaic characterization. I-V curve and P-V curve of a photovoltaic device based on ITO/ZnO/BFO-CSD/LSMO-PLD transferred on Nb-STO under illumination (405 nm, $P_{in} = 350 \text{ mW} \cdot \text{cm}^{-2}$). V_{oc} , I_{sc} and P_{mp} obtained from the graph are used to calculate the fill factor (FF) and power conversion efficiency (PCE) with the equations presented.

Chapter 7

Conclusions and perspectives

This thesis has been devoted to the emerging field of freestanding epitaxial oxides introducing for the first time the use of chemical deposition techniques in order to provide a cost-effective and scalable platform to investigate the enormous opportunities that complex oxide membranes can offer. I have explored the use of $\text{Sr}_3\text{Al}_2\text{O}_6$ sacrificial layer to prepare a wide variety of freestanding complex oxides including CoFe_2O_4 (CFO), $\text{La}_{0.7}\text{Sr}_{0.3}\text{MnO}_3$ (LSMO) and BiFeO_3 (BFO). The backbone of this thesis has been the development of the synthetic processes to prepare most of the oxide films and heterostructures by either atomic layer deposition (ALD) or chemical solution deposition (CSD) and identify the key parameters to ultimately control film crystallinity, morphology and stability and integrate them into a functional device.

7.1 Conclusions

Sacrificial layer development

First, it has been developed a facile and low-cost chemical route to prepare water-soluble epitaxial $\text{Sr}_3\text{Al}_2\text{O}_6$ (SAO) thin films to be used as sacrificial layer. Two solution processes based on metal nitrate and metalorganic precursors have been investigated and compared, and the metal nitrate route has been chosen as a more robust and reliable approach to obtain the SAO phase with smooth surface morphology. Nonetheless, by means of STEM and RHEED it has been identified that upon air exposure SAO generates an amorphous capping layer which is dramatic for the subsequent growth of the epitaxial oxide.

It has been performed a systematic study on the influence of Ca substitution on SAO, $\text{Sr}_{3-x}\text{Ca}_x\text{Al}_2\text{O}_6$

(SC_xAO , $x \leq 3$) by means of advanced XRD and RHEED, demonstrating that it allows to engineer the sacrificial cell parameter and increases film crystallinity. Also, this cation engineering alters the water etching rate of the sacrificial improving its ambient stability and minimizing the formation of the amorphous capping layer.

Thus, for the first time it has been developed a CSD process for reliable SC_xAO sacrificial layers.

Key role of the deposition technique and the interface

When the synthesis of the complex oxide on the sacrificial has been attempted, it has been found that the deposition technique has a key role on the resulting structure and it is also related to the quality of the underlying SC_xAO .

It turns out that direct deposit of BFO-CSD on as-prepared SAO results in an intermixing of species forming a nanocomposite consisting of an epitaxial BiFeO_3 matrix with embedded crystalline Sr-Al-O nanoparticles, as revealed by STEM and EELS analysis, due to the softness of the sacrificial layer against solvents and the high temperature treatment.

By replacing CSD by a gas-phase and low temperature process (ALD) the direct deposit of the complex oxide (CFO, BFO) on as-prepared SC_xAO sacrificial results in polycrystalline films because of the existence of an amorphous capping layer at the interface that also facilitates interface reactivity. Nonetheless, it does not impede the release of the complex oxide membrane either by using a polymer support or by floating. $M(H)$ measurements of the CFO membranes indicate robust magnetic response and comparable to the CFO/SAO//STO and CFO//STO systems.

Hybrid approach to obtain freestanding epitaxial oxides

Aiming to avoid the presence of the amorphous capping layer, an in-situ vacuum annealing prior to the deposit of the complex oxide has been proposed to successfully recrystallize the sacrificial surface. Taking advantage of this recrystallization process, it has been designed an hybrid approach consisting of the deposition of LSMO-PLD films on in-situ vacuum-annealed SC_xAO -

CSD. This approach allows to obtain epitaxial LSMO films on solution processed SC_xAO sacrificial layers, which is an unprecedented achievement as no ex-situ direct growth of an epitaxial oxide on SC_xAO had been ever reported.

Additionally, through a meticulous study of the influence of Ca-doping SAO on LSMO properties it has been found that the larger the amount of Ca in SAO the better the LSMO film crystallinity with higher compressive strain according to the mismatch. Also, the increased stability identified in SC_xAO sacrificials is found to help minimizing interfacial diffusion with LSMO. On the other hand, LSMO on SAO shows the poorest crystalline quality in the heterostructure because the presence of the amorphous capping layer was not fully reversed during the vacuum annealing.

Upon attaching the LSMO film to a polymer support and exfoliating it from the sacrificial layer, wrinkles and cracks appear as a mechanism to release the epitaxial strain originated from the different lattice mismatch between LSMO and SC_xAO . Then, these membranes can be successfully transferred to other substrates including glass and silicon.

The $\rho(T)$ measurements of the LSMO-PLD films deposited on SC_xAO have revealed that all LSMO films are metallic at room temperature and comparable to LSMO-PLD//STO. Small variations of the $\rho(T)$ behaviour could be attributed to the as-mentioned epitaxial strain but also to cation diffusion and texture quality. LSMO membranes have been integrated into glass and the lithography process has been optimized to be able to perform electrical measurements which reveals similar electrical behavior than the one identified prior the lift-off.

Multilayer heterostructures towards functional freestanding devices

Going one step further, it has been aimed to use all the gathered knowledge to ultimately develop a freestanding multilayered functional device. The envisaged device architecture involves the combination of photoferroelectric BFO with compatible oxide components (structure, chemistry, stability, electronically). Thus, the research has been first directed to develop the ALD process for the different components of the aimed device: ZnO (electron transport layer), Al-

ZnO (transparent conducting oxide) and BFO (photoabsorber). After optimizing the growth of the different oxides by ALD they have been first integrated into a rigid substrate to fabricate a non-optimized device based on all-chemical, all-oxide components showing ferroelectric and photoresponse behavior.

Then, the know-how on LSMO-PLD epitaxial membranes has been used as a platform to move towards a freestanding device. BFO-CSD deposited on LSMO-buffered $\text{SC}_x\text{AO}/\text{STO}$ results in a high quality epitaxial multilayer that can be successfully released from the growth substrate to be thereafter integrated on arbitrary substrates.

Finally, the developed BFO-CSD/LSMO-PLD epitaxial membranes have been integrated in an all-oxide heterostructure completed by the deposition of the ZnO-ALD electron transport layer and the sputtered Sn-InO_x transparent conducting oxide. This non-optimized device showed ferroelectric and photoresponse at room temperature and there have been proposed several approaches to improve the performance.

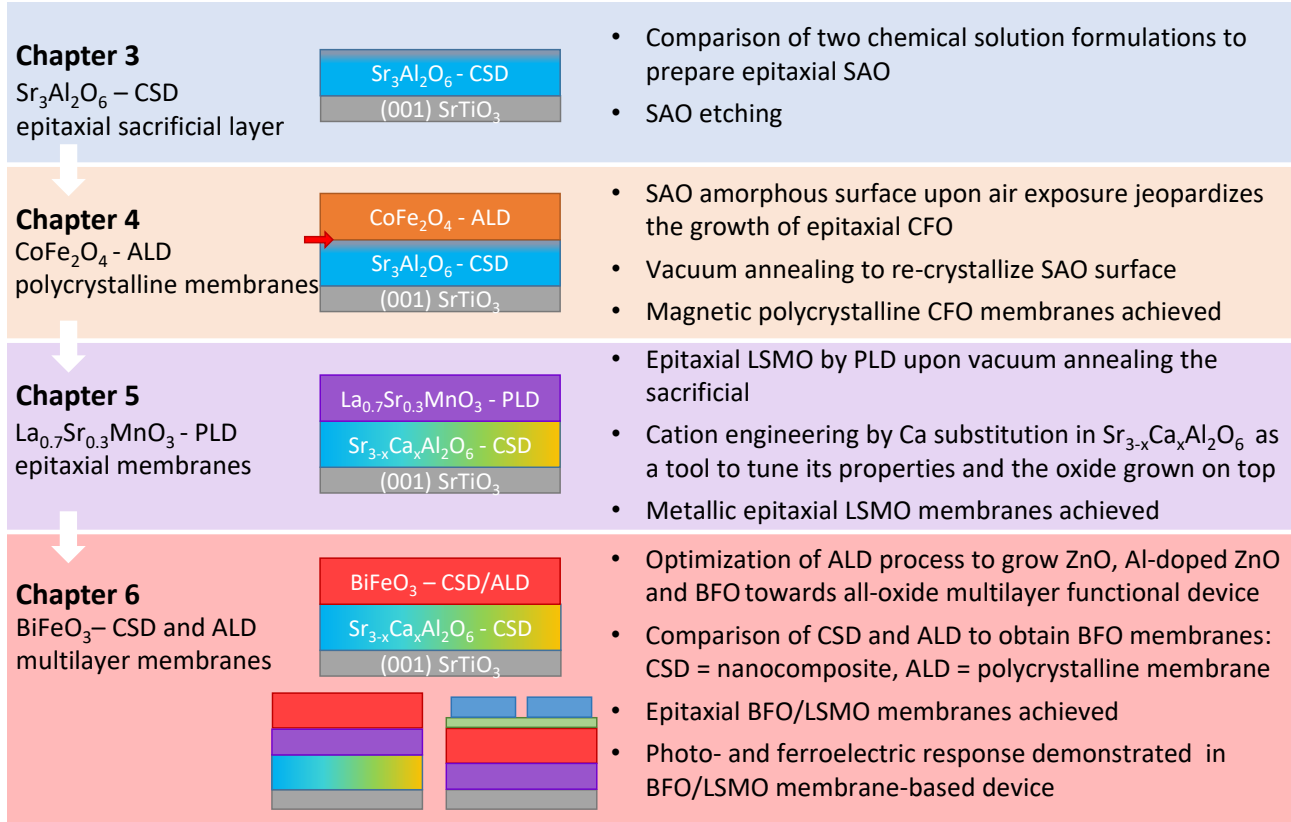


Figure 1: Summary of the main results obtained in each chapter.

7.2 Future perspectives

The development of the **SC_xAO sacrificial by CSD** appears as an appealing alternative route to the well established high-vacuum deposition techniques. SC_xAO-CSD present several advantages that make it worth to further exploit this concept. (1) The simple and low-cost process developed here can be easily integrated by other research groups to get initiated into the world of freestanding oxides. (2) The facile tuning of cation substitution of (Ba,Sr,Ca)₃Al₂O₆ by CSD could allow to easily prepare sacrificial layers with cell parameters and properties adjusted on demand. (3) The gel nature of the solution deposited sacrificial film before annealing could tentatively be used as advantage to make nanopatterned epitaxial membranes. Up to date the SC_xAO-CSD film quality is still not equated with that obtained by high-vacuum techniques, but it is envisaged that further tuning of the solution chemistry of the sacrificial, for example with polymer assisted deposition could help obtaining higher quality films.

In this work we also introduced the opportunity of **ex-situ growth** of epitaxial oxides on SC_xAO. The enhanced ambient stability of Ca-doped SAO combined with the surface recrystallization process opens the door to less restricted conditions and new deposition techniques that were inaccessible until now. It allows preparation of SC_xAO "a la carte" to broaden the range of epitaxial oxide composition and heterostructures to be delivered as membranes.

With this thesis we have pursued the goal to integrate **chemical deposition techniques** in the preparation of freestanding epitaxial complex oxide and the challenges of CSD and ALD have been investigated, to finally obtain epitaxial BFO-CSD/LSMO membranes in an hybrid approach. However, cation intermixing was identified at the interface with the sacrificial when growing the complex oxide on top (ALD, CSD and PLD). This issue remains unsolved at the end of this thesis and further studies are required. Our findings suggests that transitioning to all-ALD deposition could lead to smoother interfaces allowing in-situ annealing with a tailor-

made reactor to ultimately obtain robust heterostructures.

Furthermore, the **lift-off process** need careful optimization to improve the mechanical properties of the membranes. The use of experimental setups that allow easy exfoliation could help.

Finally, in the last chapter we introduced the idea of developing **freestanding all-oxide functional devices**. On one hand, the architecture presented as a proof of concept will be further developed in our group in the framework of a Spanish project to provide crack-free flexible photovoltaic devices. On the other hand, this creates many opportunities to investigate 2D correlated oxides and interfacial phenomena in systems that were not technically possible to fabricate. Importantly, it offers unique possibilities to control thickness and strain, in particular when transitioning to ALD processes.

To conclude, with this thesis we open new possibilities in the the emerging field of freestanding oxides, offering a feasible platform to a wider community by unfolding the challenges to prepare epitaxial complex oxide membranes by chemical methods.

Scientific Contributions

• ORCID: 0000-0003-1426-611X

• Google Scholar: Pol Sallés Perramon

Publications

P. Salles, I. Caño, R. Guzman, C. Dore, A. Mihi, W. Zhou and M. Coll. "Facile Chemical Route to Prepare Water Soluble Epitaxial $\text{Sr}_3\text{Al}_2\text{O}_6$ Sacrificial Layers for Freestanding Oxides", *Adv. Mat. Interfaces*, 2021, **8**, 5, 2001643. (Ref.¹⁷⁸)

P. Salles, R. Guzman, D. Zanders, A. Quintana, I. Fina, F. Sánchez, W. Zhou, A. Devi and M. Coll. "Bendable Polycrystalline and Magnetic CoFe_2O_4 Membranes by Chemical Methods", *ACS Appl. Mat. Interfaces*, 2022, **14**, 10, 12845-12854. (Ref.¹⁸⁰)

P. Salles, R. Guzman, A. Barrera, M. Ramis, A. Palau, W. Zhou and M. Coll. "On the role of the $\text{Sr}_{3-x}\text{Ca}_x\text{Al}_2\text{O}_6$ sacrificial layer composition for epitaxial $\text{La}_{0.7}\text{Sr}_{0.3}\text{MnO}_3$ membranes". *Adv. Funct. Mater.*, To be submitted March 2023.

Presentations and Posters

- P. Salles*, I. Caño, R. Guzmán, W. Zhou, M. Coll. "Water soluble epitaxial $\text{Sr}_3\text{Al}_2\text{O}_6$ thin films prepared by solution chemistry", *Twitter Poster Conference #IOPPposter*, Online, July **2020**, Poster.
- P. Salles*, I. Caño, R. Guzmán, W. Zhou, M. Coll. "Water soluble epitaxial $\text{Sr}_3\text{Al}_2\text{O}_6$ thin films prepared by solution chemistry for free-standing oxides", *45th International Conference and Expo on Advanced Ceramics and Composites (ICACC 2021)*, Online, February **2021**, Oral presentation.
- P. Salles*, I. Caño, R. Guzmán, W. Zhou, M. Coll. "Water soluble epitaxial $\text{Sr}_3\text{Al}_2\text{O}_6$ thin films prepared by solution chemistry for free-standing oxides", *5th Scientific Meeting of PhD Students at UAB Campus (JPhD2020)*, Online, February **2021**, Oral presentation.
- P. Salles*. "Flexible solar cells: a combination of chemistry and sacrifice", *Thesis in 4 min - UAB contest*, Bellaterra (Spain), May **2021**, Short pitch.

- P. Salles*, M. Coll. "Chemical route for freestanding complex oxides: from the preparation of $\text{Sr}_3\text{Al}_2\text{O}_6$ sacrificial layer to the final oxide properties.", *6th Scientific Meeting of PhD Students at UAB Campus (JPhD2021)*, Bellaterra (Spain), November **2021**, Oral presentation.
- P. Salles*, M. Coll. "Chemical route for freestanding complex oxides: from the preparation of $\text{Sr}_3\text{Al}_2\text{O}_6$ sacrificial layer to the final oxide properties.", *2021 MRS Fall Meeting*, Boston (USA), December **2021**, Oral presentation.
- P. Salles*, P. Machado, A. Dot, E. Dominguez, M. Coll. "Freestanding crystalline complex oxide membranes: towards flexible devices and artificial multilayered architectures", *Online meeting of Red Española de Nanolitografía (NANOLITO2022)*, Online, January **2022**, Oral presentation.
- P. Salles*, P. Machado, A. Dot, E. Dominguez, M. Coll. "Freestanding crystalline complex oxide thin films for flexible devices", *International Conference on Nanostructured Materials (NANO 2022)*, Sevilla (Spain), June **2022**, Oral presentation.

List of Abbreviations

- 2D : Two-dimensional
- 3D : Three-dimensional
- AFM : Atomic force microscopy
- ALD : Atomic Layer Deposition
- Ag : Silver
- Au : Gold
- AZO : Al-doped ZnO, Aluminium doped zinc oxide
- BFO : BiFeO₃, bismuth ferrite
- CA : Citric acid
- CFO : CoFe₂O₄, cobalt ferrite
- CSD : Chemical solution deposition
- CVD : Chemical vapour deposition
- DSC : Differential scanning calorimetry
- DTG : Derivative thermogravimetric analysis
- EDX : Energy-dispersive X-ray spectroscopy
- FWHM : Full width half maximum
- GIXRD : Grazing incidence X-ray diffraction
- GPC : Growth per cycle
- HAADF : High-angle annular dark field
- ITO : In-SnO₂, indium tin oxide
- LSMO : La_{0.7}Sr_{0.3}MnO₃, lanthanum strontium manganite
- MBE : Molecular beam epitaxy
- MOCVD : Metalorganic chemical vapour deposition
- PCE : Power conversion efficiency
- PDMS : Polydimethylsiloxane

- PET : Polyethylene terephthalate
- PFM : Piezoelectric force microscopy
- PLD : Pulsed laser deposition
- PPMS : Physical Property Measurement System
- PTFE : Polytetrafluoroethylene
- PV : Photovoltaics
- PZT : $\text{Pb}(\text{Zr}_{0.2}\text{Ti}_{0.8})\text{O}_3$
- RF : Radio frequency
- RHEED : Reflection high-energy electron diffraction
- rms : root mean square
- RSM : Reciprocal space map (also named Q-plot)
- SAO : $\text{Sr}_3\text{Al}_2\text{O}_6$, strontium aluminate
- SC_xAO : $\text{Sr}_{3-x}\text{Ca}_x\text{Al}_2\text{O}_6$
- SE : Spectroscopic ellipsometry
- SEM : Scanning electron microscopy
- Si: Silicon
- SQUID : Superconducting quantum interference device
- STEM : Scanning transmission electron microscopy
- STO : SrTiO_3 , strontium titanate
- TEM : Transmission electron microscopy
- TGA : Thermogravimetric analysis
- UV-vis : Ultraviolet-visible
- VdW : Van der Waals
- XPS : X-ray photoelectron spectroscopy
- XRD : X-ray diffraction
- XRR : X-ray reflectometry
- YBCO : $\text{YBa}_2\text{Cu}_3\text{O}_7$

List of Tables

1.1	Sacrificial layer compositions	12
1.2	(Ca, Sr, Ba) ₃ Al ₂ O ₆ characteristics	17
2.1	ALD general conditions for the deposition of A _x B _y O _z oxides. A, B = metalorganic precursors, O = co-reactant (same co-reactant chemistry used for both precursors), F = flow mode, PB = pressure-boost mode.	46
S1	Texture analysis of SC _x AO films and LSMO on SC _x AO and STO.	125
S1	Bibliographic summary of the optimal ALD growth conditions used to prepare AZO films as TCO.	160
S2	BFO-ALD: bibliographic summary	163

List of Figures

1.1	Main applications of complex oxides	3
1.2	Heteroepitaxial growth	5
1.3	Freestanding epitaxial oxide films: opportunities and applications.	6
1.4	Lift-off technologies for freestanding epitaxial oxide films.	8
1.5	Compatible sacrificial layers with epitaxial complex oxides	12
1.6	Crystal structure of $\text{Sr}_3\text{Al}_2\text{O}_6$	16
1.7	Statistics of publications about the SAO sacrificial layer	18
1.8	CSD process	21
1.9	Examples of CSD epitaxial oxides	22
1.10	ALD binary process	24
1.11	Combination of ALD cycles to prepare complex oxides	26
1.12	Periodic table of complex oxides deposited by ALD	27
1.13	Epitaxial growth of complex oxides by ALD	28
1.14	Outline of this thesis	32
2.1	CSD solution preparation	34
2.2	CSD spin coating	35
2.3	CSD thermal treatment	36
2.4	CSD equipment: spin coating N_2 chamber and tubular furnace	38
2.5	SC_xAO thermal profile	39
2.6	ALD cycle for the preparation of a binary oxide	41
2.7	ALD temperature window	42
2.8	ALD commercial Savannah 100 ALD system	43
2.9	ALD precursors	44

2.10	ALD process	45
2.11	ALD home-built equipment	47
2.12	Configuration of a PLD deposition chamber	49
2.13	XRD Bragg diffraction	54
2.14	XRD	55
2.15	Reflection high-energy electron diffraction (RHEED)	57
2.16	Sample preparation for STEM	59
2.17	Scanning electron microscopy (SEM-EDX)	60
2.18	X-Ray reflectometry (XRR)	62
2.19	SQUID setup for magnetic measurements	65
5.1	Sketch of the process followed to fabricate LSMO membranes and RHEED analysis for SAO.	112
5.2	RHEED analysis of the different SC_xAO sacrificial layers and LSMO-PLD films	113
5.3	Structural analysis of LSMO/ SC_xAO //STO heterostructures by XRD	114
5.4	Z-contrast HAADF-STEM cross-sections.	116
5.5	Temperature-dependent resistivity of LSMO/ SC_xAO //STO heterostructures . .	119
5.6	Freestanding LSMO on PET after the selective etching of the SC_xAO sacrificial layers.	120
5.7	LSMO membrane transfer to arbitrary substrates and resistivity measurements.	121
S1	AFM of SC_xAO //STO, LSMO/ SC_xAO //STO and LSMO//PET	123
S2	RHEED and AFM ambient stability analysis of SC_xAO films	124
S3	Additional XRD θ - 2θ scans for the LSMO/ SC_xAO //STO heterostructures. . . .	125
S4	STEM-EELS map of a LSMO/SAO//STO heterostructure	126
S5	Z-contrast HAADF-STEM cross-section of LSMO/ SC_1AO //STO.	126
S6	Crack density calculation of LSMO membranes	126
S7	XPS analysis of a LSMO membrane	127
S8	RHEED analysis of a $CoFe_2O_4$ grown by PLD on vacuum annealed SAO	127
6.1	Example of a thin film photovoltaic heterostructure.	132

6.2	Towards all-oxide photovoltaics: approaches followed	135
6.3	Characterization of ZnO deposits at 160 °C	136
6.4	Optical and electrical characterization of AZO films deposited at 160°C	137
6.5	Cycling sequences used to prepare BFO-ALD on (001) STO substrates.	141
6.6	Cycling sequence effect on BFO-ALD films: XRD analysis	141
6.7	Post-annealing temperature effect on BFO-ALD films	143
6.8	XPS spectra of a BFO-ALD film	145
6.9	All-oxide photovoltaic device	146
6.10	Towards freestanding BFO-based heterostructures	148
6.11	BFO-CSD / SAO //STO heterostructure	149
6.12	BFO-CSD/SAO nanocomposite	150
6.13	BFO-ALD / SC ₂ AO //STO heterostructure and subsequent membrane	152
6.14	BFO-CSD/LSMO/SC ₂ AO//STO heterostructure	153
6.15	BFO-CSD/LSMO membrane on PET after SC ₂ AO etching	154
6.16	PFM analysis of BFO-CSD/LSMO membrane	156
6.17	Photoferroelectric all-oxide heterostructure device from epitaxial BFO-CSD/LSMO membrane	157
S1	AZO: AFM topographic images of films with different Zn:Al cycle ratio	160
S2	AZO: Influence of Al-doping in crystallinity	161
S3	AZO: Deposition temperature effect on electrical properties	162
S4	AZO: XRR spectra of from different Zn:Al ratios	162
S5	BFO-ALD: Subcycle arrangement effect on surface morphology	164
S6	Encountered drawbacks in the all-oxide functional heterostructure fabrication . .	165
S7	BFO-ALD: PFM analysis	165
S8	BFO-ALD: Float-on freestanding BFO membrane on Cu grid	165
S9	BFO-ALD: GIXRD analysis of BFO membrane on PET	166
S10	BFO-CSD/LSMO/SAO//STO heterostructure	167
S11	BFO-CSD/LSMO membrane: PFM analysis	168

S12	Macroscopic ferroelectric characterization: P_r calculation	168
S13	Photovoltaic characterization: FF and PCE calculations	169
1	Summary of the main results obtained in each chapter.	174

Bibliography

- ¹ M. Coll, J. Fontcuberta, M. Althammer, M. Bibes, H. Boschker, A. Calleja, G. Cheng, M. Cuoco, R. Dittmann, B. Dkhil, I. El Baggari, M. Fanciulli, I. Fina, E. Fortunato, C. Frontera, S. Fujita, V. Garcia, S. Goennenwein, C.-G. Granqvist, J. Grollier, R. Gross, A. Hagfeldt, G. Herranz, K. Hono, E. Houwman, M. Huijben, A. Kalaboukhov, D. Keeble, G. Koster, L. Kourkoutis, J. Levy, M. Lira-Cantu, J. MacManus-Driscoll, J. Mannhart, R. Martins, S. Menzel, T. Mikolajick, M. Napari, M. Nguyen, G. Niklasson, C. Paillard, S. Panigrahi, G. Rijnders, F. Sanchez, P. Sanchis, S. Sanna, D. Schlom, U. Schroeder, K. Shen, A. Siemon, M. Spreitzer, H. Sukegawa, R. Tamayo, J. van den Brink, N. Pryds, and F. M. Granozio. Towards Oxide Electronics: a Roadmap. *Applied Surface Science*, 482:1–93, July 2019. 10.1016/j.apsusc.2019.03.312.
- ² X. Obradors and T. Puig. Coated conductors for power applications: materials challenges. *Supercond. Sci. Technol.*, 27(4):044003, April 2014. 10.1088/0953-2048/27/4/044003.
- ³ J. F. Scott. Applications of Modern Ferroelectrics. *Science*, 315(5814):954–959, February 2007. 10.1126/science.1129564.
- ⁴ D. Lu, S. Crossley, R. Xu, Y. Hikita, and H. Y. Hwang. Freestanding Oxide Ferroelectric Tunnel Junction Memories Transferred onto Silicon. *Nano Letters*, 19(6):3999–4003, June 2019. 10.1021/acs.nanolett.9b01327.
- ⁵ S. Munjal and N. Khare. Valence Change Bipolar Resistive Switching Accompanied With Magnetization Switching in CoFe_2O_4 Thin Film. *Scientific Reports*, 7(1):12427, September 2017. 10.1038/s41598-017-12579-x.
- ⁶ P. Rozier and J. M. Tarascon. Review—li-rich layered oxide cathodes for next-generation li-ion batteries: Chances and challenges. *Journal of The Electrochemical Society*, 162(14):A2490–A2499, 2015. 10.1149/2.0111514jes.
- ⁷ J. E. Spanier, V. M. Fridkin, A. M. Rappe, A. R. Akbashev, A. Polemi, Y. Qi, Z. Gu, S. M. Young, C. J. Hawley, D. Imbrenda, G. Xiao, A. L. Bennett-Jackson, and C. L. Johnson. Power conversion efficiency exceeding the Shockley–Queisser limit in a ferroelectric insulator. *Nature Photonics*, 10(9):611–616, September 2016. 10.1038/nphoton.2016.143.
- ⁸ J. Kreisel, M. Alexe, and P. A. Thomas. A photoferroelectric material is more than the sum of its parts. *Nature Materials*, 11(4):260–260, April 2012. 10.1038/nmat3282.
- ⁹ D. G. Schlom, L.-Q. Chen, C. J. Fennie, V. Gopalan, D. A. Muller, X. Pan, R. Ramesh, and R. Uecker. Elastic strain engineering of ferroic oxides. *MRS Bull.*, 39(2):118–130, February 2014. 10.1557/mrs.2014.1.
- ¹⁰ D. Pesquera, G. Herranz, A. Barla, E. Pellegrin, F. Bondino, E. Magnano, F. Sanchez, and J. Fontcuberta. Surface symmetry-breaking and strain effects on orbital occupancy in transition metal perovskite epitaxial films. *Nature Communications*, 3(1):1189, November 2012. 10.1038/ncomms2189.
- ¹¹ J. H. Haeni, P. Irvin, W. Chang, R. Uecker, P. Reiche, Y. L. Li, S. Choudhury, W. Tian, M. E. Hawley, B. Craigo, A. K. Tagantsev, X. Q. Pan, S. K. Streiffer, L. Q. Chen, S. W. Kirchoefer, J. Levy, and D. G. Schlom. Room-temperature ferroelectricity in strained SrTiO_3 . *Nature*, 430(7001):758–761, August 2004. 10.1038/nature02773.
- ¹² H. Kum, D. Lee, W. Kong, H. Kim, Y. Park, Y. Kim, Y. Baek, S.-H. Bae, K. Lee, and J. Kim. Epitaxial growth and layer-transfer techniques for heterogeneous integration of materials for electronic and photonic devices. *Nat Electron*, 2(10):439–450, October 2019. 10.1038/s41928-019-0314-2.
- ¹³ D. Rasic, J. Narayan, D. Rasic, and J. Narayan. *Epitaxial Growth of Thin Films*. IntechOpen, September 2019. 10.5772/intechopen.82745.
- ¹⁴ The interface is still the device. *Nature Materials*, 11(2):91–91, February 2012. 10.1038/nmat3244.
- ¹⁵ B. J. H. Stadler. Vapor Processes. In *Materials Processing*, pages 513–588. Elsevier, 2016. 10.1016/B978-0-12-385132-1.00007-0.
- ¹⁶ L. Dai, F. An, J. Zou, X. Zhong, and G. Zhong. Freestanding inorganic oxide films for flexible electronics. *Journal of Applied Physics*, 132(7):070904, August 2022. 10.1063/5.0103092.
- ¹⁷ G. Dong, S. Li, M. Yao, Z. Zhou, Y.-Q. Zhang, X. Han, Z. Luo, J. Yao, B. Peng, Z. Hu, H. Huang, T. Jia, J. Li, W. Ren, Z.-G. Ye, X. Ding, J. Sun, C.-W. Nan, L.-Q. Chen, J. Li, and M. Liu. Super-elastic ferroelectric single-crystal membrane with continuous electric dipole rotation. *Science*, 366(6464):475–479, October 2019. 10.1126/science.aay7221.

- ¹⁸ S. Wang, J. Xu, W. Wang, G.-J. N. Wang, R. Rastak, F. Molina-Lopez, J. W. Chung, S. Niu, V. R. Feig, J. Lopez, T. Lei, S.-K. Kwon, Y. Kim, A. M. Foudeh, A. Ehrlich, A. Gasperini, Y. Yun, B. Murmann, J. B.-H. Tok, and Z. Bao. Skin electronics from scalable fabrication of an intrinsically stretchable transistor array. *Nature*, 555(7694):83–88, March 2018. 10.1038/nature25494.
- ¹⁹ K.-I. Park, J. H. Son, G.-T. Hwang, C. K. Jeong, J. Ryu, M. Koo, I. Choi, S. H. Lee, M. Byun, Z. L. Wang, and K. J. Lee. Highly-Efficient, Flexible Piezoelectric PZT Thin Film Nanogenerator on Plastic Substrates. *Adv. Mater.*, 26(16):2514–2520, April 2014. 10.1002/adma.201305659.
- ²⁰ Y. Li, C. Xiang, F. M. Chiabrera, S. Yun, H. Zhang, D. J. Kelly, R. T. Dahm, C. K. R. Kirchert, T. E. L. Cozannet, F. Trier, D. V. Christensen, T. J. Booth, S. B. Simonsen, S. Kadhodazadeh, T. S. Jespersen, and N. Pryds. Stacking and Twisting of Freestanding Complex Oxide Thin Films. *Advanced Materials*, page 2203187, July 2022. 10.1002/adma.202203187.
- ²¹ A. J. Yang, K. Han, K. Huang, C. Ye, W. Wen, R. Zhu, R. Zhu, J. Xu, T. Yu, P. Gao, Q. Xiong, and X. Renshaw Wang. Van der Waals integration of high-k perovskite oxides and two-dimensional semiconductors. *Nat Electron*, 5(4):233–240, April 2022. 10.1038/s41928-022-00753-7.
- ²² S. S. Hong, M. Gu, M. Verma, V. Harbola, B. Y. Wang, D. Lu, A. Vailionis, Y. Hikita, R. Pentcheva, J. M. Rondinelli, and H. Y. Hwang. Extreme tensile strain states in $\text{La}_{0.7}\text{Ca}_{0.3}\text{MnO}_3$ membranes. *Science*, 368(6486):71–76, April 2020. 10.1126/science.aax9753.
- ²³ Q. Wang, J. Wang, H. Fang, Y. Chen, Y. Han, H. Liu, D. Wang, P. Zhang, C. Shi, J. Guo, B. He, L. Zheng, and W. Lü. Polarization Evolution in Morphology-Engineered Freestanding Single-Crystalline BaTiO_3 Membranes. *J. Phys. Chem. C*, page acs.jpcc.2c04404, September 2022. 10.1021/acs.jpcc.2c04404.
- ²⁴ Y. Li, E. Zatterin, M. Conroy, A. Pylypets, F. Borodavka, A. Björling, D. J. Groenendijk, E. Lesne, A. J. Clancy, M. Hadjimichael, D. Kepaptsoglou, Q. M. Ramasse, A. D. Caviglia, J. Hlinka, U. Bangert, S. J. Leake, and P. Zubko. Electrostatically Driven Polarization Flop and Strain-Induced Curvature in Free-Standing Ferroelectric Superlattices. *Advanced Materials*, 34(15):2106826, April 2022. 10.1002/adma.202106826.
- ²⁵ G. Dong, Y. Hu, C. Guo, H. Wu, H. Liu, R. Peng, D. Xian, Q. Mao, Y. Dong, Y. Zhao, B. Peng, Z. Wang, Z. Hu, J. Zhang, X. Wang, J. Hong, Z. Luo, W. Ren, Z. Ye, Z. Jiang, Z. Zhou, H. Huang, Y. Peng, and M. Liu. Self-Assembled Epitaxial Ferroelectric Oxide Nanospring with Super-Scalability. *Advanced Materials*, 34(13):2108419, April 2022. 10.1002/adma.202108419.
- ²⁶ B. Peng, R.-C. Peng, Y.-Q. Zhang, G. Dong, Z. Zhou, Y. Zhou, T. Li, Z. Liu, Z. Luo, S. Wang, Y. Xia, R. Qiu, X. Cheng, F. Xue, Z. Hu, W. Ren, Z.-G. Ye, L.-Q. Chen, Z. Shan, T. Min, and M. Liu. Phase transition enhanced superior elasticity in freestanding single-crystalline multiferroic BiFeO_3 membranes. *Sci. Adv.*, 6(34):eaba5847, August 2020. 10.1126/sciadv.aba5847.
- ²⁷ S. Cai, Y. Lun, D. Ji, P. Lv, L. Han, C. Guo, Y. Zang, S. Gao, Y. Wei, M. Gu, C. Zhang, Z. Gu, X. Wang, C. Addiego, D. Fang, Y. Nie, J. Hong, P. Wang, and X. Pan. Enhanced polarization and abnormal flexural deformation in bent freestanding perovskite oxides. *Nat Commun*, 13(1):5116, August 2022. 10.1038/s41467-022-32519-2.
- ²⁸ G. Rijnders and D. H. A. Blank. Build your own superlattice. *Nature*, 433(7024):369–370, January 2005. 10.1038/433369a.
- ²⁹ S. R. Bakaul, C. R. Serrao, M. Lee, C. W. Yeung, A. Sarker, S.-L. Hsu, A. K. Yadav, L. Dedon, L. You, A. I. Khan, J. D. Clarkson, C. Hu, R. Ramesh, and S. Salahuddin. Single Crystal Functional Oxides on Silicon. *Nat Commun*, 7(1):10547, April 2016. 10.1038/ncomms10547.
- ³⁰ T. Wang, R.-C. Peng, G. Dong, Y. Du, S. Zhao, Y. Zhao, C. Zhou, S. Yang, K. Shi, Z. Zhou, M. Liu, and J. Pan. Enhanced Energy Density at a Low Electric Field in PVDF-Based Heterojunctions Sandwiched with High Ion-Polarized BTO Films. *ACS Applied Materials & Interfaces*, 14(15):17849–17857, April 2022. 10.1021/acsami.2c02327.
- ³¹ S. Puebla, T. Pucher, V. Rouco, G. Sanchez-Santolino, Y. Xie, V. Zamora, F. A. Cuellar, F. J. Mompean, C. Leon, J. O. Island, M. Garcia-Hernandez, J. Santamaria, C. Munuera, and A. Castellanos-Gomez. Combining Freestanding Ferroelectric Perovskite Oxides with Two-Dimensional Semiconductors for High Performance Transistors. *Nano Lett.*, 22(18):7457–7466, September 2022. 10.1021/acs.nanolett.2c02395.
- ³² L. Han, Y. Fang, Y. Zhao, Y. Zang, Z. Gu, Y. Nie, and X. Pan. Giant Uniaxial Strain Ferroelectric Domain Tuning in Freestanding PbTiO_3 Films. *Advanced Materials Interfaces*, 7(7):1901604, April 2020. 10.1002/admi.201901604.
- ³³ P. Cendula, S. Kiravittaya, Y. F. Mei, C. Deneke, and O. G. Schmidt. Bending and wrinkling as competing relaxation pathways for strained free-hanging films. *Phys. Rev. B*, 79(8):085429, February 2009. 10.1103/PhysRevB.79.085429.
- ³⁴ H. Liu, H. Yuan, G. Dong, K. Wu, G. Liu, J. Sun, Z. Zhou, and M. Liu. Tunable Friction Properties of Periodic Wrinkled BaTiO_3 Membranes. *Adv Materials Inter*, page 2102316, March 2022. 10.1002/admi.202102316.
- ³⁵ L. Wang and T. Sasaki. Titanium Oxide Nanosheets: Graphene Analogues with Versatile Functionalities. *Chem. Rev.*, 114(19):9455–9486, October 2014. 10.1021/cr400627u.

- ³⁶ D. Li, H. Zhao, L. Li, B. Mao, M. Chen, H. Shen, W. Shi, D. Jiang, and Y. Lei. Graphene-Sensitized Perovskite Oxide Monolayer Nanosheets for Efficient Photocatalytic Reaction. *Adv. Funct. Mater.*, 28(52):1806284, December 2018. 10.1002/adfm.201806284.
- ³⁷ V. Nicolosi, M. Chhowalla, M. G. Kanatzidis, M. S. Strano, and J. N. Coleman. Liquid Exfoliation of Layered Materials. *Science*, 340(6139):1226419, June 2013. 10.1126/science.1226419.
- ³⁸ D. Pesquera, A. Fernandez, E. Khestanova, and L. W. Martin. Freestanding Complex-Oxide Membranes. *J. Phys.: Condens. Matter*, 34:383001, July 2022. 10.1088/1361-648X/ac7dd5.
- ³⁹ C. Gerhard and M. Stappenbeck. Impact of the Polishing Suspension Concentration on Laser Damage of Classically Manufactured and Plasma Post-Processed Zinc Crown Glass Surfaces. *Applied Sciences*, 8(9):1556, September 2018. 10.3390/app8091556.
- ⁴⁰ H. S. Kum, H. Lee, S. Kim, S. Lindemann, W. Kong, K. Qiao, P. Chen, J. Irwin, J. H. Lee, S. Xie, S. Subramanian, J. Shim, S.-H. Bae, C. Choi, L. Ranno, S. Seo, S. Lee, J. Bauer, H. Li, K. Lee, J. A. Robinson, C. A. Ross, D. G. Schlom, M. S. Rzechowski, C.-B. Eom, and J. Kim. Heterogeneous integration of single-crystalline complex-oxide membranes. *Nature*, 578(7793):75–81, February 2020. 10.1038/s41586-020-1939-z.
- ⁴¹ M. Park, B. Bae, T. Kim, H. S. Kum, and K. Lee. 2D materials-assisted heterogeneous integration of semiconductor membranes toward functional devices. *Journal of Applied Physics*, 132(19):190902, November 2022. 10.1063/5.0122768.
- ⁴² H.-J. Liu, C.-K. Wang, D. Su, T. Amrillah, Y.-H. Hsieh, K.-H. Wu, Y.-C. Chen, J.-Y. Juang, L. M. Eng, S.-U. Jen, and Y.-H. Chu. Flexible Heteroepitaxy of CoFe_2O_4 /Muscovite Bimorph with Large Magnetostriction. *ACS Appl. Mater. Interfaces*, 9(8):7297–7304, March 2017. 10.1021/acsami.6b16485.
- ⁴³ Y. Kim, S. S. Cruz, K. Lee, B. O. Alawode, C. Choi, Y. Song, J. M. Johnson, C. Heidelberger, W. Kong, S. Choi, K. Qiao, I. Almansouri, E. A. Fitzgerald, J. Kong, A. M. Kolpak, J. Hwang, and J. Kim. Remote epitaxy through graphene enables two-dimensional material-based layer transfer. *Nature*, 544(7650):340–343, April 2017. 10.1038/nature22053.
- ⁴⁴ W. Kong, H. Li, K. Qiao, Y. Kim, K. Lee, Y. Nie, D. Lee, T. Osadchy, R. J. Molnar, D. K. Gaskill, R. L. Myers-Ward, K. M. Daniels, Y. Zhang, S. Sundram, Y. Yu, S.-h. Bae, S. Rajan, Y. Shao-Horn, K. Cho, A. Ougazzaden, J. C. Grossman, and J. Kim. Polarity governs atomic interaction through two-dimensional materials. *Nature Mater*, 17(11):999–1004, November 2018. 10.1038/s41563-018-0176-4.
- ⁴⁵ Q. Gan, R. A. Rao, C. B. Eom, J. L. Garrett, and M. Lee. Direct measurement of strain effects on magnetic and electrical properties of epitaxial SrRuO_3 thin films. *Applied Physics Letters*, 72(8):978, June 1998. 10.1063/1.120603.
- ⁴⁶ Y. Qi, J. Kim, T. D. Nguyen, B. Lisko, P. K. Purohit, and M. C. McAlpine. Enhanced Piezoelectricity and Stretchability in Energy Harvesting Devices Fabricated from Buckled PZT Ribbons. *Nano Letters*, 11(3):1331–1336, March 2011. 10.1021/nl104412b.
- ⁴⁷ D. M. Paskiewicz, R. Sichel-Tissot, E. Karapetrova, L. Stan, and D. D. Fong. Single-Crystalline SrRuO_3 Nanomembranes: A Platform for Flexible Oxide Electronics. *Nano Letters*, 16(1):534–542, January 2016. 10.1021/acs.nanolett.5b04176.
- ⁴⁸ D. J. Baek, D. Lu, Y. Hikita, H. Y. Hwang, and L. F. Kourkoutis. Mapping cation diffusion through lattice defects in epitaxial oxide thin films on the water-soluble buffer layer $\text{Sr}_3\text{Al}_2\text{O}_6$ using atomic resolution electron microscopy. *APL Materials*, 5(9):096108, September 2017. 10.1063/1.4994538.
- ⁴⁹ J. J. Schermer, P. Mulder, G. J. Bauhuis, M. M. A. J. Voncken, J. van Deelen, E. Haverkamp, and P. K. Larsen. Epitaxial Lift-Off for large area thin film III/V devices. *physica status solidi (a)*, 202(4):501–508, March 2005. 10.1002/pssa.200460410.
- ⁵⁰ L. Pellegrino, M. Biasotti, E. Bellingeri, C. Bernini, A. S. Siri, and D. Marre. All-Oxide Crystalline Microelectromechanical Systems: Bending the Functionalities of Transition-Metal Oxide Thin Films. *Advanced Materials*, 21(23):2377–2381, June 2009. 10.1002/adma.200803360.
- ⁵¹ D. Pesquera, E. Parsonnet, A. Qualls, R. Xu, A. J. Gubser, J. Kim, Y. Jiang, G. Velarde, Y. Huang, H. Y. Hwang, R. Ramesh, and L. W. Martin. Beyond Substrates: Strain Engineering of Ferroelectric Membranes. *Advanced Materials*, 32(43):2003780, October 2020. 10.1002/adma.202003780.
- ⁵² D. Pesquera, E. Khestanova, M. Ghidini, S. Zhang, A. P. Rooney, F. Maccherozzi, P. Riego, S. Farokhipoor, J. Kim, X. Moya, M. E. Vickers, N. A. Stelmashenko, S. J. Haigh, S. S. Dhessi, and N. D. Mathur. Large magnetoelectric coupling in multiferroic oxide heterostructures assembled via epitaxial lift-off. *Nature Communications*, 11(1):3190, December 2020. 10.1038/s41467-020-16942-x.
- ⁵³ Y.-W. Chang, P.-C. Wu, J.-B. Yi, Y.-C. Liu, Y. Chou, Y.-C. Chou, and J.-C. Yang. A Fast Route Towards Freestanding Single-Crystalline Oxide Thin Films by Using $\text{YBa}_2\text{Cu}_3\text{O}_{7-x}$ as a Sacrificial Layer. *Nanoscale Research Letters*, 15(1):172, December 2020. 10.1186/s11671-020-03402-0.

- ⁵⁴ Y. Bourlier, B. Berini, M. Fregnaux, A. Fouchet, D. Aureau, and Y. Dumont. Transfer of Epitaxial SrTiO₃ Nanothick Layers Using Water-Soluble Sacrificial Perovskite Oxides. *ACS Applied Materials & Interfaces*, 12(7):8466–8474, February 2020. 10.1021/acsami.9b21047.
- ⁵⁵ H. Peng, N. Lu, S. Yang, Y. Lyu, Z. Liu, Y. Bu, S. Shen, M. Li, Z. Li, L. Gao, S. Lu, M. Wang, H. Cao, H. Zhou, P. Gao, H. Chen, and P. Yu. A Generic Sacrificial Layer for Wide-Range Freestanding Oxides with Modulated Magnetic Anisotropy. *Advanced Functional Materials*, page 2111907, April 2022. 10.1002/adfm.202111907.
- ⁵⁶ Y. Zhang, L. Shen, M. Liu, X. Li, X. Lu, L. Lu, C. Ma, C. You, A. Chen, C. Huang, L. Chen, M. Alexe, and C.-L. Jia. Flexible Quasi-Two-Dimensional CoFe₂O₄ Epitaxial Thin Films for Continuous Strain Tuning of Magnetic Properties. *ACS Nano*, 11(8):8002–8009, August 2017. 10.1021/acsnano.7b02637.
- ⁵⁷ R. Takahashi and M. Lippmaa. Sacrificial Water-Soluble BaO Layer for Fabricating Free-Standing Piezoelectric Membranes. *ACS Applied Materials & Interfaces*, 12(22):25042–25049, June 2020. 10.1021/acsami.0c05830.
- ⁵⁸ F. M. Chiabrera, S. Yun, Y. Li, R. T. Dahm, H. Zhang, C. K. R. Kirchert, D. V. Christensen, F. Trier, T. S. Jespersen, and N. Pryds. Freestanding Perovskite Oxide Films: Synthesis, Challenges, and Properties. *Annalen der Physik*, page 2200084, June 2022. 10.1002/andp.202200084.
- ⁵⁹ L. Shen, L. Wu, Q. Sheng, C. Ma, Y. Zhang, L. Lu, J. Ma, J. Ma, J. Bian, Y. Yang, A. Chen, X. Lu, M. Liu, H. Wang, and C.-L. Jia. Epitaxial Lift-Off of Centimeter-Scaled Spinel Ferrite Oxide Thin Films for Flexible Electronics. *Advanced Materials*, 29(33):1702411, 2017. 10.1002/adma.201702411.
- ⁶⁰ B. Zhang, C. Yun, and J. L. MacManus-Driscoll. High Yield Transfer of Clean Large-Area Epitaxial Oxide Thin Films. *Nano-Micro Letters*, 13(1):39, December 2021.
- ⁶¹ Q. Wang, H. Fang, D. Wang, J. Wang, N. Zhang, B. He, and W. Lü. Towards a Large-Area Freestanding Single-Crystal Ferroelectric BaTiO₃ Membrane. *Crystals*, 10(9):733, August 2020. 10.3390/cryst10090733.
- ⁶² J. Kang, D. Shin, S. Bae, and B. H. Hong. Graphene transfer: key for applications. *Nanoscale*, 4(18):5527–5537, August 2012. 10.1039/C2NR31317K.
- ⁶³ F. An, K. Qu, G. Zhong, Y. Dong, W. Ming, M. Zi, Z. Liu, Y. Wang, B. Qi, Z. Ding, J. Xu, Z. Luo, X. Gao, S. Xie, P. Gao, and J. Li. Highly Flexible and Twistable Freestanding Single Crystalline Magnetite Film with Robust Magnetism. *Adv. Funct. Mater.*, page 2003495, May 2020. 10.1002/adfm.202003495.
- ⁶⁴ M. Yao, Y. Li, B. Tian, Q. Mao, G. Dong, Y. Cheng, W. Hou, Y. Zhao, T. Wang, Y. Zhao, Z. Jiang, M. Liu, and Z. Zhou. Freestanding single-crystal Ni_{0.5}Zn_{0.5}Fe₂O₄ ferrite membranes with controllable enhanced magnetic properties for flexible RF/microwave applications. *J. Mater. Chem. C*, 8(47):17099–17106, 2020. 10.1039/D0TC04342G.
- ⁶⁵ A. Hiraoka, K. Fujiwara, and H. Nishikawa. Preparation of flexible thin films from epitaxially grown anatase Nb: TiO₂ using water-soluble Sr₃Al₂O₆ sacrificial layer. *Elect Comm in Japan*, 104(4), December 2021. 10.1002/ecj.12331.
- ⁶⁶ R. Xu, J. Huang, E. S. Barnard, S. S. Hong, P. Singh, E. K. Wong, T. Jansen, V. Harbola, J. Xiao, B. Y. Wang, S. Crossley, D. Lu, S. Liu, and H. Y. Hwang. Strain-induced room-temperature ferroelectricity in SrTiO₃ membranes. *Nat Commun*, 11(1):3141, December 2020. 10.1038/s41467-020-16912-3.
- ⁶⁷ J. Huang, D. Zhang, J. Liu, and H. Wang. Freestanding La_{0.7}Sr_{0.3}MnO₃:NiO vertically aligned nanocomposite thin films for flexible perpendicular interfacial exchange coupling. *Materials Research Letters*, 10(4):287–294, April 2022. 10.1080/21663831.2022.2041502.
- ⁶⁸ Z. Lu, Y. Yang, L. Wen, J. Feng, B. Lao, X. Zheng, S. Li, K. Zhao, B. Cao, Z. Ren, D. Song, H. Du, Y. Guo, Z. Zhong, X. Hao, Z. Wang, and R.-W. Li. Cooperative control of perpendicular magnetic anisotropy via crystal structure and orientation in freestanding SrRuO₃ membranes. *npj Flex Electron*, 6(1):9, December 2022. 10.1038/s41528-022-00141-3.
- ⁶⁹ G. Dong, S. Li, T. Li, H. Wu, T. Nan, X. Wang, H. Liu, Y. Cheng, Y. Zhou, W. Qu, Y. Zhao, B. Peng, Z. Wang, Z. Hu, Z. Luo, W. Ren, S. J. Pennycook, J. Li, J. Sun, Z. Ye, Z. Jiang, Z. Zhou, X. Ding, T. Min, and M. Liu. Periodic Wrinkle-Patterned Single-Crystalline Ferroelectric Oxide Membranes with Enhanced Piezoelectricity. *Advanced Materials*, 32(50):2004477, December 2020. 10.1002/adma.202004477.
- ⁷⁰ J. Bouaziz, C. Cancellieri, B. Rheingans, L. P. H. Jeurgens, and F. La Mattina. Advanced Epitaxial Lift-Off and Transfer Procedure for the Fabrication of High-Quality Functional Oxide Membranes. *Advanced Materials Interfaces*, 10(2), 2023. 10.1002/admi.202201458.
- ⁷¹ K. Gu, T. Katayama, S. Yasui, A. Chikamatsu, S. Yasuhara, M. Itoh, and T. Hasegawa. Simple Method to Obtain Large-Size Single-Crystalline Oxide Sheets. *Advanced Functional Materials*, page 2001236, May 2020. 10.1002/adfm.202001236.
- ⁷² G. Zhong, F. An, K. Qu, Y. Dong, Z. Yang, L. Dai, S. Xie, R. Huang, Z. Luo, and J. Li. Highly Flexible Freestanding BaTiO₃-CoFe₂O₄ Heteroepitaxial Nanostructure Self-Assembled with Room-Temperature Multiferroicity. *Small*, page 2104213, November 2021. 10.1002/sml.202104213.

- ⁷³ Z. Xie, Z. Li, H. Lu, Y. Wang, and Y. Liu. Etching Sr₃Al₂O₆ sacrificial layer to prepare freestanding GBCO films with high critical current density. *Ceramics International*, 47(10):13528–13532, May 2021. 10.1016/j.ceramint.2021.01.211.
- ⁷⁴ K. Han, L. Wu, Y. Cao, H. Wang, C. Ye, K. Huang, M. Motapothula, H. Xing, X. Li, D.-C. Qi, X. Li, and X. Renshaw Wang. Enhanced Metal–Insulator Transition in Freestanding VO₂ Down to 5 nm Thickness. *ACS Appl. Mater. Interfaces*, 13(14):16688–16693, April 2021. 10.1021/acsami.1c01581.
- ⁷⁵ P. Singh, A. Swartz, D. Lu, S. S. Hong, K. Lee, A. F. Marshall, K. Nishio, Y. Hikita, and H. Y. Hwang. Large-Area Crystalline BaSnO₃ Membranes with High Electron Mobilities. *ACS Appl. Electron. Mater.*, 1(7):1269–1274, July 2019. 10.1021/acsaem.9b00215.
- ⁷⁶ L. Gong, M. Wei, R. Yu, H. Ohta, and T. Katayama. Significant Suppression of Cracks in Freestanding Perovskite Oxide Flexible Sheets Using a Capping Oxide Layer. *ACS Nano*, page acsnano.2c08649, November 2022. 10.1021/acsnano.2c08649.
- ⁷⁷ R. Frisenda, E. Navarro-Moratalla, P. Gant, D. Perez De Lara, P. Jarillo-Herrero, R. V. Gorbachev, and A. Castellanos-Gomez. Recent progress in the assembly of nanodevices and van der Waals heterostructures by deterministic placement of 2D materials. *Chemical Society Reviews*, 47(1):53–68, 2018. 10.1039/C7CS00556C.
- ⁷⁸ J. A. Alonso, I. Rasines, and J. L. Soubeyroux. Tristrontium dialuminum hexaoxide: an intricate superstructure of perovskite. *Inorg. Chem.*, 29(23):4768–4771, November 1990. 10.1021/ic00348a035.
- ⁷⁹ A. S. Brand and J. W. Bullard. Dissolution Kinetics of Cubic Tricalcium Aluminate Measured by Digital Holographic Microscopy. *Langmuir*, 33(38):9645–9656, September 2017. 10.1021/acs.langmuir.7b02400.
- ⁸⁰ A. K. Prodjosantoso, B. J. Kennedy, and B. A. Hunter. Synthesis and Structural Studies of Strontium-Substituted Tricalcium Aluminate Ca_{3-x}Sr_xAl₂O₆. *Aust. J. Chem.*, 53(3):195, 2000. 10.1071/CH99142.
- ⁸¹ D. Lu, D. J. Baek, S. S. Hong, L. F. Kourkoutis, Y. Hikita, and H. Y. Hwang. Synthesis of freestanding single-crystal perovskite films and heterostructures by etching of sacrificial water-soluble layers. *Nature Mater*, 15(12):1255–1260, December 2016. 10.1038/nmat4749.
- ⁸² S. S. Hong, J. H. Yu, D. Lu, A. F. Marshall, Y. Hikita, Y. Cui, and H. Y. Hwang. Two-dimensional limit of crystalline order in perovskite membrane films. *Sci. Adv.*, 3(11):eaao5173, November 2017. 10.1126/sciadv.aao5173.
- ⁸³ H. Sun, J. Wang, Y. Wang, C. Guo, J. Gu, W. Mao, J. Yang, Y. Liu, T. Zhang, T. Gao, H. Fu, T. Zhang, Y. Hao, Z. Gu, P. Wang, H. Huang, and Y. Nie. Nonvolatile ferroelectric domain wall memory integrated on silicon. *Nat Commun*, 13(1):4332, December 2022. 10.1038/s41467-022-31763-w.
- ⁸⁴ D. Ji, S. Cai, T. R. Paudel, H. Sun, C. Zhang, L. Han, Y. Wei, Y. Zang, M. Gu, Y. Zhang, W. Gao, H. Huan, W. Guo, D. Wu, Z. Gu, E. Y. Tsymlal, P. Wang, Y. Nie, and X. Pan. Freestanding crystalline oxide perovskites down to the monolayer limit. *Nature*, 570(7759):87–90, June 2019. 10.1038/s41586-019-1255-7.
- ⁸⁵ Z. Lu, J. Liu, J. Feng, X. Zheng, L.-h. Yang, C. Ge, K.-j. Jin, Z. Wang, and R.-W. Li. Synthesis of single-crystal La_{0.67}Sr_{0.33}MnO₃ freestanding films with different crystal-orientation. *APL Materials*, 8(5):051105, May 2020. 10.1063/1.5145029.
- ⁸⁶ T. Wang, G. Dong, Y. Ma, H. Liu, Z. Zhou, and M. Liu. Stress-induced controllable magnetic properties in flexible epitaxial Mn_{0.5}Zn_{0.5}Fe₂O₄ ferrite films. *Journal of Materiomics*, 8(3):596–600, December 2021. 10.1016/j.jmat.2021.12.001.
- ⁸⁷ W. Hou, M. Yao, R. Qiu, Z. Wang, Z. Zhou, K. Shi, J. Pan, M. Liu, and J. Hu. Epitaxial lift-off of flexible single-crystal magnetite thin films with tunable magnetic performances by mechanical deformation. *Journal of Alloys and Compounds*, 887:161470, December 2021. 10.1016/j.jallcom.2021.161470.
- ⁸⁸ L. Zhang, D. Zhang, L. Jin, B. Liu, H. Meng, X. Tang, M. Li, S. Liu, Z. Zhong, and H. Zhang. Fabrication and broadband ferromagnetic resonance studies of freestanding polycrystalline yttrium iron garnet thin films. *APL Materials*, 9(6):061105, June 2021. 10.1063/5.0054595.
- ⁸⁹ Y. Chen, X. Yuan, S. Shan, C. Zhang, R. Liu, X. Zhang, W. Zhuang, Y. Chen, Y. Xu, R. Zhang, and X. Wang. Significant Reduction of the Dead Layers by the Strain Release in La_{0.7}Sr_{0.3}MnO₃ Heterostructures. *ACS Appl. Mater. Interfaces*, 14(34):39673–39678, August 2022. 10.1021/acsami.2c12899.
- ⁹⁰ P. T. P. Le, J. E. ten Elshof, and G. Koster. Epitaxial lift-off of freestanding (011) and (111) SrRuO₃ thin films using a water sacrificial layer. *Sci Rep*, 11(1):12435, December 2021. 10.1038/s41598-021-91848-2.
- ⁹¹ J. Wang, Y. Liang, Y. Wang, S. Yang, X. Zhang, X. Huang, Y. Wang, Z. Liang, J. Ma, H. Zhang, Q. Chen, J. Ma, Y.-H. Lin, and L. Wu. Refreshment of SrTiO₃ Substrate for Layer Peeling-off using Sacrificial Sr₃Al₂O₆. *Advanced Materials Interfaces*, n/a(n/a):2202111, January 2023. 10.1002/admi.202202111.

- ⁹² D. Lu, Y. Hikita, D. J. Baek, T. A. Merz, H. Sato, B. Kim, T. Yajima, C. Bell, A. Vailionis, L. F. Kourkoutis, and H. Y. Hwang. Strain Tuning in Complex Oxide Epitaxial Films Using an Ultrathin Strontium Aluminate Buffer Layer. *Phys. Status Solidi RRL*, 12(3):1700339, March 2018. 10.1002/pssr.201700339.
- ⁹³ Y. S. Kim, J. Song, C. Hwang, X. Wang, H. Wang, J. L. MacManus-Driscoll, H. Song, and S. Cho. Nanoporous Films and Nanostructure Arrays Created by Selective Dissolution of Water-Soluble Materials. *Adv. Sci.*, 5(11):1800851, November 2018. 10.1002/advs.201800851.
- ⁹⁴ R. Ning, S. Y. Jung, H. Choi, B.-h. Lee, M.-S. Kim, H.-J. Choi, J. Y. Lee, J. S. Park, S.-J. Jung, H. W. Jang, S. O. Won, H. J. Chang, J.-S. Jang, K. H. Lee, B. C. Lee, and S.-H. Baek. Selective Area Epitaxy of Complex Oxide Heterostructures on Si by Oxide Hard Mask Lift-Off. *Electronic Materials Letters*, November 2022. 10.1007/s13391-022-00386-0.
- ⁹⁵ Z.-D. Luo, M.-M. Yang, and M. Alexe. Dissolvable Memristors for Physically Transient Neuromorphic Computing Applications. *ACS Applied Electronic Materials*, 2(2):310–315, February 2020. 10.1021/acsaelm.9b00670.
- ⁹⁶ D. Dutczak, T. Jüstel, C. Ronda, and A. Meijerink. Eu²⁺ luminescence in strontium aluminates. *Physical Chemistry Chemical Physics*, 17(23):15236–15249, June 2015. 10.1039/C5CP01095K.
- ⁹⁷ J. E. ten Elshof. 4 - Chemical solution deposition techniques for epitaxial growth of complex oxides. In G. Koster, M. Huijben, and G. Rijnders, editors, *Epitaxial Growth of Complex Metal Oxides*, Woodhead Publishing Series in Electronic and Optical Materials, pages 69–93. Woodhead Publishing, January 2015. 10.1016/B978-1-78242-245-7.00004-X.
- ⁹⁸ C. Glynn and C. O'Dwyer. Solution Processable Metal Oxide Thin Film Deposition and Material Growth for Electronic and Photonic Devices. *Advanced Materials Interfaces*, 4(2):1600610, January 2017. 10.1002/admi.201600610.
- ⁹⁹ I. Bretos, R. Jimenez, J. Ricote, and M. L. Calzada. Low-temperature crystallization of solution-derived metal oxide thin films assisted by chemical processes. *Chemical Society Reviews*, 47(2):291–308, 2018. 10.1039/C6CS00917D.
- ¹⁰⁰ J. M. Vila-Funqueiriño, B. Rivas-Murias, J. Rubio-Zuazo, A. Carretero-Genevriér, M. Lazzari, and F. Rivadulla. Polymer assisted deposition of epitaxial oxide thin films. *Journal of Materials Chemistry C*, 6(15):3834–3844, 2018. 10.1039/C8TC00626A.
- ¹⁰¹ J. M. Vila-Funqueiriño, J. Gazquez, C. Magen, G. Saint-Girons, R. Bachelet, and A. Carretero-Genevriér. Epitaxial La_{0.7}Sr_{0.3}MnO₃ thin films on silicon with excellent magnetic and electric properties by combining physical and chemical methods. *Science and Technology of Advanced Materials*, 19(1):702–710, December 2018. 10.1080/14686996.2018.1520590.
- ¹⁰² L. Soler, J. Jareño, J. Banchewski, S. Rasi, N. Chamorro, R. Guzman, R. Yañez, C. Mocuta, S. Ricart, J. Farjas, P. Roura-Grabulosa, X. Obradors, and T. Puig. Ultrafast transient liquid assisted growth of high current density superconducting films. *Nature Communications*, 11(1):344, December 2020. 10.1038/s41467-019-13791-1.
- ¹⁰³ P. Machado, M. Scigaj, J. Gazquez, E. Rueda, A. Sanchez-Diaz, I. Fina, M. Gibert-Roca, T. Puig, X. Obradors, M. Campoy-Quiles, and M. Coll. Band Gap Tuning of Solution-Processed Ferroelectric Perovskite BiFe_{1-x}Co_xO₃ Thin Films. *Chem. Mater.*, 31(3):947–954, February 2019. 10.1021/acs.chemmater.8b04380.
- ¹⁰⁴ B. Yang, L. Jin, R. Wei, X. Tang, L. Hu, P. Tong, J. Yang, W. Song, J. Dai, X. Zhu, Y. Sun, S. Zhang, X. Wang, and Z. Cheng. Chemical Solution Route for High-Quality Multiferroic BiFeO₃ Thin Films. *Small*, 17(9):1903663, March 2021. 10.1002/smll.201903663.
- ¹⁰⁵ B. Rivas-Murias, J. Manuel Vila-Funqueiriño, and F. Rivadulla. High quality thin films of thermoelectric misfit cobalt oxides prepared by a chemical solution method. *Scientific Reports*, 5(1):11889, December 2015. 10.1038/srep11889.
- ¹⁰⁶ X. Obradors, T. Puig, M. Gibert, A. Queralto, J. Zabaleta, and N. Mestres. Chemical solution route to self-assembled epitaxial oxide nanostructures. *Chemical Society Reviews*, 43(7):2200, 2014. 10.1039/c3cs60365b.
- ¹⁰⁷ A. Carretero-Genevriér, T. Puig, X. Obradors, and N. Mestres. Ferromagnetic 1D oxide nanostructures grown from chemical solutions in confined geometries. *Chemical Society Reviews*, 43(7):2042–2054, 2014. 10.1039/C3CS60288E.
- ¹⁰⁸ L. Fei, M. Naemi, G. Zou, and H. Luo. Chemical Solution Deposition of Epitaxial Metal-Oxide Nanocomposite Thin Films: Chemical Solution Deposition of Metal-Oxide Thin Films. *The Chemical Record*, 13(1):85–101, February 2013. 10.1002/tr.201200022.
- ¹⁰⁹ S. M. Baber, Q. Lin, G. Zou, N. Haberkorn, S. A. Baily, H. Wang, Z. Bi, H. Yang, S. Deng, M. E. Hawley, L. Civale, E. Bauer, T. M. McCleskey, A. K. Burrell, Q. Jia, and H. Luo. Magnetic Properties of Self-Assembled Epitaxial Nanocomposite CoFe₂O₄:SrTiO₃ and CoFe₂O₄:MgO Films. *The Journal of Physical Chemistry C*, 115(51):25338–25342, December 2011. 10.1021/jp2068232.
- ¹¹⁰ P. Cayado, H. Rijckaert, E. Bruneel, M. Erbe, J. Hänisch, I. Van Driessche, and B. Holzapfel. Importance of the pyrolysis for microstructure and superconducting properties of CSD-grown GdBa₂Cu₃O_{7-x}-HfO₂ nanocomposite films by the ex-situ approach. *Scientific Reports*, 10(1):19469, December 2020. 10.1038/s41598-020-75587-4.

- ¹¹¹ Q. X. Jia, T. M. McCleskey, A. K. Burrell, Y. Lin, G. E. Collis, H. Wang, A. D. Q. Li, and S. R. Foltyn. Polymer-assisted deposition of metal-oxide films. *Nature Materials*, 3(8):529–532, August 2004. 10.1038/nmat1163.
- ¹¹² H. Wang. *Epitaxial growth of complex functional oxide thin films by green and sustainable chemical solution methods*. PhD thesis, December 2020.
- ¹¹³ C. Pop, B. Villarejo, F. Pino, B. Mundet, S. Ricart, M. de Palau, T. Puig, and X. Obradors. Growth of all-chemical high critical current $\text{YBa}_2\text{Cu}_3\text{O}_{7-\delta}$ thick films and coated conductors. *Superconductor Science and Technology*, 32(1):015004, January 2019. 10.1088/1361-6668/aaea4e.
- ¹¹⁴ E. Carlos, R. Martins, E. Fortunato, and R. Branquinho. Solution Combustion Synthesis: Towards a Sustainable Approach for Metal Oxides. *Chemistry – A European Journal*, 26(42):9099–9125, July 2020. 10.1002/chem.202000678.
- ¹¹⁵ S. M. George. Atomic Layer Deposition: An Overview. *Chemical Reviews*, 110(1):111–131, January 2010. 10.1021/cr900056b.
- ¹¹⁶ M. Coll and M. Napari. Atomic layer deposition of functional multicomponent oxides. *APL Materials*, 7(11):110901, November 2019. 10.1063/1.5113656.
- ¹¹⁷ T. Suntola. Atomic layer epitaxy. *Materials Science Reports*, 4(5):261–312, January 1989. 10.1016/S0920-2307(89)80006-4.
- ¹¹⁸ J. A. van Delft, D. Garcia-Alonso, and W. M. M. Kessels. Atomic layer deposition for photovoltaics: applications and prospects for solar cell manufacturing. *Semiconductor Science and Technology*, 27(7):074002, July 2012. 10.1088/0268-1242/27/7/074002.
- ¹¹⁹ S. Sinha, D. K. Nandi, S.-H. Kim, and J. Heo. Atomic-layer-deposited buffer layers for thin film solar cells using earth-abundant absorber materials: A review. *Solar Energy Materials and Solar Cells*, 176:49–68, March 2018. 10.1016/j.solmat.2017.09.044.
- ¹²⁰ S. Lee, J.-H. Han, S.-H. Lee, G.-H. Baek, and J.-S. Park. Review of Organic/Inorganic Thin Film Encapsulation by Atomic Layer Deposition for a Flexible OLED Display. *JOM*, 71(1):197–211, January 2019. 10.1007/s11837-018-3150-3.
- ¹²¹ A. Pearse, T. Schmitt, E. Sahadeo, D. M. Stewart, A. Kozen, K. Gerasopoulos, A. A. Talin, S. B. Lee, G. W. Rubloff, and K. E. Gregorczyk. Three-Dimensional Solid-State Lithium-Ion Batteries Fabricated by Conformal Vapor-Phase Chemistry. *ACS Nano*, 12(5):4286–4294, May 2018. 10.1021/acsnano.7b08751.
- ¹²² B. Zhang and Y. Qin. Interface Tailoring of Heterogeneous Catalysts by Atomic Layer Deposition. *ACS Catalysis*, 8(11):10064–10081, November 2018. 10.1021/acscatal.8b02659.
- ¹²³ E. Alvaro and A. Yanguas-Gil. Characterizing the field of Atomic Layer Deposition: Authors, topics, and collaborations. *PLOS ONE*, 13(1):e0189137, January 2018. 10.1371/journal.pone.0189137.
- ¹²⁴ A. Devi. ‘Old Chemistries’ for new applications: Perspectives for development of precursors for MOCVD and ALD applications. *Coordination Chemistry Reviews*, 257(23):3332–3384, December 2013. 10.1016/j.ccr.2013.07.025.
- ¹²⁵ H. C. M. Knoops, T. Faraz, K. Arts, and W. M. M. E. Kessels. Status and prospects of plasma-assisted atomic layer deposition. *Journal of Vacuum Science & Technology A*, 37(3):030902, May 2019. 10.1116/1.5088582.
- ¹²⁶ D. Muñoz-Rojas and J. MacManus-Driscoll. Spatial atmospheric atomic layer deposition: a new laboratory and industrial tool for low-cost photovoltaics. *Mater. Horiz.*, 1(3):314–320, 2014. 10.1039/C3MH00136A.
- ¹²⁷ P. S. Maydannik, T. O. Kääriäinen, K. Lahtinen, D. C. Cameron, M. Söderlund, P. Soininen, P. Johansson, J. Kuusipalo, L. Moro, and X. Zeng. Roll-to-roll atomic layer deposition process for flexible electronics encapsulation applications. *Journal of Vacuum Science & Technology A*, 32(5):051603, September 2014. 10.1116/1.4893428.
- ¹²⁸ SALD - Spatial ALD Innovators. <https://spatialald.com/>.
- ¹²⁹ A. J. M. Mackus, M. J. M. Merckx, and W. M. M. Kessels. From the Bottom-Up: Toward Area-Selective Atomic Layer Deposition with High Selectivity. *Chemistry of Materials*, 31(1):2–12, January 2019. 10.1021/acs.chemmater.8b03454.
- ¹³⁰ K. J. Kanarik, S. Tan, and R. A. Gottscho. Atomic Layer Etching: Rethinking the Art of Etch. *The Journal of Physical Chemistry Letters*, 9(16):4814–4821, August 2018. 10.1021/acs.jpcclett.8b00997.
- ¹³¹ S. D. Elliott. Atomic-scale simulation of ALD chemistry. *Semiconductor Science and Technology*, 27(7):074008, July 2012. 10.1088/0268-1242/27/7/074008.
- ¹³² A. J. M. Mackus, J. R. Schneider, C. MacIsaac, J. G. Baker, and S. F. Bent. Synthesis of Doped, Ternary, and Quaternary Materials by Atomic Layer Deposition: A Review. *Chemistry of Materials*, 31(4):1142–1183, February 2019. 10.1021/acs.chemmater.8b02878.

- ¹³³ P. Sundberg and M. Karppinen. Organic and inorganic–organic thin film structures by molecular layer deposition: A review. *Beilstein Journal of Nanotechnology*, 5:1104–1136, July 2014. 10.3762/bjnano.5.123.
- ¹³⁴ J. Multia and M. Karppinen. Atomic/Molecular Layer Deposition for Designer’s Functional Metal–Organic Materials. *Advanced Materials Interfaces*, 9(15):2200210, 2022. 10.1002/admi.202200210.
- ¹³⁵ V. Miikkulainen, M. Leskelä, M. Ritala, and R. L. Puurunen. Crystallinity of inorganic films grown by atomic layer deposition: Overview and general trends. *Journal of Applied Physics*, 113(2):021301, January 2013. 10.1063/1.4757907.
- ¹³⁶ H. H. Sønsteby, A. Yanguas-Gil, and J. W. Elam. Consistency and reproducibility in atomic layer deposition. *Journal of Vacuum Science & Technology A*, 38(2):020804, March 2020. 10.1116/1.5140603.
- ¹³⁷ H. H. Sonsteby, H. Fjellvag, and O. Nilsen. Functional Perovskites by Atomic Layer Deposition – An Overview. *Advanced Materials Interfaces*, 4(8):1600903, 2017. 10.1002/admi.201600903.
- ¹³⁸ M. Vehkamäki, M. Ritala, M. Leskelä, A. C. Jones, H. O. Davies, T. Sajavaara, and E. Rauhala. Atomic Layer Deposition of Strontium Tantalate Thin Films from Bimetallic Precursors and Water. *Journal of The Electrochemical Society*, 151(4):F69, February 2004. 10.1149/1.1648025.
- ¹³⁹ P. Yu, S. M. J. Beer, A. Devi, and M. Coll. Fabrication of $Gd_xFe_yO_z$ films using an atomic layer deposition-type approach. *CrystEngComm*, 23(3):730–740, 2021. 10.1039/D0CE01252A.
- ¹⁴⁰ A. V. Plokhikh, M. Falmbigl, I. S. Golovina, A. R. Akbashev, I. A. Karateev, M. Y. Presnyakov, A. L. Vasiliev, and J. E. Spanier. Formation of $BiFeO_3$ from a Binary Oxide Superlattice Grown by Atomic Layer Deposition. *ChemPhysChem*, 18(15):1966–1970, August 2017. 10.1002/cphc.201700407.
- ¹⁴¹ A. V. Plokhikh, I. A. Karateev, M. Falmbigl, A. L. Vasiliev, J. Lapano, R. Engel-Herbert, and J. E. Spanier. Toward a Low-Temperature Route for Epitaxial Integration of $BiFeO_3$ on Si. *The Journal of Physical Chemistry C*, 123(19):12203–12210, May 2019. 10.1021/acs.jpcc.8b12486.
- ¹⁴² J. D. Emery, C. M. Schlepütz, P. Guo, R. P. H. Chang, and A. B. F. Martinson. Epitaxial Atomic Layer Deposition of Sn-Doped Indium Oxide. *Crystal Growth & Design*, 16(2):640–645, February 2016. 10.1021/acs.cgd.5b01086.
- ¹⁴³ M. Coll, J. M. Montero Moreno, J. Gazquez, K. Nielsch, X. Obradors, and T. Puig. Low Temperature Stabilization of Nanoscale Epitaxial Spinel Ferrite Thin Films by Atomic Layer Deposition. *Advanced Functional Materials*, 24(34):5368–5374, September 2014. 10.1002/adfm.201400517.
- ¹⁴⁴ H. H. Sonsteby, E. Skaar, O. S. Fjellvag, J. E. Bratvold, H. Fjellvag, and O. Nilsen. A foundation for complex oxide electronics – low temperature perovskite epitaxy. *Nature Communications*, 11(1):2872, June 2020. 10.1038/s41467-020-16654-2.
- ¹⁴⁵ A. V. Plokhikh, I. S. Golovina, M. Falmbigl, I. A. Karateev, A. L. Vasiliev, J. Lapano, R. Engel-Herbert, and J. E. Spanier. A low-temperature route for producing epitaxial perovskite superlattice structures on (001)-oriented $SrTiO_3$ /Si substrates. *Journal of Materials Chemistry C*, 9(38):13115–13122, 2021. 10.1039/D1TC01988K.
- ¹⁴⁶ Spin Coating: Complete Guide to Theory and Techniques. <https://www.ossila.com/en-eu/pages/spin-coating>.
- ¹⁴⁷ R. W. Schwartz. Chemical Solution Deposition of Perovskite Thin Films. *Chemistry of Materials*, 9(11):2325–2340, November 1997. 10.1021/cm970286f.
- ¹⁴⁸ X. Obradors, F. Martinez-Julian, K. Zalamova, V. R. Vlad, A. Pomar, A. Palau, A. Llodes, H. Chen, M. Coll, S. Ricart, N. Mestres, X. Granados, T. Puig, and M. Rikel. Nucleation and mesostrain influence on percolating critical currents of solution derived $YBa_2Cu_3O_7$ superconducting thin films. *Physica C: Superconductivity and its Applications*, 482:58–67, November 2012. 10.1016/j.physc.2012.04.020.
- ¹⁴⁹ G. D. Botsaris, E. G. Denk, G. S. Ersan, D. J. Kirwan, G. Margolis, M. Ohara, R. C. Reid, and J. Tester. CRYSTALLIZATION—PART I. ANNUAL REVIEW - ”Transport Phenomena of Nucleation and Crystal Growth”, May 2002. 10.1021/ie50718a009. <https://pubs.acs.org/doi/pdf/10.1021/ie50718a009>.
- ¹⁵⁰ T. Schneller, R. Waser, M. Kosec, and D. Payne, editors. *Chemical Solution Deposition of Functional Oxide Thin Films*. Springer Vienna, Vienna, 2013. 10.1007/978-3-211-99311-8.
- ¹⁵¹ D. Peeters, A. Sadlo, K. Lowjaga, O. Mendoza Reyes, L. Wang, L. Mai, M. Gebhard, D. Rogalla, H.-W. Becker, I. Giner, G. Grundmeier, D. Mitoraj, M. Grafen, A. Ostendorf, R. Beranek, and A. Devi. Nanostructured Fe_2O_3 Processing via Water-Assisted ALD and Low-Temperature CVD from a Versatile Iron Ketoiminate Precursor. *Advanced Materials Interfaces*, 4(18):1700155, September 2017. 10.1002/admi.201700155.
- ¹⁵² H. C. M. Knoops, S. E. Potts, A. A. Bol, and W. M. M. Kessels. 27 - Atomic Layer Deposition. In T. F. Kuech, editor, *Handbook of Crystal Growth (Second Edition)*, Handbook of Crystal Growth, pages 1101–1134. North-Holland, Boston, January 2015. 10.1016/B978-0-444-63304-0.00027-5.

- ¹⁵³ M. Coll, J. Gazquez, I. Fina, Z. Khayat, A. Quindeau, M. Alexe, M. Varela, S. Trolier-McKinstry, X. Obradors, and T. Puig. Nanocrystalline Ferroelectric BiFeO₃ Thin Films by Low-Temperature Atomic Layer Deposition. *Chemistry of Materials*, 27(18):6322–6328, September 2015. 10.1021/acs.chemmater.5b02093.
- ¹⁵⁴ HeatWave Labs. <https://www.cathode.com/>.
- ¹⁵⁵ F. Craciun, T. Lippert, and M. Dinescu. Pulsed Laser Deposition: Fundamentals, Applications, and Perspectives. In K. Sugioka, editor, *Handbook of Laser Micro- and Nano-Engineering*, pages 1–33. Springer International Publishing, Cham, 2020. 10.1007/978-3-319-69537-2_7 – 1.
- ¹⁵⁶ S. Shrestha, M. Coile, M. Zhu, M. Souri, J. Kim, R. Pandey, J. W. Brill, J. Hwang, J.-W. Kim, and A. Seo. Nanometer-Thick Sr₂IrO₄ Freestanding Films for Flexible Electronics. *ACS Applied Nano Materials*, 3(7):6310–6315, July 2020. 10.1021/acnanm.0c01351.
- ¹⁵⁷ G. Koster, M. Huijben, A. Janssen, and G. Rijnders. Growth studies of heteroepitaxial oxide thin films using reflection high-energy electron diffraction (RHEED). In *Epitaxial Growth of Complex Metal Oxides*, pages 3–29. Elsevier, 2015. 10.1016/B978-1-78242-245-7.00001-4.
- ¹⁵⁸ Scanning Electron Microscopy. <https://www.nanoscience.com/techniques/scanning-electron-microscopy/>.
- ¹⁵⁹ M. A. Moram and M. E. Vickers. X-ray diffraction of III-nitrides. *Reports on Progress in Physics*, 72(3):036502, March 2009. 10.1088/0034-4885/72/3/036502.
- ¹⁶⁰ J. Moulder and J. Chastain. *Handbook of X-ray Photoelectron Spectroscopy: A Reference Book of Standard Spectra for Identification and Interpretation of XPS Data*. Physical Electronics Division, Perkin-Elmer Corporation, 1992.
- ¹⁶¹ M. Buchner, K. Höfler, B. Henne, V. Ney, and A. Ney. Tutorial: Basic principles, limits of detection, and pitfalls of highly sensitive SQUID magnetometry for nanomagnetism and spintronics. *Journal of Applied Physics*, 124(16):161101, October 2018. 10.1063/1.5045299.
- ¹⁶² M. A. Garcia, E. Fernandez Pinel, J. de la Venta, A. Quesada, V. Bouzas, J. F. Fernandez, J. J. Romero, M. S. Martin Gonzalez, and J. L. Costa-Kramer. Sources of experimental errors in the observation of nanoscale magnetism. *Journal of Applied Physics*, 105(1):013925, January 2009. 10.1063/1.3060808.
- ¹⁶³ L. J. Van der Pauw. A Method of Measuring the Resistivity and Hall Coefficient on Lamellae of Arbitrary Shape. *Philips Technical Review*, 13:1–9, 1958.
- ¹⁶⁴ N. Balke, P. Maksymovych, S. Jesse, A. Herklotz, A. Tselev, C.-B. Eom, I. I. Kravchenko, P. Yu, and S. V. Kalinin. Differentiating Ferroelectric and Nonferroelectric Electromechanical Effects with Scanning Probe Microscopy. *ACS Nano*, 9(6):6484–6492, June 2015. 10.1021/acsnano.5b02227.
- ¹⁶⁵ I. Fina, L. Fabrega, E. Langenberg, X. Marti, F. Sanchez, M. Varela, and J. Fontcuberta. Nonferroelectric contributions to the hysteresis cycles in manganite thin films: A comparative study of measurement techniques. *Journal of Applied Physics*, 109(7):074105, April 2011. 10.1063/1.3555098.
- ¹⁶⁶ Q. Lin, H. Huang, Y. Jing, H. Fu, P. Chang, D. Li, Y. Yao, and Z. Fan. Flexible photovoltaic technologies. *J. Mater. Chem. C*, 2(7):1233, 2014. 10.1039/c3tc32197e.
- ¹⁶⁷ Y. S. Rim, S. Bae, H. Chen, N. De Marco, and Y. Yang. Recent Progress in Materials and Devices toward Printable and Flexible Sensors. *Adv. Mater.*, 28(22):4415–4440, June 2016. 10.1002/adma.201505118.
- ¹⁶⁸ Z. Liao, F. Li, P. Gao, L. Li, J. Guo, X. Pan, R. Jin, E. W. Plummer, and J. Zhang. Origin of the metal-insulator transition in ultrathin films of $\text{La}_{2/3}\text{Sr}_{1/3}\text{MnO}_3$. *Physical Review B*, 92(12):125123, September 2015. 10.1103/PhysRevB.92.125123.
- ¹⁶⁹ R. L. Z. Hoyer, J. Hidalgo, R. A. Jagt, J.-P. Correa-Baena, T. Fix, and J. L. MacManus-Driscoll. The Role of Dimensionality on the Optoelectronic Properties of Oxide and Halide Perovskites, and their Halide Derivatives. *Advanced Energy Materials*, 12(4):2100499, 2022. 10.1002/aenm.202100499.
- ¹⁷⁰ S. A. Chambers. Epitaxial Growth and Properties of Doped Transition Metal and Complex Oxide Films. *Advanced Materials*, 22(2):219–248, 2010. 10.1002/adma.200901867.
- ¹⁷¹ G. Koster, M. Huijben, and G. Rijnders. *Epitaxial Growth of Complex Metal Oxides*. Elsevier, May 2015.
- ¹⁷² J. L. MacManus-Driscoll, M. P. Wells, C. Yun, J.-W. Lee, C.-B. Eom, and D. G. Schlom. New approaches for achieving more perfect transition metal oxide thin films. *APL Materials*, 8(4):040904, 2020. 10.1063/5.0003268.
- ¹⁷³ M. Brahlek, A. S. Gupta, J. Lapano, J. Roth, H.-T. Zhang, L. Zhang, R. Haislmaier, and R. Engel-Herbert. Frontiers in the growth of complex oxide thin films: Past, present, and future of hybrid mbe. *Advanced Functional Materials*, 28(9):1702772, 2018. <https://doi.org/10.1002/adfm.201702772>.

- ¹⁷⁴ S. Han, Y. Meng, Z. Xu, J. S. Kim, Y. Li, I.-P. Roh, H. Ahn, D.-H. Kim, and S.-H. Bae. Freestanding Membranes for Unique Functionality in Electronics. *ACS Applied Electronic Materials*, January 2023. 10.1021/acsaelm.2c01411.
- ¹⁷⁵ K. T. Kang, J. Park, D. Suh, and W. S. Choi. Synergetic Behavior in 2D Layered Material/Complex Oxide Heterostructures. *Advanced Materials*, 31(34):1803732, 2019. 10.1002/adma.201803732.
- ¹⁷⁶ C. Guo and H. Huang. Design of super-elastic freestanding ferroelectric thin films guided by phase-field simulations. *Microstructures*, 2(4):21, 2022. 10.20517/microstructures.2022.20.
- ¹⁷⁷ Z. Dong, H. Chen, M. Qi, J. Shen, W. Liu, E. Guo, D. Li, Y. Zhang, and Z. Wu. Enhanced Upconversion Photoluminescence Assisted by Flexoelectric Field in Oxide Nanomembranes. *Laser & Photonics Reviews*, 16(4):2100454, April 2022. 10.1002/lpor.202100454.
- ¹⁷⁸ P. Salles, I. Caño, R. Guzman, C. Dore, A. Mihi, W. Zhou, and M. Coll. Facile Chemical Route to Prepare Water Soluble Epitaxial Sr₃Al₂O₆ Sacrificial Layers for Free-Standing Oxides. *Adv. Mater. Interfaces*, 8(5):2001643, March 2021. 10.1002/admi.202001643.
- ¹⁷⁹ Y.-Y. Pai, A. Tylan-Tyler, P. Irvin, and J. Levy. Physics of SrTiO₃-based heterostructures and nanostructures: a review. *Rep. Prog. Phys.*, 81(3):036503, March 2018. 10.1088/1361-6633/aa892d.
- ¹⁸⁰ P. Salles, R. Guzman, D. Zanders, A. Quintana, I. Fina, F. Sanchez, W. Zhou, A. Devi, and M. Coll. Bendable Polycrystalline and Magnetic CoFe₂O₄ Membranes by Chemical Methods. *ACS Appl. Mater. Interfaces*, 14(10):12845–12854, March 2022. 10.1021/acsaami.1c24450.
- ¹⁸¹ D. Li, C. Adamo, B. Y. Wang, H. Yoon, Z. Chen, S. S. Hong, D. Lu, Y. Cui, Y. Hikita, and H. Y. Hwang. Stabilization of Sr₃Al₂O₆ Growth Templates for Ex Situ Synthesis of Freestanding Crystalline Oxide Membranes. *Nano Letters*, 21(10):4454–4460, May 2021. 10.1021/acs.nanolett.1c01194.
- ¹⁸² J.-H. Park, E. Vescovo, H.-J. Kim, C. Kwon, R. Ramesh, and T. Venkatesan. Direct evidence for a half-metallic ferromagnet. *Nature*, 392(6678):794–796, April 1998. 10.1038/33883.
- ¹⁸³ Y. Wu, Y. Suzuki, U. Rüdiger, J. Yu, A. D. Kent, T. K. Nath, and C. B. Eom. Magnetotransport and magnetic domain structure in compressively strained colossal magnetoresistance films. *Applied Physics Letters*, 75(15):2295–2297, October 1999. 10.1063/1.124995.
- ¹⁸⁴ M. Cesaria, A. P. Caricato, G. Maruccio, and M. Martino. LSMO – growing opportunities by PLD and applications in spintronics. *Journal of Physics: Conference Series*, 292(1):012003, April 2011. 10.1088/1742-6596/292/1/012003.
- ¹⁸⁵ Y. Takamura, R. V. Chopdekar, E. Arenholz, and Y. Suzuki. Control of the magnetic and magnetotransport properties of La_{0.67}Sr_{0.33}MnO₃ thin films through epitaxial strain. *Appl. Phys. Lett.*, 92(16):162504, April 2008. 10.1063/1.2908051.
- ¹⁸⁶ C. Adamo, X. Ke, H. Q. Wang, H. L. Xin, T. Heeg, M. E. Hawley, W. Zander, J. Schubert, P. Schiffer, D. A. Muller, L. Maritato, and D. G. Schlom. Effect of biaxial strain on the electrical and magnetic properties of (001) La_{0.7}Sr_{0.3}MnO₃ thin films. *Appl. Phys. Lett.*, 95(11):112504, September 2009. 10.1063/1.3213346.
- ¹⁸⁷ B. Wang, L. You, P. Ren, X. Yin, Y. Peng, B. Xia, L. Wang, X. Yu, S. Mui Poh, P. Yang, G. Yuan, L. Chen, A. Rusydi, and J. Wang. Oxygen-driven anisotropic transport in ultra-thin manganite films. *Nat Commun*, 4(1):2778, December 2013. 10.1038/ncomms3778.
- ¹⁸⁸ J. Fontcuberta, M. Bibes, B. Martinez, V. Trtik, C. Ferrater, F. Sanchez, and M. Varela. Tunable epitaxial growth of magnetoresistive La_{2/3}Sr_{1/3}MnO₃ thin films. *Journal of Applied Physics*, 85(8):4800–4802, April 1999. 10.1063/1.370486.
- ¹⁸⁹ M. Sirena, N. Haberkorn, M. Granada, L. B. Steren, and J. Guimpel. Metal-insulator transition induced by postdeposition annealing in low doped manganite films. *Journal of Applied Physics*, 105(3):033902, February 2009. 10.1063/1.3073894.
- ¹⁹⁰ C. Ge, K.-J. Jin, L. Gu, L.-C. Peng, Y.-S. Hu, H.-Z. Guo, H.-F. Shi, J.-K. Li, J.-O. Wang, X.-X. Guo, C. Wang, M. He, H.-B. Lu, and G.-Z. Yang. Metal-Insulator Transition Induced by Oxygen Vacancies from Electrochemical Reaction in Ionic Liquid-Gated Manganite Films. *Advanced Materials Interfaces*, 2(17):1500407, 2015. 10.1002/admi.201500407.
- ¹⁹¹ Z. Fang, I. V. Solovyev, and K. Terakura. Phase Diagram of Tetragonal Manganites. *Physical Review Letters*, 84(14):3169–3172, April 2000. 10.1103/PhysRevLett.84.3169.
- ¹⁹² J. Huang, H. Wang, X. Sun, X. Zhang, and H. Wang. Multifunctional La_{0.67}Sr_{0.33}MnO₃ (LSMO) Thin Films Integrated on Mica Substrates toward Flexible Spintronics and Electronics. *ACS Appl. Mater. Interfaces*, 10(49):42698–42705, December 2018. 10.1021/acsaami.8b16626.
- ¹⁹³ W. Hou, S. Zhao, T. Wang, M. Yao, W. Su, Z. Hu, Z. Zhou, and M. Liu. Manipulation of microwave magnetism in flexible La_{0.7}Sr_{0.3}MnO₃ film by deformable ionic gel gating. *Applied Surface Science*, 563:150074, October 2021. 10.1016/j.apsusc.2021.150074.

- ¹⁹⁴ C.-C. Chiu, Y.-W. Chang, Y.-C. Shao, Y.-C. Liu, J.-M. Lee, S.-W. Huang, W. Yang, J. Guo, F. M. F. de Groot, J.-C. Yang, and Y.-D. Chuang. Spectroscopic characterization of electronic structures of ultra-thin single crystal $\text{La}_{0.7}\text{Sr}_{0.3}\text{MnO}_3$. *Scientific Reports*, 11(1):5250, December 2021. 10.1038/s41598-021-84598-8.
- ¹⁹⁵ D. J. Baek, D. Lu, Y. Hikita, H. Y. Hwang, and L. F. Kourkoutis. Ultrathin Epitaxial Barrier Layer to Avoid Thermally Induced Phase Transformation in Oxide Heterostructures. *ACS Appl. Mater. Interfaces*, 9(1):54–59, January 2017. 10.1021/ac-sami.6b14106.
- ¹⁹⁶ J. O’Connor, B. A. Sexton, and R. S. C. Smart. *Surface Analysis Methods in Materials Science*, volume 23. 1992.
- ¹⁹⁷ A. M. Deml, V. Stevanović, A. M. Holder, M. Sanders, R. O’Hayre, and C. B. Musgrave. Tunable Oxygen Vacancy Formation Energetics in the Complex Perovskite Oxide $\text{Sr}_x\text{La}_{1-x}\text{Mn}_y\text{Al}_{1-y}\text{O}_3$. *Chemistry of Materials*, 26(22):6595–6602, November 2014. 10.1021/cm5033755.
- ¹⁹⁸ A. R. Denton and N. W. Ashcroft. Vegard’s law. *Physical Review A*, 43(6):3161–3164, March 1991. 10.1103/PhysRevA.43.3161.
- ¹⁹⁹ O. I. Lebedev, G. V. Tendeloo, S. Amelinckx, H. L. Ju, and K. M. Krishnan. High-resolution electron microscopy study of strained epitaxial $\text{La}_{0.7}\text{Sr}_{0.3}\text{MnO}_3$ thin films. *Philosophical Magazine A*, 80(3):673–691, March 2000. 10.1080/01418610008212075.
- ²⁰⁰ Y. Chen, J. A. Tilka, Y. Ahn, J. Park, A. Pateras, T. Zhou, D. E. Savage, I. McNulty, M. V. Holt, D. M. Paskiewicz, D. D. Fong, T. F. Kuech, and P. G. Evans. Seeded Lateral Solid-Phase Crystallization of the Perovskite Oxide SrTiO_3 . *The Journal of Physical Chemistry C*, 123(12):7447–7456, March 2019. 10.1021/acs.jpcc.9b00078.
- ²⁰¹ J. Santiso, J. Roqueta, N. Bagues, C. Frontera, Z. Konstantinovic, Q. Lu, B. Yildiz, B. Martinez, A. Pomar, L. Balcells, and F. Sandiumenge. Self-Arranged Misfit Dislocation Network Formation upon Strain Release in $\text{La}_{0.7}\text{Sr}_{0.3}\text{MnO}_3/\text{LaAlO}_3(100)$ Epitaxial Films under Compressive Strain. *ACS Applied Materials & Interfaces*, 8(26):16823–16832, July 2016. 10.1021/ac-sami.6b02896.
- ²⁰² J. D. Burton and E. Y. Tsymbal. Giant Tunneling Electroresistance Effect Driven by an Electrically Controlled Spin Valve at a Complex Oxide Interface. *Physical Review Letters*, 106(15):157203, April 2011. 10.1103/PhysRevLett.106.157203.
- ²⁰³ H. Zenia, G. A. Gehring, G. Banach, and W. M. Temmerman. Electronic and magnetic properties of the (001) surface of hole-doped manganites. *Physical Review B*, 71(2):024416, 2005. 10.1103/PhysRevB.71.024416.
- ²⁰⁴ Z. Liao and J. Zhang. Metal-to-insulator transition in ultrathin manganite heterostructures. *Applied Sciences*, 9(1):144, 2019. 10.3390/app9010144.
- ²⁰⁵ H. Taghinejad, A. A. Eftekhar, P. M. Campbell, B. Beatty, M. Taghinejad, Y. Zhou, C. J. Perini, H. Moradinejad, W. E. Henderson, E. V. Woods, X. Zhang, P. Ajayan, E. J. Reed, E. M. Vogel, and A. Adibi. Strain relaxation via formation of cracks in compositionally modulated two-dimensional semiconductor alloys. *npj 2D Materials and Applications*, 2(1):1–8, April 2018. 10.1038/s41699-018-0056-4.
- ²⁰⁶ A. Castellanos-Gomez, V. Singh, H. S. J. van der Zant, and G. A. Steele. Mechanics of freely-suspended ultrathin layered materials. *Annalen der Physik*, 527(1-2):27–44, 2015. 10.1002/andp.201400153.
- ²⁰⁷ U. K. Bhaskar, N. Banerjee, A. Abdollahi, Z. Wang, D. G. Schlom, G. Rijnders, and G. Catalan. A flexoelectric microelectromechanical system on silicon. *Nature Nanotechnology*, 11(3):263–266, March 2016. 10.1038/nnano.2015.260.
- ²⁰⁸ A. Gomez, J. M. Vila-Fungueiriño, R. Moalla, G. Saint-Girons, J. Gazquez, M. Varela, R. Bachelet, M. Gich, F. Rivadulla, and A. Carretero-Genevri. Electric and Mechanical Switching of Ferroelectric and Resistive States in Semiconducting BaTiO_3 - δ Films on Silicon. *Small*, 13(39):1701614, 2017. 10.1002/sml.201701614.
- ²⁰⁹ D. P. Kumah, J. H. Ngai, and L. Kornblum. Epitaxial Oxides on Semiconductors: From Fundamentals to New Devices. *Advanced Functional Materials*, 30(18):1901597, 2020. 10.1002/adfm.201901597.
- ²¹⁰ J. Wang, J. B. Neaton, H. Zheng, V. Nagarajan, S. B. Ogale, B. Liu, D. Viehland, V. Vaithyanathan, D. G. Schlom, U. V. Waghmare, N. A. Spaldin, K. M. Rabe, M. Wuttig, and R. Ramesh. Epitaxial BiFeO_3 Multiferroic Thin Film Heterostructures. *Science*, 299(5613):1719–1722, March 2003. 10.1126/science.1080615.
- ²¹¹ C. Paillard, X. Bai, I. C. Infante, M. Guennou, G. Geneste, M. Alexe, J. Kreisel, and B. Dkhil. Photovoltaics with Ferroelectrics: Current Status and Beyond. *Advanced Materials*, 28(26):5153–5168, 2016. 10.1002/adma.201505215.
- ²¹² X. Han, Y. Ji, and Y. Yang. Ferroelectric Photovoltaic Materials and Devices. *Advanced Functional Materials*, 32(14):2109625, 2022. 10.1002/adfm.202109625.
- ²¹³ Y. Sheng, I. Fina, M. Gospodinov, and J. Fontcuberta. Bulk photovoltaic effect modulated by ferroelectric polarization back-switching. *Applied Physics Letters*, 120(24):242901, June 2022. 10.1063/5.0094837.

- ²¹⁴ S. Y. Yang, J. Seidel, S. J. Byrnes, P. Shafer, C.-H. Yang, M. D. Rossell, P. Yu, Y.-H. Chu, J. F. Scott, J. W. Ager, L. W. Martin, and R. Ramesh. Above-bandgap voltages from ferroelectric photovoltaic devices. *Nature Nanotechnology*, 5(2):143–147, February 2010. 10.1038/nnano.2009.451.
- ²¹⁵ M. Alexe and D. Hesse. Tip-enhanced photovoltaic effects in bismuth ferrite. *Nature Communications*, 2(1):256, March 2011. 10.1038/ncomms1261.
- ²¹⁶ A. Bhatnagar, A. Roy Chaudhuri, Y. Heon Kim, D. Hesse, and M. Alexe. Role of domain walls in the abnormal photovoltaic effect in BiFeO₃. *Nature Communications*, 4:2835, November 2013. 10.1038/ncomms3835.
- ²¹⁷ J. Wu, Z. Fan, D. Xiao, J. Zhu, and J. Wang. Multiferroic bismuth ferrite-based materials for multifunctional applications: Ceramic bulks, thin films and nanostructures. *Progress in Materials Science*, 84:335–402, December 2016. 10.1016/j.pmatsci.2016.09.001.
- ²¹⁸ T. Amrillah, Y. Bitla, K. Shin, T. Yang, Y.-H. Hsieh, Y.-Y. Chiou, H.-J. Liu, T. H. Do, D. Su, Y.-C. Chen, S.-U. Jen, L.-Q. Chen, K. H. Kim, J.-Y. Juang, and Y.-H. Chu. Flexible Multiferroic Bulk Heterojunction with Giant Magnetoelectric Coupling via van der Waals Epitaxy. *ACS Nano*, 11(6):6122–6130, June 2017. 10.1021/acsnano.7b02102.
- ²¹⁹ T. Amrillah, A. Hermawan, C. P. Wulandari, A. D. Muthi'Ah, and F. M. Simanjuntak. Crafting the multiferroic BiFeO₃-CoFe₂O₄ nanocomposite for next-generation devices: A review. *Materials and Manufacturing Processes*, 36(14):1579–1596, October 2021. 10.1080/10426914.2021.1945096.
- ²²⁰ R. Nechache, C. Harnagea, S. Li, L. Cardenas, W. Huang, J. Chakrabartty, and F. Rosei. Bandgap tuning of multiferroic oxide solar cells. *Nature Photonics*, 9(1):61–67, January 2015. 10.1038/nphoton.2014.255.
- ²²¹ D. G. Schlom, L.-Q. Chen, C.-B. Eom, K. M. Rabe, S. K. Streiffer, and J.-M. Triscone. Strain Tuning of Ferroelectric Thin Films. *Annual Review of Materials Research*, 37(1):589–626, 2007. 10.1146/annurev.matsci.37.061206.113016.
- ²²² F. Sun, D. Chen, X. Gao, and J.-M. Liu. Emergent strain engineering of multiferroic BiFeO₃ thin films. *Journal of Materiomics*, 7(2):281–294, March 2021. 10.1016/j.jmat.2020.08.005.
- ²²³ R. J. Zeches, M. D. Rossell, J. X. Zhang, A. J. Hatt, Q. He, C.-H. Yang, A. Kumar, C. H. Wang, A. Melville, C. Adamo, G. Sheng, Y.-H. Chu, J. F. Ihlefeld, R. Erni, C. Ederer, V. Gopalan, L. Q. Chen, D. G. Schlom, N. A. Spaldin, L. W. Martin, and R. Ramesh. A Strain-Driven Morphotropic Phase Boundary in BiFeO₃. *Science*, 326(5955):977–980, November 2009. 10.1126/science.1177046.
- ²²⁴ S. Li, F. Chen, R. Schafraneck, T. J. M. Bayer, K. Rachut, A. Fuchs, S. Siol, M. Weidner, M. Hohmann, V. Pfeifer, J. Morasch, C. Ghinea, E. Arveux, R. Günzler, J. Gassmann, C. Körber, Y. Gassenbauer, F. Säuberlich, G. V. Rao, S. Payan, M. Maglione, C. Chirila, L. Pintilie, L. Jia, K. Ellmer, M. Naderer, K. Reichmann, U. Böttger, S. Schmelzer, R. C. Frunza, H. Uršič, B. Malič, W.-B. Wu, P. Erhart, and A. Klein. Intrinsic energy band alignment of functional oxides. *physica status solidi (RRL) – Rapid Research Letters*, 8(6):571–576, 2014. 10.1002/pssr.201409034.
- ²²⁵ S. Rühle, A. Y. Anderson, H.-N. Barad, B. Kupfer, Y. Bouhadana, E. Rosh-Hodesh, and A. Zaban. All-Oxide Photovoltaics. *J. Phys. Chem. Lett.*, 3(24):3755–3764, December 2012. 10.1021/jz3017039.
- ²²⁶ T. Minami. Transparent conducting oxide semiconductors for transparent electrodes. *Semiconductor Science and Technology*, 20(4):S35–S44, April 2005. 10.1088/0268-1242/20/4/004.
- ²²⁷ D.-J. Lee, H.-M. Kim, J.-Y. Kwon, H. Choi, S.-H. Kim, and K.-B. Kim. Structural and Electrical Properties of Atomic Layer Deposited Al-Doped ZnO Films. *Advanced Functional Materials*, 21(3):448–455, February 2011. 10.1002/adfm.201001342.
- ²²⁸ Y. Wu, F. Cao, and X. Ji. Optical and electrical properties of Al-doped ZnO thin films by atomic layer deposition. *Journal of Materials Science: Materials in Electronics*, 31(20):17365–17374, October 2020. 10.1007/s10854-020-04292-9.
- ²²⁹ S. Estandia, J. Gazquez, M. Varela, N. Dix, M. Qian, R. Solanas, I. Fina, and F. Sanchez. Critical effect of the bottom electrode on the ferroelectricity of epitaxial Hf_{0.5}Zr_{0.5}O₂ thin films. *Journal of Materials Chemistry C*, 9(10):3486–3492, 2021. 10.1039/D0TC05853J.
- ²³⁰ T. Tynell and M. Karppinen. Atomic layer deposition of ZnO: a review. *Semiconductor Science and Technology*, 29(4):043001, April 2014. 10.1088/0268-1242/29/4/043001.
- ²³¹ L. G. Gerling, S. Mahato, A. Morales-Vilches, G. Masmitja, P. Ortega, C. Voz, R. Alcubilla, and J. Puigdollers. Transition metal oxides as hole-selective contacts in silicon heterojunctions solar cells. *Solar Energy Materials and Solar Cells*, 145:109–115, February 2016. 10.1016/j.solmat.2015.08.028.
- ²³² X. Jiang, Y. Liu, Y. Zang, Y. Liu, T. Gao, N. Zheng, Z. Gu, Y. Yang, D. Wu, and Y. Nie. Uniaxial strain induced anisotropic bandgap engineering in freestanding BiFeO₃ films. *APL Materials*, 10(9):091110, September 2022. 10.1063/5.0095955.

- ²³³ R. Guo, L. You, W. Lin, A. Abdelsamie, X. Shu, G. Zhou, S. Chen, L. Liu, X. Yan, J. Wang, and J. Chen. Continuously controllable photoconductance in freestanding BiFeO₃ by the macroscopic flexoelectric effect. *Nature Communications*, 11(1):2571, December 2020. 10.1038/s41467-020-16465-5.
- ²³⁴ Q. Shi, E. Parsonnet, X. Cheng, N. Fedorova, R.-C. Peng, A. Fernandez, A. Qualls, X. Huang, X. Chang, H. Zhang, D. Pesquera, S. Das, D. Nikonov, I. Young, L.-Q. Chen, L. W. Martin, Y.-L. Huang, J. Iñiguez, and R. Ramesh. The role of lattice dynamics in ferroelectric switching. *Nature Communications*, 13(1):1110, March 2022. 10.1038/s41467-022-28622-z.
- ²³⁵ S. C. Abrahams and J. L. Bernstein. Remeasurement of the structure of hexagonal ZnO. *Acta Crystallographica Section B: Structural Crystallography and Crystal Chemistry*, 25(7):1233–1236, July 1969. 10.1107/S0567740869003876.
- ²³⁶ S.-Y. Pung, K.-L. Choy, X. Hou, and C. Shan. Preferential growth of ZnO thin films by the atomic layer deposition technique. *Nanotechnology*, 19(43):435609, October 2008. 10.1088/0957-4484/19/43/435609.
- ²³⁷ F. Solis-Pomar, E. Martinez, M. F. Melendrez, and E. Perez-Tijerina. Growth of vertically aligned ZnO nanorods using textured ZnO films. *Nanoscale Research Letters*, 6(1):524, September 2011. 10.1186/1556-276X-6-524.
- ²³⁸ J. W. Elam, Z. A. Sechrist, and S. M. George. ZnO/Al₂O₃ nanolaminates fabricated by atomic layer deposition: growth and surface roughness measurements. *Thin Solid Films*, 414(1):43–55, July 2002. 10.1016/S0040-6090(02)00427-3.
- ²³⁹ D. Dimitrov, C.-L. Tsai, S. Petrov, V. Marinova, D. Petrova, B. Napoleonov, B. Blagoev, V. Strijkova, K. Y. Hsu, and S. H. Lin. Atomic Layer-Deposited Al-Doped ZnO Thin Films for Display Applications. *Coatings*, 10(6):539, June 2020. 10.3390/coatings10060539.
- ²⁴⁰ M. I. Hossain, A. Mohammad, W. Qarony, S. Ilhom, D. R. Shukla, D. Knipp, N. Biyikli, and Y. H. Tsang. Atomic layer deposition of metal oxides for efficient perovskite single-junction and perovskite/silicon tandem solar cells. *RSC Advances*, 10(25):14856–14866, April 2020. 10.1039/D0RA00939C.
- ²⁴¹ R. Chwang, B. J. Smith, and C. R. Crowell. Contact size effects on the van der Pauw method for resistivity and Hall coefficient measurement. *Solid-State Electronics*, 17(12):1217–1227, December 1974. 10.1016/0038-1101(74)90001-X.
- ²⁴² N. P. Dasgupta, S. Neubert, W. Lee, O. Trejo, J.-R. Lee, and F. B. Prinz. Atomic Layer Deposition of Al-doped ZnO Films: Effect of Grain Orientation on Conductivity. *Chemistry of Materials*, 22(16):4769–4775, August 2010. 10.1021/cm101227h.
- ²⁴³ P. Banerjee, W.-J. Lee, K.-R. Bae, S. B. Lee, and G. W. Rubloff. Structural, electrical, and optical properties of atomic layer deposition Al-doped ZnO films. *Journal of Applied Physics*, 108(4):043504, August 2010. 10.1063/1.3466987.
- ²⁴⁴ M.-L. Lin, J.-M. Huang, C.-S. Ku, C.-M. Lin, H.-Y. Lee, and J.-Y. Juang. High mobility transparent conductive Al-doped ZnO thin films by atomic layer deposition. *Journal of Alloys and Compounds*, 727:565–571, December 2017. 10.1016/j.jallcom.2017.08.207.
- ²⁴⁵ Z. Gao and P. Banerjee. Review Article: Atomic layer deposition of doped ZnO films. *Journal of Vacuum Science & Technology A*, 37(5):050802, September 2019. 10.1116/1.5112777.
- ²⁴⁶ Y. Li, R. Yao, H. Wang, X. Wu, J. Wu, X. Wu, and W. Qin. Enhanced Performance in Al-Doped ZnO Based Transparent Flexible Transparent Thin-Film Transistors Due to Oxygen Vacancy in ZnO Film with Zn–Al–O Interfaces Fabricated by Atomic Layer Deposition. *ACS Applied Materials & Interfaces*, 9(13):11711–11720, April 2017. 10.1021/acsami.7b02609.
- ²⁴⁷ A. Yanguas-Gil, J. A. Libera, and J. W. Elam. Modulation of the Growth Per Cycle in Atomic Layer Deposition Using Reversible Surface Functionalization. *Chemistry of Materials*, 25(24):4849–4860, December 2013. 10.1021/cm4029098.
- ²⁴⁸ B. Marchand, P. Jalkanen, V. Tuboltsev, M. Vehkamäki, M. Puttaswamy, M. Kemell, K. Mizohata, T. Hatanpää, A. Savin, J. Räisänen, M. Ritala, and M. Leskelä. Electric and Magnetic Properties of ALD-Grown BiFeO₃ Films. *The Journal of Physical Chemistry C*, 120(13):7313–7322, April 2016. 10.1021/acs.jpcc.5b11583.
- ²⁴⁹ M. Puttaswamy, M. Vehkamäki, K. Kukli, M. C. Dimri, M. Kemell, T. Hatanpää, M. J. Heikkilä, K. Mizohata, R. Stern, M. Ritala, and M. Leskelä. Bismuth iron oxide thin films using atomic layer deposition of alternating bismuth oxide and iron oxide layers. *Thin Solid Films*, 611:78–87, July 2016. 10.1016/j.tsf.2016.05.006.
- ²⁵⁰ H. H. Sønsteby, E. Skaar, H. Fjellvåg, and O. Nilsen. Effect of Subcycle Arrangement on Direct Epitaxy in ALD of LaNiO₃. *ACS Applied Electronic Materials*, 3(1):292–298, January 2021. 10.1021/acsaelm.0c00855.
- ²⁵¹ C. D. Pham, J. Chang, M. A. Zurbuchen, and J. P. Chang. Synthesis and Characterization of BiFeO₃ Thin Films for Multiferroic Applications by Radical Enhanced Atomic Layer Deposition. *Chemistry of Materials*, 27(21):7282–7288, November 2015. 10.1021/acs.chemmater.5b02162.
- ²⁵² N. Deepak, P. Carolan, L. Keeney, P. F. Zhang, M. E. Pemble, and R. W. Whatmore. Bismuth Self-Limiting Growth of Ultrathin BiFeO₃ Films. *Chemistry of Materials*, 27(19):6508–6515, October 2015. 10.1021/acs.chemmater.5b03034.

- 253 M. J. Müller, K. Komander, C. Höhn, R. van de Krol, and A. C. Bronneberg. Growth of Bi_2O_3 Films by Thermal- and Plasma-Enhanced Atomic Layer Deposition Monitored with Real-Time Spectroscopic Ellipsometry for Photocatalytic Water Splitting. *ACS Applied Nano Materials*, 2(10):6277–6286, October 2019. 10.1021/acsnm.9b01261.
- 254 H. Shima, K. Nishida, T. Yamamoto, T. Tadokoro, K. Tsutsumi, M. Suzuki, and H. Naganuma. Large refractive index in BiFeO_3 - BiCoO_3 epitaxial films. *Journal of Applied Physics*, 113(17):17A914, May 2013. 10.1063/1.4794878.
- 255 A. R. Akbashev, A. V. Plokhikh, D. Barbash, S. E. Lofland, and J. E. Spanier. Crystallization engineering as a route to epitaxial strain control. *APL Materials*, 3(10):106102, October 2015. 10.1063/1.4933064.
- 256 A. R. Akbashev, G. Chen, and J. E. Spanier. A Facile Route for Producing Single-Crystalline Epitaxial Perovskite Oxide Thin Films. *Nano Letters*, 14(1):44–49, January 2014. 10.1021/nl4030038.
- 257 S. J. A. Moniz, R. Quesada-Cabrera, C. S. Blackman, J. Tang, P. Southern, P. M. Weaver, and C. J. Carmalt. A simple, low-cost CVD route to thin films of BiFeO_3 for efficient water photo-oxidation. *Journal of Materials Chemistry A*, 2(9):2922–2927, February 2014. 10.1039/C3TA14824F.
- 258 F. Tyholdt, S. Jørgensen, H. Fjellvåg, and A. E. Gunnæs. Synthesis of Oriented BiFeO_3 Thin Films by Chemical Solution Deposition: Phase, Texture, and Microstructural Development. *Journal of Materials Research*, 20(8):2127–2139, August 2005. 10.1557/JMR.2005.0263.
- 259 H. Fan, G. Wang, and L. Hu. Infrared, Raman and XPS spectroscopic studies of Bi_2O_3 - B_2O_3 - Ga_2O_3 glasses. *Solid State Sciences*, 11(12):2065–2070, December 2009. 10.1016/j.solidstatesciences.2009.09.007.
- 260 M. Qian, I. Fina, M. C. Sulzbach, F. Sanchez, and J. Fontcuberta. Synergetic Electronic and Ionic Contributions to Electroresistance in Ferroelectric Capacitors. *Advanced Electronic Materials*, 5(3):1800646, 2019. 10.1002/aem.201800646.
- 261 F. Zavaliche, S. Y. Yang, T. Zhao, Y. H. Chu, M. P. Cruz, C. B. Eom, and R. Ramesh. Multiferroic BiFeO_3 films: domain structure and polarization dynamics. *Phase Transitions*, 79(12):991–1017, December 2006. 10.1080/01411590601067144.
- 262 Y. Zheng, J. Gao, C. Han, and W. Chen. Ohmic Contact Engineering for Two-Dimensional Materials. *Cell Reports Physical Science*, 2(1):100298, January 2021. 10.1016/j.xcrp.2020.100298.
- 263 L. You, N. T. Chua, K. Yao, L. Chen, and J. Wang. Influence of oxygen pressure on the ferroelectric properties of epitaxial BiFeO_3 thin films by pulsed laser deposition. *Physical Review B*, 80(2):024105, July 2009. 10.1103/PhysRevB.80.024105.
- 264 T. Yang, J. Wei, Y. Guo, Z. Lv, Z. Xu, and Z. Cheng. Manipulation of Oxygen Vacancy for High Photovoltaic Output in Bismuth Ferrite Films. *ACS Applied Materials & Interfaces*, 11(26):23372–23381, July 2019. 10.1021/acsnami.9b06704.
- 265 Y. Zhou, C. Wang, S. Tian, X. Yao, C. Ge, E.-J. Guo, M. He, G. Yang, and K. Jin. Switchable ferroelectric diode and photovoltaic effects in polycrystalline BiFeO_3 thin films grown on transparent substrates. *Thin Solid Films*, 698:137851, March 2020. 10.1016/j.tsf.2020.137851.
- 266 R. Jimenez, C. Alemany, M. Calzada, A. Gonzalez, J. Ricote, and J. Mendiola. Processing effects on the microstructure and ferroelectric properties of strontium bismuth tantalate thin films. *Applied Physics A*, 75(5):607–615, November 2002. 10.1007/s003390101072.
- 267 Y. Geng, L. Guo, S.-S. Xu, Q.-Q. Sun, S.-J. Ding, H.-L. Lu, and D. W. Zhang. Influence of Al Doping on the Properties of ZnO Thin Films Grown by Atomic Layer Deposition. *The Journal of Physical Chemistry C*, 115(25):12317–12321, June 2011. 10.1021/jp2023567.
- 268 K. Zhao, J. Xie, Y. Zhao, D. Han, Y. Wang, B. Liu, and J. Dong. Investigation on Transparent, Conductive $\text{ZnO}:\text{Al}$ Films Deposited by Atomic Layer Deposition Process. *Nanomaterials*, 12(1):172, January 2022. 10.3390/nano12010172.
- 269 B.-Y. Oh, J.-H. Kim, J.-W. Han, D.-S. Seo, H. S. Jang, H.-J. Choi, S.-H. Baek, J. H. Kim, G.-S. Heo, T.-W. Kim, and K.-Y. Kim. Transparent conductive $\text{ZnO}:\text{Al}$ films grown by atomic layer deposition for Si-wire-based solar cells. *Current Applied Physics*, 12(1):273–279, January 2012. 10.1016/j.cap.2011.06.017.
- 270 Y.-T. Liu, C.-S. Ku, S.-J. Chiu, H.-Y. Lee, and S.-Y. Chen. Ultrathin Oriented BiFeO_3 Films from Deposition of Atomic Layers with Greatly Improved Leakage and Ferroelectric Properties. *ACS Applied Materials & Interfaces*, 6(1):443–449, January 2014. 10.1021/am404498y.
- 271 P. Jalkanen, V. Tuboltsev, B. Marchand, A. Savin, M. Puttaswamy, M. Vehkamäki, K. Mizohata, M. Kemell, T. Hatanpää, V. Rogozin, J. Räisänen, M. Ritala, and M. Leskelä. Magnetic Properties of Polycrystalline Bismuth Ferrite Thin Films Grown by Atomic Layer Deposition. *The Journal of Physical Chemistry Letters*, 5(24):4319–4323, December 2014. 10.1021/jz502285f.
- 272 A. Majtyka, A. Nowak, B. Marchand, D. Chrobak, M. Ritala, J. Räisänen, and R. Nowak. Structure-Dependent Mechanical Properties of ALD-Grown Nanocrystalline BiFeO_3 Multiferroics. *Journal of Nanomaterials*, 2016:1–7, 2016. 10.1155/2016/5348471.

- ²⁷³ I. S. Golovina, M. Falmbigl, A. V. Plokhikh, T. C. Parker, C. Johnson, and J. E. Spanier. Effect of annealing conditions on the electrical properties of ALD-grown polycrystalline BiFeO₃ films. *Journal of Materials Chemistry C*, 6(20):5462–5472, 2018. 10.1039/C7TC05755E.
- ²⁷⁴ A. Afzal, Y. Javed, S. Hussain, A. Ali, M. Yaqoob, and S. Mumtaz. Enhancement in photovoltaic properties of bismuth ferrite/zinc oxide heterostructure solar cell device with graphene/indium tin oxide hybrid electrodes. *Ceramics International*, 46(7):9161–9169, May 2020. 10.1016/j.ceramint.2019.12.166.
- ²⁷⁵ P. Salles, A. Barrera, R. Guzman, M. Ramis, A. Palau, W. Zhou, and M. Coll. On the role of the Sr_{3-x}Ca_xAl₂O₆ sacrificial layer composition for epitaxial La_{0.7}Sr_{0.3}MnO₃ membranes. *Adv. Funct. Mater.*, To be submitted, March 2023.